Trinity College Dublin
Coláiste na Tríonóide, Baile Átha Cliath
The University of Dublin

Two-Dimensional Materials for Tissue Engineering and Neural Interfacing Applications

Jack Philip Maughan

A thesis presented for the degree of
Doctor in Philosophy
in the subject of Physics

Research institute

School of Physics, Trinity College Dublin, Ireland

Advanced Materials and Bioengineering Research Centre (AMBER), Dublin, Ireland

Supervisor

Prof. Jonathan N. Coleman

Chemical Physics of Low-dimensional Nanostructures

School of Physics

Trinity College Dublin

Co-supervisor

Prof. Fergal J. O'Brien

Tissue Engineering Research Group

Department of Anatomy and Regenerative Medicine

Royal College of Surgeons in Ireland

2025

Abstract

The pages of a book behave very strangely compared to a block of wood – two-dimensional (2D) nanomaterials are no different. Offering unique properties that differ from their bulk counterparts, this simple change in dimensionality unlocks a world of applications that has the potential to revolutionize biomedical research. In this thesis, I explore some of these extraordinary properties, demonstrating how they may be harnessed to advance nerve and bone regeneration strategies, and to create innovative neural interfacing devices. Focusing primarily on graphene and 2D boron, this work showcases the wide-reaching impact of these versatile materials.

In Chapter 2, graphene was applied to the challenge of neuronal medical device development, with a focus on neuronal regeneration using electrical stimulation. A soft, electrically conductive, and biocompatible collagen-graphene composite material (NeuroGraph) was developed, with diverse fabrication capabilities into scaffolds, microneedles, and bioelectronic circuits. Electrical stimulation on NeuroGraph substrates led to a significant enhancement in neurite outgrowth and cellular morphology, demonstrating its potential as a promising platform material for electroconductive tissue regeneration.

Building on this, in Chapter 3 the graphene formulation was further refined for biocompatibility and conductivity, and a flexible, biocompatible polymer-graphene composite system was developed by combining the graphene formulation with polycaprolactone (PolyGraph). The electrochemical properties of this material were enhanced by surface roughening with NaOH, and coating with conductive AuPd. This enabled the creation of flexible, high-performance microelectrode neural interfaces with significant potential for applications in both electrical stimulation therapies and bidirectional neural interfacing.

Finally, demonstrating the breadth of possibilities in the field of 2D materials, in Chapter 4 boron nanoplatelets exfoliated from a non-layered precursor using liquid-phase exfoliation were combined with collagen to form collagen-boron (BColl) scaffolds. By leveraging the 2D morphology of the nanoplatelets alongside the intrinsic bioactivity of boron and support of a collagen matrix with tailored characteristics for bone repair, these scaffolds were shown to enhance osteogenesis, angiogenesis, and neurogenesis, all while preventing infection, inflammation, and stiffness mismatch. Taken together, these results showcase boron's potential to offer multifunctional benefits to clinically relevant aspects of next-generation bone biomaterial development.

Though this work represents only a microcosm of the immense potential that 2D nanomaterials hold for biomedical applications, the findings presented herein highlight key challenges and opportunities within the field. The versatility of these materials presents a promising vision for future devices and treatments, smoothing the trade-off between physicochemical and biological properties. As our understanding of the nanoscale world and the complex interplay between it and the vast landscape of regenerative medicine and neural interfacing deepens, these materials could fundamentally reshape how we approach regeneration and augmentation.

Acknowledgements

Without pretension, genuinely – where do I begin? It's cliché to say that this thesis could not have happened without the people around me – cliché, but true. From supervisors and colleagues lifting me up when science and fortune knocked me down, to friends and family who were my many ports during a sometimes stormy four years, professionally and personally. I have the deepest gratitude for the life I have, the people I love, and for how lucky I am to be where I am.

Without further ado, the first people I need to thank are my supervisors, Prof. Jonathan Coleman and Prof. Fergal O'Brien. When this project first came to my attention in the final year of my undergrad, it seemed like the universe had arranged this collaboration just for me. It's been a genuine honour to work for not one but two incredibly talented scientists, whose drive, direction, and excellence in their respective fields are inspirations for many. I also extend my thanks to the Advanced Materials and Bioengineering Research (AMBER) Centre, Science Foundation Ireland and the IRFU Charitable Trust for providing financial support, as well as boosting and encouraging our research at every step, and to the School of Physics and Tissue Engineering Research Groups in TCD and RCSI respectively for hosting our research. To all of my collaborators on projects throughout my PhD, it was a pleasure working with you all.

It's a rare enough position to be straddling two groups in one PhD – however, far from feeling like an outsider in either group, the wonderful people in the Coleman Group in TCD and the Tissue Engineering Research Group in RCSI always made me feel like I had a true home in both labs. I could go on for hours (just try and stop me) about all those who have helped me throughout this process, so here we go. To Cian Gabbett, never mind what they say about you – you're a wonderful man, and I couldn't have asked for a better desk-mate these 4 years. May your sword stay sharp, and your outlook stay sunny! Luke & Eoin, our fates have been tied to each other for *eight* years now – from whiskey-tinged lockdown dinners to growing together as scientists, I'm excited to see where our careers take us next. James, for fielding what were, in hindsight, inane questions at the beginning (and for probably a while after the beginning) of my PhD with grace and humour, I am forever grateful. To all the rest of the Coleman group past and present, let no-one ever say that physicists aren't amazing craic – Adam, Tian, Kev, Harneet, Bharathi, Rebekah, Yash, Dómhnall, Shixin, Anthony, Dan, Oran(s), Emmet, Jose, Mark, Dom, Seán and Joe, you are all the thermodynamically-favoured solvents to my layered nanomaterials.

Taking a short jaunt across the cobblestones, down Dawson Street, and into 123 St. Stephen's Green, there are not enough kind words to say about our rag-tag group of little TERGlings – here's just a few. Pedro – you took in this lost little nanoscientist who didn't know his arse from his astrocyte, and you gave me the confidence to *actually* believe I could make progress and finish my PhD. You were the biology sensei to put all others to shame! Martyna, there's a vibe I have with certain people where all sense goes out the window and our communication is just pure goofing around, and to have that with you in the lab brightened many a day – stay cool, stay creative, and stay Corkonian. They say you don't win friends with salad, but you should make friends with Liam – your humour, Simpsons references and our shared love of sad-girl-indie music are very special to me, even if you are from Athlone. Cian, while you are already the most delightfully humble and kind man to have graced our halls, I must bestow upon you one more prize – the Goodest Guy Going, 2024. With every smile, joke, and word of wisdom, you've really earned this one! Matthew, when you find someone with the same exercise brain-worm as you, you can't help but immediately click – you may be big and strong, but you're not strong enough to break the bond we share (but don't try anyway, just in case). Javier, ¡qué hombre! Always with a smile on your face, an infectious curiosity that shines from you, and a damn fine moustache (also on your face), you've been a pleasure to share this time with. Pádraig, you've always been a PPI to me – a perfect pal, incredible! We still need to do that race. Tara, ever calm, ever collected, ever kind, we need more people like you in the world. Elizabeth and Vera, ye and Martyna are the most inspiring trio of ladies, and damn fine lunch company! Juan Carlos and Hadeel, I love that ye are always up for a little chat (and an All Rosey coffee). Ian, when you were suddenly landed with a mid-20s physicist who seemed to think you were his supervisor, you took it all in your stride beautifully! I cannot tell you how many times talking to you has made me feel better, whether about my own work, career in science, or just life in general. You're one of the best scientists I've ever met, and I'm continually inspired by your drive and creativity – looking forward to seeing that all flourish in a future Woods Group! Adrian, the steady hand at the wheel of the Spinal Cord team, you're an absolutely wonderful person to work with, and I promise I haven't held any grudge for all the Mayo slander over the years… or have I? And Becky, for always bringing style to the office, and for being a kind ear many, many times. To all the folks I am rapidly running out of the space to mention (Vincent, Giulio, Chris, Meric, Katelyn, Austyn, Arlyng, Anthony, Joanna, Donagh, Mark, Annie, Hólmfríður, Julia, Rena, Sandra, Avelino, Claudio, Marko, Francisco, Michela, Rachael, Eavan, Louise, Adrián, Antonio, Fran, Jess, Joanne, KK, Marcin, Raghad, Mariangela, Nezar, Ronja, Shan, Sina, Bingbing, Tom, and

many more!), thank you for so many lunches, late lab evenings, office chats, conference adventures, and for being the great people that you are.

My life was a hell of a lot more than just this PhD these last few years (thankfully), and without the support of my incredible friends and family, I'd have been up a graphene-y creek without so much as a spatula to paddle. Running has kept me sane (or appropriately insane) for years, but I ascribe that more to the wonderful people (my tireless coach Iain, Juno, Joe, Peter, Eavan, Moya, Grace, Sinéad, Ev, Joanne, Fiona, Oren, Conor, Jordan, Kirsten, James, Jen, Quinn, Seán, Matthieu, Eoin K, Luke, Laura, Pierre, Dylan, Fintan, Seán, Caron, Claire, Rory, Michael, John, Al(l)an, and many, many more) in DUHAC, Clonliffe Harriers A.C and elsewhere than to the running itself! To many more chatty miles together, with all this post-PhD free time I'm sure to have. To the folks from home (JB, Simon, Hussey, Ciarán, Jordan, Bill, Robin, David, and Ethan) you've seen me grow from a wee 'un up until now, and I can't thank ye enough for keeping my head screwed on, for keeping my life light, and for trips I look forward to all year! To Rowan and Brian, for deep talks and absolutely nonsensical chats over lunch and cups of tea, I am so incredibly lucky to have you two fine gentlemen in my life. To my Schols friends, the TCD gravy train may have ended, but our friendships sure haven't!

And last but most definitely not least, to my extraordinary family – Mam, Dad, Grace and Daragh, Granny, Grandad, and my wonderful aunts, uncles, and cousins – you have all helped so much more than you know. Dealing with someone going through a PhD, putting up with their complaints, checking in on them, being their rock through the hardest of times both personally and professionally, and doing it all while being the most loving, kindest, funniest people is worthy of a PhD in its own right. From the bottom of my heart, thank you – you have all made me the person I am today, and this is as much yours as it is mine.

It has been a wild journey, and I'm a very different person now than I was when I started this PhD. Thanks to the support of each and every one of you, I have hope and faith that the only way from here is towards happiness. As a sign off, those of you who know me will know I'm a fiend for quoting song lyrics – so, to paraphrase one of my own: you are all the best of me. You make me come alive.

List of Publications, Presentations & Awards

Publications

1. *Cyclic Production of Biocompatible Few-Layer Graphene Ink with in-Line Shear-Mixing for Inkjet-Printed Electrodes and Li-Ion Energy Storage.* – Carey, T.; Alhourani, A.; Tian, R.; Seyedin, S.; Arbab, A.; **Maughan, J.**; Šiller, L.; Horvath, D.; Kelly, A.; Kaur, H.; Caffrey, E.; Kim, J. M.; Hagland, H. R.; Coleman, J. N. – npj 2D Materials and Applications, 2022, https://doi.org/10.1038/s41699-021-00279-0.

2. *Highly Conductive Networks of Silver Nanosheets* – Kelly, A. G.; O'Reilly, J.; Gabbett, C.; Szydłowska, B.; O'Suilleabhain, D.; Khan, U.; **Maughan, J.**; Carey, T.; Sheil, S.; Stamenov, P.; Coleman, J. N. – Small, 2022, https://doi.org/10.1002/smll.202105996.

3. *Liquid Phase Exfoliation of Nonlayered Non-van Der Waals Iron Trifluoride (FeF_3) into 2D-Platelets for High-Capacity Lithium Storing Cathodes.* – Chen, T.; Kaur, H.; McCrystall, M.; Tian, R.; Roy, A.; Smith, R.; Horvath, D. V.; **Maughan, J.**; Konkena, B.; Venkatesan, M.; Synnatschke, K.; Carey, T.; Liu, J.; Pepper, J.; Zhang, R.; Backes, C.; Nicolosi, V.; Xia, H.; Coleman, J. N. – FlatChem, 2022, https://doi.org/10.1016/j.flatc.2022.100360.

4. *Collagen/Pristine Graphene as an Electroconductive Interface Material for Neuronal Medical Device Applications.* – **Maughan, J.**; Gouveia, P. J.; Gonzalez, J. G.; Leahy, L. M.; Woods, I.; O'Connor, C.; McGuire, T.; Garcia, J. R.; O' Shea, D. G.; McComish, S. F.; Kennedy, O. D.; Caldwell, M. A.; Dervan, A.; Coleman, J. N.; O'Brien, F. J. – Applied Materials Today, 2022, https://doi.org/10.1016/j.apmt.2022.101629. *Basis for Chapter 2

5. *Applying Patient and Public Involvement in Preclinical Research: A Co-created Scoping Review.* – Carroll, P.; Dervan, A.; Maher, A.; McCarthy, C.; Woods, I.; Kavanagh, R.; Beirne, C.; Harte, G.; O'Flynn, D.; O'Connor, C.; McGuire, T.; Leahy, L. M.; Gonzalez, J. G.; Stasiewicz, M.; **Maughan, J.**; Gouveia, P. J.; Murphy, P. J.; Quinlan, J.; Casey, S.; Holton, A.; Smith, É.; Moriarty, F.; O'Brien, F. J.; Flood, M. – Health Expectations, 2022, https://doi.org/10.1111/hex.13615.

6. *The Role of Patient and Public Involvement (PPI) in Pre-Clinical Spinal Cord Research: An Interview Study* – Carroll, P.; Dervan, A.; McCarthy, C.; Woods, I.; Beirne, C.; Harte, G.; O'Flynn, D.; O'Connor, C.; McGuire, T.; Leahy, L. M.; Gonzalez, J. G.; Stasiewicz, M.; **Maughan, J.**; Quinlan, J.; Smith, É.; Moriarty, F.; O'Brien, F. J.; Flood, M., 2023. – PLOS One, 2024, https://doi.org/10.1101/2023.07.19.23292756.

7. *A Biomimetic, Bilayered Antimicrobial Collagen-Based Scaffold for Enhanced Healing of Complex Wound Conditions* – McGrath, M.; Zimkowska, K.; Genoud, K. J.; **Maughan, J.**; Gutierrez Gonzalez, J.; Browne, S.; O'Brien, F. J. – ACS Applied Materials & Interfaces, 2023, https://doi.org/10.1021/acsami.2c18837.

8. *Knot Architecture for Biocompatible and Semiconducting Two-Dimensional Electronic Fibre Transistors.* – Carey, T.; **Maughan, J.**; Doolan, L.; Caffrey, E.; Garcia, J.; Liu, S.; Kaur, H.; Ilhan, C.; Seyedin, S.; Coleman, J. N. – Small Methods, 2024, https://doi.org/10.1002/smtd.202301654.

9. *Cold sprayed Ta-Ag composites: Mechanistic insight into enhanced corrosion resistance and antibacterial ability* – Yu, P.; Perumal, G.; Genoud, K. J.; **Maughan, J.**; O'Brien, F. J.; Barbizon, D.; Xie, Y.; Yin, S.; Lupoi, R. – Corrosion Science, *2024*, https://doi.org/10.1016/j.corsci.2024.112284.

10. *Electrostimulation via a 3D-printed, biomimetic, neurotrophic, electroconductive scaffold for the promotion of axonal regrowth after spinal cord injury* – Leahy, L.; Woods, I.; Gutierrez-Gonzalez, J.; **Maughan, J.**; O'Connor, C.; Stasiewicz, M.; Kaur, K.; Monaghan, M. G.; Dervan, A.; O'Brien, F. J. – Materials Today, 2024, https://doi.org/10.1016/j.mattod.2024.07.015.

11. *Boron Nanoplatelets as an Osteogenic, Anti-Microbial and Mechanically Reinforcing Additive for Biomaterial Scaffolds for Bone Repair* – **Maughan, J.;** Kaur, H.; Prendeville, L.; Carey, T.; O'Connor, C.; Synnatschke, K.; Palomeque, J. C.; Woods, I; O'Brien, F. J.; Coleman, J. N. – Submitted to Advanced Composites and Hybrid Materials for review, 2025. *Basis for Chapter 4

12. *Potassium-ion Battery Cathodes with Potassium Ferricyanide Nanoplatelets: Thin Platelets and Thick Electrodes Unlock High Areal Capacity and Excellent Rate Performance* – Kaur, H.; **Maughan, J.**; Submitted to Advanced Energy Materials for review, 2024.

13. *3D-printed, biomimetic, conductive MXene-microfiber composite scaffolds enhance the axonal growth-promoting characteristics of electrical stimulation.* – Woods, I.; Spurling, D.; Sunil, S.; **Maughan, J.**; Gutierrez Gonzalez, J.; Dervan, A.; Nicolosi, V.; O'Brien, F. J. – bioRxiv, 2024.

Presentations

1. Graphene in Healthcare, *2021, Online*
2. Graphene Online, *2021, Online*
3. Nature – Technologies in Neuroengineering, *2022, Online*
4. Bioengineering in Ireland, *2022, Galway, Ireland*
5. Tissue Engineering and Regenerative Medicine International Society EU Meeting, *2022, Krakow, Poland*
6. European Society for Biomaterials, *2022, Bordeaux, France*
7. Graphene Week, *2022, Munich, Germany*
8. 2D Materials for Biomedical Applications, *2022 – Symposium organiser Maughan, J., with plenary speaker Prof. Kostas Kostarelos, Dublin, Ireland*
9. Neuroscience Ireland Young Investigator Symposium, *2022, Dublin, Ireland*
10. AMBER Conference, *2023, Limerick, Ireland*
11. Neuroscience Ireland Early Career Researcher Panel, *2023, Dublin, Ireland*
12. AMBER Conference, *2024, Dublin, Ireland*
13. Graphene Week, *2024, Prague, Czechia*
14. Materials Research Society Fall Meeting, *2024, Boston, USA*

Awards

1. AMBER Image Competition, Best Image – *Connected Clusters, with Dr. Tara McGuire*
2. RCSI Research Day Image Competition, Best Image – *Gilded Scaffolds, with Dr. Cian O'Connor*
3. AMBER Conference 2024, Best Poster in Health Theme – *2D Boron Nanosheets as an Osteogenic, Anti-Microbial and Mechanically Reinforcing Additive for Bone Tissue Engineering Scaffolds*
4. Graphene Week 2024, Best Poster on Sustainable Use of Graphene – *PolyGraph: Biocompatible and Flexible Graphene Composites for Neural Interfacing Devices*
5. AMBER Collaboration Fund 2024 – *Enhanced catalytic efficiency for LDPE degradation by liquid phase exfoliation of Fe-doped ceria to form 2D nanosheets, with Rachel Breen, University College Cork*
6. Engineers Ireland Medal Finalist, Bioengineering in Ireland 2025 – *A Trip to Another Dimension – 2D Materials for Tissue Repair and Advanced Neural Interfaces*

Table of Contents

List of Figures & Tables

Chapter 1

Chapter 2

Chapter 3

Chapter 4

List of Abbreviations

AFM – Atomic force microscopy

ALP – Alkaline phosphatase

ANOVA – Analysis of variance

AuPd – Gold-palladium alloy

BCI – Brain-computer interface

BColl – Boron-collagen composites

BMP – Bone morphogenic protein

β-NGF – Nerve growth factor-beta

BSA – Bovine serum albumin

CA – Chronoamperometry

CIC – Charge injection capacity

CP – Chronopotentiometry

CNS – Central nervous system

CSC – Charge storage capacity

CV – Cyclic voltammetry

CVD – Chemical vapour deposition

DHT – Dehydrothermal

DRG – Dorsal root ganglia

ECM – Extracellular matrix

ECoG – Electrocorticography

EDX – Energy-disperse X-ray spectroscopy

EEG – Electroencephalogram

EIS – Electrochemical impedance spectroscopy

ELISA – Enzyme linked immunosorbent assay

EPR – Enhanced permeability and retention

ES – Electrical stimulation

FBR – Foreign-body response

FBS – Fetal bovine serum

FDM – Fused deposition modelling

fMRI – Functional magnetic resonance imaging

GelGr – Gelatin-stabilised graphene

GO – Graphene oxide

H&E – Haematoxylin & eosin

HyA – Hyaluronic acid

IL – Interleukin

IPA – Isopropanol

iPSC – Induced pluripotent stem cell

LCC – Liquid cascade centrifugation

LDH – Lactate dehydrogenase

LPE – Liquid phase exfoliation

MEA – Micro-electrode array

MNA – Micro-needle array

MPCN – Mouse primary cortical neuron

NaOH – Sodium hydroxide

NeuroGraph – Collagen-graphene composites

NMP – N-methyl-2-pyrrolidone

PBS – Phosphate-buffered saline

PCL – Polycaprolactone

PDMS – Polydimethylsiloxane

PEDOT:PSS – Poly(3,4-ethylenedioxythiophene):polystyrene sulfonate

PEG – Polyethylene glycol

pG – Pristine graphene

PNS – Peripheral nervous system

PolyGraph – Polymer-graphene composites

PVA – Polyvinyl alcohol

PVP – Polyvinylpyrrolidone

PVPGr – Polyvinylpyrrolidone-stabilised graphene

rGO – Reduced graphene oxide

rMSC – Mesenchymal stem cells, isolated from rats

ROS – Reactive oxygen species

RT – Room temperature

SC – Sodium cholate

SCGr – Sodium cholate-stabilised graphene

SDC – Sodium deoxycholate

SEM – Scanning electron microscopy

SLA – Stereolithography

SNR – Signal-to-noise ratio

TEM – Transmission electron microscopy

TGA – Thermogravimetric analysis

TMDC – Transition metal dichalcogenide

TrypGr – Trypsin-treated gelatin-stabilised graphene

µCT – Micro computed tomography

VEGF-A – Vascular endothelial growth factor-A

VT – Voltage transients

XRD – X-ray diffraction

Declaration

I declare that this thesis has not been submitted as an exercise for a degree at this or any other university and it is entirely my own work.

I agree to deposit this thesis in the University's open access institutional repository or allow the Library to do so on my behalf, subject to Irish Copyright Legislation and Trinity College Library conditions of use and acknowledgement.

I note that this thesis includes collaborative work, duly acknowledged in the text where appropriate.

I consent to the examiner retaining a copy of the thesis beyond the examining period, should they so wish (EU GDPR May 2018).

Signed: 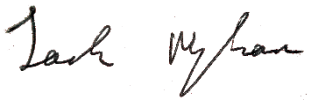 Date: 26th of November 2024

Beauty, Nearby

Ask the artist in the gutter
What propels each new try
Or the poet in the café
Why write one more line
They stare for a moment
Then softly reply
"It goes without saying,
There's beauty, nearby"

Ask the wife on the wards
Why she's there every night
Or the rebel in solitary
How she continues her fight
They look past you, yearning,
For days to come and gone by
"I choose to believe
There's beauty, nearby"

Ask the drunk on the towpath
What keeps him alive
Or the child in the warzone
How they keep from crying
They cast a long glance
At the birds, flying high
"One day I'll escape
To the beauty, nearby"

There's a good time coming
Be it ever so far away
By lake water lapping
Or on pavements grey
I reach for the moments
Of hope, come to stay
It's clear to me now
There's beauty,
Someday

"Perhaps I could best describe my experience of doing mathematics in terms of entering a dark mansion. You go into the first room and it's dark, completely dark. You stumble around, bumping into the furniture. Gradually, you learn where each piece of furniture is. And finally, after six months or so, you find the light switch and turn it on. Suddenly, it's all illuminated and you can see exactly where you were. Then you enter the next dark room..."

—

Andrew John Wiles, mathematician famous for proving Fermat's Last Theorem

Chapter 1 Introduction

Edwin Abbott Abbott's seminal work "Flatland: A Romance of Many Dimensions", released in 1884[1], marked the first time many readers had thought deeply about the concept of dimensions. Yes, they may have said, the world has things that are *thin*, and things that are *long*, even those that are *point-like*, but what difference does it make? This question belies a world of difference between the dimensions we move through, and few places is this more apparent than at the nanoscale. Dimensionality has an effect in ways we appreciate without thinking about – after all, it's harder to light a fire with a block of wood than with a sheet of paper – and in ways that continue to surprise us. It's how we leverage the dimensionality of materials that unlocks a world of new possibilities, in electronics, chemistry, biomedicine, and beyond. In this thesis, I will dive into some of the biomedical applications of two-dimensional materials, specifically in the fields of tissue engineering, regenerative medicine, and neural interfacing.

The first study (**Chapter 2**) focused on the development of a graphene-collagen (NeuroGraph) composite for neural tissue engineering. This work showed that electrical stimulation, delivered via a conductive, biocompatible NeuroGraph substrate, could enhance the outgrowth of primary neurons grown on its surface. This has important implications for electrical stimulation and conductive substrate-mediated tissue engineering in both the peripheral and central nervous systems. Building on this work, the second study (**Chapter 3**) developed a graphene-polycaprolactone composite (PolyGraph) with optimal biocompatibility and conductivity, and demonstrated its use for the fabrication of flexible microneedle-based neural interfacing electrode arrays. The electrical properties of PolyGraph were optimised to pave the way for future delivery of electrical stimulation to neurons in a hydrogel, and the recording of action potentials from neurons in a brain slice model. Both are important abilities for neural interfaces, thus

indicating the potential promise and versatility of PolyGraph for the fabrication of multimodal neural interfacing devices. Finally, to explore the vast world of 2D materials beyond graphene, the last study (**Chapter 4**) demonstrated the use of 2D boron nanoplatelets in bone tissue engineering, showing that boron-loaded collagen (BColl) scaffolds led to a significant increase in mineralisation. This study also showed that boron loading caused a shift towards a scaffold environment more favourable to angiogenesis and neurogenesis, and more hostile to inflammation and microbial infiltration, each key outcomes for effective bone regeneration.

Taken together, these studies demonstrate a significant advance in our understanding of the applications of 2D nanomaterials to tissue engineering, regenerative medicine, and neural interfacing devices. These applications are enabled in large part by the unique dimensionality of these materials, unlocking properties which would otherwise be impossible to achieve with the bulk. In this section, I will explore how these materials are synthesised, rendered biocompatible, and applied to a wide range of fields within biomedicine and biomedical engineering - establishing this work relative to the literature, and explaining how it moves our understanding forwards.

1.1 2D Materials

Although the concept of dimensionality in materials has been explored and exploited, deliberately and accidentally, for thousands of years[2,3], the discovery of quasi-two-dimensional materials, where one of the dimensions of the material is <100 nm, has come relatively recently. The first 2D material synthesised (on purpose) was graphene, a 2D allotrope of carbon that was isolated by Andre Geim and Kostya Novoselov in 2004, by mechanical exfoliation of highly oriented pyrolytic graphite[4]. This discovery set off a cascade of research into both graphene and a huge range of other 2D materials[5–9], which offered superb properties that were unachievable using bulk materials. To illustrate why, imagine a book - this thesis for example. About the only danger when reading a book, aside from being bored to death, is papercuts[10]. However, it's not the book itself that gives you a papercut, but the individual pages – kudos to you if you manage to get a papercut from the spine of this book. This brief thought experiment shows that the pages of the book function as quasi-2D sheets, and therefore have properties (in this case, sharpness) that differ from the book as a whole. The same principle is true for nanomaterials. There are two ways that differing dimensionalities can lead to new properties. Firstly, the *intrinsic* properties of the materials can change due to the dimensionality. For instance, the conductivity of graphene

or β_{12}-borophene arises due to delocalisation of π-electrons across the atomic bonds[11], with electrons no longer being shared between the entire lattice of the graphite, and acting as free charge carriers, a feature which is diminished in bulk graphite, and not present at all in bulk boron[12]. The second way that these properties can arise is independent of the material itself, and solely due to the 2D nature of the material – this includes mechanical reinforcement, enhanced specific surface area, and network effects. It is worth noting that dimensionality is not an on-off switch, but a spectrum – many systems behave in a highly layer-dependent manner[13–16].

As more materials have been successfully exfoliated and added to the menagerie of existing 2D materials[17–19], more properties have been made available. If an insulating 2D material is required, for example in transistor gate dielectrics, hexagonal boron nitride may be used[20]. If a semiconductor is required, MoS_2, WSe_2 or other transition metal dichalcogenides (TMDCs) are a good choice[21]. Properties such as thermal conductivity[22], fluorescence[23], high mechanical strength[24], magnetism[25,26], tuneable electrical[16,27] and optical bandgaps[28,29], tuneable absorbance[28,29], high reactivity[30], photothermal effects[31] and even superconductivity[32] can be found in materials in the 2D family[33,34]. Perhaps the most consequential property of 2D materials is their much higher surface area to volume ratio compared to other dimensionalities. The surface area:volume ratio for nanosheets will be higher than it is for spherical nanoparticles provided the radius of the nanoparticle is greater than 1.5 times the thickness of the nanosheet, as derived in Fig 1.1. This has a multitude of consequences, since more of the active material is exposed to the environment at a given time than for any other material morphology[33], allowing for more efficient drug delivery per unit of material[35], and for the production of highly capacitive electrodes for batteries and electronics[36].

Nanoplatelet

$$\text{Volume} = l \times w \times t$$

$$\text{Area} = 2 \times l \times w$$

$$\text{Area:Volume} = \frac{2 \times \cancel{l \times w}}{\cancel{l \times w} \times t} = \frac{2}{t}$$

Nanoparticle

$$\text{Volume} = \frac{4}{3}\pi r^3$$

$$\text{Area} = 4\pi r^2$$

$$\text{Area:Volume} = \frac{\cancel{4}\ \cancel{\pi} r^{\cancel{2}}}{\cancel{\frac{4}{3}}\ \cancel{\pi} r^{\cancel{3}}} = \frac{3}{r}$$

Surface Area to Volume Ratio

$$\therefore \text{Area:Volume}_{\text{nanoplatelet}} > \text{Area:Volume}_{\text{nanoparticle}}$$

$$\text{when } \frac{2}{t} > \frac{3}{r}$$

$$2r > 3t$$

$$t < \frac{2r}{3}$$

*Fig. 1.1 – **Surface Area:Volume Ratio of 2D Materials vs. Nanoparticles:** Derivation showing that the surface area:volume ratio will be larger for thin nanosheets than for the vast majority of nanoparticles.*

Beyond the surface area, the simple fact that the edges of these materials are atomically sharp can lead to anti-microbial activity[37,38] and other edge effects[39]. Finally, the nanoscale dimensions of these materials lead to strong quantum confinement of electrons and phonons, which can lead to photoluminescent effects[40,41], and open the door for the study of novel physical phenomena such as confined excitons, with a view to the development of quantum devices[42].

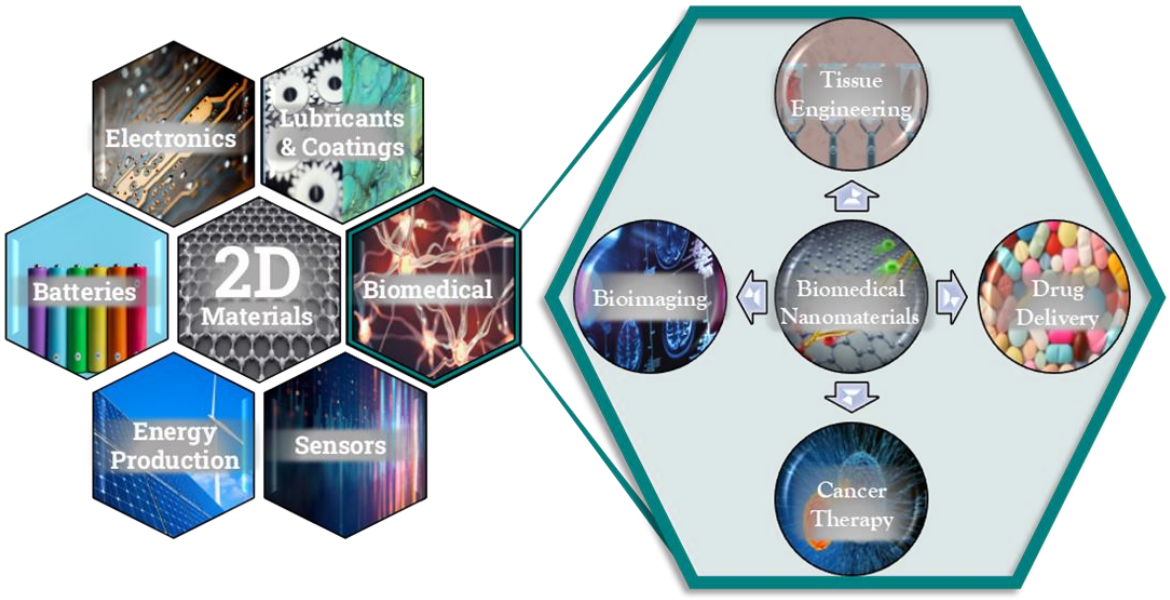

*Fig. 1.2 – **Applications of 2D Materials:** 2D materials have applications across science and technology, with some of the most promising applications arising in the biomedical field – this schematic shows some of the most active areas of research that leverage the novel properties of 2D materials for critical applications.*

These extraordinary properties have been leveraged for a wide range of applications beyond those already mentioned, including electronics[27,43–46], batteries[47–54], coatings & lubricants[55–57], energy production[58–60], catalysis[61], and biomedical applications[62–77] (Fig. 1.2). For biomedical applications in particular, the unique properties and processability of 2D materials unlock a plethora of possibilities and applications. These include anti-microbial effects[78–81], drug delivery[82–89], bio-sensing[90–92], bio-imaging[86,93], cancer therapy[65,94,95], mechanical reinforcement[24,96,97], bioelectronics[98–102] and tissue engineering[72,103,104].

While many theses have been and will be written about the innumerable properties and applications of 2D materials, this work will focus primarily on two members of this family, both elemental 2D materials (Xenes) – graphene and 2D boron.

1.1.1 Graphene

In the realm of 2D materials, the graphene family (**Fig. 1.3**), which includes pristine graphene (pG), graphene oxide (GO)[105], and reduced graphene oxide (rGO)[106], has attracted significant attention thanks to the extraordinary electrical, thermal and mechanical properties of its members[24,98,100,107]. The pG basal plane consists of a one atom thick layer of sp^2 hybridised carbon atoms arranged in a planar honeycomb structure[4], which can be functionalised using a range of techniques[108]. This structure endows graphene with remarkable, layer-dependent properties such as high electron mobility of up to 200,000 $cm^2/V{\cdot}s$[109], excellent electrical conductivity[107], thermal conductivity between 2-4 $kW/m{\cdot}K$[110], and a Young's modulus of around 1 TPa[109], making it one of the strongest known materials.

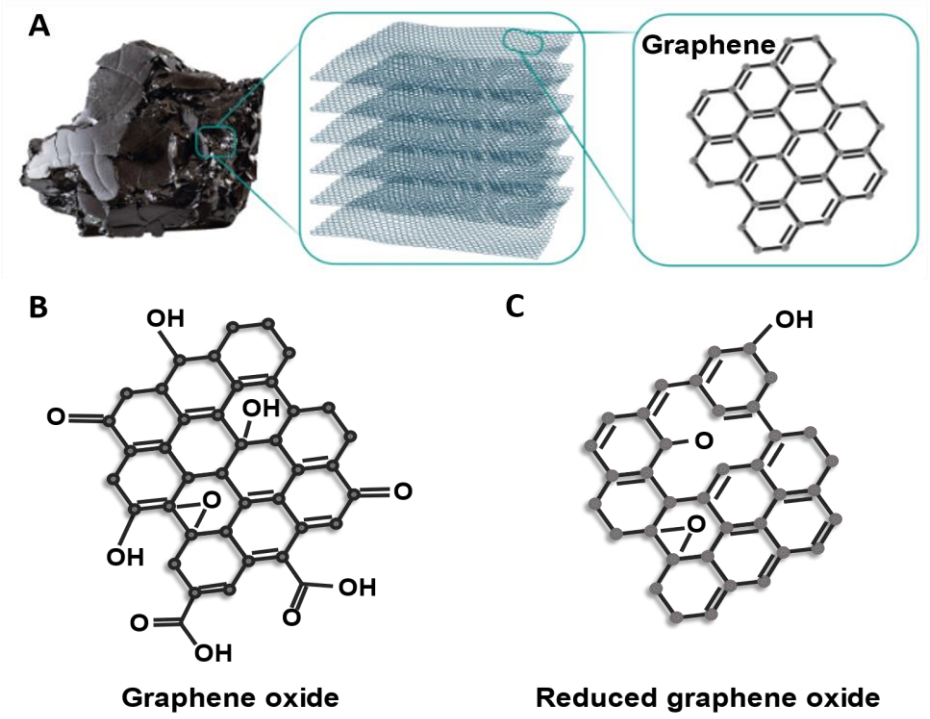

Fig. 1.3 – Graphite and the Graphene Family: *Graphite consists of stacked layers of carbon atoms arranged in a hexagonal honeycomb pattern, which, when separated, are known as pristine graphene (pG) (A). These layers can be synthesised with oxide functional groups, in which case they are known as graphene oxide (GO) (B), which can then be reduced to form reduced graphene oxide (rGO) (C).*

GO is distinguished by the presence of plentiful surface and edge oxides such as =O, –COOH, and –OH. These functional groups have the benefit of rendering the surface hydrophilic and providing additional linkage sites for further functionalisation[108] – however, they also disrupt the basal plane of the resultant nanosheets, resulting in a sharp decrease in nanosheet conductivity compared to pG[111]. To partially restore the conductivity of pG, rGO is synthesised by reducing GO in order to recover the delocalised π-electron structure. While this process improves the

conductivity relative to GO, it typically remains lower than pG, due to defects and incomplete removal of functional groups[112]. Nevertheless, rGO represents a middle ground between the hydrophilic nature of GO and the superior electrical properties of pG.

Pristine graphene, while offering the highest electrical conductivity[105,107], strength[113], and processability[107] of the family, poses challenges for biomedical applications, due to its hydrophobicity and the resulting potential for aggregation, cytotoxicity and immune response. These challenges and approaches to address them will be discussed in **Sections 1.1.3.3** and **1.2.1**.

1.1.2 Boron

Boron, the fifth member of the periodic table, occurs in a number of allotropes (**Fig. 1.4**), the most common amongst which are the crystalline α-rhombohedral, β-rhombohedral and α-tetragonal forms, and amorphous forms including a fine brown powder and a glassy solid[114] **(Fig. 1.4 B)**. As an additive, boron has found widespread applications, from those that are seemingly run of the mill, such as its use in bleaching agents for washing detergents[115], to those as exotic as its use in neutron shields for nuclear reactors[116]. Most notably for this work, boron also functions as an essential trace mineral for a range of biological functions – this will be discussed in more detail in **Section 1.2.3**.

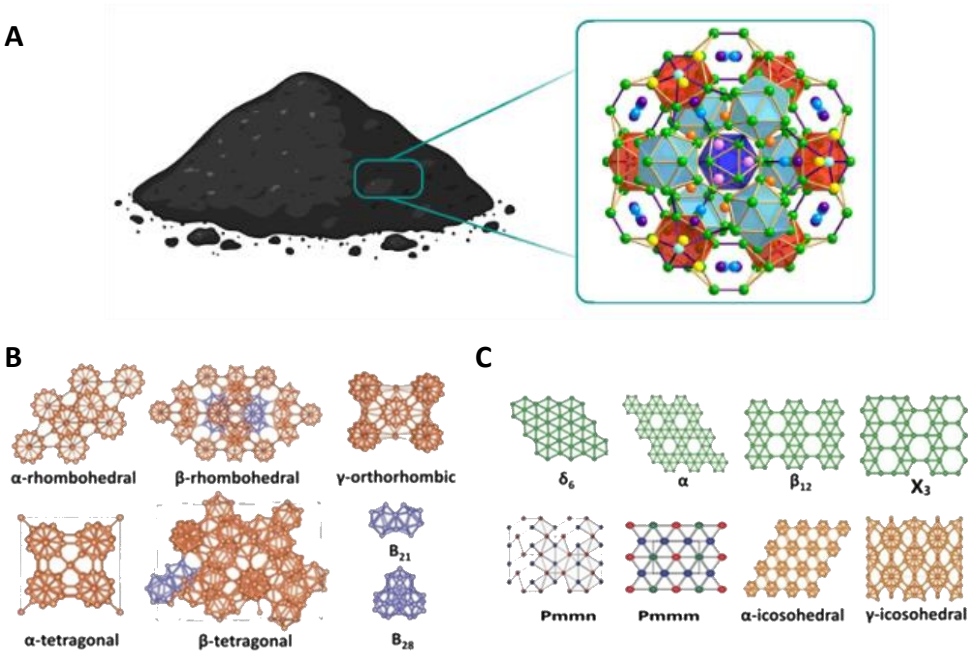

*Fig. 1.4 – **Boron and the Borophene Family:** **A)** Boron comes in a wide variety of allotropes, including β-rhombohedral, the most common crystalline allotrope. **B)** Other allotropes are possible, and have a diverse range of stabilities, properties, and abundances. **C)** When exfoliated to form borophene, there are a number of stable polymorphs, the most common of which is β_{12}-borophene. Adapted from Widom & Mihalkovič 2007[117] (A) and Kumar et al. 2024[118] (B,C).*

When exfoliated into its 2D morphology, boron takes two primary forms. The first is borophene, a boron allotrope arising from the transition at low thickness to a different crystal structure, a regime in which conductivity and other superlative properties emerge[11,119]. There are several sub-allotropes of borophene itself, such as *2-Pmmn*, *8-Pmmn*, β_{12} and χ_3 borophene[120] (**Fig. 1.4 C**). Borophene was first experimentally realised in 2015, and has until now mostly been synthesised using bottom up, substrate-supported approaches such as chemical vapour deposition and molecular beam epitaxy, onto substrates such as Ag(111)[121,122], Au(111)[123] and Cu(111)[124,125]. Recent studies have even achieved freestanding β_{12}-borophene allotropes, a feat previously thought impossible due to the influence of the substrate on borophene crystallinity[126–128]. These difficult fabrication conditions, requiring specially chosen substrates and an ultra-high vacuum environment, spurred a push towards alternative syntheses of borophene and boron nanoplatelets, such as liquid phase exfoliation.

The second form of 2D boron is boron nanoplatelets, with the same crystallinity as bulk boron. Top-down approaches such as LPE have demonstrated efficient exfoliation of boron nanoplatelets consisting of β-rhombohedral boron[12,129–136]. Recent research suggests that these sheets consist of planar arrangements of icosahedral boron sub-units, cleaved along the {001} planes with the assistance of naturally-occurring crystal stacking defects in the bulk crystal[129], as opposed to undergoing a shift to a borophene-like phase.

One major limitation of both borophene and boron nanoplatelets is their tendency to oxidise[126,137–139], which can degrade their electrical conductivity and other desirable properties[140,141]. While borophene synthesised under inert conditions retains its superlative characteristics, ambient exposure often leads to rapid oxidation, making it difficult to fully exploit its potential in practical applications. This means that regardless of which phase is achieved after exfoliation, some of the superlative properties of borophene prepared under inert conditions are inaccessible to ambient synthesis techniques.

1.1.3 Synthesis of 2D Materials

There are a wide range of ways to synthesise 2D nanomaterials, generally classified into two types – bottom-up and top-down[33] (**Fig. 1.5**). Materials synthesised by the bottom-up route are assembled atom-by-atom from precursors, often using dedicated substrates and vacuum deposition conditions (**Fig. 1.5 A**). The primary bottom-up techniques used are chemical vapour

deposition (CVD), molecular beam epitaxy (MBE) and atomic layer deposition (ALD), each of which function by similar principles – gaseous precursors are either deposited on or reacted with the surface of the substrate, allowing for formation of thin, highly ordered layers. These techniques yield materials with superb, pristine qualities in many cases, with almost defect-free basal planes and large, monocrystalline sheets. However, they are also low yield, energy intensive, and require complex and costly equipment.

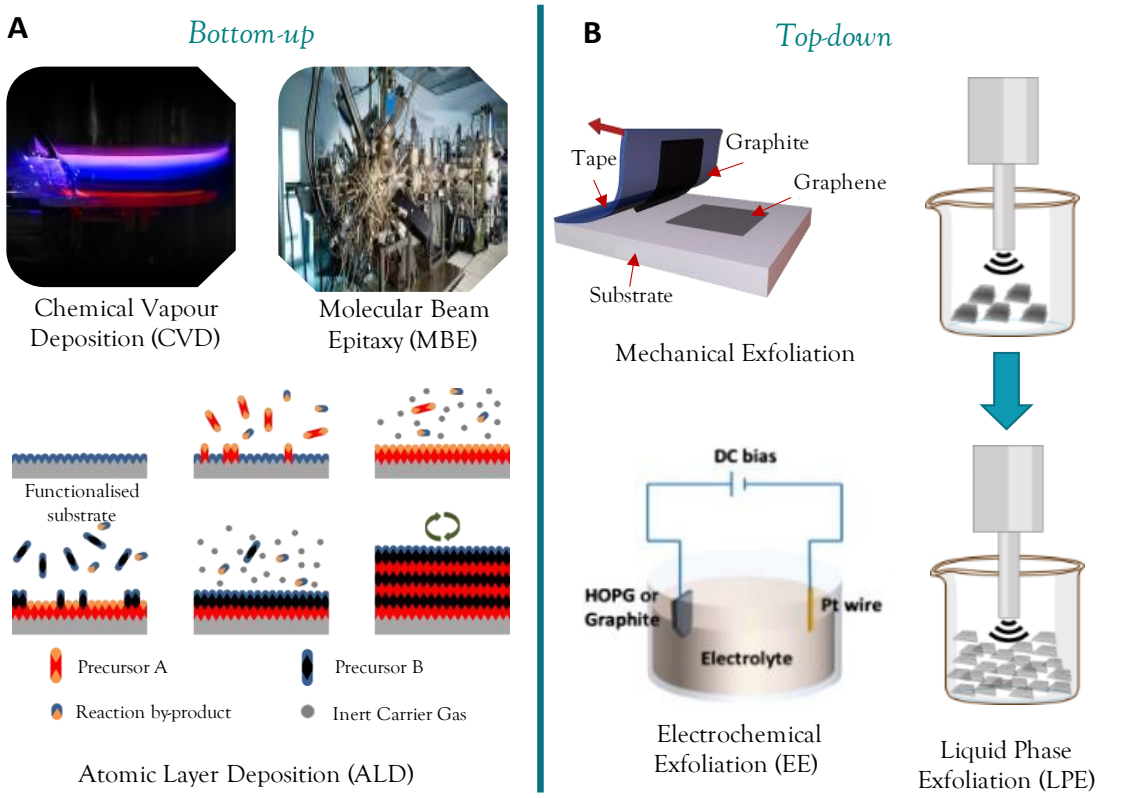

Fig. 1.5 – 2D Material Synthesis Techniques: *Illustration of a selection of the many fabrication methods available for 2D nanomaterials, categorised by whether they build the nanomaterials from nothing, using atomic or molecular precursors (bottom-up, A), or transform a bulk precursor into its nanomaterial form (top-down, B).*

Top-down approaches to exfoliation, on the other hand, function by cleaving a 2D material from a 3D bulk precursor, winnowing one of the dimensions down until it enters the nanoscale (Fig. 1.5 B). The first example, and the first technique used to synthesise 2D nanomaterials by Geim and Novoselov[4], is mechanical exfoliation. This operates by the slow, and somewhat painstaking, peeling of atomic layers from a well-aligned, layered material. However, this suffers the same double-edged sword of high quality but low yield that plagues bottom-up approaches. This takes us then to liquid phase exfoliation, a high yield, cheap and scalable exfoliation technique developed in the Coleman lab in 2008[142], which will be discussed in detail in the next section, and other advanced techniques such as electrochemical exfoliation, involving the separation of atomic layers by means of ionic intercalation[143].

1.1.3.1 Liquid Phase Exfoliation of Layered Materials

Liquid phase exfoliation (LPE, **Fig. 1.6 A**) has emerged as one of the primary methods to unlock the properties of 2D materials, due to its low cost, scalability, and high yield. As a technique, LPE offers great versatility for a range of layered materials, exploiting the weaker inter-layer bonding to enable the exfoliation of nanosheets from the bulk[142]. Following exfoliation, careful choice of solvent and surfactant/polymer stabilisers is essential, both for preventing re-aggregation of materials[144,145] by imparting inter-nanosheet electrostatic repulsion and/or steric hindrance[146] and for enhancing hydrophilicity and biocompatibility (see **Section 1.1.3.3**). Liquid cascade centrifugation (LCC, **Fig. 1.6 B**) is commonly used in conjunction with LPE – this technique works by applying progressively higher centrifugal forces to a nanomaterial dispersion to selectively isolate nanosheets of different sizes, tailoring the material dimensions to suit specific applications[147].

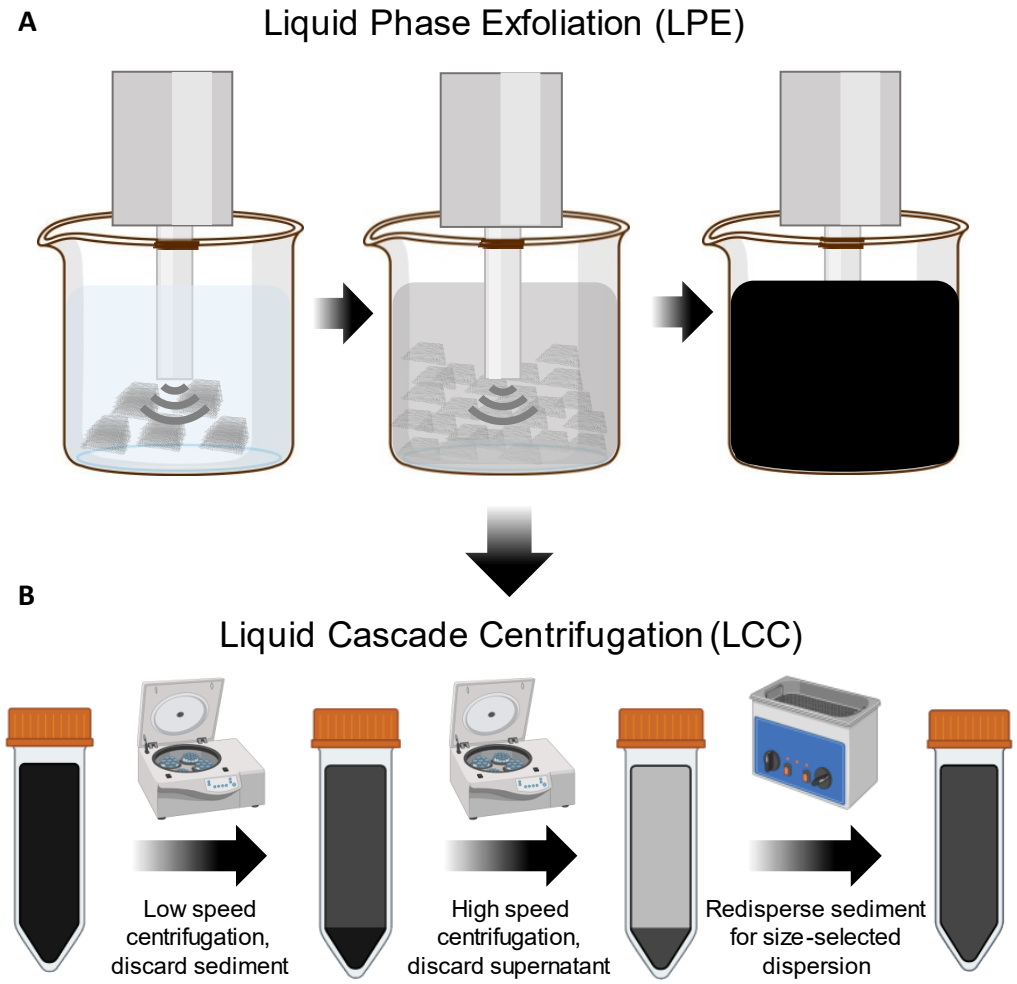

Fig. 1.6 – Liquid Phase Exfoliation of 2D Materials: ***A)*** *Liquid phase exfoliation (LPE) involves the application of sonic energy to a bulk material, leading to the exfoliation of atomic layers from each other in a thermodynamically favoured solvent/stabiliser system.* ***B)*** *LPE is often paired with liquid cascade centrifugation (LCC) to attain nanomaterial dispersions of defined, reproducible dimensions and aspect ratios.*

1.1.3.2 Liquid Phase Exfoliation of Non-layered Materials

It becomes more challenging to exfoliate non-layered materials, as there is no anisotropy in the bonding to exploit. This, taken at face value, would limit the biomedical applications of these materials, as many bioactive materials such as hydroxyapatite, collagen, and more, exist in isotropic forms. However, this difficulty can be countered to a certain extent by careful selection of the precursor material for the exfoliation process. Crystalline materials may preferentially cleave along a weaker crystal plane, even if the bonding anisotropy is less pronounced than in layered 2D material precursors such as graphite (**Fig. 1.7**)[148]. Furthermore, if LPE is not used, 2D materials can be synthesised from materials that would be otherwise impossible to process, for example using chemical vapour deposition[149–151]. As mentioned however, synthesis processes like CVD are currently expensive and low-yield, and thus optimising LPE for non-layered materials has been a focus of research in recent years[145,152–154].

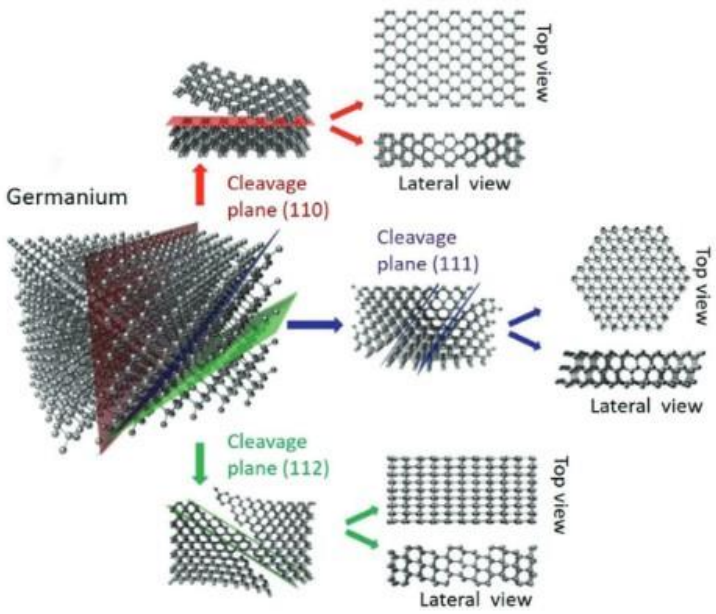

Fig. 1.7 – Liquid Phase Exfoliation of Non-Layered Materials: *Schematic illustrating liquid phase exfoliation of 2D nanomaterials from non-layered precursors, from Kaur et al.*[148].

The efficiency of LPE for non-layered materials can be enhanced in similar ways to that of LPE for layered materials – for example, cryogenic or solvothermal treatment can increase the efficiency and selectivity of LPE, and appear to be driven by the formation of cracks in a bulk precursor, which then propagate through the material. These cracks can be due to intrinsic defects in the crystal structure of the precursor[129], which are then lengthened and expanded by cryogenic[155–159] or solvothermal treatment[12]. Using these techniques, many materials previously considered impossible to exfoliate have been exfoliated, by a wide range of groups[7,9,47,148,155,158,160].

1.1.3.3 Stabilisation of 2D Materials

There are three main methods of stabilisation for 2D nanomaterials in solution, without which they would be prone to re-aggregation:

Solvent stabilisation

Choice of solvent plays a crucial role in the stability of a given nanomaterial dispersion. It has been shown that the dispersibility of a given nanomaterial in a solvent is highly dependent on the thermodynamics of the solvent, namely its surface energy[161]. Solvents with a surface energy similar to that of the nanosheets themselves minimise the enthalpy of mixing, making dispersion more thermodynamically favourable. This relationship is described by the following equation, from Cunningham et al. 2012[162]:

$$\frac{\Delta H_{mix}}{V} \approx \frac{2}{T_{NS}}\left(\sqrt{\gamma_S} - \sqrt{\gamma_{NS}}\right)^2 \qquad \text{(Eq. 1.1)}$$

Here, ΔH_{mix} represents the enthalpy of mixing, γ_S and γ_{NS} are the surface energies of the solvent and the nanosheets, T_{NS} is the thickness of the nanosheets, and V is their volume. Taking this into account, it has been shown that solvents such as N-methyl-2-pyrrolidone (NMP) and N-cyclohexyl-2-pyrrolidone (CHP) are optimal for graphene and TMDCs, as well as a range of other materials[162–164].

Surfactant stabilisation

However, transfer to deionised water or other thermodynamically disfavoured solvents[161] is often required, and in these cases it is necessary to stabilise the nanosheets against aggregation without relying on the solvent to match the surface energy of the material. To achieve this, surfactants such as sodium cholate (SC) and sodium deoxycholate (SDC), among others, are used to disperse the nanosheets. The surfactant molecules act as molecular intercalants, and by their affinity for the nanosheet surface and steric repulsion of other molecules, they prevent the re-aggregation of the material[165,166]. This approach also avoids the need for working with potentially toxic solvents such as NMP[167].

Polymer stabilisation

Finally, there are situations where still further separation is needed from the nanomaterial surface and its environment, such as for biomedical applications. This calls for exfoliation in polymers, which must be biocompatible enough to reduce the potentially deleterious effects of nanomaterials on biological systems, but also small enough so as not to disrupt inter-flake charge transfer. A wide range of polymers can be used for this type of exfoliation, as the mechanism is entirely steric - the polymer adsorbs to the surface of the nanomaterial and prevents nanosheets from aggregating with each other. However, the choice of material is non-trivial, since biocompatibility, conductivity, yield, and stability are all heavily influenced by the polymer used. Furthermore, certain polymers will adsorb preferentially to 2D material surfaces due to the presence of aromatic functional groups, such as pyrrolidones and pyrenes[168,169].

Biopolymers such as gelatin and bovine serum albumin (BSA) are commonly used to produce biocompatible nanomaterial dispersions[170], but such large polymers can greatly impact the conductivity and other network properties of the resulting nanomaterial. This is related to the radius of gyration of these polymers, and how much they limit the tunnelling of electrons between nanosheets[171–173]. To address this, smaller polymers like polyvinylpyrrolidone (PVP) or polyethylene glycol (PEG) are often used, striking a balance between conductivity and biocompatibility[169,174,175].

1.1.4 2D Material Composites

2D materials possess extraordinary properties, many of which can be most readily exploited in the form of polymer-nanomaterial composites. This is thanks to the advantageous mechanical and surface properties that a polymer can impart on the system as a whole, and to the various polymer processing methods that are unavailable for pure nanomaterials. For example, liquid phase exfoliated 2D material films often do not have a high Young's modulus or scratch resistance, rendering them prone to damage when exposed to shear forces. However, when 2D materials are mixed with polymers to form a composite, the resulting material is often stronger than the initial polymer, thanks to the reinforcing properties of 2D materials[97]. Polymer matrices are also frequently used to shield biological systems from potentially damaging effects of highly concentrated 2D materials.

1.1.4.1 Electrical Behaviour

For modelling nanomaterial composite systems, the main parameters that describe their electrical behaviour are the percolation threshold, the conductivity of the filler and the percolation exponent, as described by percolation theory[100,176], while the mechanical behaviour is usually modelled by the Rule of Mixtures[177]. Both models are controlled by the volume fraction (φ) of the nanomaterial filler in the polymer matrix. Classical percolation theory as it relates to conductivity is based on the fact that in a composite, conductivity will not be achieved until a continuous conductive path is formed across the material (Fig. 1.8). At this point, known as the percolation threshold (φ_c), there is a large jump in conductivity (σ), often several orders of magnitude, which then continues rapidly increasing within a range.

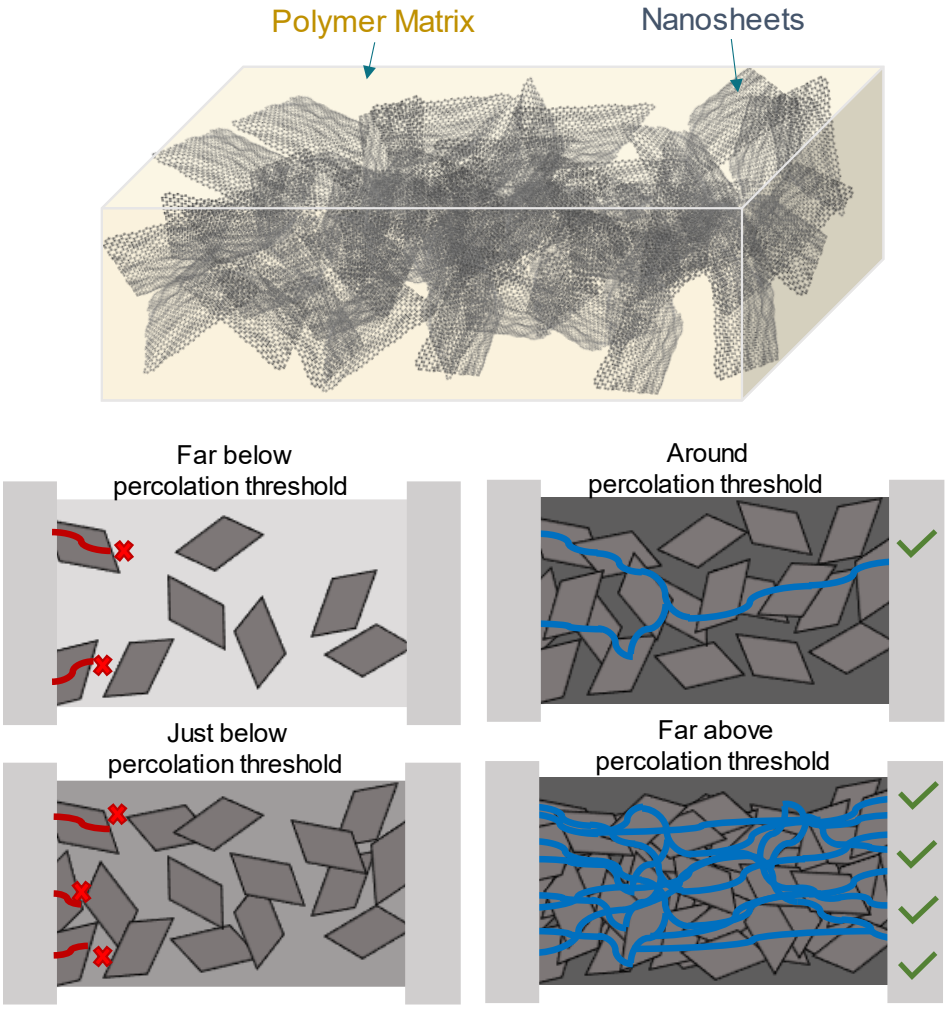

*Fig. 1.8 – **2D Nanomaterial Composite Formation and Behaviour:** **A)** Formation of a nanomaterial composite with nanosheets shown in grey, and the polymer matrix in pale yellow. **B)** Behaviour of a 2D nanomaterial composite as the nanomaterial loading is increased. Red paths represent non-conducting paths, while blue paths represent conductive paths across the sample.*

This behaviour is described by the following expression:

$$\sigma = \sigma_0(\varphi - \varphi_c)^t \qquad \text{(Eq. 1.2)}$$

Here, t is the percolation critical exponent, which describes the behaviour of the conductivity in the region of the percolation threshold and is related to the distribution of the inter-nanosheet junction resistances in the composite, and σ_0 is a constant, dependent on the specifics of the composite system and related to the underlying conductivity of the filler material. A number of factors can influence the parameters φ_c, σ_0 and t, including the aspect ratio of the nanomaterials, the polymer matrix being used, the degree of aggregation of the nanomaterial filler, and the degree of alignment of the filler[100,176]. In addition, the junction resistance and nanosheet resistance play a large role in the conductivity achievable in a given composite, as they do for nanosheet networks without filler[178].

Alignment in particular can be a difficult parameter to account for, since it is unrelated to the material properties themselves in large part, and is driven by the manufacturing process of the composite in question[179,180]. The optimal alignment is dependent on whether the system is a polymer-free network, or a polymer nanocomposite. In a nanosheet-only network, high alignment will lead to large-area face-face inter-nanosheet junctions, which will possess a decreased junction resistance, leading to higher conductivity in the network compared with flake-edge to flake-face junctions. However, in polymer nanocomposites, face-face junctions are often disrupted by polymer between the faces, increasing their resistance. This is significant, since the primary mechanism of inter-flake charge transport is electron tunnelling, which is very highly dependent on the inter-flake distance, with the efficiency of tunnelling falling off rapidly after ≈ 3 nm[178]. This means that large polymer stabilisers can greatly decrease the conductivity of a network, even as they increase the biocompatibility, which must be accounted for in any system which aims to balance conductivity with biocompatibility.

1.1.4.2 Mechanical Behaviour

The mechanical properties of nanomaterial composites are complex, and largely dictated by the Rule of Mixtures[24,177,181], with some systems also following principles of mechanical percolation[182,183]. The Rule of Mixtures states that the emergent properties of a composite system depend on the individual properties of its components, and on the ratio between them. To

discuss these properties, it is useful to define some quantities[184]. First, stress is defined as the force per unit area applied, and strain is the resulting deformation of a material. The ratio of these components is known as the modulus, giving useful information on the resistance to deformation. The plot of stress vs strain for a material gives a wide range of information on its mechanical behaviour, with materials typically grouped according to their stress response in differing strain ranges. For example, elastic behaviour is defined as the regime where the deformation returns to zero following cessation of stress, plastic behaviour is observed when an applied stress, upon exceeding a threshold known as the elastic limit, leads to permanent deformation, and viscous behaviour describes the irreversible flow of fluids and solids, causing effects such as creep and stress relaxation under consistent applied stress. Materials often exhibit a combination of these behaviours, as the mechanical response to an applied stress is often time and strain rate-dependent, leading to viscoelastic, elastoplastic, viscoplastic, or viscoelastoplastic behaviour.

These dynamic, complex mechanical properties are highly relevant to biomedical applications, due to the high mechanosensitivity and viscoelasticity of many cell types and tissues, as well as the dynamic stress environments present in the body. Of particular relevance to biomedical applications is viscoelasticity, with many biomaterials exhibiting viscoelastic behaviour in order to mimic tissue properties, which often respond to mechanical stimulus in a manner dependent on the rate of strain applied and which can exhibit stress relaxation at constant strain[185,186]. Modelling and matching of the stress relaxation behaviour of viscoelastic tissues and biomaterials is essential to prevent mechanical mismatch, tissue damage, and potential device rejection[187,188].

1.1.4.3 Fabrication

Fabrication of 2D material composites is not as trivial as it may first appear – the simplistic approach of mixing the filler with the polymer and casting it to dry can often lead to aggregation, inhomogeneity, and poor composite performance. Key factors to consider include the choice of filler, stabilisation method, polymer type and viscosity, and solvent compatibility. Furthermore, processing parameters such as dispersion technique (e.g. sonic probe, sonic bath, shaking, stirring, blending), casting technique (spin coating, mold casting, freeze-drying) and environmental factors such as temperature and humidity must be considered, as they all have significant effects on the electrical, mechanical, and biological properties of the resulting composite. While some of the emergent properties from 2D material addition are beneficial for

given applications (for example, conductivity and mechanical reinforcement), some properties can also be detrimental, such as decreased flexibility, changes in viscoelastic properties, and prolonged degradation time. This means that these properties must be balanced with each other, by taking the percolation curve and Rule of Mixtures into account where applicable. This is why achieving a homogeneous, well-dispersed composite is critical, as it lowers the electrical and mechanical percolation thresholds and allows the desirable properties of 2D materials to emerge with minimal material loading. These properties have an outsized impact on the biological interactions and biomedical applications of these materials and composites, which will be discussed in the next section.

1.2 Biomedical Applications of 2D Materials

The human instinct to improve health has continually propelled the rapid application of new materials to the advancement of medical technology and research. This has been no different for 2D materials, the advent of which has generated a great deal of interest in the biomedical research space thanks to their exceptional properties, such as high surface area, biocompatibility, and electrical conductivity. 2D materials enhance and enable important tools and techniques in the arsenal of biomedical engineers, allowing for multimodal, targeted, and biocompatible therapies and devices for a range of tissue types, diseases, and injuries – from enhancing neural interfaces to creating advanced drug delivery systems and imaging agents, 2D materials offer solutions to challenges that were previously difficult to address with conventional materials (**Fig. 1.9**).

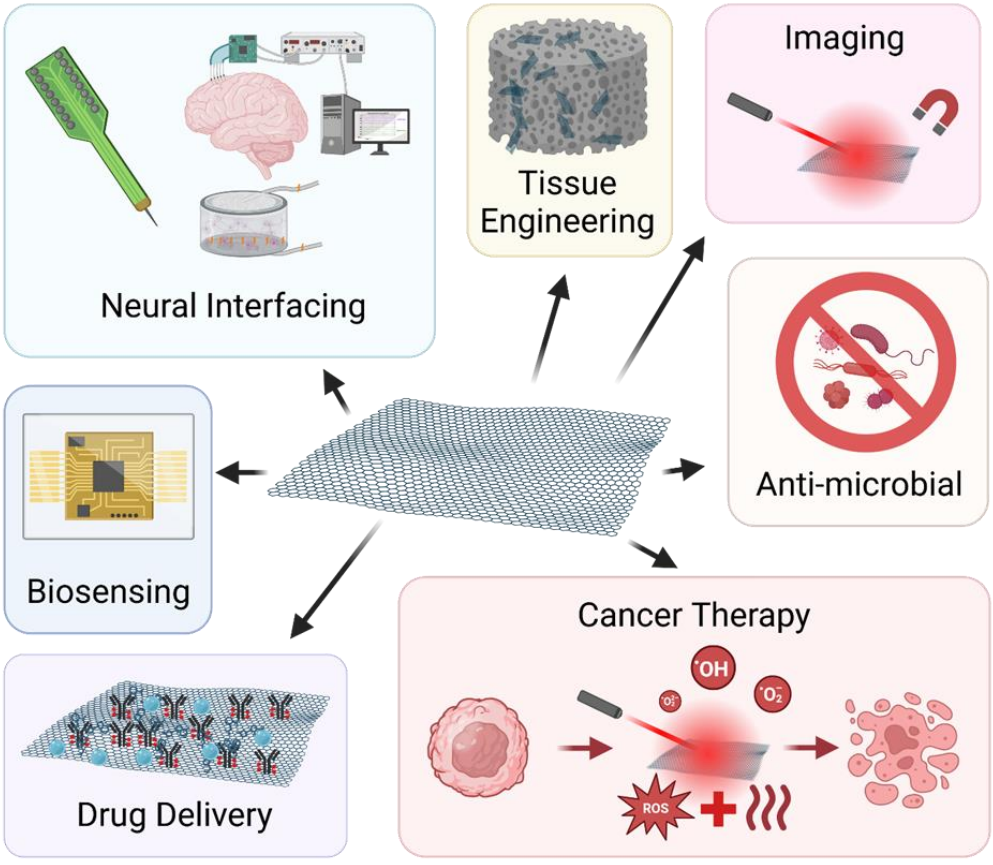

Fig. 1.9 – Biomedical Applications of 2D Materials: *2D materials have been applied to a wide range of biomedical applications, revolutionising research in many of them – from neural interfaces and biosensors to advanced drug carriers and imaging agents, the versatile properties of these materials have established their role as pivotal tools in several key niches of biomedical research.*

This section will first explore the biological properties of 2D nanomaterials, followed by an exploration of the applications of graphene, 2D boron, and other 2D nanomaterials in biomedical contexts.

1.2.1 Biocompatibility of 2D Materials

Before any new material can be applied in a biomedical setting, extensive research must first be conducted in both *in vitro* preclinical settings and clinical trials to establish safety and compatibility. This is relatively straightforward for inert, non-degradable materials used externally, but it becomes considerably more challenging, and critical, for materials designed for internal use[189,190] – particularly those which are small enough to circulate in the circulatory and lymphatic systems to reach distant parts of the body[191]. This is where the primary concern around 2D nanomaterials for biomedical applications comes into clear view – the fact that they are small enough to potentially penetrate and slice cells[192–194], are not always water-soluble, and can be prone to gathering in tissue[195–197] means that careful considerations must be made to investigate and minimise the potential side effects of these useful materials. There are three main aspects of a material's interaction with the body that must be assessed and optimised to render it suitable for use in the body – the dose-dependent cytotoxicity, immunological properties, and excretion pathways.

1.2.1.1 Cytotoxicity

The cytotoxicity of a nanomaterial depends on a wide range of factors, related to the physical and chemical properties of the material itself, as well as the specific cells and systems being studied[198]. Furthermore, as with any drug or material, the dose matters – many materials are safe up to a limit, beyond which cytotoxicity as well as systematic deleterious effects begin to occur[199,200]. Factors such as nanomaterial composition, size, concentration and functionalisation, as well as the exposure route (e.g. in free suspension vs. in composite form, or intravenously vs. dermally[201]) have a significant impact on the potential cytotoxicity of the material. Here we discuss several of these key parameters:

Material composition

The material composition of a nanomaterial is a critical determinant of its cytotoxicity. For example, nanosheets formed of highly reactive materials, or those which dissolve into toxic ions/byproducts, can cause apoptosis and necrosis by a wide range of mechanisms[198,201,202]. Furthermore, the redox potential of materials is dictated by its composition, impacting the rate of production of potentially harmful reactive oxygen species[201]. However, the impact of material composition and the associated cellular response is more subtle than simply "toxic" and

"non-toxic" – cell-specific responses have been observed to commonly used nanomaterials. For example, graphene oxide has been shown to have dose-dependent cytotoxicity with fibroblasts[203], while exhibiting no significant cytotoxicity with A549 cells[204]. This is just one example of the many conflicting reports, underscoring the impact of factors such as size, coating, and material-specific cellular interactions in nanomaterial cytotoxicity[205].

Dimensions

Nanomaterials are frequently on a scale similar to that of the cells which they are in contact with, thus small changes in the lateral size or thickness of the nanosheets can have an outsized impact on the cytotoxicity, by mediating the biodistribution, accumulation, cellular uptake, and blood-brain barrier crossing potential[192,201]. For example, smaller nanosheets are more likely to penetrate into cells, potentially causing internal damage and decreasing cell viability[201]. Larger, thinner, more flexible nanosheets on the other hand may wrap and "suffocate" a cell in certain circumstances[206–208]. Changing the dimensions of the nanomaterial often has downstream effects, not only on the biological interactions, but on the physicochemical properties of the material, requiring a fine balance to be struck between desirable physical properties and minimal cytotoxicity.

Beyond initial cytotoxic effects, nanosheet dimensions also have a large impact on the excretion pathways a nanomaterial can take, with studies showing a relationship between larger, thicker nanosheets and slower urinary and renal excretion[195,196,209], with one study finding that only quantum dots of up to 6 nm in radius could be excreted by the kidneys[210]. This is due to the limitations of the anatomical structure of the kidneys and liver, where glomeruli, hepatic lobules and the cells therein can only process materials up to a certain size limit[211,212]. For some applications, the downstream effects of the nanomaterial size can be contradictory – for example, small nanosheets can be excreted more rapidly, but also show higher accumulation at a target site due to the enhanced permeability and retention (EPR) effect[197,213]. Therefore, a balance must be struck between circulation time and accumulation characteristics.

Surface coating & charge

Since one of the main draws of 2D nanomaterials is their enormous specific surface area, it stands to reason that the surface properties of these materials have an outsized impact on their biological interactions. In the simplest example, if a material is hydrophilic, it is likely to be safely excreted

from the body, while if it is hydrophobic, it is likely to remain at the site of injection/implantation chronically, potentially causing inflammation and tissue dysfunction. Hydrophilicity can be improved using a wide array of surfactant and polymer coatings, each of which serve to greatly improve the cellular interactions of the materials[198]. It is, nonetheless, not the only surface property relevant to the cytotoxicity. Diverse properties such as the toxicity of any stabilisers or the concentration of defects in the material can each have a large impact on the biological interactions of these materials, for example by modulating the release of reactive oxygen species (ROS)[214–216]. Similarly, the oxide groups on GO and similar materials can also cause cytotoxicity due to the formation of ROS[205,217–221]. However, less-oxidised graphene derivatives can also lead to ROS generation, charge transfer and hydrophobically-induced cytotoxicity[222–224].

To increase biocompatibility while maintaining advantageous network properties, nanomaterials are often functionalised with hydrophilic, biosafe molecules such as polyethylene glycol (PEG), pyrene derivatives, and polyvinylpyrrolidone (PVP) among others, avoiding direct cellular contact[225–228]. Finally, the charge of the surface of a nanomaterial has an outsized impact on the interactions of cells with the material, due to its impact on the composition of the protein corona formed, and on the nature of the cellular membrane interactions[229]. Positively charged coatings are generally preferable, due to the increased rate of protein adsorption and induction of a pro-regenerative immune signalling cascade[229].

Aggregation

Many nanomaterials, particularly those which have not undergone sufficient surface optimisation as discussed in **Section 1.1.3.3**, are prone to aggregation and agglomeration in physiological environments due to the thermodynamically disfavoured interaction between hydrophobic nanomaterials and aqueous solvents[230]. Exacerbated by the varying pH and protein profiles found in the body, this can lead to nanomaterial precipitation, triggering inflammation and other harmful effects at the site of application. The degree of aggregation significantly influences the extent of these negative effects, with higher levels of aggregation being associated with worse outcomes[230,231]. Furthermore, aggregated nanomaterials are more likely to be retained in sensitive tissues such as the kidneys, liver and in the lymphatic system, potentially causing a harmful build up over long term exposure, leading to inflammation and fibrosis[232–234].

1.2.1.2 Immune Response

Since nanomaterials are fundamentally miniscule foreign bodies in the bloodstream and lymph fluid, if the immune system takes notice, it will spark a phagocytic response by monocytes and macrophages. This response is similar to the foreign body response seen after device implantation, which causes complications such as osteolysis and glial encapsulation for orthopaedic and neural implants respectively[235,236]. This response marks the nanomaterials for engulfment and excretion, and greatly reduces their circulation time in the body. Materials with low hydrophilicity, unusual surface groups or chemistry are particularly susceptible to this, as they are more likely to set off the immune system's alarms[197].

The key driver of immune cell interactions with nanomaterials, however, is not so much the identity of the nanomaterials themselves as it is the identity they take on after exposure to bodily fluids, as well as aforementioned factors like dimensions and aggregation. In physiological conditions, they will rapidly become surrounded by a biocorona of plasma proteins, the composition of which alters what immune cells "see" when they encounter the material[197,237], influencing whether it triggers an inflammatory response, causes immunotoxicity, or is excreted without incident[238]. To take advantage of this biocoronation effect, many polymers, both biological and synthetic, have been used to synthesise "biocorona-by-design" layers on the surface of nanomaterials, in order to effectively evade engulfment and excretion by the immune system before the nanomaterials have had time to fulfil their function[197,239].

1.2.1.3 Long-term Response and Excretion

While the short-term cytotoxic and immune response of cells to nanomaterials can be measured accurately *in vitro* over the course of several weeks, it is considerably more difficult to predict long-term interactions with complex *in vivo* biological systems[240]. Some applications require the temporary presence of nanomaterials – in these cases, nanomaterials which do not naturally break down under physiological conditions must be effectively excreted lest they remain at the site of implantation/injection indefinitely. This can cause interference with biological processes in the surrounding area by causing an immune response, fibrotic encapsulation, and in the worst cases, potentially posing a cancer risk[241,242]. Other applications, such as composite materials and coatings used in implantable devices, require long-term implantation and even integration of nanomaterials, in which case high, stable biocompatibility takes precedence over degradability and excretion.

For applications in the first category, the mechanisms of nanomaterial excretion are varied and highly material- and system-dependent, as discussed above, but in general materials will find their way either into the circulatory or lymphatic systems, where they travel onwards through the liver or kidneys, and are excreted[197,243–245]. This is where the hydrophilicity mentioned earlier becomes critical – materials that have low dispersibility in aqueous solutions will tend to precipitate, particularly in regions of slow fluid flow such as the liver, where they are then deposited, potentially leading to a dangerous mass of material which can cause fibrosis and a foreign body response. This can be alleviated by two means – 1) by using materials that can be degraded enzymatically, or naturally degrade under physiological conditions, or 2) by using materials that are so hydrophilic as to be capable of passing through the entire excretion pathway without significant precipitation or deposition. As discussed earlier, surface coating can be used to render a nanomaterial surface hydrophilic, decreasing its clearance time – for example, Liu et al. have shown that functionalisation with varying molecular weights of polyethylene glycol (PEG) has an outsized impact on the renal and hepatobiliary clearance rate of single-walled carbon nanotubes[246], while Phillips et al. have shown that PEGylation of silicon nanoparticles dictates their fate, with non-pegylated particles ending up in the liver, and PEGylated particles being excreted via the urinary system[247].

In summary, the biocompatibility of 2D nanomaterials is complex, and highly treatment-, tissue-, and material-dependent. It therefore must be optimised on a case-by-case basis to ensure minimal cytotoxicity, immune response, and nanomaterial accumulation. Moving forward, strategies such as surface functionalization and polymeric encapsulation will be essential to unlock the full potential of 2D nanomaterials *in vitro*, *in vivo* and in clinic, ensuring relevant safety metrics and high therapeutic efficacy are achieved. In the next sections, we will focus on the biomedical applications of two 2D materials, graphene and 2D boron, which serve as examples of the significant potential of the 2D material family.

1.2.2 Graphene for Biomedical Applications

Graphene, as the first 2D material discovered, has had the most research dedicated to its biomedical applications. With its high aspect ratio sheets and stability it quickly became the material of choice for early research into nanomaterial-based drug delivery[248,249], mechanical reinforcement of biomaterials[250], cancer theranostics[249,251–253], and anti-microbial effects[78,206–208,254–257], as well as tissue engineering and neural interfacing applications, which will be discussed in detail in **Sections 1.3** and **1.4** respectively.

To enable these biomedical applications, the biocompatibility of graphene and its derivatives has been assessed across a very wide range of cell types[77,105,218,258–266]. Due to its extraordinary conductivity and the resulting potential for applications at the neural interface[267–270], its interaction and compatibility with the cells of the central and peripheral nervous systems (neurocompatibility) is of particular interest in this thesis.

Focusing on pG, it is more difficult to produce consistently high-quality, high-yield and biocompatible pG compared to graphene oxide (GO) or reduced graphene oxide (rGO), which has slowed research into its biological application[194,271–273], despite its superior material properties[107,274]. This has also led to inconsistent reports regarding its neurocompatibility[275–278]. Cells exposed to pG suspensions[259,276] or seeded directly on pure pG surfaces have been reported to suffer cellular damage[279] and apoptosis[276], with neurons also showing altered excitability when directly exposed to pG[269]. On the other hand, pG has also shown promise in several studies for the enhancement of neurogenesis, neural growth and electrical signalling in cells grown on graphene substrates[258,280–287]. Recent reports indicate that the biocompatibility can be enhanced by controlling crystalline quality[277], modifying surface chemistry[288,289], and non-covalent surface functionalization, while retaining its favourable mechanical, thermal, optical and electrical properties[142,225,275].

A distinction must be made between the biocompatibility of smooth, monolayer graphene such as that synthesized by CVD[277,285,290–292], and graphene nanosheets synthesized by techniques such as LPE or electrochemical exfoliation[263,293]. In addition to this, the neurocompatibility of pristine graphene (pG) and its derivatives GO and rGO are often quite different, due to their significantly differing surface chemistries[203,294,295]. This diversity in surface morphologies and chemistries, coatings and material dimensions make it impossible to ascribe a one-size-fits-all judgement as to the biocompatibility of graphene or its derivatives, meaning that rigorous testing must be carried out for each new tissue and application.

One way to circumvent the toxicity of many nanomaterials is by encapsulation in a polymer composite, enhancing biocompatibility while maintaining advantageous electrical properties[97,170,259]. This also allows researchers to take advantage of the properties both of the nanomaterial filler and the polymer matrix, enabling multifunctional materials and scaffolds. Graphene and its derivatives in particular lend themselves well to incorporation in composites,

wherein it can be used to induce conductivity and anti-microbial effects, yield mechanical reinforcement, and increase surface roughness and cellular adhesion, among other beneficial properties[278]. Graphene materials have been combined with a wide array of polymer matrices, with a variety of target tissues and effects. For example, work in our lab and others has shown that pG bound into collagen substrates is non-inflammatory[259,296], supporting the growth of directly seeded cardiomyocytes[170], and enhancing the effect of electrical stimulation on spinal cord neurons[101,260]. Graphene scaffolds have also been produced with a wide variety of structures, from porous foams and fibre networks to hydrogels[278,297,298], reflecting the flexibility in processing that composite systems afford researchers.

1.2.3 Boron for Biomedical Applications

While graphene dominated the early research into 2D materials, as exfoliation techniques have progressed, more 2D materials have come to the fore. This flexibility in composition offers an even greater diversity of properties, allowing researchers to expand the potential of 2D materials for biomedical applications. Boron, a key trace element in the human body, is one such example. Positively influencing bone health[299–301], osteogenesis[302–307], angiogenesis[308,309] and wound healing[310], among other biological systems[299,301], systemic boron supplementation has been studied, along with boron-containing compounds successfully being used for bone tissue engineering applications[304,308,311–313]. Boron-containing compounds such as boric acid, borax, and borate esters have also found broad utility in biomedical applications[314–318].

Of most relevance to this thesis are the biomedical applications of elemental 2D boron and borophene. With its superb neutron capture cross section[319], boron and 2D boron have seen early use in fields such as cancer therapy[132,320–322], where they are used to effect boron neutron capture therapy (BNCT)[323]. 2D boron has also seen preliminary applications in bioimaging[134] and biosensing[324–326]. Boron itself has not previously been shown to have antimicrobial activity, but boron-derived compounds have[327–329]. 2D boron in particular offers potential beyond that of bulk 3D particles, as its high surface area, enhanced edge effects, and ability to reinforce polymers enables scaffolds to address more of the key aspects of tissue regeneration simultaneously, and with greater efficiency, as discussed in **Section 1.1**. Of course, while further study of 2D boron is warranted to assess its cytotoxicity, and to developed approaches to reduce it[132,330], these unique properties indicate that 2D boron could play a significant role in emerging bone tissue engineering technologies.

1.2.4 Other 2D Materials for Biomedical Applications

Graphene and boron are only the tip of the iceberg, however. While we will not delve into them in any great detail, 2D materials have revolutionised many existing fields in biotechnology, as illustrated in **Fig. 1.9**. To pick just one example, one of the most vibrant fields of research in biomedicine is cancer therapy, with each new material and biomedical innovation holding the potential to impact the almost 20 million cases of cancer that occur every year worldwide[331]. 2D materials have been applied to effect efficient photodynamic[94,332], photothermal[31,333–335], and chemotherapy[336], thanks to their unusual optical and thermal properties. This alone would cement 2D materials as an essential tool in the biologist and bioengineer's belt, but that would be to say nothing of their applications to biosensing[66,337–339], bioimaging[66], drug delivery[35], antimicrobial activity[206,255,256] and more[63,67,340]. Tissue engineering and neural interfacing will be discussed in much greater detail in **Sections 1.3** and **1.4** respectively. In summary, while there are significant safety considerations that must be taken into account when using 2D nanomaterials in biomedical applications, the potential upside is such that their continued use is not only justified, but potentially revolutionary across a wide range of fields.

1.3 Tissue Engineering and Regenerative Medicine

Of the wide range of frontiers laid out before us in biomedicine, one of the most compelling is tissue engineering, a concept first proposed by Langer and Vacanti in 1993[341,342]. The basic principle of tissue engineering centres on the use of scaffolds – artificial constructs designed to support the proliferation of cells and deposition of tissue across a gap which would otherwise be impossible to bridge[343]. The scaffolds act as temporary architectures to direct and support cellular growth (Fig. 1.10), and are subsequently resorbed or integrated into the tissue, with the integration or degradation rate tailored based on the tissue being repaired or replaced[344].

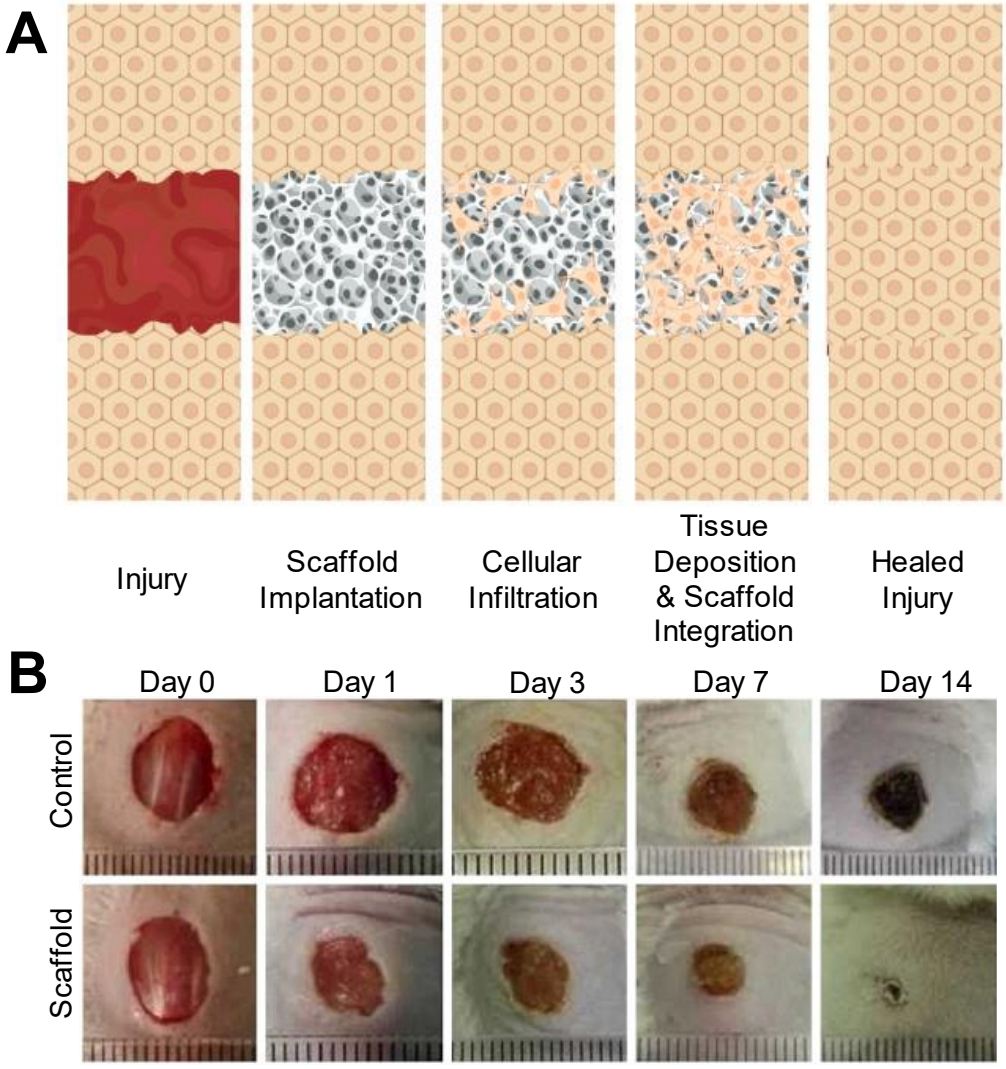

*Fig. 1.10 – **Tissue Engineering: A)** Schematic of the process of basic scaffold-mediated tissue engineering, showing the infiltration of cells to a supportive scaffold, followed by its subsequent degradation and integration into the healed tissue and **B)** Images showing accelerated healing due to a tissue engineering scaffold consisting of a 3D bioprinted gelatin-alginate scaffold in an in vivo mouse skin wound model, with a pronounced effect on the size of the wound after 14 days (adapted from Liu et al. 2016[345]).*

Tissue engineering holds promise for a vast array of applications, ranging from the repair of damaged or diseased tissue[346] to the fabrication of *de novo* organs and body parts[347]. Given the remarkable diversity of tissues in the body, the composition, geometry, and material properties must be meticulously tuned. The porosity[348–350], stiffness[351–353], conductivity[354], surface properties[355,356] and alignment[357,358] are all key factors to optimise in each new system[343], to ensure that the engineered tissue both functions effectively and integrates harmoniously with the body. Furthermore, as with any device designed for implantation, the foreign body response of the surrounding tissue must be carefully managed – this can be achieved by modulating the device stiffness[351,353], adapting the surface topography and coating[359], and including anti-inflammatory molecules[359,360].

Scaffolds often serve as the platform for more sophisticated therapeutic strategies, however. A wide range of other therapies can be applied in conjunction with scaffolds, such as cells[361], growth factors[362,363], genes[364–366], 2D materials[72,90,367], nanoparticles, and proteins, each of which enhance tissue regrowth, repair, replacement or improvement. Owing to this flexibility, tissue engineering can be used to enable repair of a wide range of biological tissues, including muscular[368], bone[369], cardiovascular[370,371], and nervous tissue[372]. In this thesis, we will focus on neural and bone tissue engineering, which exemplify the vast potential within this field.

1.3.1 Neural Tissue Engineering

With kilometres worth of nerves providing essential and complex functions to every part of the human body, nerve repair is a critical component of recovery from any devastating injury. There are two primary subfields of nerve repair: spinal cord injury, which is often incurable due to the formation of an impenetrable glial scar[373], and repair of peripheral nerve injuries, which also have the potential to be severely debilitating should they extend past a critical length[374]. These subfields operate in different biological subsystems, the central nervous system (CNS), and peripheral nervous system (PNS), respectively, with each system posing unique challenges. The approaches to repair in both systems generally take the form of using a scaffold to guide neurons and axons through the injury site, aiming to promote full regrowth over a period of time – many adjuvant therapies have been applied on these scaffolds to enhance this regrowth, such as nerve growth factors[375], RNA delivery[376], and electrical stimulation[377].

1.3.1.1 Peripheral Nerves

Peripheral nerve repair requires the regrowth of highly aligned nerve fibres across an injury, a task more challenging than simply the regeneration of isotropic tissue. Peripheral nerve defects exhibit the innate potential to regrow up to a critical defect size (typically ~1.5 – 3 cm[378]), and regeneration can be accelerated beyond this using suitable scaffolds. As the distal axons beyond a nerve injury die off due to Wallerian degeneration[379], proximal axons must bypass the injury site and regenerate not only the injured tissue, but the lost axonal tracts beyond the injury. With the symptoms of peripheral nerve injury ranging from uncomfortable sensations (or, conversely, complete loss of sensation) to severe pain or paralysis, rapid regeneration of these nerves is critical[374]. While autografts, allografts and xenografts can be used, the risks of infection, donor site morbidity, and immune rejection make artificial scaffolds a promising option[378].

The techniques required to direct nerve cells across a scaffold to their distal targets are varied, including the use of aligned pore scaffolds[380,381], electrical stimulation[382,383], multi-phasic conduit designs[381,384,385], stem cell therapies to assist with healthy cellular function and signalling[386–389], and growth factor delivery[390]. While existing therapies can lead to improvements in functional outcomes, the prevalence of nerve injuries and their devastating consequences mean there is a drive towards improving the effectiveness of these technologies to enhance both the speed and quality of nerve regeneration, leading to improved patient outcomes and shorter recovery times[378].

1.3.1.2 Spinal Cord

The spinal cord is the most important collection of nerve tissue in the human body outside of the brain, and functions as an essential transmission highway for sensory and motor signals to from the brain. Injuries along its course can lead to anything from limb dysfunction or incontinence to such severe outcomes as full quadriplegia or death, depending on the location and severity of the injury[391]. The critical nature of the spinal cord, as well as the devastating personal, physical, and socioeconomic consequences of spinal cord injuries, make it a prime candidate for tissue engineering strategies.

However, there are several ways the spinal cord as a system exhibits considerably more complexity than other tissue types, including peripheral nerves. Like peripheral nerves, the tissue itself is highly anisotropic and complex, with axons required to reach the correct distal targets in order

for function to be restored. One of the most vexing challenges that spinal cord repair poses to therapeutic interventions is the presence of the fibroglial scar, which develops during the intermediate-chronic injury phase[392], and blocks the natural regrowth of neurons across the injury site[393,394] (Fig. 1.11). The scar develops as a result of inflammation caused by the injury, and serves an important function, reducing secondary inflammation and preventing further cellular damage[393,395]. However, the scar also acts as a double-edged sword, as it also presents a physical barrier to axonal regeneration, while simultaneously secreting inhibitory factors to surrounding nerve cells[373,395]. In this way, it functions effectively as a stop sign for axonal regeneration.

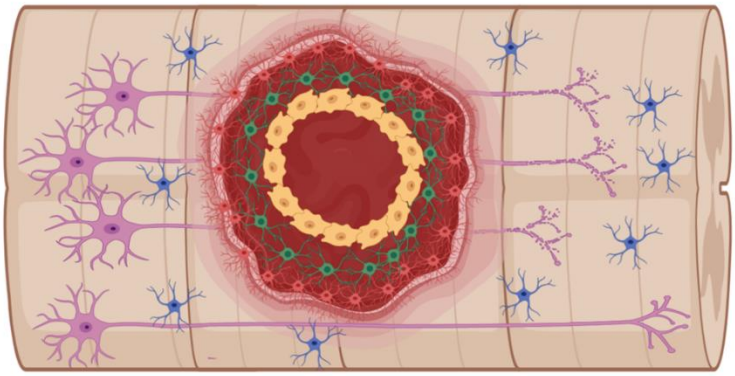

*Fig. 1.11 – **Spinal Cord Injury:** Schematic of the injured spinal cord, with a glial scar formed by astrocytes, microglia, and oligodendrocytes progenitor cells blocking the successful reconnection of neurons to their distal targets, both physically and by the release of inhibitory factors to surrounding neurons.*

Thus, in order to effectively address a spinal cord injury, the scar must not be removed completely, but ameliorated by various perforative approaches, such as knockdown of connexin-43 binding proteins[395–397]. The downstream effect of the glial scar is that spinal cord neurons exhibit poor regenerative potential, due to the cascade of inhibitory factors released by cells following injury. This means that even following successful amelioration of the scar, natural regrowth is unlikely, and regenerative approaches such as tissue engineering scaffolds, electrical stimulation, and the combination thereof are critical tools to help drive and direct cellular growth across injury sites. Developments such as aligned pore, patient-specific architectures[398–400], electroconductive frameworks[398,401], and growth-factor containing extracellular matrices (ECMs)[351,402] have all seen promise for regeneration of injured spinal cord tissue in pre-clinical studies. To extend the previous metaphor, if the glial scar is a stop sign for axonal growth, scaffolds allow us to build a road, and electrical stimulation has the potential to allow us to increase the speed limit.

1.3.2 Bone Tissue Engineering

Bone tissue engineering has long been a key focus in regenerative medicine, since natural bone repair is limited to small defects and simple geometries[403]. Similarly to neural tissue, above a critical defect size cells simply cannot find their way across the injury site without the assistance of a scaffold. Thus, scaffolds including bioglasses[304,307,308,404,405], polycaprolactone frameworks[406,407] and porous collagen/hydroxyapatite sponges[406,408] have been developed to support the regrowth of cells, while maintaining the mechanical integrity of the surrounding tissue and allowing nutrient diffusion. Many of these bone repair scaffolds are designed for eventual integration into the healed bone, as mineralisation occurs within and around the scaffold, as illustrated in **Fig. 1.12 A** and **Fig. 1.12 B**.

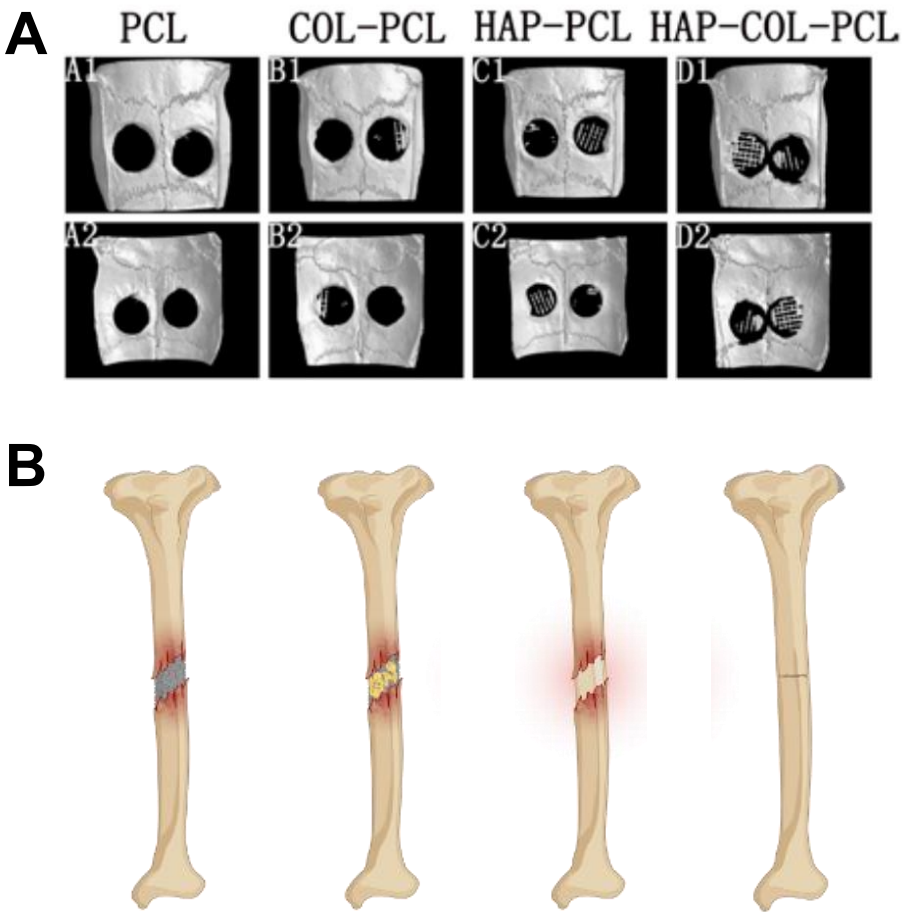

*Fig. 1.12 – **Bone Tissue Engineering:** **A)** μCT images showing enhanced tissue regrowth with help of collagen/hydroxyapatite/PCL scaffolds from Qi et al. 2016[406] **B)** Schematic illustrating the progression of bone tissue regrowth following implantation of a porous scaffold.*

Osteogenesis, the formation of new bone via mineralisation and the primary target of bone repair scaffolds, can be enhanced by two key processes: *osteoinduction* (stimulating new bone growth) and *osteoconduction* (supporting existing bone growth). Both processes are essential for effective bone healing, as osteoinduction initiates bone regeneration while osteoconduction ensures that the scaffold guides this growth in a controlled manner[409]. Bone tissue is complex and multifaceted, with significant vascularisation and innervation required for healthy function. Furthermore, implantation of any scaffold poses a risk of infection arising from surgical intervention, and foreign body responses driven by the immune system.

Therefore, in order to effectively heal bone tissue, the cellular response of not only bone, but of nerve and epithelial cells must be optimised to enhance *neurogenesis* (the formation of new nerves) and *angiogenesis* (the formation of new blood vessels)[410,411], while minimising the risks of inflammation or infection. This requires multifunctional scaffolds containing potent scaffold additives, such as bone morphogenetic protein-2 (BMP-2), hydroxyapatite, and a wide range of bioactive ions, which reduce the risk of infection, rejection or inflammation upon implantation[412–414].

1.3.2.1 Bioactive Molecules

A common approach for enhancing bone regeneration involves the use of bioactive elements such as Mg^{2+} and Ca^{2+}, which are metabolised by bone to encourage osteogenesis[405,415–417], angiogenesis[415,417,418] and neurogenesis[417,419]. The mechanisms behind these effects are varied, depending on the specific cell type and ion involved, and typically involve the activation of signalling pathways such as the BMP or Wnt/β-catenin pathways, leading to the upregulation of key osteogenic and angiogenic genes and proteins[300,302,405].

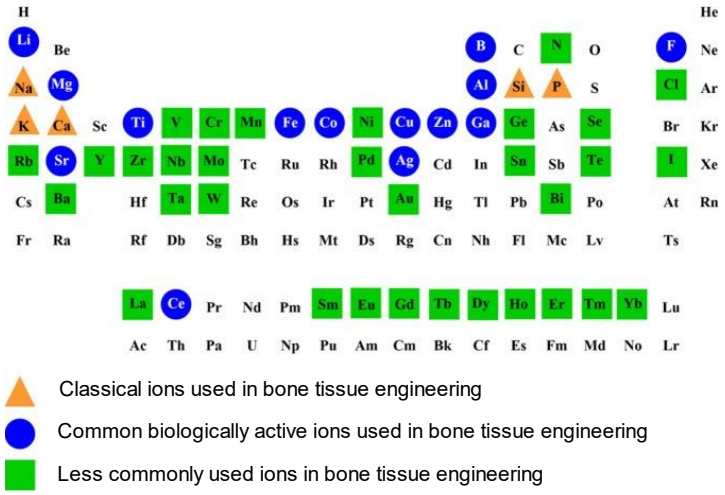

Fig. 1.13 – Bioactive Elements used for Bone Tissue Engineering: *Periodic table containing elements used for bone tissue engineering (from Pantulap et al. 2021[405]), highlighting the diversity of therapeutic options.*

Among the many bioactive elements (**Fig. 1.13**), boron is of particular interest due to its positive effect on both osteogenesis and angiogenesis, whether administered to bone cells *in vitro* via a scaffold[304,307,309,312,417], or to an organism systematically[299,301,303]. However, the mechanisms explaining ion-mediated growth often do not fully account for boron, which typically does not exist in the B^{3+} form due to the high ionisation energies needed to achieve this state. To resolve this, some work suggests that it is the release of bio-active boron compounds (for example, borates and boron oxides)[420,421], rather than elemental boron itself, that leads to the beneficial effects. Regardless of the specific mechanism, boron is known to upregulate the sodium-borate co-transporter NaBC1, which activates the BMP and MAPK pathways, promoting osteogenic and angiogenic effects[300,422].

In conclusion, tissue engineering is a dynamic area of research with broad applications across a range of biological systems, promising not only enhanced regeneration of lost or damaged tissue, but also the potential for creation of new tissue, accurate disease models, and devices designed to seamlessly integrate with biological tissues. These innovations set the stage for progress in related fields such as neural interfacing, which is the focus of the next section.

1.4 Neural Interfaces

Neural interfaces are one of the most exciting prospects in biotechnology, and, if fully realised, have the potential to be life changing. Neural interfaces, defined in this thesis as devices in contact with neural tissue for the purpose of electrical stimulation or recording, have a long history. Beginning with the development of the electroencephalogram (EEG) in 1924 by Hans Berger[423], and continuing through non-invasive devices, to invasive electrocorticogram (ECoG) devices[424–429], microneedle arrays[430–432], and even neural threads[433–436], the field is progressing at a rapid pace.

As a technology, these devices lie at an interesting intersection between medical treatment and technological enhancement – this is reflected in the public perception of the devices, with stories about brain-computer interfaces often focusing on their potential to enable revolutionary technological advancements[437,438], and on ethical questions that they surface regarding privacy, autonomy, and the potential for human enhancement[439,440]. However, in the present day, much of the research is focused on the treatment, diagnosis and understanding of the multitude of neurological conditions afflicting the human brain, as well as the battle against paralysis and debilitating injuries to the central and peripheral nervous systems[441].

One of the most promising recent developments in neural interfacing is the integration of 2D nanomaterials[442–444]. The unique properties of these materials, such as their high conductivity, surface area, and flexibility, make them ideal for creating more efficient and durable neural interfaces. This section will explore some of the main material, device and electrical considerations when designing neural interfacing devices, how they intersect with 2D nanomaterial research, and how this might inform future neural interfacing devices.

1.4.1 Materials for Neural Interfacing

Neural interfaces have long been fabricated from metals and highly doped semiconductors such as silicon[268,445,446]. Such biologically foreign, stiff materials can lead to scarring, particularly over the course of chronic implantation and when combined with under-optimised geometries, fixations, and device locations[236,447–449]. This in turns leads to performance degradation and device failure over a short timeframe, requiring costly and invasive surgery to replace the interface[450,451]. In the pursuit of high-resolution neural interfacing with complex devices,

improving the mechanical properties of neural interfacing materials to enhance device longevity and the stability of their performance is essential.

Therefore, recent work has focused on using more flexible, biologically compatible materials for neural interfacing electrodes[268,452–455], such as conductive polymers[446,456–461], thin metals[450,454,462] and nanomaterials[442–444,463–466]. However, while the biological safety of a material is paramount, the electrical performance of a device is also critical for both short- and long-term function[99,467–469]. Traditional materials often have these parameters at odds with each other – some materials have optimal electrical properties but high stiffness or low processability, such as metals and silicon (Fig. 1.14), while others excel from a stiffness and cytotoxicity perspective, but generally underperform in their electrical properties, such as traditional biomaterials[470,471].

The balance between these properties is therefore the key to unlocking the potential of these devices. To achieve this balance, recent research has investigated the use of 2D-material based composites for neural interfacing devices[463,472]. 2D material composites are unique in allowing researchers to take advantage of the superlative properties of 2D materials, while simultaneously leveraging the high biocompatibility, flexibility and processability of the chosen polymer matrix, ameliorating many of the issues faced by traditional electrode materials (Fig. 1.14). Furthermore, their properties can be tuned for a given application by adjusting the loading of nanomaterial in the matrix, offering versatility and tunability that is difficult to achieve using single-phase materials.

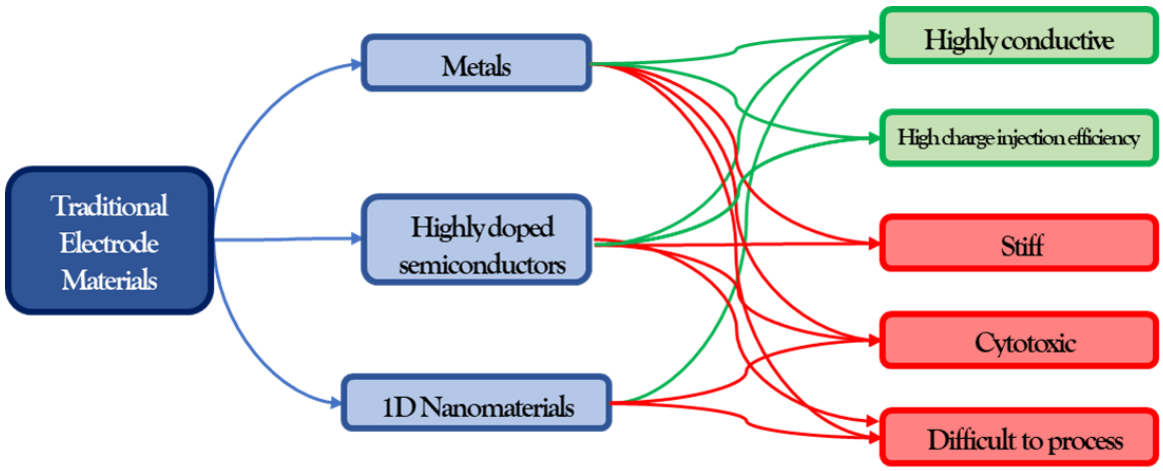

*Fig. 1.14 – **Traditional Electrode Materials:** Traditional electrode materials have many advantages as regards their electrical properties, but tend to fall down on their biological and mechanical properties, as well as their processability. 2D materials have emerged as viable contenders to address these problems, while maintaining electrical performance.*

1.4.1.1 Electrical Properties

The electrical properties of neural interfaces are critical for both short- and long-term functionality. Conductivity, impedance, capacitance and the electrochemical potential window all play crucial roles in determining device performance, for stimulation and recording[473,474].

Conductivity

The bulk conductivity of an electrode material, along with its surface impedance and the electrolyte resistance, dictate the overall charge transfer dynamics of an electrode/electrolyte system. High bulk conductivities allow for smaller device footprints and lower power consumption, due to the reduced voltage required to effect stimulation. For recording, higher bulk conductivity improves the signal:noise ratio due to reduced thermal noise and improved charge transfer, discussed in more detail in the next section.

Furthermore, while surface impedance is largely dictated by the topological and electrochemical properties of the interface, it is also indirectly influenced by the bulk conductivity[475]. Higher conductivity facilitates more efficient charge transfer to and from the interface by increasing the availability of charge carriers, thereby reducing the resistive component of the impedance. Lower surface impedance is particularly advantageous for low-noise recording electrodes, as discussed in the next section.

Impedance

The impedance (Z) of an electrode material is a critical determinant of its electrochemical behaviour, with implications for stimulation and particularly recording applications[473,474]. Measured using electrochemical impedance spectroscopy, there is much information that can be gleaned from the resulting spectra. The impedance of an electrode is reported either in the form of a Nyquist (Re(Z) *vs.* –Im(Z)) or Bode spectrum ($|Z|$ *vs.* f (Hz) and Phase(Z), where $|Z|$ and f are plotted on log scales), or at a specific frequency, often 1 kHz for ease of comparison between reports[473]. The charge transfer resistance of an interface then represents the resistive component of the simplified Randles equivalent circuit (**Fig. 1.15**), and can be interpreted as the resistance to transferring an electron from the electrode to the electrolyte via an electrochemical reaction, for example, the electrolysis of water. This resistance is derived from the impedance spectrum of an electrode, as the diameter of the semicircular region on a Nyquist plot, or as the difference between the high-frequency impedance and the low-frequency impedance given by the Bode plot.

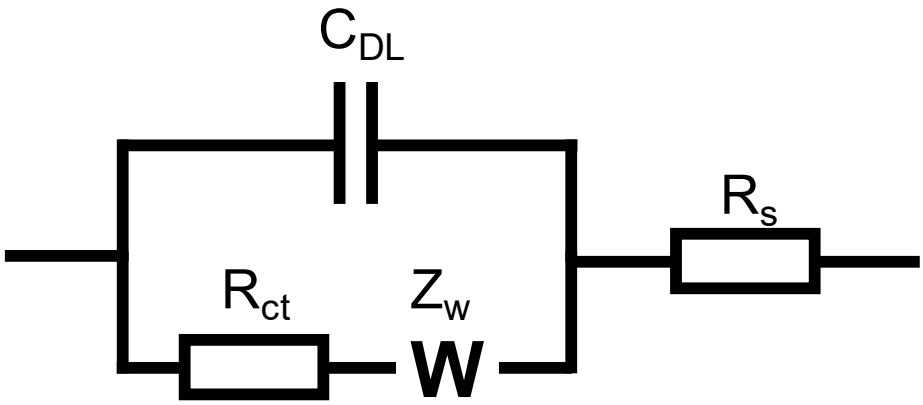

Fig. 1.15 – Electrochemical Equivalent Circuit for Typical Biomedical Electrode/Electrolyte Interface: *Randles equivalent circuit for biomedical electrodes, allowing electrochemical analysis and modelling. C_{DL} is the double-layer capacitance at the electrode-electrolyte interface, R_{ct} is the charge transfer resistance, Z_W is the Warburg element representing diffusion in the electrolyte, and R_s is the solution resistance.*

It is generally desired to lower the impedance and charge transfer resistance in the case of stimulatory and recording electrodes, as the lower the impedance, the higher the current that can be delivered to effect stimulation without requiring a potential outside of the electrochemical potential window for the surrounding tissue, at which point the electrolysis of water and the evolution of toxic electrochemical species would accelerate. Furthermore, the thermal (Johnson-Nyquist) noise v_n of an electrode scales with the impedance according to the following equation from Boehler et al. 2020[473], where T is temperature, Δf is the noise frequency band, k is the Boltzmann constant, and $Re(Z)$ is the real part of the impedance:

$$v_n = \sqrt{4kT\Delta f \times Re(Z)} \qquad \text{(Eq. 1.3)}$$

Thus, in order to achieve sufficient signal:noise ratios (discussed further in **Section 1.4.3**), the impedance must be reduced[473,474,476,477]. The impedance and charge transfer resistance can be lowered using a range of approaches, including increasing the electrochemical surface area by nanostructuring or roughening, and using conductive coatings such as gold/palladium, conductive polymers or nanomaterials[474]. (**Fig. 1.17**). For example, Castagnola et al. show a significant decrease in the electrode impedance and increase in the signal:noise ratio following coating of their electrodes with PEDOT, a common conductive polymer[478].

Cutoff Frequency

Related to the impedance is the cutoff frequency, defined as the frequency at which the phase angle of the electrode reaches -45°, and representing the point at which the signal magnitude has been reduced by 3 dB with respect to the pass band, to use the analogy of a band-pass filter[473].

This parameter has implications for the range of frequencies that the electrode can accurately measure, with those below the cutoff frequency significantly attenuated and non-linearly distorted[479]. For neural interfacing applications, the typical frequency range of potentials is on the order of 1 kHz, and as such this is commonly used as a maximum value for the cutoff frequency[473].

Electrochemical potential window for safe stimulation

As water is ever-present in physiological environments, care must be taken while stimulating to avoid the induction of electrolysis, which produces potentially cytotoxic species (OH^-, H^+, H_2 and free electrons) and induces significant changes in pH[473]. The rate of evolution of these species is dependent on the voltage according to the Butler-Volmer equation[473,480], so the electrochemical potential window defines the range of voltages within which the tissue can be safely stimulated. This window varies depending on the specific properties of the electrode and the electrolyte being tested, but for aqueous solutions is typically in the region of 1.23 V[481].

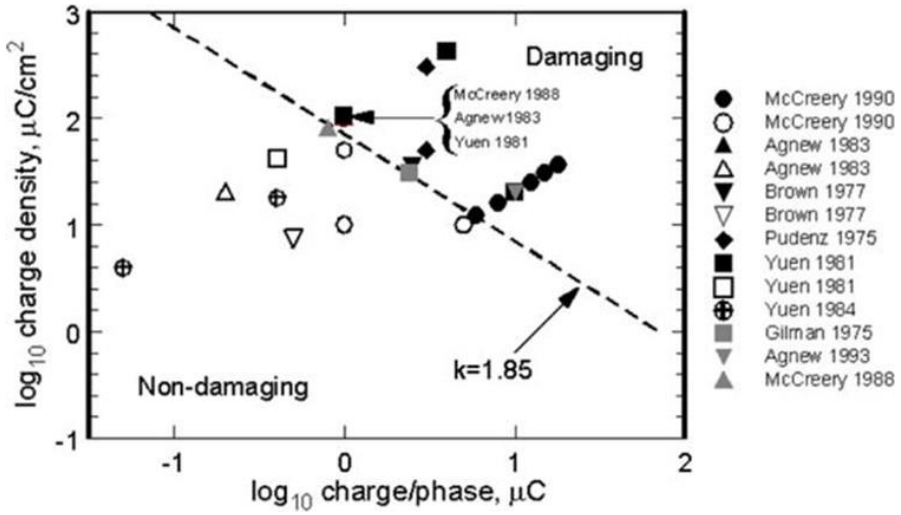

Fig. 1.16 – Shannon Equation for Tissue Damage Threshold: *Empirical data upon which Shannon equation is based, from Cogan et al. 2016, with k set to 1.85*[482].

A more nuanced approach to predict the damage caused by electrical stimulation can be found in the Shannon equation, an empirical formula describing the boundary between damaging and non-damaging stimulation, based on the charge density applied (σ), and the total current delivered per pulse (Q). The equation forms a line on the plot of $log(\sigma)$ vs. $log(Q)$, as shown in **Fig. 1.16**, where the dashed line is given by:

$$\log(\sigma) = k - \log(Q) \qquad \text{(Eq. 1.4)}$$

where k is an adjustable parameter usually chosen between 1.5 and 2[482].

Charge storage capacity (CSC)

The charge storage capacity of an electrode is closely related to the capacitance of the interface, and measures how much charge can be built up at the interface with the electrolyte. It can be enhanced via surface roughening to increase the specific surface area of the electrode, using a range of techniques, including etching (**Fig. 1.17**), nanostructuring, and coating with a rough/particulate layer[473,474]. It is typically measured by cyclic voltammetry, and usually defined as the integral of the CV curve in the cathodic region. It is worth noting that the CSC can be misleading, as only a small fraction of the charge built up is actually available for injection during a given stimulation pulse. As such, it can be an informative technique when examining the effect of treatments or differences between materials, but when interested in the absolute quantities of charge injected, metrics such as charge injection capacity are preferred[473].

Maximum charge injection capacity (CIC_{max})

Addressing the drawbacks of the charge storage capacity as a performance metric is the maximum charge injection capacity (CIC_{max}), a measure of how much of the charge stored on an electrode can be safely transferred to an electrolyte or tissue without resulting in the creation of deleterious electrochemical species or damaging voltage spikes. The CIC_{max} is a commonly used figure of merit for both stimulatory and recording electrodes, and is typically measured by analysis of transient voltage spikes in response to a current pulse[473,483]. The CIC_{max} is thus defined as the maximum current density that leads to a voltage spike still within the electrochemical potential window. When considering the CIC_{max} of a material, it is critical to account for its dependence on the pulse width. Typically, as the pulse width increases, so will the CIC_{max} – however, this is associated with a *decrease* in current density, which can push the stimulation intensity below the rheobase, or the minimum intensity of a pulse of indefinite duration which will activate a neuron. This in turn is related to the chronaxie, the pulse duration at which the threshold intensity is twice the rheobase, by the chronaxie-rheobase (or strength-duration) curve. This trade-off has important implications for both the required material properties, and for the design of stimulation parameters[484,485], discussed further in **Section 1.4.4**.

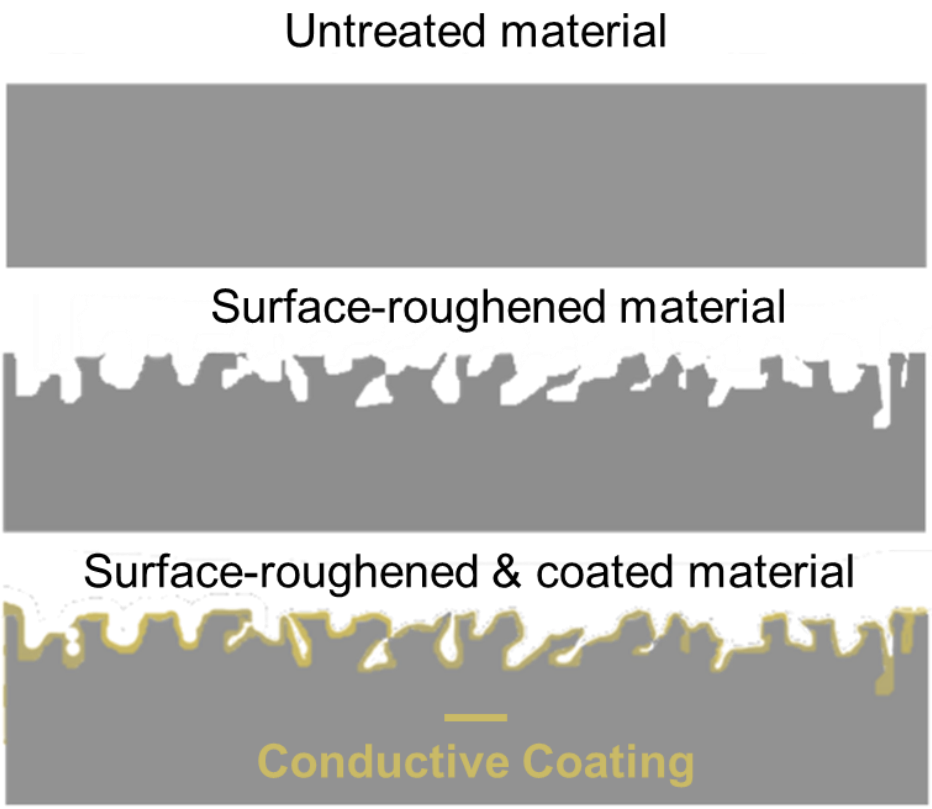

*Fig. 1.17 – **Surface Treatment of Composites for Enhanced Electrical Properties:** Demonstration of enhancement of electrical properties of composite by surface roughening and coating with a conductive material, to increase the specific surface area and decrease the impedance respectively.*

1.4.1.2 Mechanical Properties

As shown in **Fig. 1.18** and discussed in **Section 1.1.4.2**, the mechanical properties of a material are second only to the electrical properties in terms of their importance for device design. While properties such as viscoelasticity and plasticity are highly relevant in biomedical applications, the two most relevant properties are the *hardness*, defined here as the resistance to an object being pressed into the surface of a material, and the *stiffness*, a term that refers to the resistance of a material to resist elastic deformation in response to an applied force. The hardness, which is tunable by changing the material composition or by application of soft coatings such as biohybrids or hydrogels[351,486,487], can be loosely viewed as the local mechanical properties which cells primarily experience and respond to. Meanwhile, the material stiffness determines the micromotion of an implant, and its compliance with the surrounding tissues. This can be tuned by reducing device dimensions and careful design of tethering and implantation techniques[474]. Both properties need to be optimised, as tissue damage and inflammation can be caused by both high stiffness, leading to repeated impact and friction of the surrounding tissue with the implant, and by high hardness, which causes mechanosensitive glial cells to initiate a foreign body

response[488,489]. This response is driven in its early stages by neuron-supportive astrocytes and immune-surveillant microglia activated by a range of interconnected biochemical pathways such as integrin and stretch-activated ion channel signalling[489–491]. Independent of the cause, this response eventually leads to post-implantation microhaemorrhage, followed by eventual gliosis and device encapsulation, preventing electrical signals from passing through or out of the device[492,493].

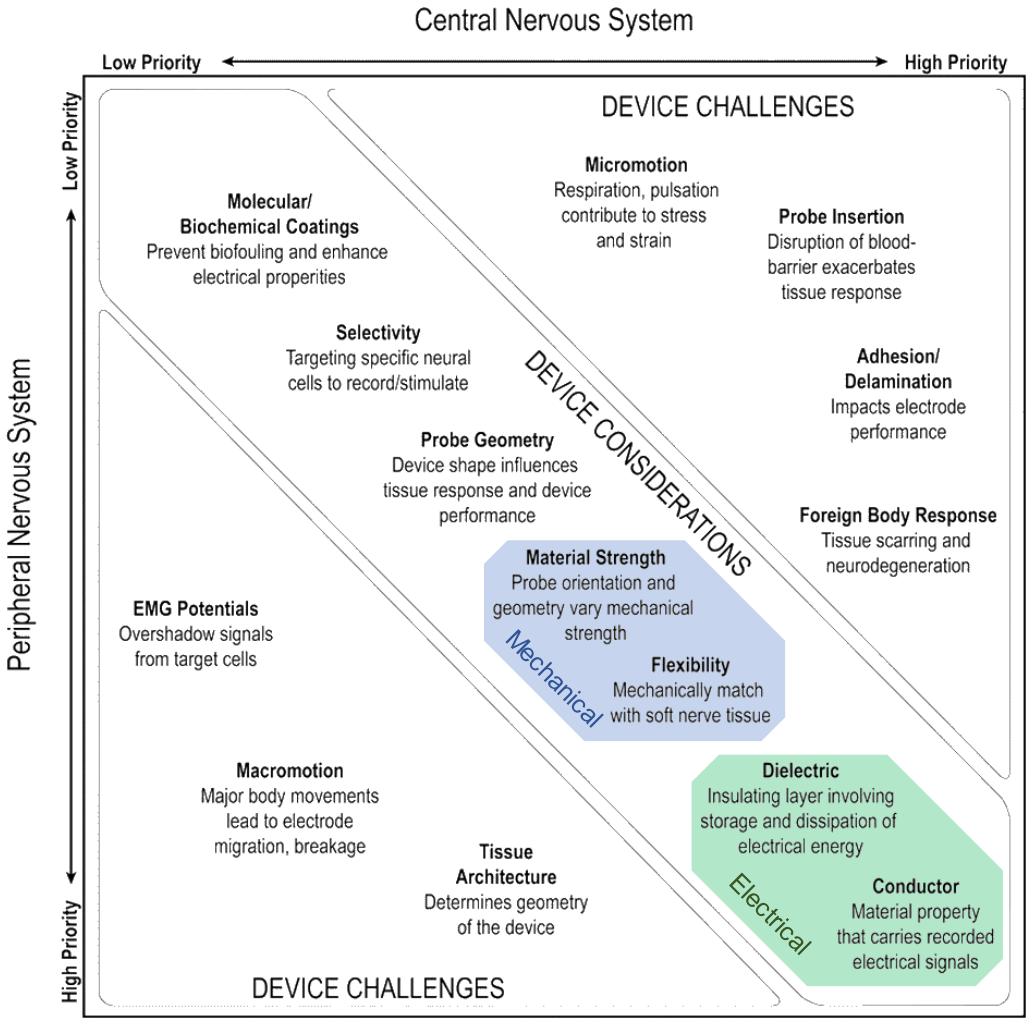

Fig. 1.18 – Material & Device Considerations for Neural Interfacing Devices: *Matrix of material, device, and environmental challenges for central nervous system (CNS) and peripheral nervous system (PNS) interfacing devices, demonstrating the complexities involved in high-resolution, robust neural interfacing. Adapted from Wellman et al. 2018*[268].

As a benchmark, the compressive modulus of the CNS has been estimated at 0.5 kPa to 1.2 kPa[351], so biomaterials and scaffolds should aim to achieve stiffnesses in this region, as neurons exhibit enhanced viability and outgrowth on soft substrates[351], a relevant consideration for materials that are being used for neuronal growth and stimulation. Approaches such as hydrogel coatings, thin-film electronics, and biohybrid electrodes have all been applied to better

align the mechanical properties of neural interfaces with the surrounding tissue, improving device lifetime and electrode integration[268,486,494,495].

However, a key limitation of these approaches is that the conductive component of the electrode remains stiff, and thus a potential source of stiffness mismatch and scarring. To overcome this issue, recent electrode designs look to incorporate softer conductive materials which more closely mimic the physicochemical properties of neuronal tissue[236,267,441,492,494,496], improving the neurocompatibility and subsequent implant lifespan. To enhance neuroprosthetic device compatibility *in vivo*, the electrodes themselves may be soft, typically hydrogels, composites with conductive nanomaterials[271,274,463,494], or conductive polymers[271,497–500], or they may be coated or encased in a softer material[262,501–503]. Carbon allotropes such as graphene and carbon nanotubes are particularly attractive due to their unique mechanical, thermal, optical, and electrical properties[107,463]. This, in conjunction with soft surface coatings and free-floating device tethering techniques, allows for the fabrication of highly conformable, flexible neural interfacing devices[474].

1.4.2 Electrical Stimulation for Tissue Regeneration and Neural Signal Control

Electrical stimulation of tissues has a diverse range of applications, from enhancement of tissue engineering scaffolds, restoration of lost function by restoring extant dormant tissue, or control and interrogation of PNS and CNS signals and behaviour. Based on the application of electrical impulses or electric fields to tissue, it has been shown to enhance cellular function and proliferation in a wide range of tissues and cell types, including cardiomyocytes[371,504], neurons[101,377], glial cells[505,506] and bone cells[507–512], among others[513–515] (Fig. 1.19).

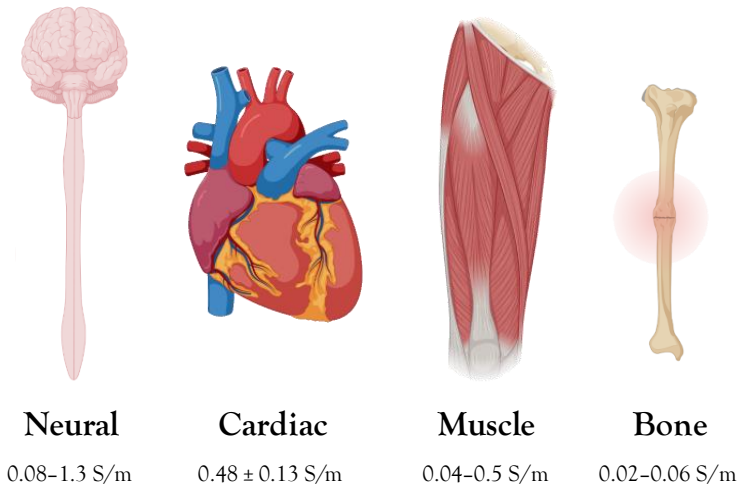

Fig. 1.19 – Electroactive Tissues: Electroactive tissues and their conductivities, from Zarrintaj et al.[516].

As the most prominent electrically active tissue in the body, and one of the most active areas of research for both stimulatory and recording electrodes, we will focus on neurons in this thesis. Discussion of the mechanism of electrical stimulation in other cell types can be found in Siwei et al. 2020[517] and Chen et al. 2019[518].

The effects of electrical stimulation on neurons are complex, highly tissue- and site-dependent[519], and change significantly with time and other stimulation parameters[519]. Generally, external stimulus is designed to contribute to the polarisation of the cell, thus making it more likely to exceed its action potential, and thus fire – in this regard, the electrical stimulation acts somewhat like a catalyst in chemical reactions[520]. This effect is governed by the polarisation of the membrane potential caused by an external stimulus, leading to ion flow across the membrane and neuronal activation[519]. Repeated firing in this manner leads to strengthening in connected neural pathways, via long term potentiation[519,521]. Electrical stimulation may also increase the expression of various growth-associated genes and proteins[522], often in an asymmetric manner, leading to cellular migration by electrotaxis[518].

Early work in this space has shown that culture of neural and cardiac cells on conductive substrates, combined with electrical stimulation, can enhance their growth, and thus the repair of the injured tissue[101,170]. However, much optimisation is still required, with respect to the stimulation modalities used (e.g. direct vs. indirect, biomimetic vs. supraphysiological, magnetic vs. electrical), the materials used to deliver and direct it, and the parameters used (e.g. frequency, voltage, waveform, etc.). This complex interplay between stimulation modalities, devices, and parameters[377], layered on top of the dynamic, diverse tissue environments in which it is applied[517], renders electrical stimulation a useful but poorly understood therapy, with the potential for significant regenerative effects if thoroughly optimised.

The applications of electrical stimulation extend far beyond tissue engineering. Stimulation electrodes, when placed in the brain, or around the spinal cord or peripheral nerves, can be used to modulate neural activity, deliver electrical signals, and thus change neural circuitry, dynamics and eventually function. This ability has been leveraged to a great extent in devices such as deep-brain stimulation electrodes, cochlear implants and cardiac pacemakers, and is an area of active research in the brain-computer interfacing space, with functional electrical stimulation (FES) allowing users to regain some control over lost functions[523–525].

1.4.3 Recording for Neural Signal Interrogation and Modulation

Going beyond the regenerative and modulatory effects of electrical stimulation to the interrogation of electrical signals is not a trivial feat, but it has the potential to revolutionise our understanding of the brain, its circuity and its disorders[441]. When electrodes are able to record from the brain or nerves with high spatial and temporal resolution, we can use those insights to assess the progress and pathologies of neurological dysfunction, and perhaps most importantly, use it to train brain-computer interfaces. Devices for neuronal recording require markedly different configurations than those designed for broad electrical stimulation, with smaller electrode footprints to enhance spatial resolution and high channel counts to allow discrimination of signals and to increase the dimensionality of the dataset[526]. Furthermore, while material requirements may be somewhat simpler for recording electrodes (with the impedance being the key parameter), the downstream processing and associated chain of electronics can be significantly more complex when compared to stimulation setups, due to the necessity for amplification, smoothing, digitisation, visualisation and further signal processing[527].

The figures of merit relevant for recording electrodes differ significantly from those of interest for stimulation electrodes. The ability to distinguish neural signals of varying magnitudes (excitatory/inhibitory post-synaptic potentials, local field potentials, action potentials, etc.) is key, and defined by the signal to noise ratio (SNR), defined below with reference to the maximum and minimum voltages (V_{max} and V_{min}) and the root-mean-square voltage (V_{RMS}) of the trace.

$$SNR = \frac{V_{max} - V_{\min}}{2 \times V_{RMS}} \qquad \text{(Eq. 1.5)}$$

The SNR in turn is determined by a chain of interlinked factors, beginning with dimensional, material and electrochemical properties, through the experimental setup, environmental noise, and gain, and finally by the signal processing algorithms[527]. Electrodes should ideally be able to reliably discriminate signals on the order of 100 µV, with an SNR of at least 5:1 over the course of long-term recordings[474].

1.4.4 Stimulation Signal Parameters

The diversity of signal parameters is as broad as the range of materials and devices used to deliver them[377]. With dependencies on the cell type, maturity, and desired outcome, there is no one-size-fits-all stimulation paradigm for all systems, but there are some general empirically derived rules of thumb to consider when optimizing a novel stimulation setup.

1.4.4.1 Pulse Width

The pulse width of a stimulation cycle varies depending on the desired outcomes from stimulation. The pulse width must be long enough to deliver adequate charge to the tissue, but not so long that excess charge buildup causes the voltage to exceed the electrochemical window. The pulse width in particular has a striking impact on the charge injection capacity, dictating how much total charge is delivered for a particular current density. As discussed in **Section 1.4.1.1**, the required pulse width is informed by the chronaxie-rheobase curve, which dictates the minimum pulse duration necessary for effective stimulation to occur[484,485].

1.4.4.2 Frequency

The frequency at which stimulation is delivered is dependent not only on the cell type used, but on the level of cellular maturity, and the behaviour the study is aiming to stimulate[377]. Work by Tang-Schomer in 2018[528] has demonstrated that low frequency stimulation (0.5-20 Hz) leads to improved axonal extension and alignment when compared to high frequency stimulation (200-2000 Hz). This indicates that cells are sensitive to the frequency delivered, possibly due to their intrinsic firing frequency and refractory period following activation[529]. Other research, investigating the supraphysiological kilohertz stimulation regime, has shown that while there are unique benefits to this regime, there are also specific caveats such as synaptic fatigue and blocking of action-potential conduction that occur at such high frequencies[530]. This must be balanced with research showing that for brain stimulation, low-frequency stimulation is the most likely to cause inhibitory effects on neuronal firing, with the effect being highly dependent on the composition of the surrounding brain tissue[531]. In summary, the target frequency will depend on whether tissue regrowth, neural excitation/inhibition, or circuit remodelling is desired, the location of the stimulatory electrode, the maturity of the cells, and several other factors.

1.4.4.3 Duration

The duration of stimulation applied is also highly dependent on the desired outcomes. Some cells require long periods in culture to develop neurites, extend along an electric field, and become mature cells. Furthermore, whether cells are stimulated continuously or in a pulsed manner (i.e. the duty cycle of the stimulation) has a large impact on the outcome of stimulation. Breaks between stimulation pulses can on one hand allow for neurite growth and relaxation of

electrochemical gradients, while preventing hyperpolarisation of cells and buildup of toxic stimulation byproducts. On the other hand, this can allow for neurite regression & loss of stimulated effects[377]. Often, where high intensities are required to deliver the required effect, pulsed stimulation will be necessary to reduce the damage associated with higher electric fields[377,518]. The wide range of stimulation durations can be seen in the literature review in **Fig. 1.20 A**, based on Bertucci et al. 2019[377].

1.4.4.4 Waveform

The polarity and the waveform of the signal is a factor that must be taken into account, both from an electrochemical standpoint, and from a biological one. Stimulation can be delivered either by AC or DC waveforms, with sinusoidal, square, triangular, sawtooth or other waveforms used for AC stimulation[377]. Biphasic, charge-balanced waveforms are typically used to minimise the buildup of electrochemical species[473]. However, in some cases DC stimulation has been demonstrated to yield beneficial effects, provided the other pulse parameters are tuned to avoid electrolysis[377] and hyperpolarisation. For example, as mentioned above, pulsed stimulation can allow for electrochemical gradients to relax, minimising the damage caused by the electric fields. Furthermore, the directionality of neuronal growth appears to be dependent on the waveform, with Nguyen et al. 2014 finding that both AC and DC stimulation were capable of causing neurite outgrowth, but that only DC stimulation seemed to drive directional growth towards the nearest electrode[532]. This is a key consideration for scaffolds and other such devices which are designed to assist neurons to bridge a gap[533,534].

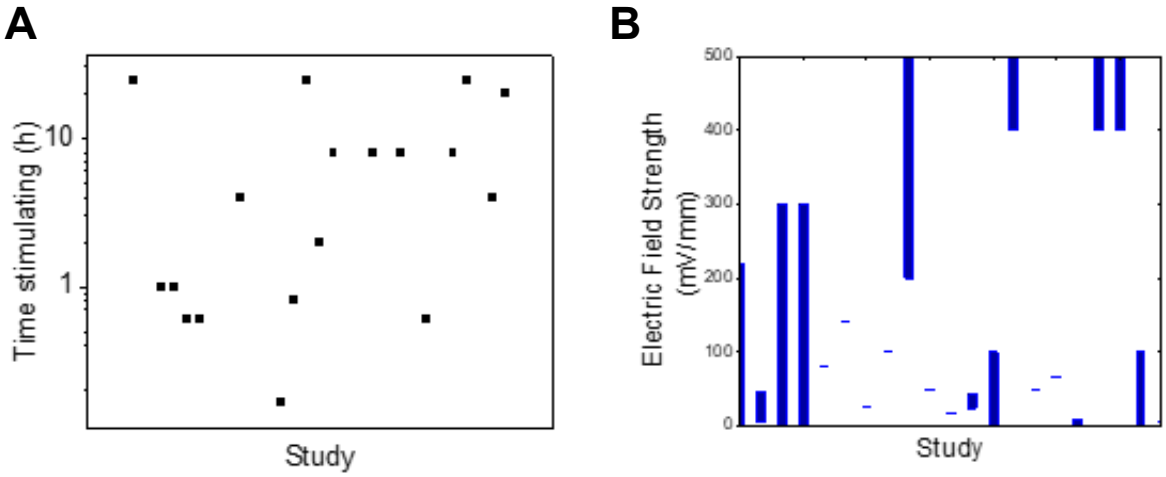

*Fig. 1.20 – **Electrical Stimulation Parameters for Neurons:** Literature review of stimulation durations (A) and electric field strength (B) adapted from Bertucci et al. 2019[377], demonstrating the wide range of stimulation parameters found in the literature. Bars in B represent ranges of field strength, while dashes are point values.*

1.4.4.5 Voltage

The voltage of the stimulation pulse must be carefully chosen, in order to avoid 1) leaving the electrochemical potential window, causing the evolution of toxic electrochemical by-products, or 2) causing the current density in the tissue to exceed the tissue damage thresholds for stimulation, which are commonly defined as 30 μC/cm^2 for macro-electrodes[482,535], and 4 nC per stimulation phase for micro-electrodes[536]. The voltage is often expressed as the electric field across a tissue during stimulation, which varies depending on the other parameters. In the data presented in **Fig. 1.20 B**, adapted from Bertucci et al.[377], the average stimulation electric field lies around 200 mV/mm. Within the safe voltage limits, the cellular response to differing intensities of electrical stimulation is highly variable, even temporally[519], so care must be taken to optimise the electric field on a case-by-case basis to avoid cytotoxicity induced by electrochemical species, hyperpolarisation, or excitotoxicity from excessive neural firing.

1.4.5 Neural Interfacing Devices

Neural interface design has evolved significantly over time, and has gone down diverse paths depending on the desired application (**Fig. 1.21**). Stimulation devices are distinct from recording devices, which are different still from bidirectional interfaces, due to the differing and occasionally conflicting design constraints imposed by the environment and application. This section focuses on bidirectional, invasive devices, rather than non-invasive modalities such as EEG and fMRI, reviews on which can be found in Abiri et al.[537] and deCharms et al.[538] respectively. These devices can be further sub-classified by their level of invasiveness – the least invasive being subdermally implanted EEG, followed by epidural and subdural (or epicortical) electrodes, which are placed above and below the dura mater respectively. The latter devices, often referred to as electrocorticography (ECoG) devices, consist of arrays of either passive or active electrode sites, which are used to communicate with the surface layers of the brain[427,539].

Modern ECoG devices such as mesh electronics allow flexible, high channel count interfacing across a wide portion of the cortex, in a minimally invasive fashion[540,541]. At the next level of invasiveness are intracortical devices such as microneedle or shank-based arrays which penetrate the upper layers of the brain, known as the cortex. These devices allow for finer control over stimulated regions and recording volumes, but are also more prone to inducing scarring and reactive gliosis. Finally, the most invasive type of device penetrates deep into the brain, the

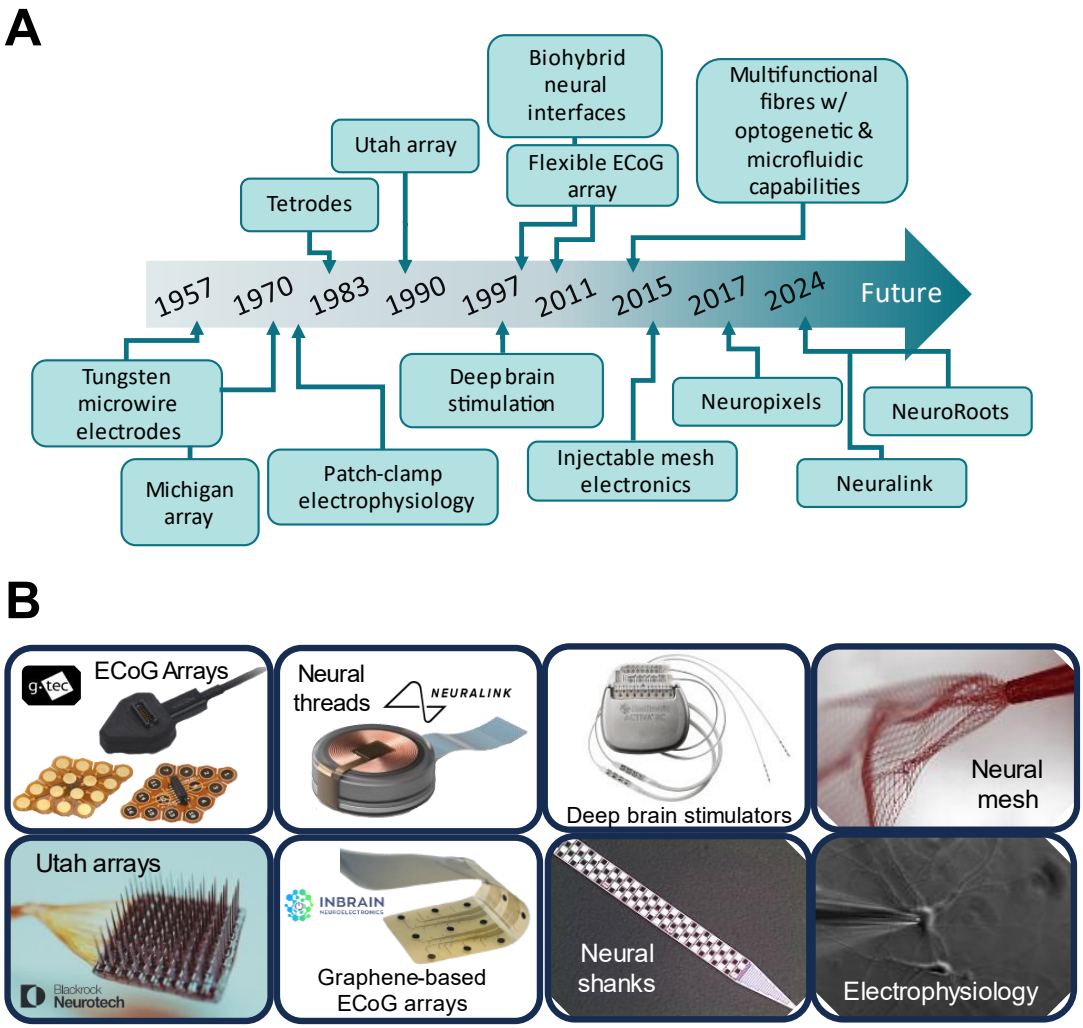

*Fig. 1.21 – **Neural Interfacing Devices:** **A)** Development of electrode technologies over the past ~60 years, demonstrating the progression towards high-resolution, flexible devices. Adapted & updated from Hong & Lieber 2019[526]. **B)** Schematic of various neural interfacing devices – clockwise from top left: GTec electrocorticography array[542], neural thread-based neural interface from Neuralink[436,543], deep brain stimulation probes from Medtronic (Activa RC[544]), neural mesh electrode from the Lieber Research Group in Harvard University[545], electrophysiological recording using a patch-clamp electrode[546], neural shank electrodes from Neuropixels[547], electrocorticography array from InBrain Neuroelectronics[548], and Utah microelectrode array from Blackrock Neurotech[549].*

cerebrum, and are known as intracerebral devices. These include deep brain stimulation electrodes, used for the treatment of certain neurological disorders such as Parkinson's, along with psychiatric disorders such as refractory depression or obsessive-compulsive disorder. Each additional level of invasiveness offers a trade-off of higher spatial and temporal resolution (Fig. 1.22) and larger accessible brain volume for increased scarring and complication risk, and decreased device lifetime.

As a result, much research is currently directed at either 1) increasing the resolution of non-invasive techniques such as EEG/fMRI and ultrasound, or 2) reducing the impact of invasive

devices. It remains to be seen which approach will be the most effective and practical in the long run, and it is likely to remain highly application-dependent in the future. While there are many potential device designs, and a vast parameter space to optimise (flexibility, device geometry, device fixation, device encapsulation, signal & data transfer, voxel size, etc.), this section will focus on the two most relevant modalities to this work – stimulatory substrates and scaffolds (the subject of Chapter 2), and microneedle-based neural interfacing devices (the subject of Chapter 3).

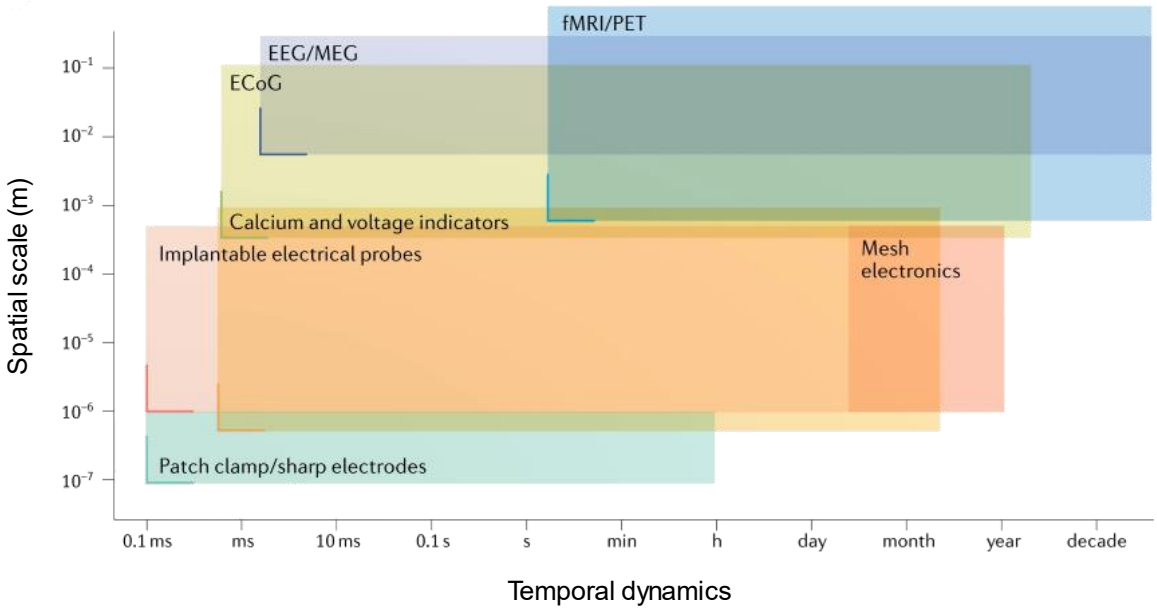

*Fig. 1.22 – **Spatiotemporal Limitations of Existing Neural Interfaces:** Illustration of trade-off between spatial and temporal resolution for neural interfacing devices, reproduced from Hong & Lieber 2019*[526].

1.4.5.1 Stimulation Substrates & Scaffolds

Two of the more basic implementations of neural interfacing treatment are 1) the use of conductive materials and 2) the use of electrical stimulation to enhance neural regrowth and differentiation. While each technique works well in isolation, they exhibit synergistic effects when applied in unison. The potential for the co-application of these technologies is shown by the use of conductive materials as substrates for electrical stimulation delivery, such as spinal cord[101,260] and peripheral nerve repair scaffolds[497,522,550,551]. As electrically active cells, neurons thrive on substrates which are capable of mimicking the electrically conductive environment they prefer to grow on[522,552]. This means that even in the absence of electrical stimulation, the presence of conductive materials can enhance the growth of cells[553]. For example, carbon nanotubes[554], conductive polymers[555], and graphene[288,290] have each been used to enhance the growth of neurons.

The mechanism of this effect is unclear, and appears to be dependent on the configuration of the stimulation – it has been suggested that proteins adhere more effectively to the polarised surface of conductive nanomaterials[556], or that the conductive substrate influences the resting membrane potentials of neurons[557]. Conductive substrates are capable of synergistically enhancing the effect of stimulation, since they are capable of picking up and directing electrical fields in a controlled manner, as shown by recent work in our lab, where electroconductive frameworks lead to enhanced neurite outgrowth in non-conductive ECM channels contained within the frameworks[398].

It has been shown that culture of neural and cardiac cells on conductive substrates, combined with the application of electrical stimulation, can enhance their growth, and thus the repair of the injured tissue[377]. Graphene in particular has shown great promise in this field, with previous work in our lab and others demonstrating the potential for graphene to direct and enhance the effect of electrical stimulation of neurons and cardiac cells *in vitro*[101,170,260]. Scaffolds, discussed in detail in **Section 1.3**, have recently been combined with electroconductive frameworks and stimulators in order to enhance regrowth and restoration of function[398,401,558]. For example, Feng et al. 2023 has demonstrated a MXene-based hydrogel for differentiation of neural stem cells under the influence of stimulation[559], and Han et al. 2021 has demonstrated an annular graphene substrate for application of wireless stimulation[560].

1.4.5.2 Microneedle-based Electrode Arrays

For applications that require higher resolution, smaller electrode sites, and deeper penetration into the cortex than typical flat ECoG devices, microneedle-based electrode arrays are a popular choice. The archetypal microneedle electrode array is the Utah array (**Fig. 1.21 B**), consisting of an array of long needles, occasionally with varying lengths, typically fabricated from silicon. These devices have been developed further into shank-based devices such as Michigan arrays, which combine the concept of the multi-electrode shank with the microneedle array, allowing for more recording sites and thus higher resolution. In each of these cases, the optimisation of the device design, such as needle density, pitch, geometry, and most critically material composition is essential, since scarring can occur rapidly if not carefully considered, leading to encapsulation of the device and a loss of function[268,561]. Electrical properties must also be optimised, as the small electrode sites desired for high resolution necessarily lead to higher impedance, which can in turn cause high noise. This has driven the push for highly electrically performant materials, allowing for the fabrication of smaller, higher resolution electrode sites.

1.4.5.3 *Future Devices*

Clearly, the key trade-offs in neural interfacing are between biological integration, spatial resolution & coverage, electrical performance, and device lifetime. This has been corroborated by a survey of researchers from academia and industry at the Cambridge Bioelectronics Symposium, which established that the most important properties currently lacking in bioelectronics materials are biocompatibility/degradability, flexibility, and stability[441]. Each of the devices shown in **Fig. 1.21 B**, and each technology therein, has its own unique benefits and drawbacks (**Fig. 1.22**), and thus are appropriate for different device applications. The next evolution of neural interfaces will need to have more, higher resolution channels, while being more flexible, penetrating deeper, and being more robust against scarring and degradation of function, in order to effectively drive treatments for neurological disease and neurotrauma, as well as human enhancement, forwards.

One promising class of designs for these novel interfaces are those consisting of neural threads – long, flexible probes that are inserted into the brain at various points, to effectively interface both intra- and sub-cortically[474]. Devices of this class include Neuralink's device, recently implanted into its second patient[436,562], NeuroRoots, developed between Stanford and Cambridge Universities[563], and the work being carried out in the group of Polina Anikeeva at MIT into multipotent neural fibres with both electrode and microfluidic drug delivery capabilities[564,565]. Various approaches may be taken to enhance the properties of these electrodes further, such as the implementation of biohybrid systems, rendering the interface between the biological system and the electrodes as seamless as possible[486,566]. Graphene and other nanomaterials show great potential for application in this space, thanks to their built-in flexibility, superb electrical performance, and ease of processability[442–444,463–466]. The keys to further development of these devices will be high-resolution microfabrication techniques, combined with novel, flexible and biocompatible electrode materials and device configurations[474]. The neural interfacing devices of the future will need to be multifunctional, robust, and high resolution, in order to fully unlock the vast potential of this field for technological advancement and improvement of health[474,567,568].

1.5 Objectives and Aims

This thesis investigates the biomedical applications of two-dimensional nanomaterials, with a specific focus on their potential in tissue engineering and neural interfacing applications. First, we aimed to apply graphene to the challenge of neuronal medical device development, with a focus on neuronal regeneration using electrical stimulation – stimulation delivered *via* graphene substrates led to a significant enhancement in neurite outgrowth and cellular morphology, yielding a versatile platform material for electroconductive tissue regeneration. Building on this, we set out to refine our graphene formulation further to achieve higher biocompatibility and conductivity. This material was then used to develop flexible, biocompatible microneedle-based neural interfaces, with enhanced electrochemical performance and the potential to effect neuronal stimulation and recording. These devices hold significant potential for applications in both electrical stimulation therapies and bidirectional neural interfacing. Finally, demonstrating the breadth of possibilities in the field, we aimed to show that boron nanosheets are an effective multifunctional additive for enhancing bone repair, by tapping into the innate bioactivity of boron, the distinctive properties of 2D nanomaterials, and the well-established properties of collagen scaffolds.

In pursuit of these research goals, the following objectives and associated aims were established:

Objective 1: Develop a flexible, biocompatible and electroconductive graphene composite for enhancing the electrical stimulation of neurons (***Chapter 2***). Specifically, the individual aims were to:

1.1. Optimise fabrication of conductive, biocompatible collagen-graphene composites and test their biocompatibility with neural and immune cells *in vitro*.
1.2. Utilize collagen-graphene composites to enhance the axonal growth-promoting effects of electrical stimulation on primary neurons.
1.3. Demonstrate the versatility and potential of the composite material in tissue engineering, neural interfacing, and bioelectronics applications by fabricating porous scaffolds, microneedle arrays, and 3D-printed circuits.

Objective 2: Develop a graphene composite microneedle-based flexible microelectrode array, and assess its neuronal stimulation and recording abilities, towards non-scarring, multi-channel neural interfacing devices (*Chapter 3*). The specific aims were as follows:

2.1. Develop and characterise the optimal pristine graphene formulation from a range of candidates, based on biological and electrical parameters.
2.2. Combine optimal PVP-stabilised graphene with polycaprolactone (PCL), a biocompatible polymer, to form graphene-polymer composites (PolyGraph) and investigate their biological interactions with neuronal and glial cells.
2.3. Enhance and measure the electrochemical properties of PCL-graphene composites by NaOH treatment and coating with a conductive gold-palladium layer.
2.4. Develop a PCL-graphene microneedle-based electrode array with a flexible hyaluronic acid backing, and demonstrate its potential as a bidirectional neural interfacing electrode using a custom stimulation bioreactor, and electrophysiological measurements of mouse brain slices.

Objective 3: Produce biocompatible polymer-stabilised boron nanosheets, and investigate their potential as a multifunctional additive in bone tissue engineering scaffolds, thus demonstrating the broader potential of 2D nanomaterials in tissue engineering (*Chapter 4*). Specifically, the individual aims were to:

3.1. Synthesise boron nanosheets from a non-layered precursor by liquid phase exfoliation (LPE) and characterize their physical and biological characteristics.
3.2. Fabricate boron-collagen (BColl) composite films and 3D scaffolds by lyophilisation.
3.3. Investigate the biocompatibility and osteogenic potential of these 3D scaffolds with physiologically relevant bone cells.
3.4. Demonstrate the functional effects of this material by assessing the anti-microbial, angiogenic, neurogenic and anti-inflammatory effects of boron loading.

Chapter 2

Collagen/Pristine Graphene as an Electroconductive Interface Material for Neuronal Medical Device Applications

Note

This work was carried out as a collaboration with researchers in the Tissue Engineering Research Group in the RCSI, and forms the contents of the first publication from this PhD, entitled "Collagen/Pristine Graphene as an Electroconductive Interface Material for Neuronal Medical Device Applications", published in Applied Materials Today in 2022[101]. For narrative and completeness purposes, the relevant data will be included, and it will be marked using a † where the work was carried out by/with collaborators.

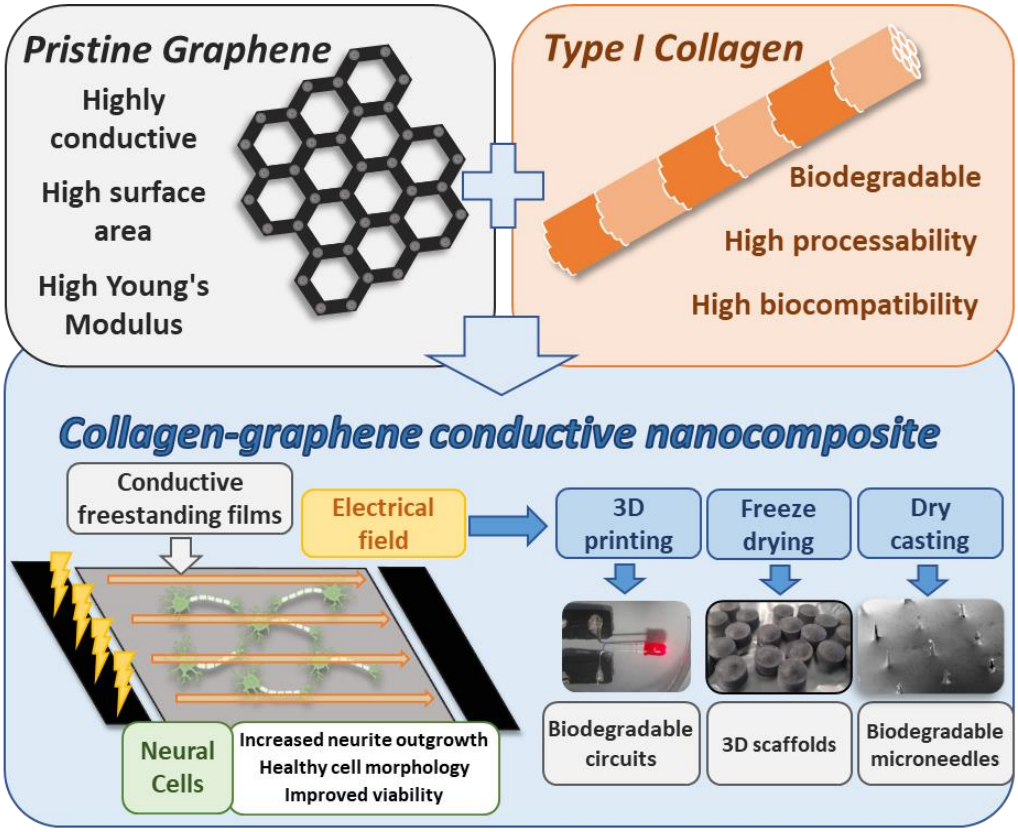

Fig. 2.1 – Pristine graphene (pG) suspensions were obtained through liquid-phase exfoliation via sonication from graphite in gelatin solution. Collagen/pG composites were fabricated to create films and microneedle arrays by dry casting, 3D porous structures through freeze drying, and bioelectronic circuits through 3D printing. Material properties can be tuned by changing collagen concentration and loading of pG. The composites trophically supported the growth of several different neural cell types and facilitated electrical stimulation of cortical neurons to enhance their growth. Together, these results demonstrate the versatility of NeuroGraph composites as a platform that balances biocompatibility and physiologically relevant conductivity with robust mechanical properties that allow for the fabrication of a range of next-generation medical devices for neural applications.

2.1 Introduction

With their advent in the 1940s[569], the fundamental component of electrical stimulation devices is a conductive electrode, designed to connect organic tissue to an electronic device without disturbing normal tissue function. Many devices employ metal-based electrodes, which have ideal electrical properties, but the disparity in their physicochemical properties compared to the softer neural tissues often leads to glial cell-induced scarring and long-term inflammation[236,449]. This 'foreign body response' is driven in its early stages largely by neuron-supportive astrocytes and immune-surveillant microglia, and leads to post-implantation microhaemorrhage and scarring which can limit long term performance[492,493]. To overcome this issue, recent electrode designs look to incorporate softer conductive materials which more closely mimic the physicochemical properties of neuronal tissue[236,267,492,494,496], improving the neurocompatibility and subsequent implant lifespan.

Foremost among the candidates for these new softer electrodes are conductive nanomaterial composites[271,463,494,497]. Carbon allotropes are particularly attractive due to their unique mechanical, thermal, optical, and electrical properties[274,463]. Among the various carbon allotropes, the graphene family, consisting of pristine graphene (pG), graphene oxide (GO)[105], and reduced graphene oxide (rGO)[106], have been identified as strong potential candidates for application at the neural interface[267–270]. pG in particular possesses excellent electrical conductivity, strength, and processability[107,274] in addition to high biocompatibility[77,227,570], and has thus emerged as the lead candidate material in this thesis. Softer electrodes fabricated using these materials have many potential applications, one of the most promising of which is nerve repair, a critical component of recovery from any devastating injury[571]. Tackling the challenge of nerve repair often involves the use of porous, biomimetic scaffolds, either biologically derived such as autografts or allografts, or artificially synthesized using biomaterials, to guide neurons and axons through the injury site and promote functional regrowth[384,571,572]. These scaffolds are often combined with additional therapies to enhance this regrowth, such as nerve growth factors[375], RNA delivery[376], and electrical stimulation[377,398].

Of these therapies, electrical stimulation is one of the most promising. Based on the application of electrical impulses or electric fields to tissue, it has been shown to enhance cellular function and proliferation in a wide range of tissues and cell types, including cardiomyocytes[504],

neurons[101,377], glial cells[505,506] and bone cells[507–511], among others[513–515]. The effects of electrical stimulation on neurons are complex, highly tissue- and site-dependent[519], and change significantly with time and other stimulation parameters[519]. Generally, the stimulus is designed to contribute to the polarisation of the cell, thus making it more likely to exceed its action potential, and thus fire – in this regard, the electrical stimulation acts somewhat like a catalyst in chemical reactions[520]. Electrical stimulation can be delivered and enhanced by a wide range of device morphologies, from flat stimulation substrates[101,170] and 3D, porous, and electroconductive scaffolds[398,508,573,574], to more complex devices for high-resolution or patient-specific applications, such as microelectrode arrays[575,576] and 3D printed nerve guidance conduits[398]. This breadth of potential device configurations calls for a material that is not only conductive and biocompatible, but processable into a wide range of morphologies.

Developing an innately biocompatible and electroconductive composite that does not require further functionalisation steps, yet is versatile enough to produce complex geometries, is an attractive solution to the challenge of electrical stimulation for nerve repair. We therefore propose that a combination of collagen and pristine graphene (NeuroGraph) is an ideal candidate for interfacing with and electrically stimulating the central and peripheral nervous systems, leading to improved neuronal growth. We identify this material as a promising platform for neural tissue engineering and next-generation electrical stimulation devices.

2.1.1 Objectives & Aims

The overall objective of this chapter was to develop a flexible, biocompatible and electroconductive graphene composite for enhancing the electrical stimulation of neurons, and demonstrate its versatile processability. Specifically, the individual aims were to:

1. Optimise fabrication of conductive, biocompatible collagen-graphene composites and test their biocompatibility with neural and immune cells *in vitro*.
2. Utilise collagen-graphene composites to enhance the axonal growth-promoting effects of electrical stimulation on primary neurons.
3. Demonstrate the versatility and potential of the composite material in tissue engineering, neural interfacing, and bioelectronics applications by fabricating porous scaffolds, microneedle arrays, and 3D-printed circuits.

2.2 Materials and Methods

2.2.1 Preparation and characterization of collagen-graphene (NeuroGraph) films

Fabrication of collagen-graphene films

Pristine graphene filler was liquid-phase exfoliated via sonication using a probe sonicator (Hielscher UP200S, 200W) from a high concentration graphite suspension (50 mg/mL) in a gelatin stabiliser (from porcine skin, gel strength 300, Sigma)/deionized water solution (30 mg/mL). The composite materials were created by mixing with a matrix of type I collagen (bovine tendon, 5 mg/mL, milled form, Collagen Solutions). Briefly, the composite suspension was blended with a homogenizer (T18/20 Ultra-Turrax®, VWR) at 15000 RPM for 1 h until homogenous, and composite substrates were prepared via room temperature (RT) evaporation, with graphene content varied from 0 to 60 wt% of the final substrate mass. For viability testing, freestanding films were prepared by casting 20 mL of slurry onto a 60 mm × 60 mm Teflon plate. For electrical stimulation testing, 1 mL of slurry was cast onto a 22 mm × 22 mm glass coverslip. All films then underwent dehydrothermal (DHT) crosslinking treatment for 24 h at 105 °C under vacuum[577].

Mechanical testing of collagen-graphene films

For the evaluation of mechanical properties, film samples of 40 mm length and 4 mm width were cut. Film thicknesses ranged between 20 µm and 50 µm and were measured using a micrometer (Mitutoyo). Samples were incubated in phosphate buffered saline solution (PBS) for at least 30 min at room temperature. A separate batch of samples were kept in the dry state. The 'top' and 'bottom' sections were secured in grips connected to a Zwick Z2.5 single column testing instrument, which was equipped with a 50 N load cell. Samples were subjected to uniaxial tensile testing parallel to the length of the film at a constant rate of 5 mm per minute until sample failure. Stress-strain curves were generated and used to calculate the mechanical properties of the samples. A MATLAB code (**Fig. A1.10**) was used to determine the mechanical properties of the samples. The slope of the first 10% of the stress-strain curve was used as the Young's modulus of the material, as the modulus at low strain is the most relevant to this work, in the toe region of the collagen stress-strain curve. To investigate the maximum elastic modulus in the linear region of the stress-strain curve, the code was modified to scan the stress-strain curve within set 10% sample windows, and calculate the slope and corresponding correlation coefficient of a linear

regression within each window. The window with the highest slope was used as the maximum elastic modulus value for the sample.

Thermogravimetric analysis (TGA) of collagen-graphene composite films to assess thermal degradation

To assess the thermal degradation behaviour of the composites, TGA of composite films was carried out using a thermogravimetric analyser (Q50-0783, TA Instruments, Delaware, USA) in an open platinum pan, under an O_2 atmosphere. Fragments (10 mg) of composite films of weight fractions 0, 10, 30 and 60 wt%, were ramped at 20 °C/min to 900 °C and held isothermal at 900 °C for 5 min to ensure complete combustion.

2.2.2 Surface contact angle measurements to assess surface hydrophilicity

To assess the hydrophilicity of the composite surface, the surface contact angle of the composite substrates was analysed by placing 2 µL of deionized water onto the sample using an OCA 40 system (DataPhysics Instruments GmbH, Filderstadt, Germany). The contact angle was then measured using a video setup and SCA20 software (DataPhysics Instruments).

2.2.3 Structural characterization of collagen-graphene composite structures via scanning electron microscopy (SEM)

To assess composite surface topography, SEM imaging was carried out. Prior to imaging, sample preparation for dry cast film samples consisted of sectioning with a 10 mm biopsy puncture and mounting on a metal stub. Microneedle arrays were cut out of the mold using a scalpel, and mounted on carbon tape on a metal stub using silver paint. Scaffolds were bisected using a tissue chopper (McElwain, USA), and mounted on carbon tape on a metal stub. Next, samples were sputter coated with an 80:20 mixture of gold and palladium to a thickness of 4 nm using a Cressington 108 auto sputter coater. Imaging was then conducted using a Zeiss Ultra FE-SEM using the InLens detector at an accelerating voltage of 5 kV, an aperture size of 30 µm and a working distance of 5 mm, with images acquired at varying magnifications.

2.2.4 Characterization of surface topography by atomic force microscopy (AFM)

To assess the surface topography of the composites, AFM was carried out on a scanning probe microscope (NanoSurf) in tapping mode under ambient conditions using aluminium-coated

silicon cantilevers (OTESP-R3). Average image sizes were 10 × 10 μm^2 at scan rates of 0.5 Hz with 1024 lines per image and an aspect ratio of 1. Images were analysed using NanoSurf CoreAFM.

2.2.5 Assessment of electrical conductivity

Bulk electrical conductivity was determined using the four-point probe method with a probe head (SP4-40180TRJ, Lucas Signatone) connected to a source meter instrument (Model 2450, Keithley). Film samples of the collagen-graphene composite material were cut with a scalpel into 4 cm^2 squares, and readings were made in their dry state at RT. Voltage readings were obtained by sourcing current in the ±10 mA interval to screen the linear region of the films according to Ohm's law.

2.2.6 Analysis of composite material degradation in physiological conditions

To determine the degradation behaviour of the composite in physiological conditions, 6 mm diameter circular samples of collagen and collagen-graphene (0, 10, 30, 60 wt% gelatin-stabilised graphene) were placed in wells of a 24 well plate and 1 mL of 0.1 mg/mL collagenase (Sigma-Aldrich, Ireland) in PBS was added to each well. Samples were weighed at time points between 1 h and 9 h, and the change in mass was plotted as percent of initial mass vs. time.

2.2.7 Cell culture for biocompatibility assessment and stimulation experiments

Culture of neuronal and glial cell lines

Several cell types of the neuronal lineage were tested with the collagen-graphene composites including: human neuroblastoma cell line (SH-SY5Y; CRL-2266, ATCC), mouse motor neuron cell line (NSC-34; Cedarlane Laboratories), human astrocytes (primary cell line, ScienCell, USA), mouse microglia cell line (N9[578,579]; RRID:CVCL_0452; kindly provided by the School of Pharmacy and Biomolecular Sciences, RCSI). SH-SY5Y cells were grown and maintained in growth media containing 1:1 mixture of Eagle's Minimum Essential Medium and F12 Medium (Sigma, USA), supplemented with the following components: fetal bovine serum to a final concentration of 10% (FBS, Biosera, Ireland), 1% Penicillin/Streptomycin (P/S, ScienCell, USA), and 4 mM L-glutamine (Sigma, USA). The N9 microglial line were grown and maintained in media containing RPMI (Sigma, USA), 10% FBS (Biosera, Ireland), 1% P/S (ScienCell, USA), and 4 mM L-glutamine (Sigma, USA). The NSC-34 cell line were grown and maintained in

growth media consisting of Dulbecco's Modified Eagle Medium (DMEM, Sigma) with 10% FBS (Biosera, Ireland), 1% P/S (ScienCell, USA) and 4 mM L-glutamine (Sigma, USA). Astrocytes were grown and maintained in astrocyte growth media – astrocyte media (ScienCell, USA), 1% P/S, 1% FBS (Biosera, Ireland), 1% astrocyte growth supplement (ScienCell, USA). All cells were seeded on flat circular samples cut with a biopsy punch (10 mm). All cell types were seeded at a density of 25,000 cells per film, with the exception of astrocytes, which were seeded with a lower density of 20,000 cells per film. Firstly, each sample was mounted on a sample holder insert (Cell Crowns, Scaffdex, Sigma). Prior to seeding the cells, each crown-mounted sample was sterilized by sequentially washing in ethanol solution (70%), allowing the sample to dry completely, exposing the sample to UV light for 30 min in a sterile cell culture hood, and finally dip washing the sample with 10% P/S solution in Dulbecco's phosphate buffered saline (DPBS). Afterwards, each crown was washed briefly in 0.1 M PBS, transferred into new 24 well plates filled with culture media, and incubated (37 °C, 5% CO_2).

Culture of induced pluripotent stem cell (iPSC) derived neuronal cell lines

iPSC neural precursor cells were derived from iPSCs as previously described[580] and were derived into neurons. Neurons were cultured in iPSC neural maintenance media (NMM) (iPSC Neural Maintenance Medium – DMEM/F12 & Neurobasal medium (Gibco, UK) (1:1), 1% P/S, 1% GlutaMAX, 1% MEM-NEAA, 0.2% N21 (Biotechne, UK), 10 ng/mL FGF (Peprotech, UK), 1% B27 (Gibco, UK)). Cells were then passaged by first removing culture media, and then incubating in accutase (4 min to 6 min, RT). Cells were next collected and diluted in media before centrifugation (1000 RPM, 3 min). Cells were then gently resuspended with minimal trituration in NMM and plated onto Celltrex (1:100, R&D Systems, UK) coated 6-well plates for further expansion. Alternatively, cells were counted and seeded according to the following protocol for iPSC neurons.

Assessment of iPSC-derived neuron biocompatibility with collagen-graphene films

To assess long term neuronal survival and growth on collagen-graphene films, developing 20 day old iPSC-derived neurons were seeded onto collagen or collagen-graphene films (5×10^4 cells/coverslip) in 100 µL droplets before flooding the wells with NMM the following day. iPSC neurons were also treated with 50 µM of ROCK inhibitor Y-27632 dihydrochloride (Axon Medchem, Netherlands) for 24 h to aid neuronal survival post-seeding. Half of the media

was then replaced with fresh NMM every 24 h to 48 h until cells were fixed in 4% PFA (20 mins, RT), washed (3 × DPBS) and stored at 4 °C.

Culture of primary mouse neurons for electrical stimulation

For primary neuron isolates, cortical neurons were harvested under RCSI ethical approval (REC202005013) from E18 mouse pups. Briefly, isolated cortices (N = 6 per collection) were collected in cold 0.1 M PBS before 5 mL of a papain (40 U/ml, Worthington), Deoxyribonuclease (100 U/ml Worthington) solution containing 30 mM glucose in Hank's Balanced Salt Solution (Sigma-Aldrich Ireland) was pipetted onto the tissue drop by drop (approximately 1 drop per second to avoid osmotic shock) to gently dissociate the cells and incubated for 45 min at 37 °C at 5% CO_2. Subsequently, the papain solution was gently removed and 1 mL of plating media (Neurobasal Plus Medium, 2% B27 Plus Supplement, 0.5 mM GlutaMAX supplement (all from Gibco) and 10% Heat Inactivated Horse Serum (Sigma) was then added. The tissue was then gently dissociated using Fire Polished Pasteur pipettes (Fisher Scientific) by gently titrating the solution 15-20 times. Thereafter, the neurons were counted using a haemocytometer and plated at a seeding density of 5×10^5 cells in a large droplet of plating media onto each film and incubated overnight at 37 °C and 5% CO_2. The next day, each well was then flooded with 3 mL complete media (plating media without the addition of horse serum). 1 mL of media in each well was changed every two days. On day five of the electrical stimulation experiments, all plated neurons were first washed in 1X PBS before being fixed with 4% paraformaldehyde (PFA) in PBS for 15 min, washed three times in PBS and then blocked in a solution of PBS containing 0.1% Triton-X100 (PBS-Tx) and 4% Bovine Serum Albumin (Sigma, USA) for 1 h.

2.2.8 In vitro electrostimulation of neuronal cells

To assess the cellular response to electrical stimulation on conductive composite films, mouse primary cortical neuronal isolates were exposed to electrical field stimulation routines in vitro through an in-plate electrode system (8 well plate C-Dish, IonOptix) connected to an external pacing controller (C-Pace EP, IonOptix). Prior to each daily stimulation regime, the electrodes were rinsed daily in autoclaved water (30 min) and then sterilized with UV exposure while submerged in 70% ethanol (30 min) in a cell culture hood. Afterwards, the electrodes were air dried inside a sterile cell culture hood, and placed in 1% P/s in PBS until use. The electrodes

were then placed into the 8 well plates containing 3 mL of the respective culture media. A half media change was done every 2 days for iPSC neurons and astrocytes, and every 3 days for the mouse primary cortical neurons. The stimulation parameters used were 4 h/day, 12 Hz, 9.8 ms pulse, and 200 mV/mm for the primary cortical neurons, which were informed by previous research into electrical stimulation of neuronal cells[377].

2.2.9 Cellular characterization of collagen-graphene films

Cell proliferation and viability tests

To assess cellular metabolic viability, Alamar Blue assays (Invitrogen, UK) were performed according to the manufacturer's instructions. Briefly, cells were incubated for 2 h at 37 °C with a 10% solution of the reagent in the appropriate fresh cell growth medium. Thereafter, the supernatant was removed, aliquoted in duplicate (100 µL ea.) into a black 96 well plate and the change in fluorescence measured using excitation 535 nm and emission 590 nm with a plate reader (Infinite M Plex, Tecan). Tested cells were re-immersed in culture media and returned to their incubator. To assess the DNA content of samples as a proxy for the cell number, and thus the cell proliferation, PicoGreen assays (ThermoFisher, USA) were performed according to the manufacturer's instructions. Briefly, the cells were lysed using lysis buffer (100 mL autoclaved DI water, 0.5 mL Triton X-100, 29 mg EDTA (Ethylenediaminetetraacetic acid), 2.12 g sodium carbonate), and samples were aliquoted in triplicate into black 96 well plates. 100 µL of the samples was mixed with buffer solution and the PicoGreen reagent, and allowed to incubate for 3 minutes before measuring the fluorescence using excitation 502 nm and emission 503 nm with a plate reader (Infinite M Plex, Tecan).

Immunohistochemical staining and fluorescence microscopy imaging

To assess cellular morphology and functional parameters such as neurite outgrowth, immunostaining and fluorescent imaging was carried out. At specific time points, samples for immunostaining were first briefly washed in PBS before being fixed with 10% formalin (Sigma-Aldrich, for cell lines) or 4% PFA (Fisher-Scientific, for primary and iPSC neurons) for approximately 15 min at room temperature, and then washed in (×3) PBS. The proteins of interest were labelled (1:500) with the following primary antibodies: Rabbit β Tubulin III Antibody (1:500, Sigma-Aldrich) in PBS with added 0.1% Triton-X100 (Sigma, USA)

and 2% bovine serum albumin to reduce non-specific binding and incubated overnight at 4 °C. The next day, the primaries were removed, the cells washed (×3) with PBS, and then incubated (1:500) with corresponding secondary antibody (Alexa Fluor® 488 Goat AntiMouse IgG Donkey Anti-Rabbit IgG Alexa Fluor® 647 (Invitrogen, UK), Goat AntiRabbit Antibody Alexa Fluor® 488 secondary antibody (1:500 Invitrogen)) for at least 2 h at RT. To fully image the morphology of growing cells, fluorescein isothiocyanate labelled phalloidin (Sigma, USA) was applied at a concentration of 50 µM for 1 h at RT. After washing (×3) in PBS, all samples were counterstained with DAPI (0.1 µg/mL) in PBS with 0.1% Triton-X100 and then mounted on slides with Fluoroshield™ (Sigma-Aldrich). Samples were imaged with fluorescence microscopy using a Leica DMIL microscope (Leica Microsystems), and the resultant images adjusted for color, brightness and contrast afterwards using Fiji (ImageJ 1.52p) software. In addition, confocal imaging using a Zeiss (710 NLO) confocal microscope was used to assess iPSC neuron and mouse primary neuron morphology. Briefly, film samples were washed with PBS after fixation (4% PFA for 15 min at RT) and then stained sequentially with phalloidin and DAPI according to the provider's indication (actin cytoskeleton/focal adhesion staining kit, Chemicon). The composite film samples were mounted on a glass slide, and acquisition was carried out in a sequential manner using 405 nm, 488 nm, and 561 nm lasers with the optimal emission for each fluorescent probe used. Samples were imaged in a Carl Zeiss LSM 710 confocal microscope (Carl Zeiss Ltd).

2.2.10 Fabrication of conductive structures using collagen-graphene composite

Fabrication of 3D porous scaffold from collagen-graphene composite

To assess the potential of the composite slurry for use in a lyophilization fabrication process which can be used to create porous scaffolds for tissue engineering applications, collagen-graphene and collagen only slurries were aliquoted in a cylindrical Teflon mold, and snap frozen for 5 min using liquid nitrogen. The scaffolds were then freeze dried for 24 h at −40 °C to obtain a lyophilized cylindrical scaffold with longitudinally oriented pores.

Mold casting of microneedle array

To investigate the use of the collagen-graphene material for microneedle electrode arrays, with potential use as electrostimulation and recording electrodes for neural interfaces, a collagen-graphene slurry (60 wt%), with a collagen concentration of 12 mg/mL, was added to a silicone microneedle mold (conical, height - 2.5 mm, 625 µm base diameter, tip diameter – 40 µm to 80 µm), fabricated according to a previous protocol[581]. The mold and slurry were then repeatedly degassed in a vacuum chamber for 30 min, to allow the slurry to penetrate the microneedles. The array was then allowed to dry under a continuous flow fume hood for 72 h at RT, and then placed in a −20 °C freezer for 4 h to assist the mold removal and to avoid damaging the needles. The microneedle array was gently peeled from the mold, before being prepared for SEM as outlined in section 2.2.3.

3D printing of collagen-graphene for bioelectronic circuits

To assess the potential of this composite material for 3D printing of bioelectronic circuits with high biocompatibility, collagen was dissolved in acetic acid and blended with graphene suspension to produce a slurry with 60 wt% graphene and final collagen concentration of 12 mg/mL. The slurry was cooled to 4 °C and printed using an Allevi 3 3D printer (Allevi Inc., USA) using a 22-gauge needle at a pressure of 20 PSI. Printed patterns were dried at 37 °C for 1 h. Silver contacts were painted onto printed collagen-graphene wires, and connected to an LED (rated at 20 mA, Radionics, Ireland) and a variable power supply (Keithley 2450 Sourcemeter, IMEX, Ireland). 20 V was passed through the circuit, with a corresponding current of 5.9 mA. Lighting was visible from 2.5 V, corresponding to 0.23 mA.

Conductivity measurements of 3D printed collagen-graphene composite

2×1 cm patches of collagen-graphene were printed onto glass slides (N=4), and their conductivity was measured using a 4-point probe (Sel-Tek, UK) connected to a Keithley 2450 Sourcemeter (IMEX, Ireland). Thickness of printed patches was measured using a micrometer.

Measurement of spreading ratio to assess printability

To assess printability of the composite, the ratio between the final width of a printed line and the gauge of the printing needle (spreading ratio) was calculated. Single straight lines, 20 mm in

length, of collagen-graphene were printed in rows of 3 on three glass slides (N=3, n=3), and width of lines was measured at the beginning, middle and end of the lines. Average width per line was divided by inner diameter of the printing needle (0.413 mm) to give the spreading ratio.

2.2.11 Statistical analysis

A minimum number of three experimental replicates (N) with at least three technical replicates (n) were used in all assessments. Prior determination of statistical significance, the ROUT method (Q=10%) was used to determine the variance in the population. All data sets were subjected to Kolmogorov–Smirnov test to assess for normality and thereafter the data tested using appropriate parametric (t-test, one- and two-way ANOVA) and non-parametric (Mann-Whitney U, one and two-way Kruskall-Wallis) tests. Post-hoc tests were performed using Tukey's multiple comparisons and Dunnett's correction where needed. All results were plotted with the standard error of mean and were considered significant when $p < 0.05$ and statistical significance was denoted by *: *$p < 0.05$, **$p < 0.01$, ***$p < 0.001$, ****$p < 0.0001$. Significances are relative to control group of timepoint unless stated otherwise. All data were plotted and analysed as means with standard error of the mean while using the software GraphPad Prism (v8.0) and OriginLab 2024.

2.3 Results & Discussion

2.3.1 Production and characterization of films of type I collagen and pristine graphene *(Aim 1)*

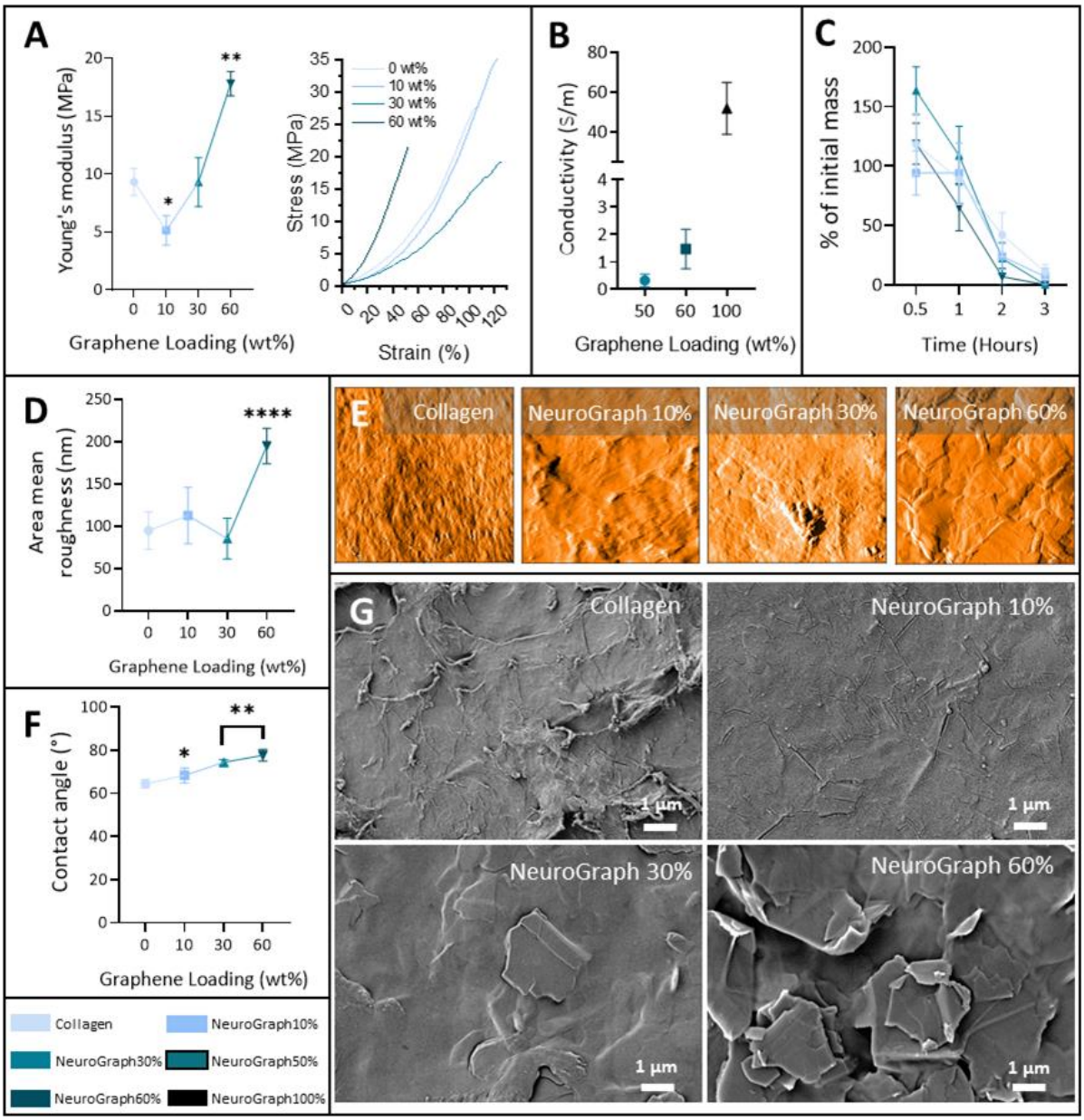

*Fig. 2.2 – **Bulk physical property characterization of collagen/pristine graphene (NeuroGraph) composite films: A)** Assessment of the Young's modulus and representative stress-strain curves of the hydrated films, as a function of pG loading, showing the robust mechanical properties of NeuroGraph. **B)** Conductivity measurements in dry state, showing the composite reaching the percolation threshold as a result of increasing pG loading. NeuroGraph 100% represents a vacuum-filtered, polymer-free network of graphene. **C)** Degradation testing of the films with different pG loadings using the enzyme collagenase (at 37 °C) revealed that pG loading has no effect on degradation rates compared to the collagen controls. **D)** NeuroGraph film arithmetical mean height (Sa) measurements showed a significant increase in surface roughness on NeuroGraph60% compared to other tested films. **E)** AFM images derived from 10 × 10 µm z-axis scans for increasing graphene loadings also showed an increase in surface irregularities with higher pG loadings. **F)** Contact angle measurements performed with deionized water droplets on the different composites showed a small but significant increase with higher pG loadings. **G)** SEM imaging of the film surfaces revealed an increase in irregular shaped surface profiles with higher pG loadings. Scalebars = 1 µm. *$p < 0.05$, **$p < 0.01$, ***$p < 0.001$, ****$p < 0.0001$.*

Building on previous work, the gelatin-stabilised graphene material used in this study had previously been developed in the Coleman & O' Brien labs[170]. This meant that the first task for our study was simply to identify the correct loading of this material into the polymer matrix for our target application. This was determined based on two primary considerations – the mechanical and the electrical properties. To assess these properties for collagen/pristine graphene (NeuroGraph), candidate composites were dry cast to produce homogeneous films of varying loadings.

The effect of increasing pG concentration on the mechanical properties of each candidate composite was assessed by performing tensile tests on PBS-hydrated films, to reproduce the conditions found in vivo. The mechanical properties of collagen are complex and anisotropic, due to its fibrillar nature[582,583]. Its properties are also highly dependent on the scale and morphology investigated, with collagen fibrils, films and hydrogels each exhibiting non-linear viscoelastic behaviour, albeit with varying stress relaxation kinetics[584,585]. The mechanical properties of collagen can be modulated using nanomaterial fillers, affecting the elastic, plastic, and stress relaxation properties significantly, in a manner dependent on the nature and amount of filler used. Following addition of 10 wt% to 30 wt% graphene to collagen, Young's modulus (E) of the composite films initially decreased, as seen in representative stress strain curves (**Fig. 2.2 A**). This may be due to the effect of pG disrupting the interaction between individual collagen fibrils at high graphene loadings, leading to weakening of the material[97,586]. However, Young's modulus of the 60 wt% composite was significantly higher (E = 17.8 MPa, $p < 0.001$) than the collagen controls (**Fig. 2.2 A**). The maximum elastic modulus in the linear region of the stress-strain curve showed a significant decrease for all formulations up until 30 wt%, while the decrease for 60 wt% was not significant (**Fig. A1.1 A**). The distinction between Young's modulus and the maximum elastic modulus of collagen arises due to the "toe" region typical of tensile stress in collagen, where collagen fibrils uncrimp, leading to a zone of lower modulus at low strains, before the linear region of the stress-strain curve. The reported Young's modulus in **Fig. 2.2 A** is simply the modulus in the first 10% strain of the stress-strain curve, as this is the most physiologically relevant region, comprising the range of strains likely to be exerted during implantation, and the maximum local strain that cells are likely to experience. This, therefore, includes the toe region. The maximum elastic modulus reported in **Fig. A1.1 A** is the maximum modulus in the linear region of the stress-strain curve, measured in 5% strain windows. A typical stress strain curve for collagen is illustrated in **Fig. A1.2**.

The ultimate tensile strength was also significantly lower for all NeuroGraph films (average UTS ≈ 16 MPa, $p < 0.0001$) (**Fig. A1.1 B**), while for the maximum strain (MS), only the highest pG loading (60 wt%) showed a significant reduction, to a maximum strain ≈ 41%, compared to the other tested films (average MS ≈ 75.19%) (**Fig. A1.1 C**), indicating a decrease in the ductility of the material. Nanomaterial reinforcement at low loadings is explained using the Rule of Mixtures for nanocomposites, while at the high loadings used in our study, the deterioration in mechanical properties, and thus deviation from the Rule of Mixtures, is likely explained by increasing filler aggregation[97,177,586].

Taken together, these data show that the mechanical properties of all NeuroGraph composites are closer to the stiffness of CNS tissues (1-100 kPa)[587] compared to that of traditional CNS electrode materials (>100 GPa)[588], and that they are on the same order of magnitude as collagen, which has been used extensively in neural tissue engineering[589]. The lower stiffness of the NeuroGraph films compared to traditional electrode materials is an important material property, as exemplified by work from Woods & O'Connor et al. in our lab, which has shown that matrix-based materials interact with glial cells in a stiffness-mediated manner[351]. The flexural modulus and the electrical performance of the material under repeated deformation may be relevant, since biomaterials can be subject to specific tensile, compressive, and flexural stresses depending on the location of the implant in the CNS (e.g. cortex versus spinal cord). However, these parameters depend largely on the design and location of the implant. The versatile processing capabilities of the NeuroGraph60% material would allow for the fabrication of devices with a range of flexural moduli, which could be adapted to fit the desired application.

Moving on then to the electrical properties, the preservation of which is a key parameter for any electroconductive material designed for biological applications[590], we determined the conductivity of all NeuroGraph candidates in the dry state (**Fig. 2.2 B**), with the percolation threshold being reached at approximately 50 wt% pG (**Fig. A1.3**). The highest conductivity (1.5 S/m) with physically stable films was achieved at 60 wt% (43.5 vol%) loading, rendering the composite sufficiently conductive for nervous tissue[591], and higher than reported previously for graphene stimulatory composites[260]. It is likely that at these higher loadings, conductivity trades off with strength, as decreasing quantities of polymer binder in a composite will likely lead to the strength of the composite relying on the relatively weak bonds between graphene flakes[97,586].

We next assessed the thermal and physiological degradation properties of the composites to determine their stability in long-term physiological conditions. Thermogravimetric analysis demonstrated a trend towards higher degradation temperature with increasing graphene loadings (**Fig. A1.1 D**), indicating higher thermal stability compared to collagen alone. This confirms the ability of the composite to undergo dehydrothermal (DHT) treatment at 105 °C without compromising the structural integrity of the material. To assess the stability and degradation capacity of the composite films under accelerated physiological conditions, each film was subjected to rapid enzymatic degradation using collagenase (0.1 mg/mL) at 37 °C. Significant loss was seen in all groups after one hour, and total loss registered after 3 hours, with no difference between all groups, indicating that pG loading does not impact the enzymatically induced breakdown kinetics of collagen in the films (**Fig. 2.1 C**). This finding indicates that the NeuroGraph composite material shares a similar degradation profile to collagen controls. Atomic force microscopy revealed surface topographical changes, with NeuroGraph60% showing increased area roughness (**Fig. 2.2 D**), as seen in AFM topographical maps (**Fig. 2.2 E**).

Following this, to determine the correlation between film hydrophobicity and topography, surface contact angles were assessed, revealing that higher pG loadings lead to significantly higher contact angles (≈ 74° cf. 65° for collagen), denoting a decrease in surface hydrophilicity (**Fig. 2.2 F**). The associated changes in surface roughness and hydrophobicity are known to affect cell attachment and biocompatibility[592,593] and may have a positive impact on the ability of the substrates to support CNS cell growth[594]. Finally, since material surface properties are critical for appropriate material-cell interaction[595], the topography of composite films with different pG loadings were investigated using scanning electron microscopy (SEM) (**Fig. 2.2 G**). In all composites, pG flakes visibly protruded from the surface, with flakes forming larger irregular 3D features on NeuroGraph60% films.

2.3.2 Characterization of neuronal and glial cell response to NeuroGraph-based films *(Aim 1)*

Next, to assess the biocompatibility of the different NeuroGraph composites, human SH-SY5Y neurons were seeded directly onto the film surfaces for 3 days, and the change in metabolic activity, DNA content and cell morphology assessed (**Fig. 2.3 A-C**). Neurons examined at 1 and 3 days after seeding grew robustly, with no difference in metabolic activity and DNA content (**Fig. 2.3 B-C**) between the film formulations, indicating the formation of a stable population of neurons on the film.

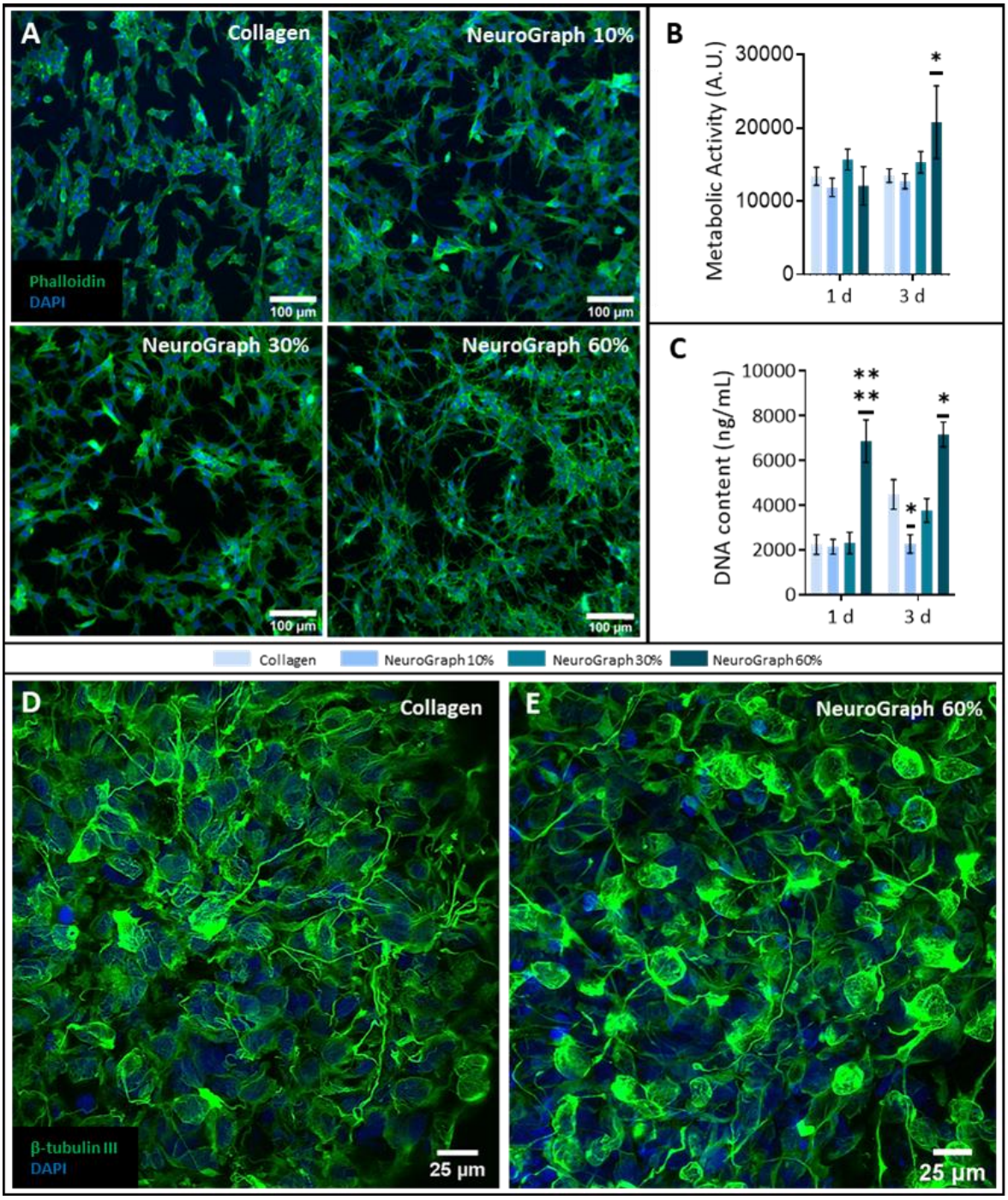

*Fig. 2.3 (†) – **Characterization of neuro-compatibility of collagen/pristine graphene films: A)** Phalloidin (actin = green) and DAPI (nuclei = blue) staining reveals that SH-SY5Y neurons grown for 3 days on the collagen (control) and different NeuroGraph composites showed no difference in morphology, with all neurons extending long neurites across the film surfaces. **B-C)** Comparison of metabolic activity (B) and DNA content (C) at 1 and 3 days after seeding indicated that neurons readily colonized all film surfaces, in particular at higher NeuroGraph loadings. **D-E) β**-tubulin III immunostaining of iPSC neurons, counterstained with DAPI for cell nuclei (blue) cultured for 15 days on collagen (D) and NeuroGraph60% (E) films equally generated dense networks of neurons that extended multiple long neurites. Scalebar in A = 100 µm, in D, E = 25 µm. *$p < 0.05$.*

The cells exhibited typical neuronal morphology, extending multiple long neurites from the cell body (Fig. 2.3 A). To verify the ability of the composites to support the growth of different neuronal types, motor neurons (NSC-34 line) were also cultured on the films and exhibited similar robust growth, with no difference seen between the controls and composite formulations

(Fig. A1.4). To further investigate the long-term impact of NeuroGraph substrates on human neuronal survival and growth, induced pluripotent stem cell-derived (iPSC) neurons were cultured on collagen and NeuroGraph60% films for 15 days.

Growing neurons on both films (Fig. 2.3 D & E) extended multiple long neurites that formed a dense meshwork, with the NeuroGraph composite exhibiting no difference to collagen controls. While several studies have assessed neuronal growth on graphene substrates, many use secondary biomaterial coatings[280–283] to improve surface biocompatibility, and may inadvertently shield the neurons from direct interaction with the material. Where neurons have been seeded directly onto graphene surfaces[105,225,570] the material supports their growth but is a poorer substrate compared to ECM-coated graphene[225]. In contrast, the ability of NeuroGraph60% to facilitate robust neural cell growth in both SHSY-5Y and NSC-34 neurons and young iPSC-derived neurons, and enhance primary neurite outgrowth compared to collagen controls (see Fig. 2.6 A-C), suggests that graphene-ECM composites provide a better environment for neuronal colonisation and growth, perhaps mediated through the irregular surface profiles (Fig. 2.2 G) which are known to strongly influence cell attachment and growth[596]. These data clearly demonstrate that the NeuroGraph60% composite supports long term survival and growth of young human-derived neurons.

The CNS is particularly sensitive to prosthetic implants and exogenous materials, and rapidly generates a foreign body response (FBR)[597] to produce dense scar tissue around the implant[373,494,496]. This process is driven by the reactions of both immunoresponsive microglial cells and astrocytes, the major supportive glial cell type in the CNS[598], which shift to reactive phenotypes that can reciprocally signal to each other through cytokine release to start developing the dense glial scar layers[599,600]. Therefore, to investigate whether the composites may induce 'injury-reactive' pro-inflammatory phenotypes we next assessed if the NeuroGraph composites impacted the growth of microglial cells (Fig. 2.4 A-C). Microglial cells seeded on all composite films exhibited a robust >3-fold increase in DNA between 1 and 3 days after seeding (Fig. 2.4 B; 1 d *vs.* 3 d, $p < 0.0001$), with cells possessing circular morphologies, typical of this cell type when grown on 2D surfaces[601]. Similarly, human-derived astrocytes seeded on the films exhibited the same prolific (>3-fold) growth with significant increases in DNA content in all groups between days 1 and 3 ($p = 0.003$) (Fig. 2.4 E), with the growing cells forming typical long dense parallel arrays of cells with elongate morphology without evidence of toxicity[602] (Fig. 2.4 D). A small number of studies have focused on astrocyte responses to graphene in vitro[603,604] and in vivo[269,602].

As was found in the present study, in general graphene-containing substrates do not appear to adversely affect astrocyte viability and proliferation[505]. However, astrocyte interaction with pure forms of graphene such as uncoated flakes can lead to cellular internalization[605] and induce changes in homeostatic function[603,605,606]. In contrast, we found no evidence of cellular stress with cell morphology, proliferation, and metabolic activity similar to cells grown on collagen films, indicating that the composites provide a stable and trophic environment for astrocyte growth.

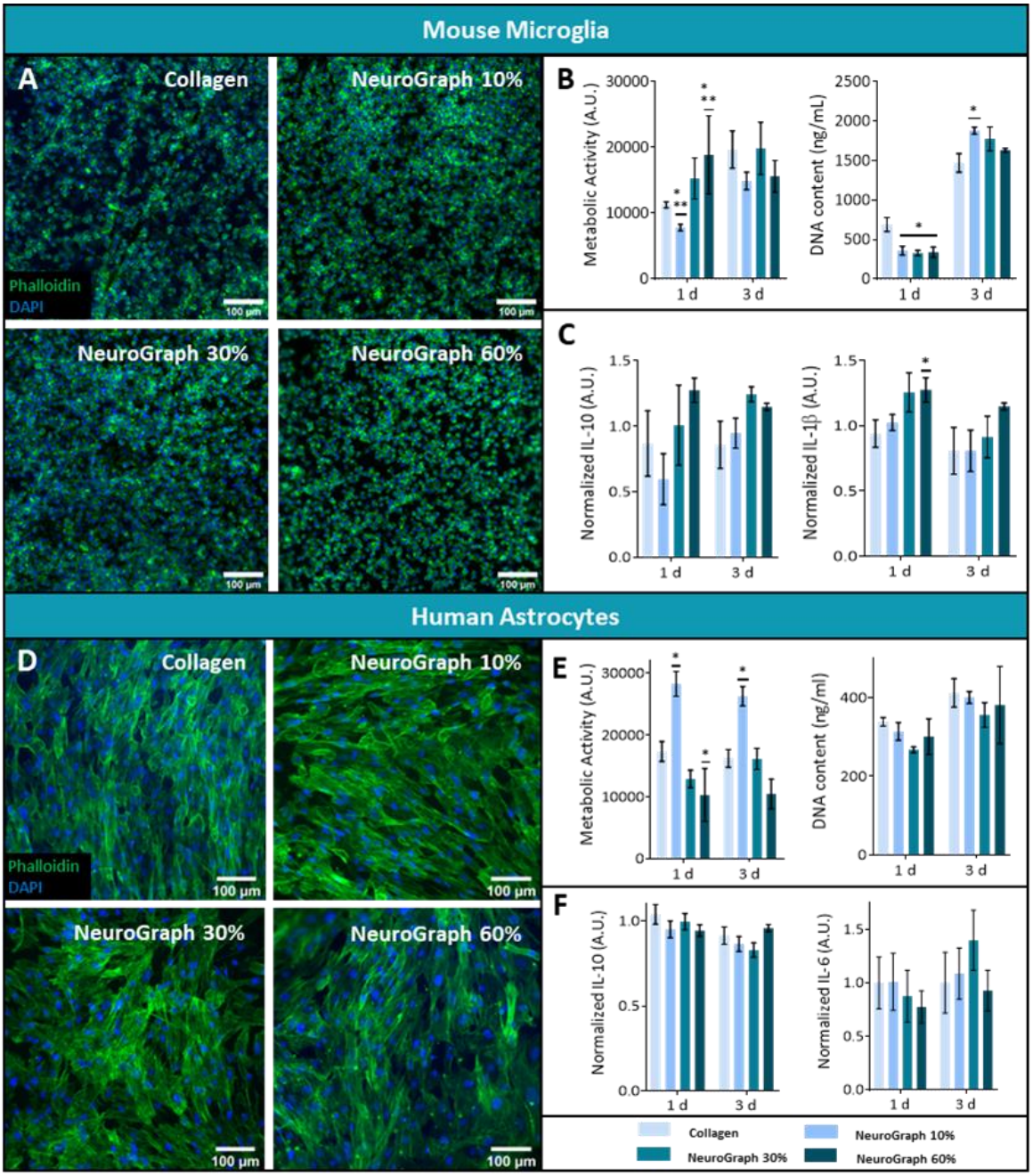

*Fig. 2.4 (†) – **Characterization of glial cell compatibility of collagen/pristine graphene films:** Microglia (A-C) and astrocytes (D-F) were grown for 3 days on NeuroGraph films to assess the effect of NeuroGraph composites on their growth, morphology, and pro-/anti-inflammatory cytokine expression profiles. **A-B)** Microglia showed typical circular morphologies when grown on the collagen and composite films (A) and exhibited metabolic activity and DNA content changes (B) indicative of rapid colonization across the film surface. **D-E)** Similarly, astrocytes exhibited typical elongate morphologies with long processes (D) and changes in metabolic and DNA content indicative of dividing cells (E). **C & F)** ELISA based analysis of the pro-inflammatory cytokines IL-1β and IL-6 released by microglia (C) and*

*astrocytes (F) respectively and the anti-inflammatory cytokine IL-10 released by both cell types indicated no difference in proinflammatory cytokine release for either cell type, and a trend for increased release of IL-10 from astrocytes, in particular cells grown on NeuroGraph60% films (F). Values shown are concentration levels (pg/mL) of test conditions normalized to controls on tissue culture polystyrene plates. Scalebars are 100 μm. *p < 0.05, **p < 0.01, ***p < 0.001.*

Since both cell types can reciprocally stimulate each other through cytokine-mediated signalling pathways[607] in the diseased and injured CNS[599], their cytokine expression profiles are robustly indicative of pro-reparative (e.g. IL-10) or pro-inflammatory (e.g. IL-1β and IL-6) activation states[607–609]. Therefore, we next investigated the effect of increasing graphene content on the release of key immunomodulatory cytokines from both cell types. For microglia, the release of pro-inflammatory IL-1β and pro-reparative IL-10 from cells grown on films was sequentially measured at 1, 2 and 3 days after seeding (**Fig. 2.4 C**). For both cytokines there was no significant change in levels between all groups, suggesting that all film types encouraged a non-polarized 'resting' phenotype, similar to reports of primary immune cell behaviour when exposed to different graphene-based structures[260,610,611].

We then investigated the release of pro-reparative IL-10 and pro-inflammatory IL-6 (**Fig. 2.4 F**) from human astrocytes grown on the films over the same 3-day period. In a similar pattern to the cytokine expression seen in microglia, there was no overall significant change in the levels of both cytokines, but there was a trend for reduced levels of IL-6 and increased IL-10 release in NeuroGraph60% films compared to other composites. When taken together, these data show the ability of both glial cell types to proliferate and colonize the film surfaces, which when coupled with no change in inflammatory IL-1β and IL-6 cytokine release and a trend for increased IL-10 expression in astrocytes indicates that both cell types rapidly grow on the films, without inducing inflammatory phenotypes.

This is significant, as graphene-mediated cellular stress has been known to affect proinflammatory cytokine release[612], which was not found for the cells grown on the NeuroGraph composites. Rather, the trend for increased astrocyte release of IL-10, a strong modulator of inflammatory cytokine production in microglial cells[613], suggests that higher graphene content may encourage non-inflammatory astrocyte phenotypes. These data thus directly address a primary concern of many electroactive materials, i.e. adverse glial cell responses, and indicate that NeuroGraph60% in particular is a strong candidate for a bio-interfacing conductive substrate. There are of course other factors specific to the in vivo foreign body response that cannot be fully accounted for by in vitro testing, such as the size, geometry, and

electrochemical properties of the implant[561,614,615]. Our use of 2D films to monitor CNS cell responses is a common approach taken by many other studies[225,258,282], as it simplifies the assessment of cell responses to materials and minimizes the ability of irregular surface features and geometries to influence cell growth[593].

The evidence from in vivo studies indicates good tolerance of graphene flakes[278] and that collagen coated electrodes induce minimal scar development[501,503], which when coupled with the rigorously demonstrated biocompatibility of the NeuroGraph composites using four different types of neurons (two cell line, one iPSC, one primary, **Fig. 2.5 A-B**) and two CNS glial cell types (**Fig. 2.4**), is strongly indicative of a well-tolerated biocompatible material composite. In addition, the robust growth of primary and iPSC-derived neurons in direct contact with the composite over two weeks is also indicative of the potential of this material for safe longer-term interaction with neuronal circuitry.

2.3.3 Assessment of the synergistic effect of electrical field stimulation and conductive NeuroGraph films on neural cell morphology and function *(Aim 2)*

With the NeuroGraph60% nanocomposite shown to be neurocompatible and to possess electroconductive properties potentially suitable for neuronal stimulation, we next assessed its ability to support primary neuron isolates and encourage axonal growth under electrostimulation. Previous electrostimulation studies demonstrated the ability of laminin-coated graphene films to support neural stem cell-derived growth[281,283]. Therefore, we reasoned that primary neuronal isolates grown directly on NeuroGraph60% films and subjected to electrostimulation should be capable of supporting the neurons and enhancing neurite outgrowth.

Mouse primary cortical neurons (MPCNs), which have previously been used in electrostimulatory studies[616], were isolated and seeded on collagen control and NeuroGraph60% films and allowed to grow for 7 days. Thereafter, the neurons were stimulated for a further 4 h/day over 5 days (12 Hz, 9.8 ms, 200 mV/mm). These stimulation parameters were established based on the existing literature, with our values falling at the lower end of the long term neuronal electrostimulatory range[377], to avoid inducing the creation of deleterious electrochemical species and field-induced cellular damage to sensitive MPCNs. The pulse width was selected to maximise the duty cycle of the stimulation using our IonOptix stimulation rig. Finally, previous work has demonstrated that low-frequency stimulation has a beneficial effect on axonal extension and directionality[377,617–619].

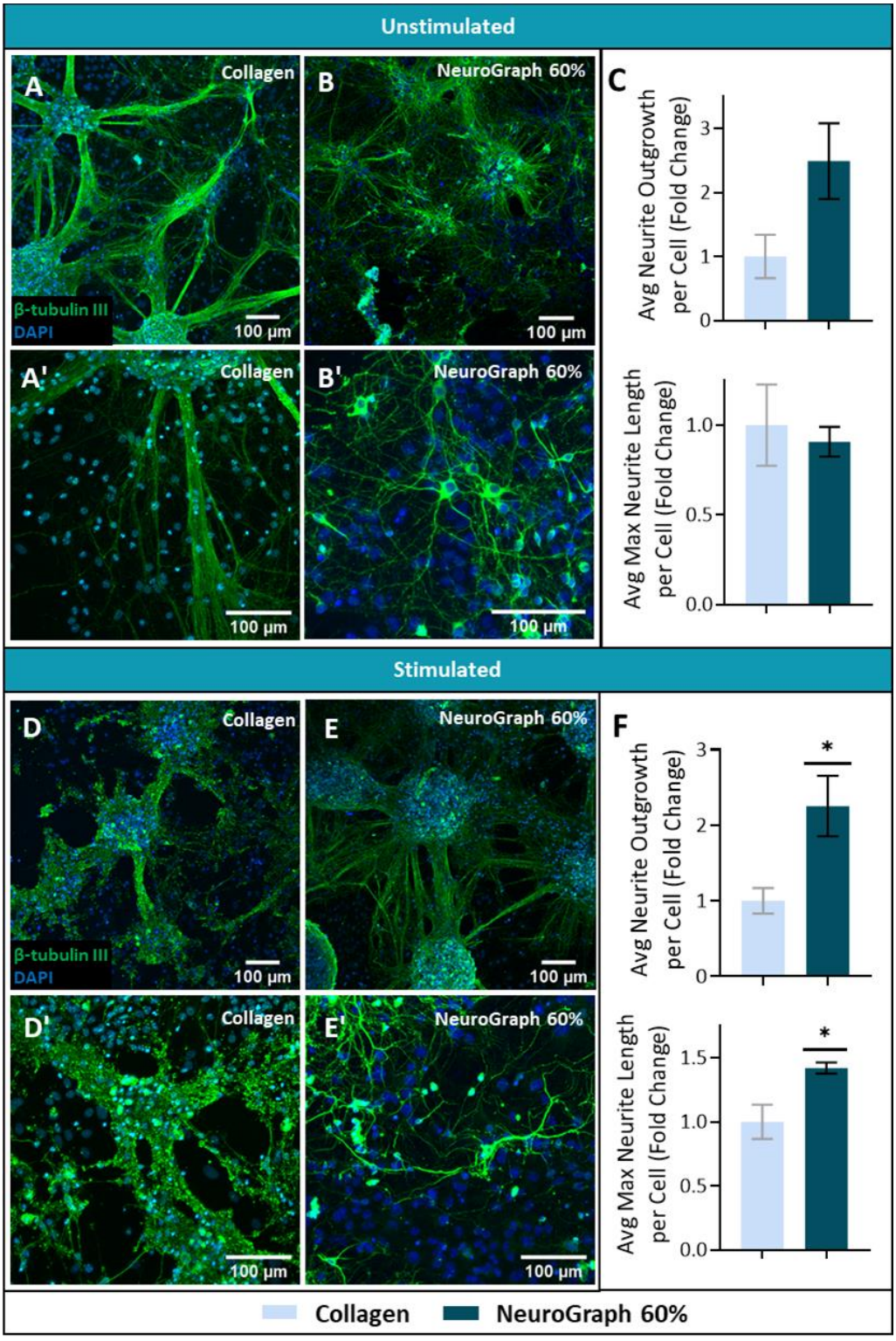

*Fig. 2.5 – **Assessment of long-term primary neuron growth and enhancement of neurite outgrowth following external electrical stimulation on NeuroGraph substrates: A-B)** DAPI and β-tubulin III stained mouse primary cortical neurons grown directly on the surface of collagen (A) and NeuroGraph60% (B), seen at higher power in (A') and (B'), exhibited robust neurite outgrowth on both substrates. **C)** Analysis of neurite outgrowth and maximum neurite length in unstimulated mouse primary cortical neurons indicated no significant difference between collagen and NeuroGraph films. **D-E)** Stimulated neurons grown for 14 days on the collagen films showed a greater fraction of neurons exhibiting cell stress, seen as beading and poor neuronal morphology (D') whereas neurons grown on NeuroGraph60% films (E) showed robust neurite outgrowth (E') and morphologies typical of healthy neurons. **F)** Neurons grown and stimulated on NeuroGraph60% films showed significant increases in neurite outgrowth and maximum neurite length compared to collagen controls. Scalebars A, B, D, E = 100 µm. *$p < 0.05$.*

While cells grew robustly on all films, the morphology of growing MPCNs on NeuroGraph60% films in both the unstimulated and the stimulated conditions (**Fig. 2.5 B & 2.5 E**) formed denser neuronal networks, and possessed longer neurites compared to neurons grown on collagen films (**Fig. 2.5 A & 2.5 D**). In general, stimulated and unstimulated MPCNs grown on collagen films contained a greater fraction of stressed/degenerating neurons (assessed by beading on neurite processes[620]) compared to those grown in NeuroGraph60% films, despite collagen previously being shown to act as a suitable substrate for neuronal culture and in vivo CNS implantation[589,621,622].

This finding may be indicative of the beneficial effect of the rougher NeuroGraph60% film surface to support neuronal growth compared to the collagen control films. MPCNs grown without stimulation on both substrates extended long neurites that often formed a complex meshwork of processes, with no significant difference in length (**Fig. 2.5 C**), although the neurons on NeuroGraph60% exhibited a near significant ($p = 0.0855$) increase in neurite length per cell. When subjected to electrical stimulation, however, cortical neurons on NeuroGraph60% films exhibited significant increases in average neurite outgrowth per cell and the average maximum neurite length when compared to stimulated neurons on collagen substrates (**Fig. 2.5 F**). A similar increase was observed for the number of intact neurites per cell (**Fig. A1.7 B & C**).

These results clearly illustrate that NeuroGraph60% films support healthy growth of cortical neurons, and are similar to findings from studies that utilised primary neurons grown on ECM-coated graphene films[280,282], again indicative of strong composite biocompatibility. More importantly, we demonstrate that NeuroGraph60% is capable of delivering electrical stimulation to support and enhance neurite outgrowth. While the in vivo parameters for electrostimulation of different neuronal types have been well explored[377], the effect of stimulation-induced neuronal growth on graphene-based materials is not well documented, although stimulating neural stem cells on ECM-coated graphene has been shown to support their differentiation and maturation[281,283]. Therefore, this study develops upon these findings and demonstrates the ability of the collagen-graphene composite to drive strong neurite outgrowth from differentiated adult neurons seeded directly onto its surface.

2.3.4 Application of NeuroGraph composites in the creation of neuronal medical devices *(Aim 3)*

With the innate stability, biocompatibility, and ability to deliver electrical stimulation of the NeuroGraph60% nanocomposite confirmed, we next aimed to assess its versatility for the fabrication of distinct medical devices for nerve and spinal cord repair. Directionally aligned scaffold microarchitectures are particularly well-suited for supporting anisotropic axonal regrowth for peripheral[522] and central nervous system applications[351]. First, lyophilized nerve guidance scaffolds were produced using directional freeze drying[384] (**Fig. 2.6 A**), with a highly aligned porous internal architecture visible under SEM (**Fig. 2.6 B**), and an electrical conductivity of $(2 \pm 0.5)\times10^{-6}$ S/m. The aligned pore structure is optimised to allow cell infiltration and drive longitudinal axonal growth along the neurotrophic conductive collagen matrix, making it an excellent candidate for regenerative medical devices. Next, microelectrode arrays are frequently used to record and/or deliver electrical stimulation to discrete neuronal populations, either to restore function, or to connect to a brain-machine interface[623,624]. Therefore, to demonstrate the ability of NeuroGraph60% to form fine micron-sized structural features, a custom 5 × 5 microneedle array, with height 2.5 mm and tip diameter 40 - 80 µm, was successfully dry cast (**Fig. 2.6 C, D**), demonstrating the potential of the composite for higher-resolution interfacing. Finally, the rapidly evolving field of bioelectronics relies on the fabrication of conductive yet biocompatible circuitry, which can be difficult to achieve because of cytotoxicity issues, the poor processability of conductive polymers or difficulties in 3D printing with traditional conductors[625]. To address this and demonstrate the potential of the NeuroGraph60% composite for 3D printing and additive manufacturing applications, it was adapted into a printable bioink, capable of producing repeatable complex electroconductive features (**Fig. 2.6 E**) with over 5-fold enhanced conductivity (**Fig. 2.6 F**, 8 S/m *cf.* 1.5 S/m for dry cast films) and low spreading ratio (**Fig. A1.9 B**). The increase in conductivity in the printed material compared with the dry-cast composites may be due to the influence of applied shear forces during printing, causing decreased alignment of the graphene flakes, thus increasing the conductivity. Alignment in polymer nanocomposites can give rise to nanosheet junctions with large amounts of polymer between them, increasing the junction resistance, thus decreasing the conductivity[178]. The high printability of the material was evidenced by the average spreading ratio achieved, 1.89 (N=3), compared to pure collagen, which reached 6.82 (N=3) (**Fig. A1.9 B**). These enhanced properties allow for the printing of circuits for bioelectronics, such as the circuit shown below used to light an LED, confirming the utility of the material (**Fig. 2.6 E & G**).

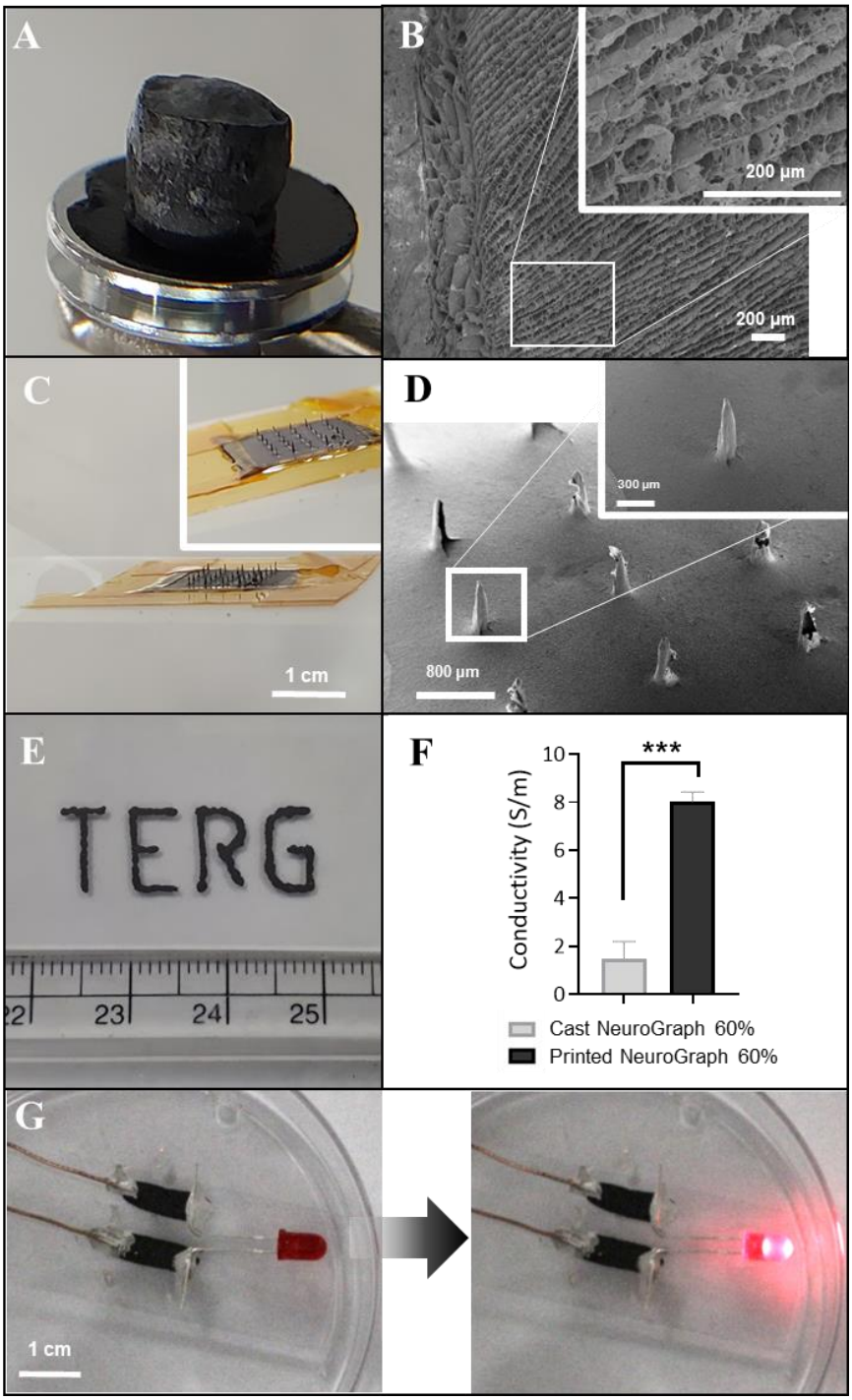

*Fig. 2.6 – **Applications of conductive collagen/pristine graphene to produce neural interfacing structures: A-B)** NeuroGraph60% was used to fabricate lyophilized porous conductive scaffolds (A) that when imaged using SEM (B) show the porous internally aligned channels. Scalebars = 200 µm. **C-D)** Microneedle arrays were fabricated using the composite to produce a 5 × 5 microneedle set (C). Each needle was 2.5 mm high and had a tip diameter of 40-80 µm. When imaged at higher power using SEM (D) the fine bore and sharp tips can be clearly seen on the individual needles. Scalebars = 800 µm and 300 µm (inset). **E-F)** The development of the NeuroGraph60% as a printable bioink allowed for the control and fine printing of complex 3D geometries (E) with physiologically relevant conductivity (F). **G)** To demonstrate the conductive function of the NeuroGraph60% bioink, a simple circuit was printed to power an LED. Scalebar represents 1 cm. ***$p < 0.001$.*

Together, these results show that NeuroGraph composites are a versatile material which can be readily adapted to a wide variety of relevant neural bioengineering applications while exhibiting excellent biocompatibility and conductivity.

2.4 Conclusions

For next-generation neural medical devices, there is an outstanding demand for the development of electroconductive materials that integrate seamlessly with delicate neural tissues. This study presents novel and versatile collagen/pristine graphene nanocomposites (NeuroGraph) that strike the key balance between physiologically relevant conductivity and neurocompatibility. We identify one formulation, NeuroGraph60%, as an ideal candidate capable of supporting and stimulating the growth of cell line, iPSC, and primary neurons. Coupled with its ability to support the proliferation of CNS astrocytes and microglia with morphologies and cytokine release profiles typical of non-inflammatory phenotypes, we identified NeuroGraph60% as a pan-CNS cell compatible nanocomposite. Demonstrating diverse functionality, NeuroGraph60% was used to deliver electrical stimulation to enhance the number and length of neurites, and to produce a range of conductive, neural-interfacing structures, including porous scaffolds, microneedle arrays, and 3D-printed circuit elements for bioelectronics. Taken together, these findings identify NeuroGraph60% as an excellent candidate nanocomposite for future neuronal medical device applications.

Chapter 3

Biocompatible, Flexible and Electrically Optimised Polymer-Graphene (PolyGraph) Composites for Neural Interfacing Devices

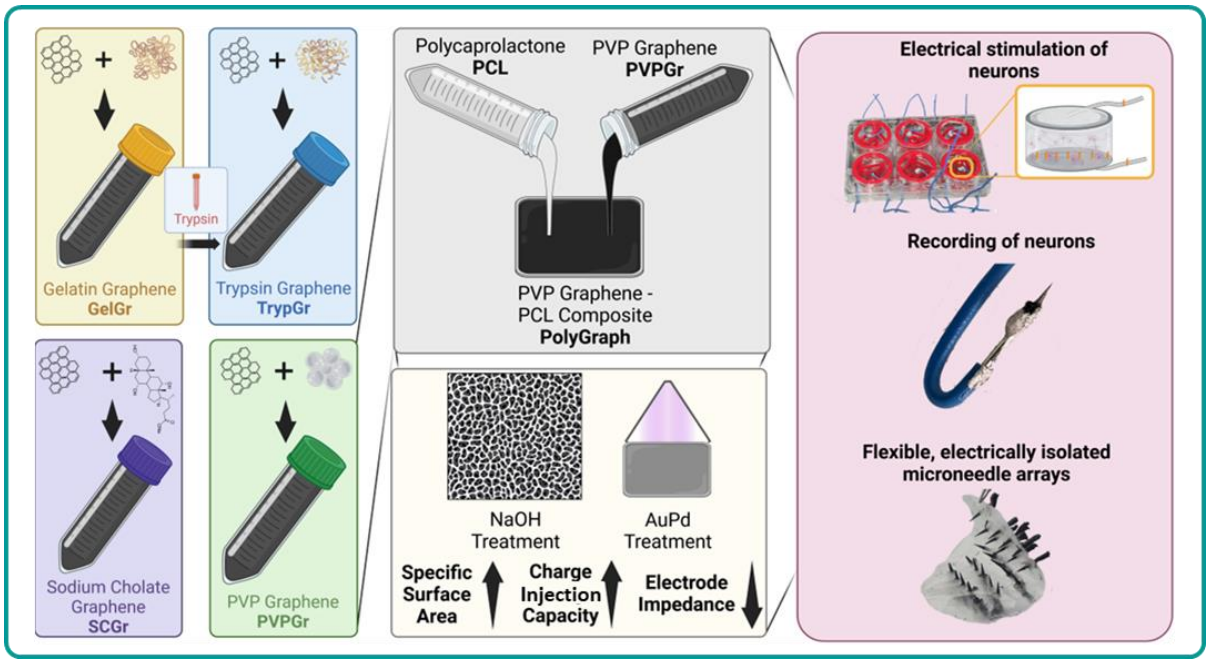

Fig. 3.1 *– Neural interfacing materials need to excel electrically, while integrating safely in the brain and central nervous system (CNS) over long time scales. Nanocomposite materials are a promising solution to this challenge, offering flexibility and electrical performance in one material. To this end, this study developed and characterised a conductive and biocompatible graphene ink, which was then used to fabricate conductive, flexible, and processable nanocomposites, called PolyGraph. To further enhance the electrical performance of PolyGraph, it was treated using NaOH immersion and AuPd coating to roughen the surface and increase its conductivity respectively. This yielded electrical properties in line with existing neural interfacing materials. Three approaches were taken to demonstrate the versatility of PolyGraph– first, a custom stimulation rig was developed to apply electrical stimulation to neurons in a 3D hydrogel system through PolyGraph electrodes. Secondly, to demonstrate the potential for recording, a PolyGraph microneedle was used as an electrophysiological recording electrode in an ex vivo murine brain slice model. Finally, a manufacturing process was developed to fabricate flexible, electrically isolated microneedle-based electrode arrays from PolyGraph. This shows that PolyGraph can form the basis for a highly biocompatible, conductive, and flexible bidirectional neural interfacing device, with implications for the development of future soft bioelectronics for neural interfacing.*

3.1 Introduction

Over the past half-century, our understanding of central nervous system (CNS) function has undergone a revolution[626–628], and the neural interfaces used to interrogate and influence CNS electrical activity in research settings have evolved in turn, due to concerted research efforts[442,443,567,629,630]. Despite these advances, novel neural interfacing technologies such as microneedle-based electrode arrays, neural threads, and mesh electronics are not yet ready to supplant the tools which currently dominate clinical neural interfacing such as

electroencephalography (EEG)[631,632] and functional magnetic resonance imaging (fMRI), due to issues with invasiveness, device lifetime, and recording stability[474]. There is therefore a push to improve the clinical readiness of these novel neural interfacing technologies, driven by the limitations of the existing dominant techniques. While non-invasive and with high temporal resolution, EEG suffers from low spatial resolution[633], and fMRI, while superior in spatial resolution, can only be used in-situ, in expensive facilities[634,635]. The gulf between the speed of technological development in invasive neural interfaces compared to their clinical implementation underscores the challenges inherent with implantable, invasive devices – they must offer durable function and resolution, without the induction of deleterious scarring, infection following implantation, or device degradation and failure. Typically, these issues do not arise for lack of innovation on device design, signal processing, or surgical techniques, but rather due to fundamental limitations of existing neural interfacing materials.

Therefore, there is a growing clinical demand for novel and versatile electroconductive materials, capable of interfacing safely and consistently with neural tissues while maintaining desirable electrode characteristics, that will enable the development of the next generation of biocompatible, flexible neural medical devices. In this chapter we explore one possible candidate material, a composite of polyvinylpyrrolidone-stabilised graphene, chosen for its high biocompatibility and conductivity, and polycaprolactone, a well-established bio-safe polymer with diverse processing capabilities. We demonstrate the potential of this PCL-graphene composite material for neural interfacing applications, and its fabrication into a neural interface prototype, consisting of an array of microneedle electrodes connected by a flexible hyaluronic acid backing.

2D nanomaterials are especially well-positioned to address the challenges mentioned above, thanks to their unique electrical, mechanical, and morphological properties when compared to bulk materials. As readily scalable, flexible materials with superlative electronic properties and diverse processing capabilities, they offer a compelling alternative to existing materials used as neural interfaces (e.g. metals, highly doped semiconductors) which often induce scarring due to their stiffness and poor biocompatibility[351,449,636], posing challenges for their clinical translation. However, to fully take advantage of the beneficial properties of 2D materials, it is necessary to alleviate concerns around hydrophilicity and biocompatibility – this is typically achieved via stabilisation. Many stabilisers have been tested, each offering benefits and drawbacks – for example, low molecular weight solvent (e.g. N-Methyl-2-pyrrolidone (NMP)) and surfactant (e.g.

sodium cholate (SC)) stabilisation offers superb electrical properties[142,166,637], but often poor biocompatibility, while high molecular weight biopolymers such as gelatin or bovine serum albumin (BSA)[101,170,296,638,639] can greatly enhance biocompatibility and prevent aggregation, but often hamper a material's electrical properties. In attempting to strike this balance, stabilisers such as pyrene derivatives[168,640], polyethylene glycol, and polyvinylpyrrolidone[169,641–644] have been assessed, offering high biocompatibility while maintaining electrical performance. Nonetheless, this balance remains difficult to achieve, and is highly dependent on the target application. Thus, stabilisers demonstrating the ability to thoroughly ameliorate the cytotoxicity of pure nanomaterials while maintaining desirable nanomaterial properties are highly sought after in biomedical research. As such, in this chapter we investigate four stabilisers for graphene liquid-phase exfoliation (LPE): gelatin-coated graphene (GelGr), trypsin-treated GelGr (TrypGr, to reduce stabiliser coating thickness via gelatin digestion), polyvinylpyrrolidone-stabilised graphene (PVPGr) and sodium cholate-stabilised graphene (SCGr).

Bringing this all together, composites of 2D materials with bio-safe polymers present interesting opportunities, offering easier processing and improved mechanical robustness when compared to pure 2D materials. Optimising for electrical performance, high biocompatibility and durable mechanical properties requires careful consideration of composite properties and precise control of manufacturing protocols, and to this end, the chosen polymer needs to meet several criteria: a relatively low molecular weight to minimize steric hindrance and maintain nanosheet conductivity, along with stability, processability, and biocompatibility. Polycaprolactone (PCL), a well-established polymer in biomedical applications[645], is one such example of a matrix that possesses optimal properties, with high biocompatibility and versatile processability by 3D printing, casting, and molding[646]. Furthermore, the adaptability of 2D material composites in terms of device morphology and fabrication techniques enables the design of flexible, multiphasic electrode systems for effective stimulation and recording. However, the use of nanomaterial composites for neural interfacing electrodes has seen little research in the literature to this point, compared to both existing neural interface materials and 2D material-only interfaces[647,648] – if optimised appropriately, they have the potential to address many of the issues present in these materials and interfaces. As such, in this chapter we demonstrate the fabrication of PCL-graphene composites for neural electrodes, and the optimisation of their electrical properties by surface treatment.

It is worth noting that a nanomaterial composite, in isolation, is far from a functional device – to this end, the development of microelectrode[561,649], microneedle[432,650], and soft biohybrid-based[486,566] systems, which stand to benefit greatly from this materials research, has drastically improved the capabilities of both *in vitro* and clinical neural interfacing. Thanks to the smaller addressable volume and voxel size offered by these micro-scale electrodes, these systems enable more precise control of external devices such as prosthetics and communicators, more accurate interpretation of neural signals, and a deeper understanding of CNS function[651,652]. These advances, particularly those in brain-computer interface (BCI) technology, hold profound medical and societal implications, offering potential solutions for neurological disorders and paralysis, and even dangling the possibility of human-machine communication if resolution and signal interpretation can be advanced sufficiently[474,567,568]. For these reasons, the target device configuration for this neural interfacing material is a microneedle-based electrode array, with PDMS sheathing to reduce electrode size, and a flexible, biocompatible hyaluronic acid backing for conformability with the brain and CNS.

Taken as a whole, in this chapter we detail the development of biocompatible, flexible graphene composites for the fabrication of a multi-channel, conformable microneedle-based electrode array, with the capacity to effect neural stimulation and recording. By simultaneously overcoming key limitations of existing microelectrode designs and addressing challenges with existing device materials, this research has significant relevance to the BCI space – new, softer materials with versatile processing capabilities are in high demand for advanced neural thread, microelectrode array, and deep brain stimulation devices[430–436,653,654].

3.1.1 Objectives & Aims

The overall objective of this chapter was to develop a graphene composite microneedle-based flexible microelectrode array, and assess its electrical properties and neuronal stimulation & recording abilities, towards non-scarring, multi-channel neural interfacing devices. The specific aims were as follows:

1. Develop and characterise the optimal pristine graphene formulation from a range of candidates, based on biological and electrical parameters.

2. Combine optimal PVP-stabilised graphene with polycaprolactone (PCL), a biocompatible polymer, to form graphene-polymer composites (PolyGraph) and investigate their biological interactions with neuronal and glial cells.
3. Enhance and measure the electrochemical properties of PCL-graphene composites by NaOH treatment and coating with a conductive gold-palladium layer.
4. Develop a PCL-graphene microneedle-based electrode array with a flexible hyaluronic acid backing, and demonstrate its potential as a bidirectional neural interfacing electrode using a custom stimulation bioreactor, and electrophysiological measurements of mouse brain slices.

3.2 Materials & Methods

3.2.1 Exfoliation of Graphene

Gelatin graphene exfoliation

Bovine gelatin, a mix of peptides and protein fragments derived from hydrolysis of collagen, was dissolved in deionised (DI) water at a concentration of 30 mg/mL. Graphite (50 mg/mL, Graphexel Ltd, UK) was then added to the gelatin solution. The dispersion was exfoliated by ultrasonication using an ultrasonic probe (VCX-750, Sonics, USA, amplitude 80%, max power 200 W, cycle 6 s on/2 s off) for 72 h at room temperature (RT). Liquid cascade centrifugation[655] was carried out to remove unexfoliated graphite and obtain size selected graphene. To separate graphene from unexfoliated graphite, the dispersion was centrifuged at 500 rpm for 45 min. The supernatant was then collected, and centrifuged at 1000 rpm for 45 min. The sediment was redispersed in DI water by bath sonication, and repeatedly washed in DI water by centrifuging the dispersion at 2000 rpm for 1 h, and finally redispersing in DI water. This was repeated until gelatinous bubbles no longer formed when the dispersion was shaken. The concentration was then measured by vacuum filtration.

Trypsin digestion of gelatin graphene

To improve the conductivity of dispersed gelatin-graphene by digesting the gelatin coating on the graphene into peptides, and thus reducing the stabiliser coating thickness, 20 mL of gelatin-graphene and 10 mL of trypsin solution (Sigma, Ireland) were placed in a beaker on a hot plate (50 °C), stirring slowly, for 8 h. The resulting dispersion was centrifuged at 6000 rpm for 90 min, and the sediment was washed twice in fresh DI water by centrifugation at 6000 rpm to remove excess trypsin and peptides.

PVP (polyvinylpyrrolidone) graphene exfoliation

40 mg/mL of graphite (Graphexel Ltd, UK) was dispersed in 80 mL isopropanol (99.9% HPLC IPA, Sigma, Ireland) with 2 mg/mL of PVP powder (Sigma, Ireland). The dispersion was then sonicated (VCX-750, Sonics, USA) for 12 h at 55% amplitude, on a 6 s on/2 s off cycle. Size selection was carried out by liquid cascade centrifugation[655]. The dispersion was first centrifuged at 1000 rpm for 90 min, and the sediment was discarded. The supernatant was then centrifuged at 6000 rpm for 90 min, and the sediment was redispersed in fresh IPA. In order to remove excess PVP, and if exchange to another solvent was required, the dispersion was centrifuged at

6000 rpm for 90 min, the supernatant was discarded, and the sediment was redispersed in the target solvent by bath sonication and agitation. This was repeated four times to ensure complete removal of excess PVP, and/or transfer into the new solvent.

The above exfoliation parameters were varied to determine the optimal parameters for conductivity and yield of the PVPGr exfoliation. A short description of each tested exfoliation is given below in Table 3.1.

Method	PVP Concentration (mg/mL)	Graphite Concentration (mg/mL)	Solvent	Sonication Time (h)	Sonication Power (W)
PVPGr A	2	50	IPA	72	250
PVPGr B	2	50	IPA	8	375
PVPGr C	2	50	IPA	12	375

Table 3.1 – Exfoliation parameters for PVP graphene optimisation testing: *Description of exfoliation parameters tested during optimisation of polyvinylpyrrolidone (PVP) based exfoliation protocol.*

Surfactant exfoliation of graphene

40 mg/mL of graphite was dispersed in 80 mL DI water, with 6 mg/mL sodium cholate surfactant (SC, Sigma, Ireland). To pretreat the dispersion and remove impurities, the dispersion was sonicated using an ultrasonic probe (VCX-750, Sonics, USA) for 1 h, (55% amplitude, max power 750 W, cycle of 6 s on/2 s off). The dispersion was then centrifuged at 6000 rpm for 60 min, and the supernatant was discarded. The sediment was redispersed in 80 mL of fresh DI water, and 2 mg/mL of SC was added. The dispersion was then sonicated for 8 h at 55% amplitude, on a 6 s on/2 s off cycle. Size selection was carried out by liquid cascade centrifugation[655]. The dispersion was first centrifuged at 1000 rpm for 90 min, and the sediment was discarded. The supernatant was then centrifuged at 6000 rpm for 90 min, and the sediment was redispersed in fresh DI water. To remove excess SC, or if solvent exchange was required, the dispersion was centrifuged at 6000 rpm for 90 min, the supernatant was discarded, and the sediment was redispersed in the target solvent by bath sonication and agitation. This was repeated twice to ensure complete removal of excess SC, and/or transfer into the new solvent.

Solvent exfoliation of graphene

40 mg/mL of graphite was dispersed in 80 mL of N-methyl-2-pyrrolidone (>99% ACS Reagent NMP, Sigma, Ireland), and sonicated at 55% amplitude (max power 750 W) with a sonic probe

(VCX-750, Sonics, USA), for 8 h. For LCC[655], the dispersion was first centrifuged at 1000 rpm for 90 min, and the sediment was discarded. The supernatant was then centrifuged at 6000 rpm for 90 min, and the sediment was redispersed in fresh NMP.

3.2.2 Physical Characterisation of Graphene

Scanning Electron Microscopy (SEM) to assess material and device morphology

Samples were sputter coated with a 5 nm layer of an 80:20 mixture of gold and palladium using a Cressington 108 auto sputter coater. Imaging was then conducted using a Zeiss Ultra FE-SEM using the InLens detector at an accelerating voltage of 3 kV, an aperture size of 30 µm and a working distance of 5 mm, with images acquired at varying magnifications.

Thermogravimetric analysis (TGA) to assess degree of polymer coating on graphene

Thermogravimetric analysis was carried out using a Q50 thermogravimetric analyser (TA Instruments, USA). The temperature was ramped from 25 °C to 1000 °C, at a ramp rate of 10 °C min^{-1} in air.

Ultra-violet/Visible Light (UV-Vis) Spectroscopy to investigate optical properties of graphene dispersion

UV-Vis spectroscopy was carried out using a Perkin-Elmer Lambda 1050+ photospectrometer and an integrating sphere, to collect information on the scattering, absorption, and extinction spectra.

Raman Spectroscopy to investigate graphene defects and lateral size

Graphene dispersed in IPA was drop cast onto silicon substrates on a hot plate at 100 °C. Raman spectroscopy was then carried out using a WITec RISE Raman system with a 633 nm laser, under ambient conditions with a spectral resolution of 2.5 cm^{-1} using a 600 g/mm grating.

Atomic Force Microscopy (AFM) to assess graphene dimensions

Using a Bruker Multimode 8 microscope, AFM was carried out to assess the thickness and lateral dimensions of the flakes. Graphene inks diluted with isopropanol at a ratio of 1:100 were drop-cast onto Si/SiO_2 substrates. Imaging of the samples was conducted using OLTESPA R3 cantilevers in ScanAsyst mode, and statistical data were derived from the analysis of 173 flakes. The lateral dimensions were calculated by computing the square root of the product of the flake length and width. Data was analysed using Gwyddion SPM software[656].

Contact Angle measurements to assess hydrophilicity of nanomaterial composites

Films of PVPGr/PCL were sectioned with a biopsy punch into flat discs. Contact angle testing was carried out using an OCA 25 contact angle goniometer (DataPhysics Instruments, USA), dispensing 5 µL per drop of deionised water. The contact angle was measured using the software provided by the manufacturer.

Mechanical Testing to measure stress-strain curves of nanomaterial composites

Mechanical testing was conducted using a Zwick Z0.5 Proline tensile tester fitted with a 100 N load cell, at a strain rate of 0.01 %/s. Samples were cut into strips, followed by clamping and testing in a uniaxial strain configuration. The mechanical properties were calculated from the stress-strain curves.

Optical Profilometry to assess surface roughness of nanomaterial composites

Three-dimensional (3D) surface profiles were obtained using a Profilm3D Optical Profiler (Filmetrics) in white-light interferometry (WLI) mode with a 50× Nikon DI objective lens. For samples thinner than 100 nm, phase shift interferometry (PSI) mode was utilized to enhance resolution. The profiler was calibrated using a gold thin film on Si/SiO_2 with a 50 nm step height, confirmed by AFM. Profiles were levelled using a three-point levelling method, and step heights were measured with ProfilmOnline (Filmetrics) software. The step heights were calculated with the histogram step-height tool, which generates a histogram of pixel heights. This data was used to determine the baseline height and the top surface of the sample, allowing for the calculation of the average step height across the area. Once the profile was drawn, it was smoothed by removing "invalid" pixels using the "remove outliers" function in ProfilmOnline, which crops the *z*-axis to eliminate stray pixels and fills in missing data with the average value of neighbouring pixels.

3.2.3 PCL-Graphene Composite Manufacture

Composites were produced by sedimenting a graphene pellet of known mass from isopropyl alcohol, by centrifugation for 90 minutes at 6 krpm. The supernatant was then discarded, and replaced with PCL dissolved in an organic solvent (dichloromethane or chloroform) at a concentration of 100 mg/mL. The composite was then dispersed using a high-power tapered sonic tip for 2 hours at an amplitude of 30%. This composite slurry was then cast into Teflon molds in thin layers, and allowed to dry in a fume hood.

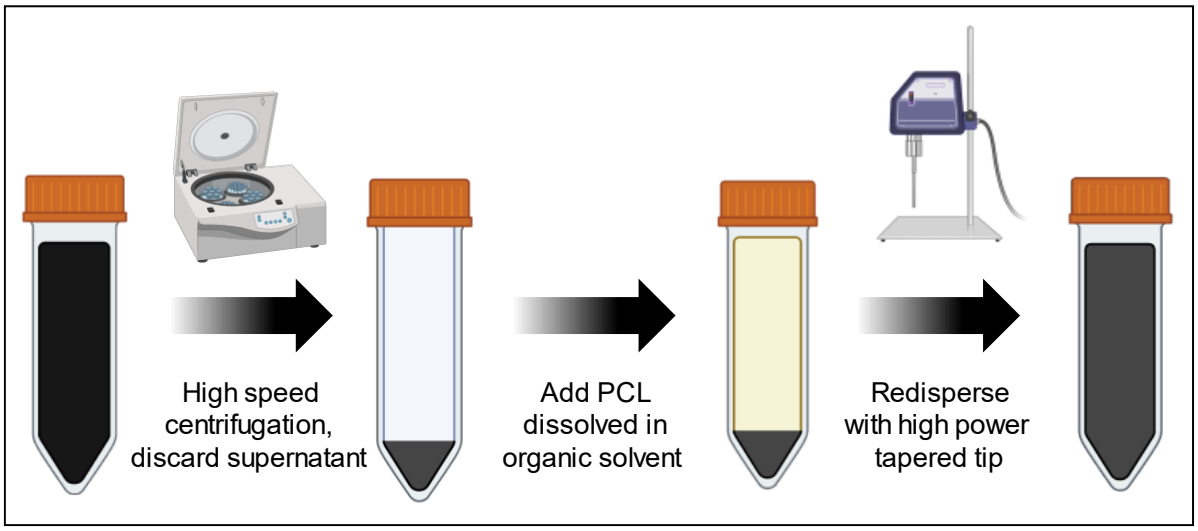

*Fig. 3.2 – **Fabrication of graphene-polymer composite slurry:** To fabricate graphene-PCL composites, graphene dispersion of a known volume and concentration was sedimented by centrifugation at 6 krpm. PCL, dissolved in an organic solvent, was added to yield a slurry of the desired concentration. This slurry was then thoroughly redispersed and disaggregated using a tapered sonic tip for 2 h.*

3.2.4 Cell Culture for Biocompatibility and Stimulation Testing

NSC-34 mouse motor neurons

NSC-34 mouse motor neurons (Cedarlane Laboratories) were grown in growth media consisting of Dulbecco's Modified Eagle Medium (DMEM, Sigma) supplemented with 10% fetal bovine serum (FBS, Biosera, Ireland), 1% Penicillin/Streptomycin (P/s, ScienCell, USA) and 4 mM L-glutamine (Sigma, USA).

SH-SY5Y human neuroblastoma cells

SH-SY5Y (CRL-2266, ATCC) cells were cultured in growth media containing a 1:1 mixture of Eagle's Minimum Essential Medium and F12 Medium (Sigma-Aldrich, Ireland), supplemented with 10% fetal bovine serum (FBS, Biosera, Ireland), 1% Penicillin/Streptomycin (P/s, ScienCell, USA), and 4 mM L-glutamine (Sigma-Aldrich, USA). For differentiation into mature neuronal cells, cells were cultured in differentiation media consisting of 50 mL Neurobasal medium (Gibco, UK), 1 mL B27 (Gibco, UK), 500 µL GlutaMAX (Sigma-Aldrich, Ireland), 1.5 µL all-trans retinoic acid (atRA, Sigma-Aldrich, Ireland).

iPSC-derived neuronal cells

iPSC neural precursor cells were derived from iPSCs as previously described[580] and were differentiated into neurons over 35 days according to protocols outlined in Nistor et al. 2015[580].

Neurons were cultured in iPSC neural maintenance media (NMM) (iPSC Neural Maintenance Medium – DMEM/F12 & Neurobasal medium (Gibco, UK) (1:1), 1% P/s, 1% GlutaMAX, 1% MEM non-essential amino acids (NEAA), 0.2% N21 (Biotechne, UK), 1% B27 (Gibco, UK) and 75 µM 2-mercaptoethanol (ThermoFisher, UK)). Cells were then passaged by first removing culture media, and incubating in accutase (4 min to 6 min, RT). Cells were next collected and diluted in media before centrifugation (1000 rpm, 3 min). Cells were then gently resuspended with minimal trituration in NMM and plated onto Celltrex (1:100, R&D Systems, UK) coated 6-well plates for further expansion. Alternatively, cells were then counted and seeded for use.

iPSC-derived astrocytes

iPSC astrocyte progenitor cells were characterized by and obtained from the Caldwell lab (TCD)[657] and were differentiated into astrocytes over 80 days using established protocols[658,659]. Cells were grown in Serio EL media[660], consisting of Advanced DMEM-F12 (Gibco, UK), 1% P/s, 1% GlutaMAX, 1% MEM non-essential amino acids (NEAA), 1% N21 (Biotechne, UK), 0.2% B27, 20 ng/mL human epidermal growth factor (EGF) and 20 ng/mL human leukaemia inhibitory factor (LIF) (Peprotech, UK) until confluent.

Primary neurons

E18 mouse pups were humanely euthanized using a standard protocol (Ethics Approval REC202005013) and dissected to isolate the cortices. In brief, six cortices per collection were harvested and placed in cold 0.1 M PBS. To gently dissociate the cells, 5 mL of a papain (40 U/ml, Worthington) and deoxyribonuclease 1 (100 U/ml, Worthington) solution, containing 30 mM glucose in Hank's Balanced Salt Solution (Sigma-Aldrich, Ireland) was pipetted onto the tissue at a rate of approximately one drop per second to prevent osmotic shock. The tissues were incubated for 45 minutes at 37°C and 5% CO_2. After incubation, the papain solution was carefully removed, and 1 mL of plating media (Neurobasal Plus Medium with 2% B27 Plus Supplement, 0.5 mM GlutaMAX supplement (all Gibco), and 10% Heat Inactivated Horse Serum (Sigma)) was added. The tissue was then gently dissociated by titration with fire-polished Pasteur pipettes (Fisher Scientific) 15-20 times. Neurons were then counted using a haemocytometer and seeded at a density of 5×10^5 cells per droplet of plating media on each film, followed by overnight incubation at 37 °C and 5% CO_2. The next day, wells were flooded with 3 mL of complete media (plating media without horse serum), and media was changed every two days (1 mL per well). On day five of electrical stimulation experiments, neurons were washed

with PBS (×1), fixed with 4% paraformaldehyde (PFA) in PBS for 15 minutes, washed again with PBS (×3), and blocked for 1 hour in PBS with 0.1% Triton-X100 and 4% Bovine Serum Albumin (Sigma, USA).

3.2.5 Biocompatibility Assessment in 2D Culture

Cells grown with nanomaterial in suspension with culture media

Graphene dispersions in IPA were centrifuged at 6000 rpm for 90 minutes, and the supernatant was replaced by fresh deionised water. This step was then repeated twice to remove any remaining IPA in the dispersion. This DI water dispersion was then autoclaved for sterilisation. Media was made up using relevant cell culture media to the desired low and high concentration conditions – 40 and 80 µg/ml. Cells were seeded at a density of 2×10^4 cells/well, and grown in standard growth media for 24 h before replacing their media with treatment media containing graphene. A full media replacement was carried out every 3 days.

Cells grown on films of nanomaterial composite

A 10 mm biopsy punch was used to cut circles from PCL-graphene films, which were mounted in sample holders (Cell Crowns, Scaffdex, Sigma-Aldrich, Ireland), and sterilised using ethanol, 30 min of UV exposure, and dip washing in 10% P/s (ScienCell, USA). Cells were then cultured on the films at a density of 1×10^4 cells/film. The well was filled with growth media, and metabolic activity and DNA content were measured at the relevant timepoints according to the manufacturer's instructions.

Immunostaining to assess cellular morphology and proliferation

To assess cellular morphology, immunostaining and fluorescent imaging was conducted. At specific time points, samples for immunostaining were briefly washed in PBS before being fixed with 10% formalin (Sigma-Aldrich, Ireland) or 4% PFA (Fisher-Scientific, Ireland) for approximately 15 min at room temperature, followed by washing (×3) in PBS. To assess mature neuronal morphology, rabbit β Tubulin III (1:1000, Sigma-Aldrich) was added to PBS containing 0.1% Triton-X100 (Sigma-Aldrich, Ireland) and 1% bovine serum albumin to reduce non-specific binding, and incubated with the cells overnight at 4°C. The next day, the cells were washed (×3) with PBS, and incubated (1:1000) with the corresponding secondary antibody (Alexa Fluor® 555 Goat Anti-Rabbit IgG, Invitrogen, UK) for at least 2 h at RT. To fully image the morphology of growing cells, both neuronal and glial, fluorescein isothiocyanate (FITC)-labelled phalloidin

(Sigma-Aldrich, Ireland) was added at a concentration of 1:1000 overnight at 4°C. After washing (×3) in PBS, all samples were counterstained with DAPI (1:1000) in PBS with 0.1% Triton-X100 and then mounted on slides with Fluoroshield™ (Sigma-Aldrich). Samples were imaged using a Zeiss AxioObserver fluorescent microscope (Carl Zeiss Ltd., USA), and the resulting images were analysed using FIJI (ImageJ 1.52p).

In addition, a confocal microscope (Zeiss 710 NLO, Carl Zeiss Ltd., USA) was used to assess morphology of cells grown in hydrogels. Stained samples were mounted on the underside of a glass slide, and acquisition was done in a sequential manner using 405, 488, and 561 nm lasers.

3.2.6 NaOH & AuPd Treatment to Enhance Electrochemical Behaviour of PCL-Graphene Composites

To enhance the electrical properties of the material, NaOH treatment was used to increase the specific surface area, while AuPd coating was used to reduce the surface impedance. Composite materials were submerged in 3 M $NaOH/H_2O$ solution for 72 h, followed by rinsing with DI water. The same samples were then coated with a ~10 nm thick layer of an 80:20 mixture of gold and palladium using a Cressington 108 auto sputter coater.

3.2.7 Electrical Characterisation of Material and Device Performance

Conductivity

DC conductivity measurements were carried out using a two-point probe setup. Thin strips of material were cut, and silver paint electrodes were applied to each end. The resistance was then measured using a Keithley Model 2450 sourcemeter, and the conductivity calculated.

Cyclic Voltammetry (CV), Electrochemical Impedance Spectroscopy (EIS) & Chronoamperometry (CA) to measure Charge Storage Capacity (CSC), impedance and electrochemical potential window

Two-electrode coin cells were fabricated with 3 mm diameter discs of electrode material, using phosphate-buffered saline as the electrolyte, and polyethylene filters as separators (**Fig. A2.8 A**) Cyclic voltammetry (CV) and electrochemical impedance spectroscopy (EIS) measurements were carried out using a Biologic VMP-300 potentiostat. CV was carried out in a potential window of ±200 mV at scan rates ranging from 1 mV/s - 30000 mV/s. EIS was carried out in the frequency range 1 Hz – 7 MHz under a potential amplitude of 10 mV. Chronoamperometry was carried out by applying a voltage in the range -1 V to 1 V in steps of 100 mV, and measuring the

magnitude of the current transient at 1 s after stimulation. Analysis was carried out using Biologic EC-Lab software, to extract the surface impedance (Z), and cut-off frequency ($f_{cut\text{-}off}$), which impact the signal to noise ratio, efficiency of stimulation, resolution of recording, and other key outputs[268].

Voltage Transients Analysis to measure Charge Injection Capacity (CIC)

Voltage transients measurements were carried out using a Swagelok three-electrode setup, featuring glassy carbon electrodes, a graphite reference electrode, and a carbon black + Teflon counter electrode, and using PBS as the electrolyte (**Fig. A2.10 A**). Chronopotentiometry was employed to deliver a current pulse at defined current densities, and subsequently measuring the voltage response. This data was analysed to extract the maximum polarisation achieved at a given current density, which in turn was used to calculate the maximum charge injection capacity (CIC_{max}) of the tested material.

3.2.8 Microneedle Array Manufacture for Flexible BCI Device Prototype

Microneedle bases were designed in AutoCAD, with the desired pitch, angle, and needle length. These designs were then 3D printed using an SLA printer (Form 2, FormLabs, USA), with a clear resin (FormLabs, USA). The molds were then washed in IPA for 30 minutes, before being cured by 60 minutes of UV exposure at 60 °C. Polydimethylsiloxane (PDMS, Sylgard 184, Ellsworth Adhesives, Ireland) was mixed and degassed, and poured over the microneedle bases in a petri dish, forming a negative mold. The molds were then cured for 2 hours at 80 °C. Finally, the negative molds were peeled away from the microneedle base carefully. This process was based on work carried out in the O'Cearbhaill lab in University College Dublin[581,661].

Microneedle arrays were fabricated by a multi-stage process, illustrated in Figure 9A. First, the desired microneedle material was cast into films, and cut into appropriately sized squares or discs. The resulting films were then placed in a negative microneedle mold, and melted at 200 °C for 24 h under vacuum, followed by mechanical compression with a spatula in order to fully penetrate all needles with the material. If a free-standing, non-isolated and inflexible device was required, the process ended here, and the microneedle array was peeled from the mold. To render the microneedle arrays flexible and isolated, excess material was scraped away from the needles while still in a melted state. Pillars of conductive PVPGr/PCL composite, dissolved in

DCM at 1.5 g/mL were then printed on to the back of the exposed microneedles using custom G-code on an FDM printer (Allevi 3, Allevi, USA). Following this, a layer of 5 mg/mL hyaluronic acid was cast and dried onto and between the pillars, to function as the flexible base. Finally, the devices were gently peeled from the mold base.

3.2.9 Assessment of Bidirectional Neural Interfacing Capabilities

Ethical declaration for ex vivo experiments

For the experiments using *ex vivo* mouse and rat tissue described herein (mouse back tissue, rat spinal cord, and mouse brain slices), tissue was obtained from animals donated as post-mortem byproducts from ongoing experiments in other groups in the RCSI, in line with our policy of reduction according to the 3Rs of animal research.

Scaffold synthesis

Hyaluronic acid (HyA) scaffolds were prepared using a modified carbodiimide chemistry process, as previously described in Woods & O'Connor et al.[351]. The sodium salt of hyaluronic acid (1.6 – 1.8 MDa from Streptococcus equi) was dissolved in deionised water (3 mg/mL). To crosslink the slurry, adipic acid dihydrazide (ADH) was added in excess, while 1-ethyl-3-(3-dimethylaminopropyl) carbodiimide (EDAC) was added to activate the carboxylate groups on the hyaluronic acid (800 mg per 1 g HyA). 1 M hydrochloric acid was used to reduce the pH to 4, and crosslinking was allowed to continue overnight. Following adjustment of the pH to 7, the following day the solution was dialyzed (6 – 8 kDa) for two cycles of 24 hours in 100 mM sodium chloride. The solution was next dialyzed in 20% ethanol, and finally in deionised water. Collagen type-IV and fibronectin solutions were next added to the solution at a concentration of 0.1 mg/ml. To form the scaffolds, the solution was freeze-dried at –40 °C in insulated Teflon moulds to form an aligned porous structure. Rehydration was carried out overnight using decreasing percentages of ethanol & deionised water solutions. Finally, the scaffolds were immersed in EDAC solution to crosslink the ECM molecules within the scaffold, followed by washing in phosphate-buffered saline before use.

Electrical stimulation of neurons in 3D scaffold culture

To assess the cellular response to electrical stimulation using graphene composite electrodes, neuroblastoma (SH-SY5Y) and iPSC-derived neuronal cells were exposed to electrical stimulation

through a custom fabricated in-plate stimulation chamber. Holders were designed and 3D printed to contain hydrogels and scaffolds, and electrodes were placed at the top and bottom of this cell chamber. The wires from these electrodes were then connected to an external pacing controller (C-Pace EP, IonOptix) via a custom circuit board designed to stimulate each well simultaneously with every pulse. A half media change was done every day. Stimulation was carried out 24 hours/day on a cycle of 55 minutes on, 5 minutes off, 12 Hz, 9.8 ms pulse, and 200 mV/mm, which was informed by previous research into electrical stimulation of neuronal cells[377], and previous successful electrical stimulation work in our lab[101].

Recording of neuronal signals in brain slice model

Individual microneedle electrodes were fabricated by removing the pillar/needle unit from the molds described in **Section 3.2.8**, following 3D printing of the pillars. These individual pillar/needle units were then NaOH and AuPd treated, and attached using silver paint to a wire. The microelectrodes were then sheathed up to just before the tip by dipping them into PDMS solution, to reduce the electrode site size and thus increase the resolution of stimulation and recording. Electrodes were then wired using BNC connectors and data was pre-amplified (SR560, Stanford Research Systems, USA), digitized (Axon DigiData 1550B, Molecular Devices) and acquired (Clampex software, Molecular Devices) at 10 kHz and low-pass filtered at 2 kHz. Analog signals were visualized using an oscilloscope (TBS1000C, Tektronix, USA). A wire coated with AuPd was used as the reference electrode. Acute 350 µm thick coronal brain slices, sectioned from a mouse brain using a vibratome and maintained in a chamber constantly perfused with oxygenated (5% O_2, 95% CO_2) artificial cerebrospinal fluid (aCSF) at 37 °C to maintain viability,

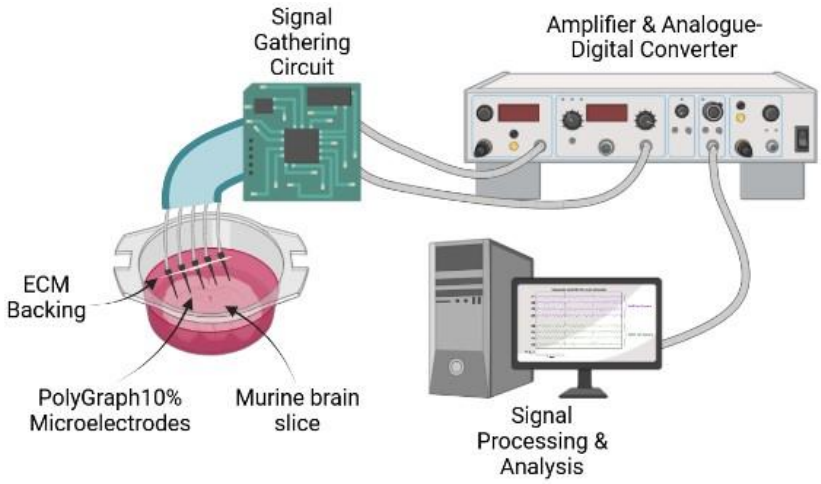

Fig. 3.3 – Bidirectional neural interfacing setup: *Schematic of stimulation or recording from brain slice model using a flexible PolyGraph neural interface.*

were then used to test the spike sensitivity of the electrodes. The microneedle electrodes were placed on the surface of the stratum radiatum of the CA1 hippocampal region, and connected *via* the pre-amplifier (gain = 100) to the recording software to capture traces. Spontaneous neuronal activity was encouraged using a high-potassium aCSF solution to increase the spiking rate.

3.2.10 Statistical analysis

A minimum of three experimental replicates (N) with at least three technical replicates (n) were used in all assessments. Prior determination of statistical significance, the ROUT method (Q=10%) was used to determine the variance in the population. All data sets were subjected to Kolmogorov–Smirnov test to assess for normality and thereafter the data tested using appropriate parametric (t-test, one- and two-way ANOVA) and non-parametric (Mann-Whitney U, one and two-way Kruskall-Wallis) tests. Post-hoc tests were performed using Tukey's multiple comparisons and Dunnett's correction where needed. All results were plotted with the standard error of mean and were considered significant when $p < 0.05$ and statistical significance was denoted by *: *$p < 0.05$, **$p < 0.01$, ***$p < 0.001$, ****$p < 0.0001$. Significances are relative to control group of timepoint unless stated otherwise. All data were plotted and analysed as means with standard error of the mean while using the software GraphPad Prism (v8.0) and OriginLab 2024.

3.3 Results and Discussion

3.3.1 Optimisation of graphene formulation from range of candidate exfoliations (Aim 1)

Physical Characteristics

For healthcare applications, there is a need for 2D materials which are highly conductive as well as exhibiting excellent biocompatibility. The first aim of this study was to overcome the trade-off between these two properties by identifying an optimal stabiliser for graphene, thereby rendering it suitable for use in the central nervous system. The optimisation process focused on two key parameters: conductivity, serving as a proxy for electrical performance, and biocompatibility. Complicating this optimisation is the fact that many biocompatible, hydrophilic stabilisers used to reduce the cytotoxicity of nanomaterials also significantly hamper their conductivity. It is hypothesized that this trade-off arises due to steric hindrance and the deterioration of inter-nanomaterial junction quality, negatively impacting the network properties of the material[662,663]. To investigate this mechanism and develop a solution, four stabilisers were evaluated for graphene liquid-phase exfoliation (LPE): gelatin-coated graphene (GelGr), trypsin-treated GelGr (TrypGr), polyvinylpyrrolidone-stabilised graphene (PVPGr) and sodium cholate-stabilised graphene (SCGr) (**Fig. 3.4 A**).

Optimization began with GelGr, used in **Chapter 2**. The gelatin coating on the graphene surface significantly impacted its electrical conductivity (12 S/m), meaning the conductivities of composites fabricated using this graphene were too low to be used for low-impedance, high-resolution interfacing[497] – however, they remained suitable for use as electrical stimulation substrates[101,664] (**Fig. 3.4 B**). The means by which the gelatin coating inhibits conductivity was further examined by employing trypsin, a protease enzyme, to digest the gelatin coating on the graphene into smaller peptide fragments[665], resulting in the TrypGr formulation. Subsequent conductivity measurements revealed a significant improvement (**Fig. 3.4 B**), suggesting that the digestion and thinning of the gelatin coating improved nanosheet junction quality, and thus enhanced network conductivity. This observation was supported by thermogravimetric (TGA) analysis, which showed greater mass loss (4.64%) for gelatin-coated graphene than for trypsin-treated gelatin-graphene (0.82%), indicative of a thinner coating (**Fig. 3.4 C**), and scanning electron microscopy (SEM) imaging, which showed disruption in the surface coating (inset, **Fig. 3.4 D**).

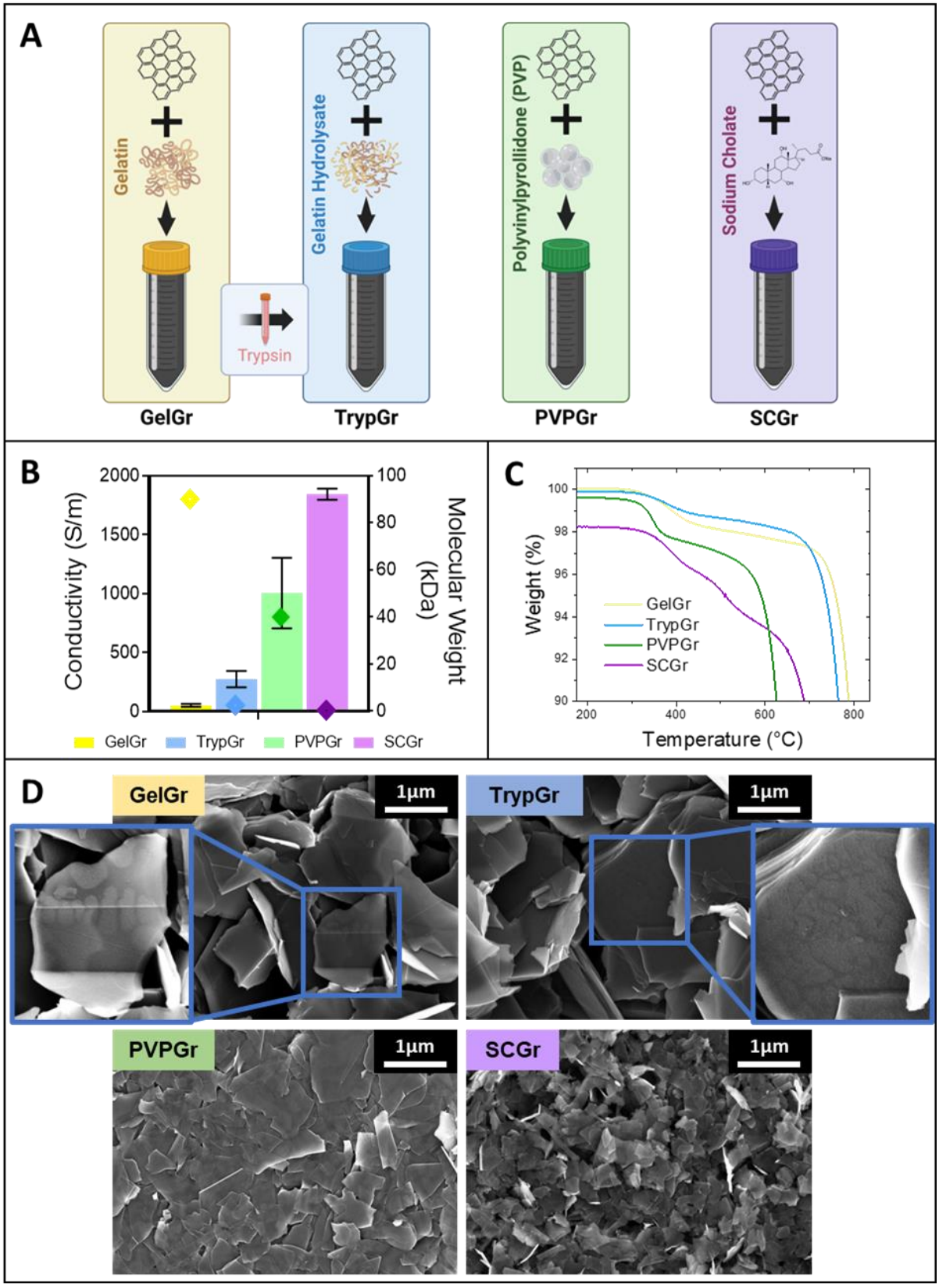

*Fig. 3.4 – **Physical characterisation of graphene candidates:** **A)** Schematic of candidate graphene formulations, showing the stabilising molecule used. **B)** Conductivity measurements of matrix-free graphene-stabiliser films (bars), with diamonds showing the molecular weight for each stabiliser. **C)** Thermogravimetric analysis (TGA) in air shows the removal of polymer coating layers, preceding decomposition of graphene at higher temperature. **D)** SEM imaging of graphene formulations, with insets showing disruption of gelatin layer following trypsin treatment. Scalebars are 1 µm.*

To enhance the quality of graphene produced, two commonly used nanomaterial stabilisers, sodium cholate (SC)[165] and polyvinylpyrrolidone (PVP)[169], were next tested. Both stabilisers exhibited significantly higher levels of conductivity than GelGr and TrypGr. This conductivity increase is likely due to a number of factors – firstly, PVP and SC are both well-established, efficient stabilisers of graphene, thanks to their high adhesion to the graphene basal plane[165,169,644]. This leads to higher-quality, thinner sheets, as visible qualitatively in the SEM images in **Fig. 3.4 D**.

Secondly, there is a distinct contribution of the molecular weight of the stabiliser to the conductivity of the graphene, highlighted by the marked increase in conductivity following the enzymatic degradation of the gelatin layer by trypsin, which isolated stabiliser molecular weight as the sole material variable by controlling for the exfoliation process. This is useful information for material design, as the molecular weight of a stabiliser not only impacts electrical properties, but biological properties such as cytotoxicity and stability[246]. Nanomaterials with insufficiently protective coatings can cause cytotoxicity due to adverse cellular interactions with the exposed nanomaterial surface. A balance must therefore be struck between biological and electrical properties, by tuning the molecular weight, graphene quality, and exfoliation parameters to achieve the desired performance metrics simultaneously.

Biological Characteristics

Having compared their physical characteristics, the next step was to establish the biocompatibility of the candidate materials based on their interactions in suspension and film forms with mouse motor neurons (NSC-34). As an initial "worst-case scenario" challenge, cells were grown in media containing a high concentration of each material for a period of 3 days (**Fig. 3.5 A**), representing an acute release of nanomaterial into the body, which poses the highest risk of cellular internalisation, wrapping, and other potentially negative cell-nanomaterial interactions. The health of the cells was assessed by measuring their metabolic activity (**Fig. 3.5 B**) and DNA content (**Fig. 3.5 C**) across 72 hours of culture with the candidate materials. Significant cytotoxicity was observed for every material tested, with the exception of PVPGr, which showed no significant decrease in DNA content or metabolic activity. This notable result indicates that minimal cytotoxicity is induced by PVP-stabilised graphene, and underscores the impact of stabiliser choice on nanomaterial biocompatibility. PVP is a commonly used biopolymer with well-established biocompatibility and biodegradability[169,641], its larger molecular weight and thus radius of gyration potentially shielding cells from direct contact with the nanomaterial and

preventing protein adsorption[666]. This is consistent with other results demonstrating the potential of aromatic group-based stabilisers such as bis-pyrene[168,667] and more traditional stabilisers such as polyethylene glycol (PEG)[175,666,668].

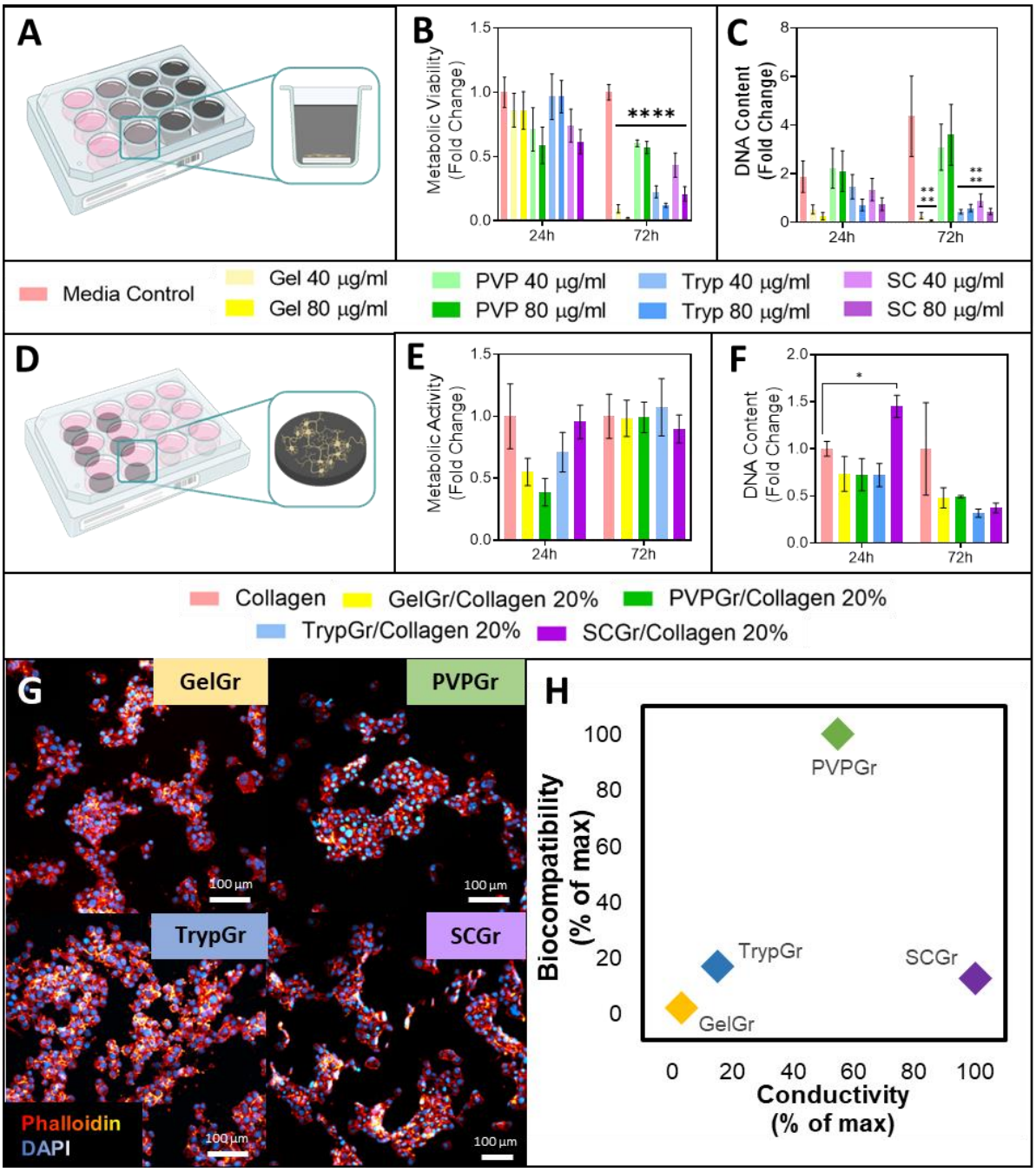

*Fig. 3.5 – **Biological characterisation of graphene candidates:** **A)** Illustration of suspension biocompatibility assays with NSC-34 cells. **B)** Metabolic activity and **C)** DNA content analysis of NSC-34 cells grown in suspension with 40 and 80 µg/mL of each graphene candidate. **D)** Illustration of collagen film biocompatibility assays with NSC-34 cells. **E)** Metabolic activity and **F)** DNA content analysis of NSC-34 cells grown on films of collagen with 20 wt% graphene loading. **G)** Representative images of cells grown on each collagen-graphene film. **H)** Chart representing balance of biocompatibility and conductivity for each graphene type, expressed as percentage of maximum DNA content and conductivity. Scalebars 100 µm. Significances: *$p < 0.05$, **$p < 0.01$, ***$p < 0.001$, ****$p < 0.0001$.*

Recognising then that many real-world applications involve less severe exposure routes such as when nanomaterials are immobilised and encapsulated in polymers, and thus cell-nanomaterial interactions are more predictable and less frequent, cell viability was next assessed on collagen-graphene composite films. Neurons were seeded on films of collagen containing 20% of each graphene formulation by weight, representing a high loading typical of those required for percolative composites (**Fig. 3.5 D**). In this case, the collagen matrix and reduced concentration of free graphene seemed to shield the neurons from damage, with no significant decrease in proliferation observed after 72 h (**Fig. 3.5 E-G**). This demonstrates that while cytotoxicity is critical to consider in the context of material degradation, it can be mitigated significantly by stabiliser and matrix choice. Considering these findings, PVPGr emerged as the most promising candidate for further study, exhibiting a strong balance of biocompatibility with supra-physiological conductivity (**Fig. 3.5 H**), making it well-suited for bioelectronic applications.

3.3.2 PVP-stabilised graphene (PVPGr) characterisation (Aim 1)

The data presented thus far highlights PVP-stabilised graphene (PVPGr) as the optimal candidate material, combining physiologically relevant conductivity with high neuronal biocompatibility. Given these promising initial results, further characterisation of this material was necessary to establish its material and biological properties. To ensure that the observed biocompatibility of PVPGr was not overly sensitive to the specific morphology of the graphene or its precise exfoliation parameters, a second experiment was conducted with mouse motor neurons exposed to a variety of PVPGr formulations, each derived from distinct exfoliation protocols (**Table 3.1**). Notably, all PVPGr formulations exhibited stable metabolic activity (**Fig. 3.6 A**) and DNA content (**Fig. 3.6 B**), far outperforming sodium cholate-stabilised graphene, which was used as a negative control. This finding underscores the broad biocompatibility of PVPGr, demonstrating that its biocompatibility is somewhat independent of the exfoliation parameters, and therefore material dimensions, within the range tested.

To gain a deeper understanding of the surface and morphological properties of PVPGr, a number of microscopic and spectroscopic analyses were carried out. First, to establish the basal plane quality of PVPGr, Raman spectroscopy was performed (**Fig. 3.6 C**). By combining the intensity ratio of the D and G peaks ($\frac{I_D}{I_G}$) with the full-width-half-maximum of the G peak ($FWHM_G$), we can discriminate between disorder localised at the edges and disorder in the basal plane of the flakes[669].

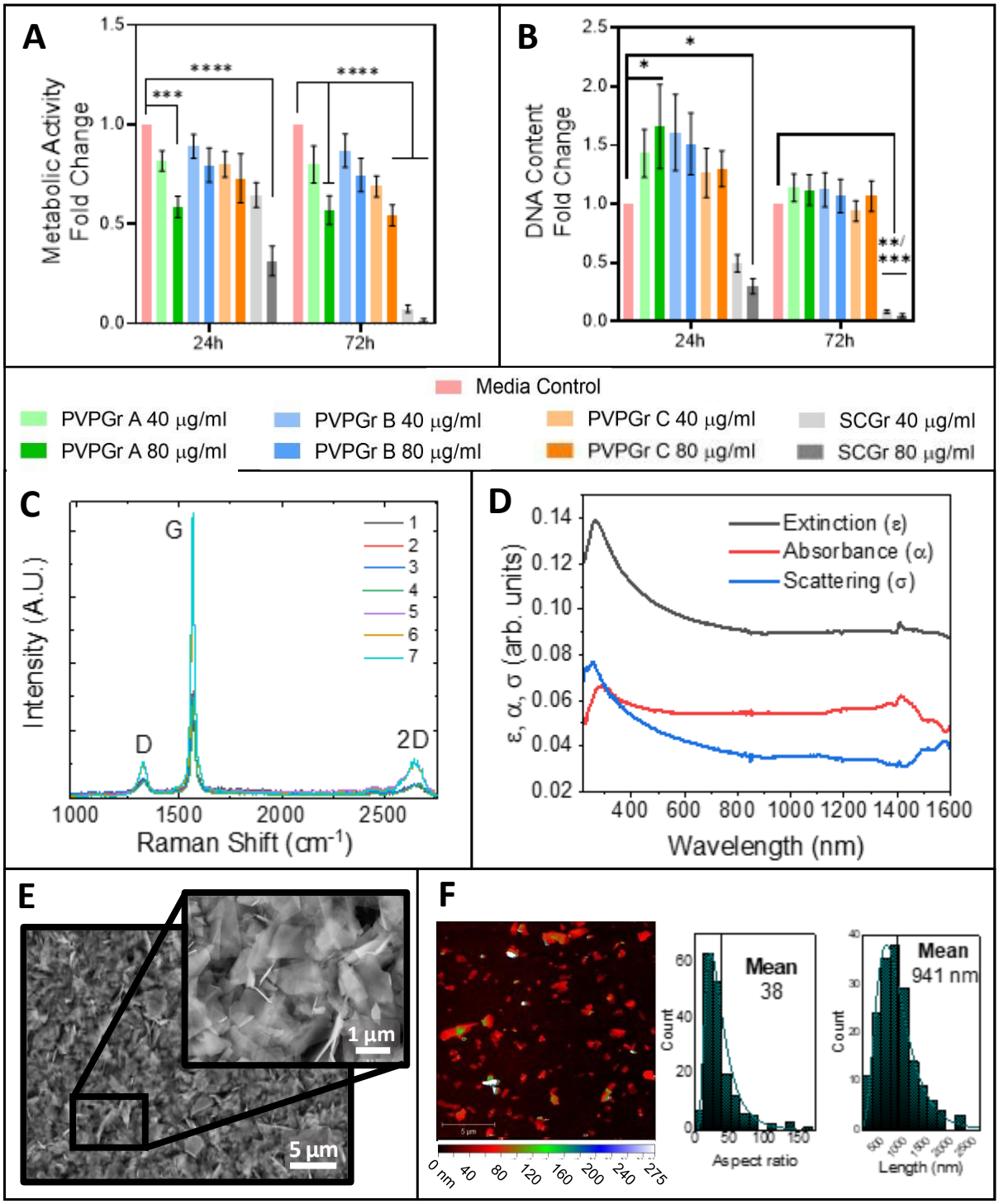

*Fig. 3.6 – **Physical & biological characterisation of PVP-stabilised graphene (PVPGr): A-B)** Metabolic activity (A) and DNA content (B) analysis of various PVPGr formulations in suspension with NSC-34 cells, showing robust biocompatibility across all formulations. **C)** Raman spectroscopy of a graphene network, with spectra typical of minimally defected graphene sheets. **D)** UV-visible light spectrum of a graphene dispersion. **E)** SEM images of a graphene network, showing thin nanosheets. **F)** AFM analysis of graphene material, showing high aspect ratios of 38 and mean lateral sizes of 941 µm (N = 173). Scalebar 5 µm. Significances: *p < 0.05, **p < 0.01, ***p < 0.001, ****p < 0.0001.*

The lack of correlation between $\frac{I_D}{I_G}$ and $FWHM_G$ in our data (**Fig. A2.3 B**) strongly suggests that the observed D peak and associated disorder are not caused by basal plane imperfections, but rather by edge defects, consistent with previously reported LPE graphene inks[293,670]. Assuming that defects are confined to the edges[671], we can estimate the average lateral size of the nanosheets (<*L*>) using the established formula $\frac{I_D}{I_G} \approx \left(\frac{I_D}{I_G}\right)_{graphite} + \frac{k}{<L>}$. k is the slope of $\frac{I_D}{I_G}$ as a function of $<L>^{-1}$, measured by transmission electron microscopy[671] at a value of 0.17. Using $\frac{I_D}{I_G} \approx 0.05\ (\pm\ 0.05)$ for our graphite[672] and an average $\frac{I_D}{I_G}$ of 0.15 for the obtained graphene flakes, we can estimate that <L> ≈ 1.13 – 3.4 μm.

UV-Vis spectroscopy showed the characteristic spectra of few-layer graphene[673,674], with a pronounced absorbance peak occurring at 284 nm (**Fig. 3.6 D**), alongside a significant degree of scattering, typical of nanomaterials[675]. SEM imaging provided visual confirmation of quality of the nanosheets produced, revealing thin nanosheets with an even size distribution (**Fig. 3.6 E**). Atomic force microscopy (AFM) was used to quantify these observations by characterising the size distribution of the graphene, yielding a mean length of 0.941 μm, and a mean aspect ratio of ~38 (**Fig. 3.6 F**), aligning well with the Raman data. Collectively, this characterisation validates the successful exfoliation of high-quality graphene sheets.

3.3.3 Manufacture and optimisation of PCL-graphene composite materials (Aim 2)

One of the key limitations of nanomaterials is the fragility of polymer-free nanomaterial networks - weak van der Waals interactions between particles lead to networks that are prone to delamination and degradation[676]. To ameliorate this, we aimed to develop a composite system that harnesses the mechanical robustness and ease of processing inherent to polymers, while preserving the exceptional properties of graphene. Our focus thus shifted to selecting an appropriate polymer matrix for encapsulating and leveraging the properties of graphene, and refining the manufacturing protocol for this composite. The chosen matrix needed to meet several criteria: a low molecular weight to minimize steric hindrance and maintain nanosheet conductivity, along with biological stability and biocompatibility. Polycaprolactone (PCL, M_w = 25 kDa), a well-established thermoplastic in biomedical applications[645,677], emerged as an ideal candidate due to its biocompatibility and versatile processability by 3D printing, casting, and molding[646]. Furthermore, the Young's modulus of homogeneous bulk PCL is ~350 MPa[678], two orders of magnitude lower than gold[679] and three orders of magnitude lower than platinum[680] or silicon[681], which has positive implications for cellular adhesion and proliferation[353,682].

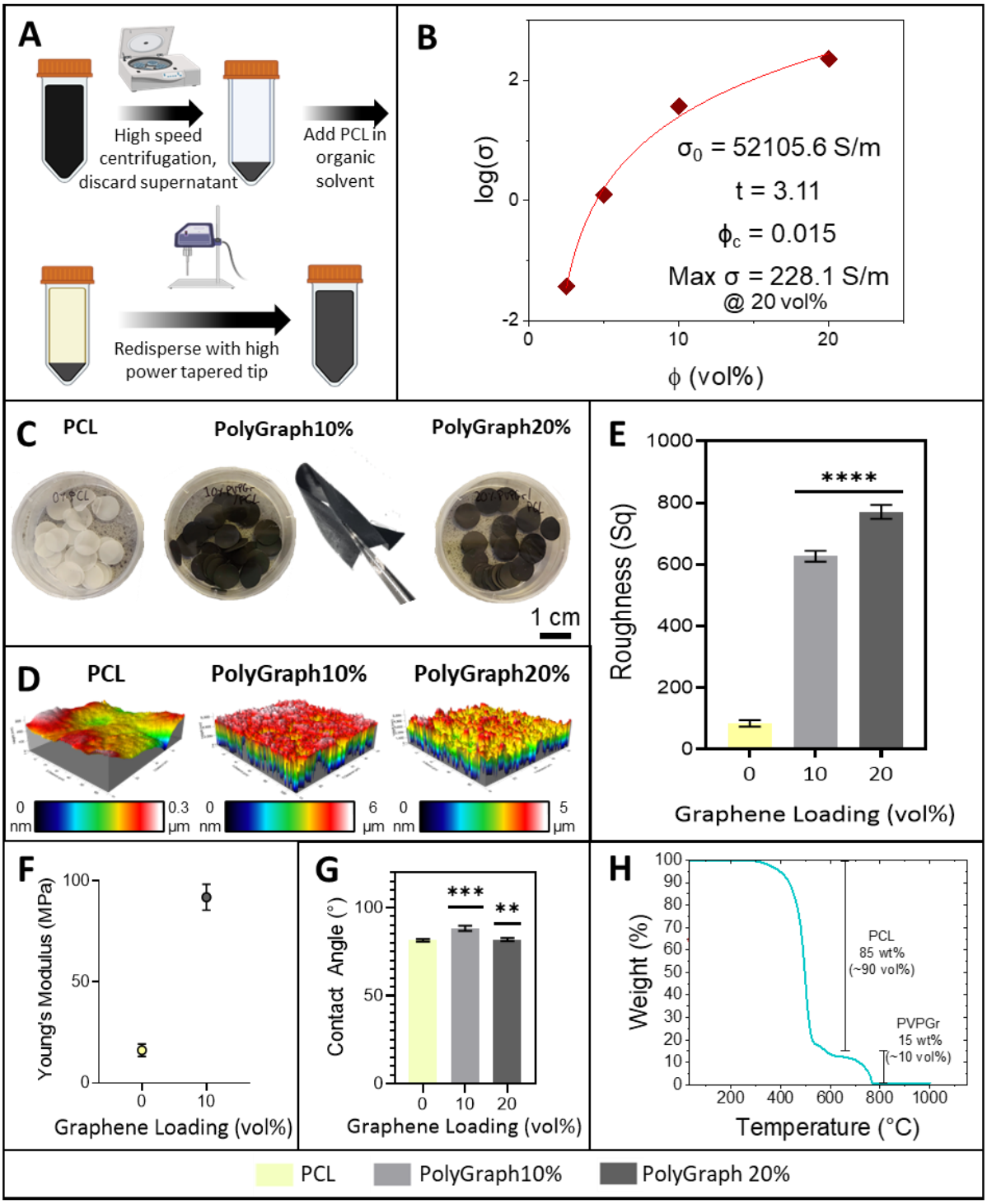

*Fig. 3.7 – **Physical characterisation of PolyGraph:** **A)** Schematic of PCL-graphene (PolyGraph) manufacture. **B)** Percolation curve and fitting parameters for Equation 2.1, for PolyGraph composites. **C)** Optical images of PolyGraph composites. **D-E)** White light interferometry data (D) for the surface roughness of PolyGraph composites, indicating increased roughness with graphene loading (E). **F)** Young's modulus of PVPGr/PCL composite materials, showing increased modulus with graphene loading. **G)** Contact angle measurements for PolyGraph composites, showing a slight increase in hydrophobicity following graphene loading. **H)** TGA of PolyGraph, verifying accurate loading of PVPGr material in composite. Significances: $*p < 0.05$, $**p < 0.01$, $***p < 0.001$, $****p < 0.0001$.*

With this candidate material established, we optimized the composite manufacturing process (Fig. 3.7 A) to produce flexible PCL-graphene (PolyGraph) composites with minimal aggregation. In order to determine the optimal graphene loading required to achieve a balance between conductivity and mechanical properties, the percolation threshold was assessed across the graphene loading range of 0.125 vol% to 20 vol% (Fig. 3.7 B). The percolation threshold was identified by fitting of the following equation from percolation theory, where φ is the volume fraction of the nanomaterial filler in the polymer matrix and φ_c is the percolation threshold. t, then, is the critical exponent which describes the behaviour of the conductivity in the region of the percolation threshold, related to the distribution of the junction resistances in the composite, and σ_0 is a constant, dependent on the specifics of the composite system and closely related to the conductivity of a polymer-free film of the filler material.

$$\sigma = \sigma_0(\varphi - \varphi_c)^t \qquad \text{Eq. 2.1}$$

Percolation was reached at ~1.45 vol%, with a critical exponent of 3.1. This critical exponent is considerably higher than the value of $t = 2$ predicted by theory[683,684], which may be explained by broadening of the distribution of both nanosheet and junction resistances due to variable polymer coating and sheet quality[683–686]. Based on this data, it was decided to continue with the 10 vol% (PolyGraph10%) and 20 vol% (PolyGraph20%) PCL-graphene composites, as they exhibited the best balance between electrical and mechanical properties.

PolyGraph10% and PolyGraph20% yielded homogeneous, flexible films, as seen in Fig. 3.7 C. Surface roughness analysis via white light profilometry (Fig. 3.7 D) revealed increased roughness in PolyGraph (Fig. 3.7 E), indicating a disruption of the smooth polymer surface by the embedded graphene nanosheets, with important implications for cellular interactions[592–594] and electrical performance. Mechanical testing of PolyGraph revealed an increase in the Young's modulus with graphene addition (Fig. 3.7 F), though it also showed a significant decrease in the ductility, as indicated by decreases in the strain at break and the maximum force (Fig. A2.4). This decrease likely arises due to the Rule of Mixtures, where weak inter-flake interactions begin to dominate at high loadings, reducing composite strength and ductility, while also changing its viscoelastic properties[687]. Contact angle measurements (Fig. 3.7 G) showed a slight but significant decrease in hydrophilicity for PolyGraph samples, likely due to changes in surface characteristics and roughness – these modifications may impact the induced foreign body response[688]. Finally, thermogravimetric analysis (TGA) confirmed that the graphene loading in the composites was consistent with the target weight and volume fractions (Fig. 3.7 H).

3.3.4 Biological characterisation of PCL-graphene composites (Aim 2)

Perhaps the most critical factor in electrode design is biocompatibility and immune response, due to the impact these parameters have on the safety and lifetime of the device following implantation[268]. As such, it was critical to establish the ability of cells to proliferate safely on the surface of the material without significant cytotoxicity.

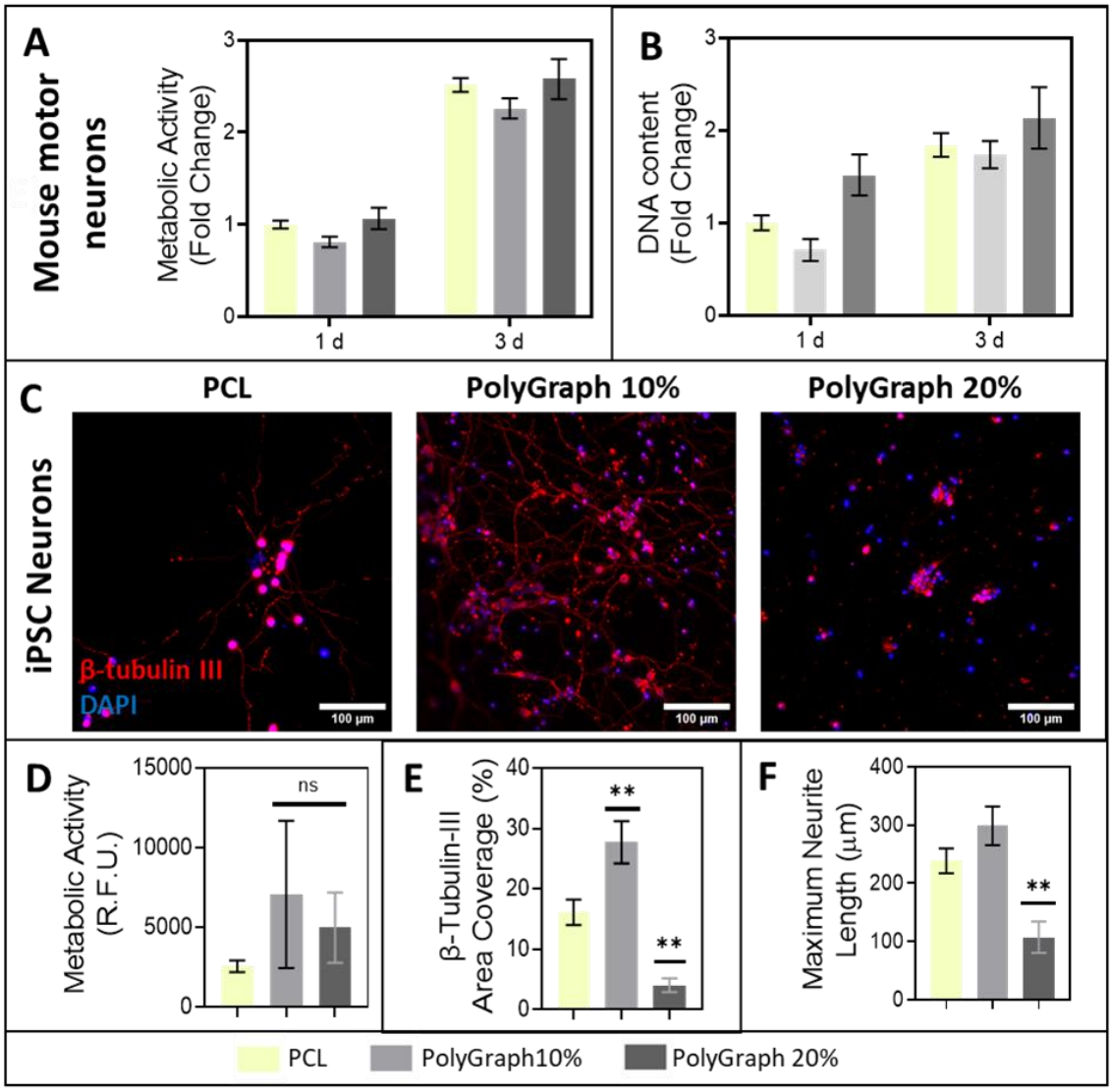

Fig. 3.8 – Biological characterisation of PolyGraph 0, 10 & 20 vol%: A-B) *Metabolic activity (A) and DNA content (B) analysis for SHSY-5Y neurons grown on the surface of PolyGraph composites for 3 days.* ***C)*** *Representative images of iPSC-derived neurons growing on the surface of PolyGraph composites for 14 days, showing robust proliferation and neurite outgrowth across surface of PolyGraph10%.* ***D)*** *Metabolic activity of iPSC neurons on PolyGraph.* ***E)*** *β-III tubulin coverage across all FOV, showing increase in neuronal coverage on PolyGraph10%.* ***F)*** *Maximum neurite length across all FOV, showing increased maximum neurite length on PolyGraph10%. Scalebars 100 µm.*

To this end, two types of neuronal cell were grown on the surface of PolyGraph of varying graphene loadings. First, a neuroblastoma-derived cell line (SHSY-5Y) was grown on PolyGraph substrates, with no significant changes in either metabolic activity (**Fig. 3.8 A**) or DNA content

(Fig. 3.8 B) indicating robust proliferation and lack of cytotoxicity. To further assess the biocompatibility of these materials with a more physiologically relevant cell type, iPSC-derived human neurons were grown on the surface of PolyGraph composite films, showing healthy extension of neurites on the chosen PolyGraph10% formulation (Fig. 3.8 C & D). This was then quantified, with PolyGraph10% exhibiting a significant increase in cellular coverage, suggesting a beneficial effect arising potentially from increased roughness and thus increased cellular adhesion, and from the conductive nature of the substrate (Fig. 3.8 E). PolyGraph10% also led to a non-significant increase in maximum neurite length (Fig. 3.8 F). Interestingly, PolyGraph20% seemed to indicate a degree of cytotoxicity, suggesting that there may be a critical loading of graphene beyond which the material's effects shift from beneficial to harmful – we posit that this is due to increased interaction with the increasingly exposed edges of the material, as seen in the SEM in Fig. 3.10 A, potentially leading to mechanical stress on the cells. These findings highlight the importance of carefully optimizing the graphene loading of our composite materials, as it is difficult to predict the biological behaviour of nanomaterials in different configurations due to complex physical interactions and effects on surface properties – this is true even when high biocompatibility has been demonstrated in suspension, as it has in Fig. 3.6.

3.3.5 Immunological characterisation of PolyGraph (Aim 2)

In addition to their biocompatibility, the foreign body response to electrodes is a critical determinant of their long-term performance, as even a small fibrotic scar can severely limit the lifetime and function of neural interfaces[689]. To investigate the immune response of iPSC-derived CNS astrocytes, key neuron-supporting cells, to our materials, they were cultured on PCL-graphene films for 7 days. In contrast to the poor cellular morphology and proliferation observed on PCL and PolyGraph20% films, cells grown on PolyGraph10% extended long processes (Fig. 3.9 A). ELISA analysis showed no significant change in release of anti-inflammatory IL-10 or pro-inflammatory IL-6 on graphene-containing films, suggesting a lack of a shift to a reactive phenotype (Fig. 3.9 C & D). Analysis of LDH release, often used as a marker for cell membrane integrity and cytotoxicity, showed a slight trend towards decreased release on PolyGraph films at day 7 (Fig. 3.9 E). In summary, PolyGraph10% films demonstrated suitable immune compatibility based on the paracrine signalling profile when cultured with physiologically relevant astrocytes, providing a promising preliminary insight into the scarring potential of this material. These results, combined with PolyGraph10%'s mechanical, electrical, and biological properties, support its potential for use in long-term neural interfaces, and it was therefore carried forward as the optimal graphene loading for subsequent experiments.

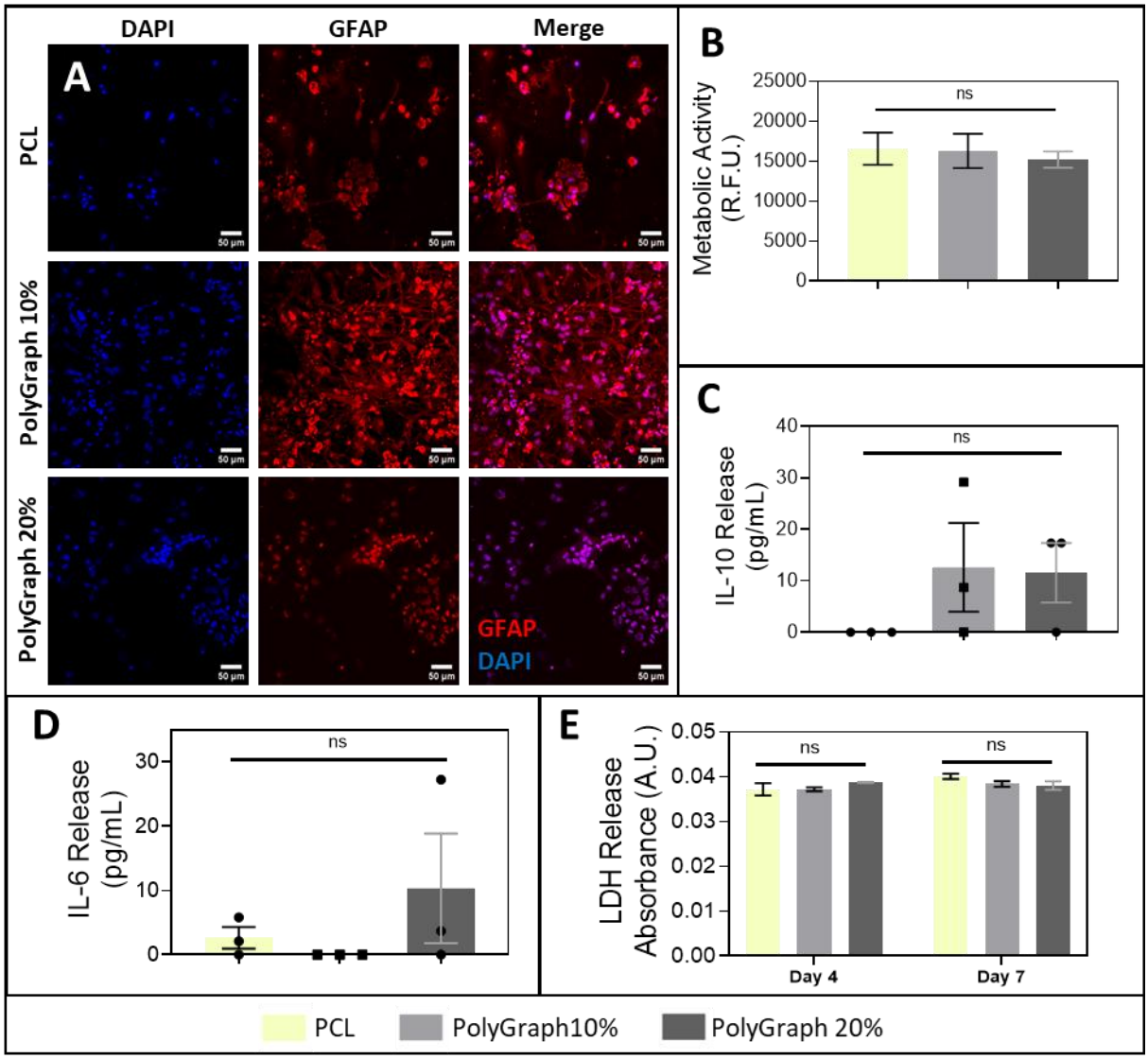

Figure 3.9 – Immunological characterisation of PolyGraph 0, 10 & 20 vol%: ***A)*** *Representative images of iPSC-derived astrocytes growing on the surface of PolyGraph composites for 14 days, showing robust proliferation and healthy cellular morphologies on PolyGraph10%.* ***B)*** *Metabolic activity of iPSC-derived astrocytes at day 14, showing no significant change.* ***C)*** *Anti-inflammatory IL-10 release of iPSC-derived astrocytes, showing no significant change on PolyGraph composites.* ***D)*** *Pro-inflammatory IL-6 release of iPSC-derived astrocytes, showing no significant change on PolyGraph composites.* ***E)*** *LDH release for iPSC-derived astrocytes, indicating no significant cytotoxic effect due to PolyGraph composites. Scalebars 50 µm. Significances: *$p < 0.05$, **$p < 0.01$, ***$p < 0.001$, ****$p < 0.0001$.*

3.3.6 Electrochemical characterisation of PolyGraph10% (Aim 3)

With the biocompatibility of PCL-graphene films with key neuronal and immune cell types established, focus was shifted to the electrochemical properties of PolyGraph10% electrodes. There are several key parameters which dictate the electrochemical performance of an electrode for stimulatory and recording applications, each of which can be tuned by material choice, post-treatment and device morphology[473]. Among these parameters, the surface impedance (Z), cut-off frequency ($f_{cut\text{-}off}$) and charge injection capacity (CIC) are the most critical, as they impact the signal to noise ratio, efficiency of stimulation, resolution of recording, and other key

outputs[268]. We aimed to assess the native electrochemical properties of untreated PolyGraph10%, followed by testing a combination of surface treatments in order to enhance these properties (**Fig. 3.10 A**).

To do this, we first endeavoured to establish a baseline for untreated PolyGraph10% films using a simple two-electrode coin cell setup for measurement of electrochemical properties (**Fig. A2.8 A**), with PolyGraph10% working and counter electrodes, and phosphate-buffered saline as the electrolyte. It is worth remembering from **Fig. 3.7** that graphene addition alone causes a marked increase in the roughness and electrochemical surface area of the composites, as corroborated by SEM imaging in **Fig. 3.10 A**, which already presents an advantage compared to solid, non-porous electrode materials. The electrochemical potential window, which describes the range of potentials within which stimulation can be safely delivered, was assessed by chronoamperometry, with the window considered to be the linear region of the relationship between the current at 1 s and the voltage applied. This window was found to be between -0.5 V and 0.5 V (**Fig. A2.8 B**), which is somewhat narrower than the thermodynamic water window of 1.23 V[690]. The impedance of PolyGraph10% was found to be 2.5 Ω cm^2 at 1 kHz (**Fig. 3.10 B**), while the charge storage capacity (CSC) was found to be 1.6 mC/cm^2 at a scan rate of 1 mV/s (**Fig. 3.10 C**). These values are on the lower end of the range of parameters found in the literature for electrode materials - stimulation electrodes typically possess CSC values in the range of 1-100 mC/cm^2 [691,692], while the impedance of both stimulation and recording electrodes is typically in the range of 0.01-1 Ω cm^2 [691,692]. However, this does not preclude the use of this material for neural applications, as untreated platinum, a very commonly used electrode material, has a charge storage capacity of only 210 µC/cm^2 [693]. Finally, the cut-off frequency, which gives information on the frequency range over which the electrode can effectively operate, was found to be ~3040 Hz, considerably higher than the 1 kHz range of action potentials[473].

These properties, while potentially sufficient for large electrodes and stimulatory applications, still required further optimization before being useful for higher resolution recording applications. In order to improve and optimize the electrochemical properties of PolyGraph10%, numerous post-treatments and their combinations were tested, to increase the specific surface area and decrease the impedance of the material, with the aim of increasing the charge storage and injection capacities and reducing the cut-off frequency.

The first approach taken to increase the specific surface area of PolyGraph10% was a copolymer dissolution technique, carried out by mixing polyvinyl alcohol (PVA), a water-soluble polymer, with PCL, to form a phase-segregated network of polymer channels. The PVA was then washed out with water, yielding a highly porous surface (**Fig. 3.10 A**). However, this fabrication process proved to be challenging, with inconsistent separation of the polymer phases meaning application to PolyGraph10% was impractical.

Next, spray coating of the composite surface with higher loading (70, 80 and 90 vol%) PCL-graphene composites was investigated (**Fig. 3.10 A**). This coating was intended to serve a dual purpose, decreasing the impedance of the surface and increasing the specific surface area and roughness. However, this did not lead to any significant change in the CSC (**Fig. A2.9**), and the lack of polymer binding for the coated surface increases the risk of device degradation. The final approach that was tested with the aim of increasing the electrochemical surface area of the PolyGraph10% electrodes was treatment with sodium hydroxide (NaOH), a well-established technique for roughening PCL[694–696]. This led to a significant increase in the CSC of the treated electrode materials, yielding an 11-fold increase to a final CSC of 17.3 mC/cm^2 (**Fig. 3.10 C**), corresponding to a volumetric capacitance of 787.4 mF/cm^3 (**Fig. A2.9 B**). Furthermore, research suggests that this roughening can have a beneficial impact on cellular adhesion and proliferation[592,593,694,696]. For comparison between materials with different electrochemical stability, these CSC measurements were taken well within their electrochemical potential windows (in the range ±0.2 V) - therefore, they do not represent the absolute maximum achievable CSC, which is proportional to the square of the applied voltage, according to the equation $E = ½CV^2$, where E is the energy stored in a double-layer of capacitance C, and V is the applied voltage[697]. This narrowed window underestimates the contribution of any reversible Faradaic processes that may occur within the water window, which can have a large impact on the CSC. Additionally, the utility of CSC as an absolute measure has been challenged by work suggesting that only a small proportion of the charge stored on an electrode is actually available for injection[473]. Because of this, we use the CSC only to compare groups, and rely on the more accurate measure of the charge injection capacity to give a sense of the absolute electrode performance. Next, to decrease the surface impedance of PolyGraph10%, AuPd treatment was

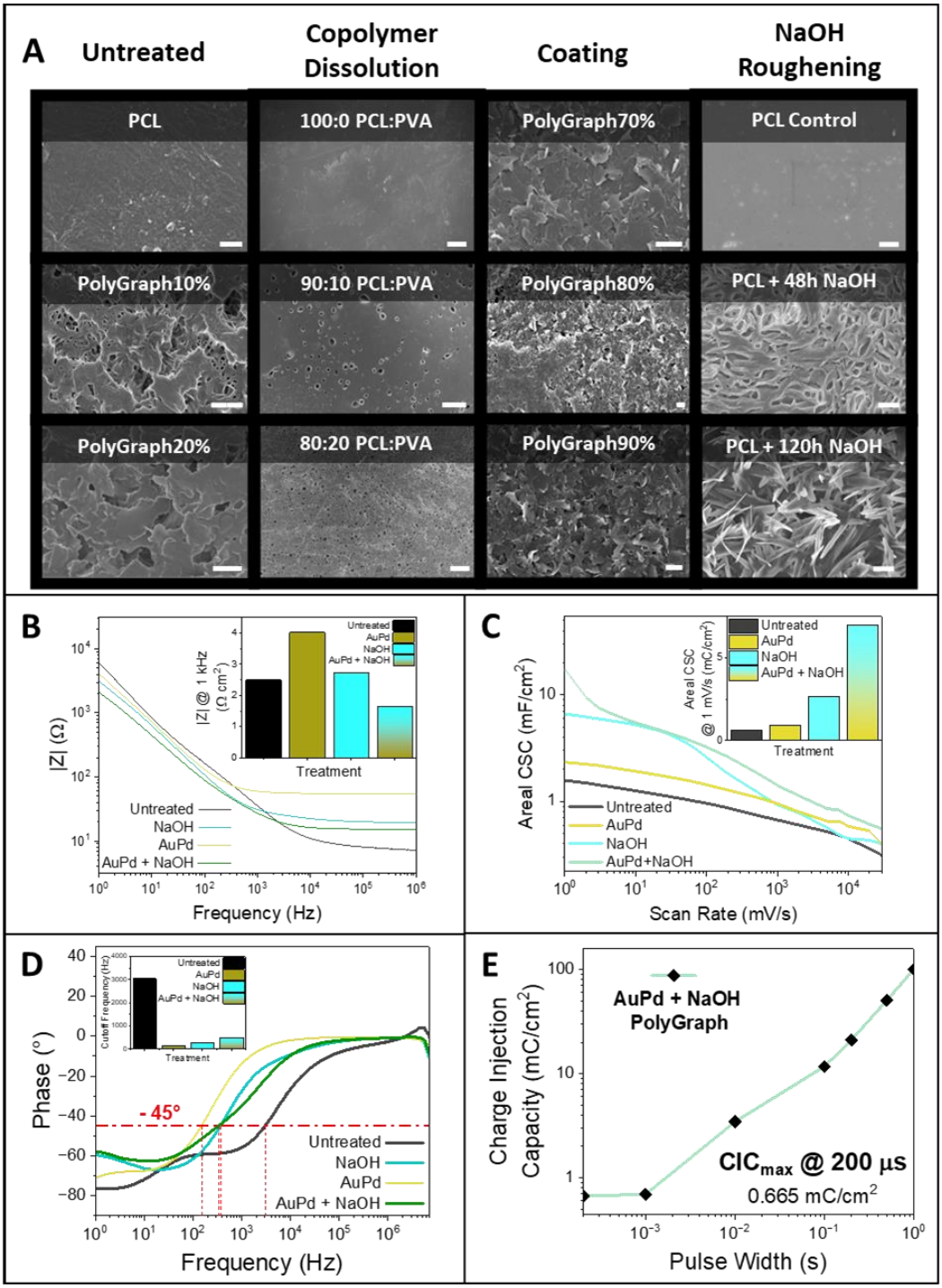

Figure 3.10 – ***Electrical optimization & characterisation of PolyGraph10%: A)*** *SEM images of various treatments for PolyGraph10% with the intent of increasing the specific surface area of the electrodes. From left to right: untreated PolyGraph10%, copolymer dissolution of PCL with PVA, spray coating of PCL with high loading PCL-graphene, NaOH treated PCL. Scalebars 2 µm, with the exception of copolymer dissolution images, for which scalebars are 100 µm.* ***B)*** *Electrochemical impedance spectroscopy (EIS) was used to determine the interfacial impedance of the electrode materials by analysis of Bode plots. Areal impedance at 1 kHz inset.* ***C)*** *Cyclic voltammetry was used to compare the charge storage capacity of the electrodes, showing a significant increase following treatment with NaOH and AuPd. CSC at 1 mV/s scan rate inset.* ***D)*** *Cut-off frequency analysis from Bode phase plots, with significant decrease observed following surface treatment as seen in inset.* ***E)*** *Voltage transients measurements of PVPGr/PCL composites were used to calculate the maximum polarisation compared to the electrochemical potential window, to find the maximum safe charge injection capacity (CIC_{max}).*

tested. AuPd is a highly conductive alloy, frequently utilized in sputter coaters to render non-conducting samples suitable for electron microscopy[698]. This treatment decreased the impedance of the composite materials significantly when used in conjunction with NaOH treatment, from 2.5 Ω cm^2 to 1.6 Ω cm^2 (**Fig. 3.10 B**), further indicating that it was the synergistic effect of both treatments that excelled, rather than either of them individually.

Based on these data, the combination of NaOH treatment and AuPd coating was chosen as the optimal treatment to improve the electrical properties of PolyGraph10% composite films, and was carried forward to further electrochemical analysis. Firstly, it was found that these treatments widened the safe electrochemical potential window to ~± 0.7 V (**Fig. A2.8 C**), enabling higher voltages and thus higher currents to be delivered during stimulation without evolution of toxic electrochemical species. We next set out to establish the cut-off frequency and charge injection capacity of the material. The cut-off frequency was measured as 495 Hz (**Fig. 3.10 D**), indicating that the treated electrodes can record in a wide frequency range. The cut-off frequency is considered a more useful indicator of electrode performance than impedance at 1 kHz, which offers only a snapshot of the Bode plot. Electrodes with a cut-off frequency <1 kHz in theory have similar impedances at 1 kHz, leading us to conclude that our electrodes are suitable for measurement of action potentials in this range[473].

Finally, the charge injection capacity, measured using a three-electrode setup (**Fig. A2.10 A**) was predictably seen to be highly dependent on the pulse width, reaching a maximum of ~100 mC/cm^2 for a long, 1 s pulse, and levelling out near 0.65 mC/cm^2 for short, 200 µs pulses (**Fig. 3.10 E**). This compares favourably with the literature, which shows a range of charge injection capacities between roughly 0.1 and 80 mC/cm^2 [483,692,699–702]. It is worth noting that due to sampling rate limitations of our equipment, it was not possible to examine lower pulse widths, nor to determine the contribution of the access voltage (V_a) to the voltage transient. As such, the values obtained can be viewed as a minimum CIC attainable with PolyGraph10%, which would increase once the access voltage is accounted for[473]. These findings demonstrate that PolyGraph10% electrodes, with their tunable electrical properties, are well-suited for advanced neural interfacing applications, with potential for both stimulation and high-resolution recording, opening new pathways for developing minimally invasive neural devices capable of addressing the complex demands of both clinical and research applications.

3.3.7 Microneedle-based Neural Interface Fabrication (Aim 4)

Having developed 10% PCL-graphene composites and enhanced their electrical characteristics by surface roughening with NaOH and coating with low-impedance AuPd, we aimed to fabricate a flexible microneedle-based neural interface using PolyGraph10% microneedle electrodes connected by a flexible hyaluronic acid backing. Miniaturization, flexibility and high channel count are essential for effective high-resolution neural interfacing[526] – to achieve these, a mold-based fabrication method was employed, avoiding expensive fabrication techniques usually used in the manufacture of neural interfacing devices, such as photolithography and chemical vapour deposition[703]. A schematic of this fabrication technique is shown in **Fig. 3.11 A**, and a render of the final device design, including a flexible ECM-based backing, is shown in **Fig. 3.11 B**. The first step in this process required melt casting of microneedle arrays of PolyGraph10% using custom silicone microneedle molds (**Fig. A2.11 A**). The backings were then scraped from these microneedles, leaving microneedles isolated in the needle holes in the mold. In order to achieve individual electrical control over each of these microneedles, PolyGraph10% pillars were 3D printed onto the back of the needles, yielding individual needle-pillar electrode pairs (**Fig. A2.11 B**). The quality of the produced microneedles was then assessed using white light interferometry (WLI, **Fig. A2.11 C**) and SEM imaging (**Fig. 3.11 C**), showing that fine needles with tip diameters of ~50 µm were achieved. The 3D printability of this material also enables fabrication of custom scaffolds and bioelectronic circuits (**Fig. A2.11 D & E**), with analysis of the print spreading ratio confirming its versatility in processing (**Fig. A2.11 F**).

A key limitation of existing electrode designs, particularly microneedle array-based designs, is the rigidity of the backing layer used, causing a significant mechanical mismatch between the device and the surrounding tissue, and leading to eventual device encapsulation. To avoid this, we demonstrate a device with electrodes that are individually isolated from each other, both mechanically and electrically, allowing high-resolution interfacing across a range of recording sites. In order to mechanically link the isolated electrodes, several thin layers of biocompatible, flexible hyaluronic acid-based extracellular matrix were cast between the needles, connecting them with a thin backing which could subsequently be peeled from the microneedle mold. This freestanding microelectrode array (**Fig. 3.11 D**) is shown to be highly flexible (**Fig. 3.11 E**) and conformable to the muscle tissue of a mouse (**Fig. 3.11 F**) and the spinal cord of a rat (**Fig. 3.11 G**), suggesting its potential applications beyond the brain and CNS.

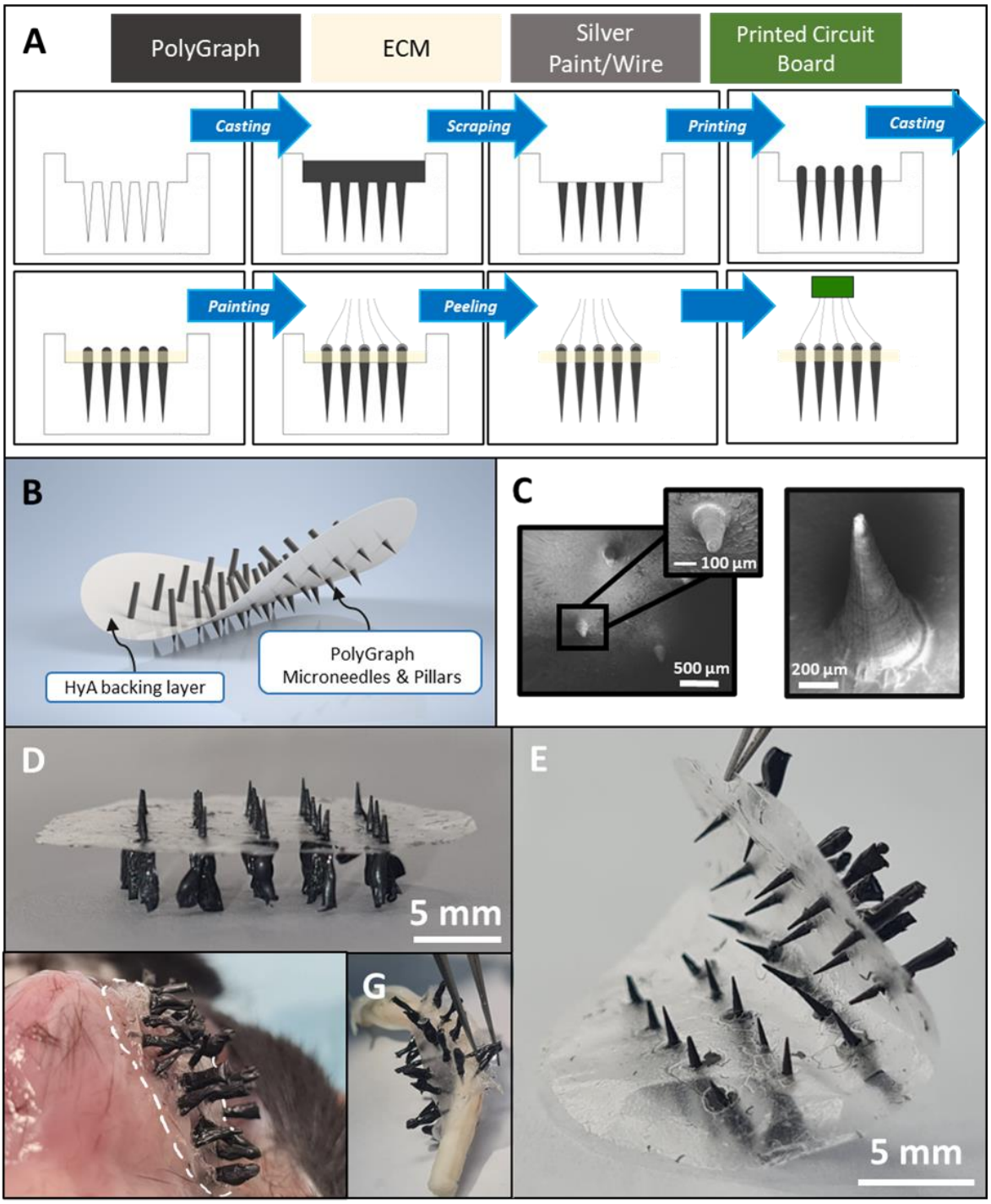

*Fig. 3.11 – **Fabrication of flexible, electrically isolated microneedle arrays using PolyGraph:** **A)** Fabrication workflow, taking advantage of composite processability by using dry casting and 3D printing. **B)** Render of an isolated microelectrode array. **C)** SEM images of PolyGraph10% microneedles. **D-G)** Optical images of flexible, isolated microelectrode array (D), demonstrating flexibility of backing (E), penetrating mouse back tissue (white outline indicates hyaluronic acid backing) (F), and wrapped around rat spinal cord (G).*

The tensile modulus of the hydrated hyaluronic acid backing was then assessed to confirm the high flexibility and thus low scarring potential of the ECM backing material – the resultant force on stretching was found to be below the limit of detection of the most sensitive load cell (5 N) available to us, indicating a highly soft, flexible material, with a stiffness likely comparing favourably with that of the native CNS tissue (<1 kPa)[351].

3.3.8 Electrical stimulation & recording using PolyGraph10% electrodes (Aim 4)

In order to assess the potential of these flexible, multi-channel electrode arrays for bidirectional neural interfacing, we developed experimental setups to effect stimulation and recording of neurons in vitro.

Electrical stimulation of iPSC-derived neurons in 3D culture

We first aimed to assess the impact of stimulation delivered using PolyGraph10% electrodes on neuronal survival and extension. This served to assess the potential of PCL-graphene composites for applications such as deep brain stimulation and bidirectional neural interfaces. A custom bioreactor was developed for stimulation of cell-laden hyaluronic acid-based porous scaffolds, which had been previously developed in our lab for CNS applications[351]. An inner chamber was 3D printed to fit inside a 6-well plate (**Fig. 3.12 A**), which was adapted with ports for wiring PolyGraph10% electrodes. The bottom of the well was sealed using agarose, and scaffolds were added between the electrodes in the central chamber. A schematic of the stimulation configuration can be seen in **Fig. 3.12 B**. Stimulation was then carried out using the optimal stimulation parameters established in **Chapter 2**[101]. Imaging of iPSC-derived neurons in both stimulated and unstimulated conditions shows that further optimization of the chamber is necessary - cells cultured in the chamber exhibited some signs of cytotoxicity, decreased neurosphere formation, stressed cellular morphology and lack of β-tubulin III staining (indicative of neuronal maturity) compared to control scaffolds maintained in a 6-well plate (**Fig. 3.12 C**).

These effects are likely due to a combination of factors, including the limited media volume and diffusion capacity of the smaller, isolated stimulation chamber, potential leaching of cytotoxic species such as silver ions from behind the protective PCL coatings on the electrodes, or residual ethylene oxide or ethanol from sterilized polylactic acid (PLA) or PCL components[704]. Given the high sensitivity of iPSC-derived neurons, which are inherently difficult to culture in 3D environments even under optimal conditions, these factors may have led to cytotoxicity in a manner that would not occur in more resilient cell types. While the current data are preliminary and incomplete, they highlight challenges related to the bioreactor's design and to the broader context of 3D electrical stimulation. Importantly, they also represent experimental progress towards achieving effective 3D electrical stimulation of scaffolds using custom nanomaterial composite electrodes. As such, further development and optimisation of this stimulation bioreactor to mitigate these issues will be an essential focus for future research based on this chapter.

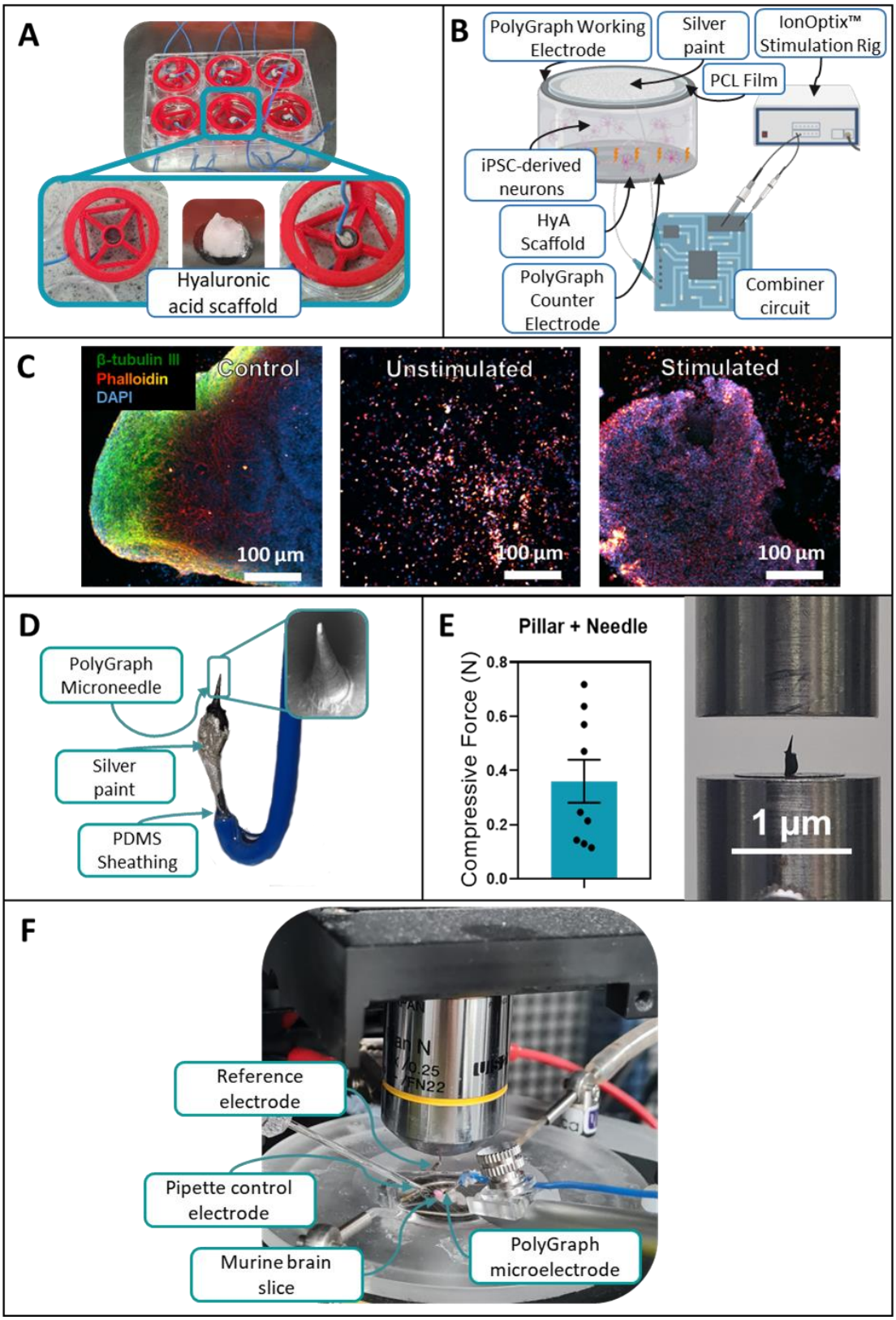

Fig. 3.12 – ***Electrical stimulation and recording using PolyGraph10% electrodes:*** ***A)*** *Images of custom electrical stimulation rig for 3D stimulation of cells in scaffolds.* ***B)*** *Schematic of neuronal stimulation setup, allowing for cell stimulation within a hyaluronic acid (HyA) scaffold.* ***C)*** *Confocal imaging of iPSC-derived neurons growing within a HyA scaffold. Scalebars are 100 µm.* ***D)*** *Microneedle recording electrode with PDMS sheathing to reduce electrode size.* ***E)*** *Compressive force testing of microneedles to assess robustness for tissue insertion.* ***F)*** *Recording of neuronal signals in ex vivo brain slice model from single microneedle using an electrophysiological setup.*

Recording of Neuronal Signals using PolyGraph10% Microneedles

Finally, to demonstrate the potential for this device as a bidirectional neural interface, we aimed to assess recording and stimulation using a single microneedle (**Fig. 3.12 D**) in an *ex vivo* brain slice model. The electrodes were sheathed using PDMS to form a small electrode site at the tip of the needle, in order to reduce the voxel size and increase the impedance, thus allowing for recording of more localised neuronal signals. In order to confirm that the needles themselves could survive the forces exerted upon implantation, compressive modulus testing was carried out on individual needle/pillar pairs, yielding an average maximum compressive force of 0.36 N (**Fig. 3.12 E**). This is sufficient to withstand typical insertion forces into brain tissue, which typically range between 0.7 and 40 mN[705] for microneedles.

Next, the microneedle electrode shown in **Fig. 3.12 D** was integrated into an electrophysiological recording system (**Fig. 3.13 E**), with the aim of recording local field potentials and evoking recordable potentials from a murine brain slice. The efficacy of recording and stimulation will be dependent on the electrochemical properties and device configuration as discussed in **Chapter 1**, each of which will impact the signal:noise ratio and thus the measurable voltage spike[474]. Preliminary experiments have been conducted using this experimental setup – however, challenges arose with the viability of brain slice cultures. Specifically, the slices exhibited a very low spiking rate, which could not be effectively increased, even following application of high-potassium solution. As a result, it was not possible to observe any action potentials using the current electrode configuration during initial testing. Combined with delays in obtaining sufficient *ex vivo* brain tissue, it has not been possible to conclude this work in the timeframe of this thesis. This being said, the work so far represents significant experimental progress in terms of material development, electrode configuration, and electronics setup towards achieving effective neuronal recording from *ex vivo* tissue using custom nanomaterial-composite based microelectrodes. Further development and optimisation of this custom electrophysiological setup for neuronal recording and stimulation is earmarked as a critical component of the future work arising from this chapter.

3.4 Conclusions

The pursuit of soft, flexible, and electrically performant neural interfaces requires advanced electroconductive materials which can balance the trade-offs of biocompatibility, degradation, and neuroinflammation with electrical performance, processability, and stiffness. To address these key requirements, this chapter developed a PCL-graphene (PolyGraph) composite by combining an electroconductive, highly biocompatible polyvinylpyrrolidone (PVP)-stabilised graphene formulation with biocompatible, processable polycaprolactone (PCL). These composites were then fabricated into a non-inflammatory, flexible microneedle neural interface, with electrical properties indicating promise for both neuronal stimulation and recording - key outcomes for successful BCIs.

First, polyvinylpyrrolidone was found to be the optimal stabiliser for liquid phase exfoliation of thin graphene nanosheets with excellent conductivity and biocompatibility with neuronal cells. PVP-stabilised graphene was then combined with polycaprolactone to form conductive PolyGraph composites, which support robust axonal extension of iPSC-derived neurons at the optimal 10 vol% loading. NaOH treatment and coating with a thin AuPd layer were used to bring the impedance (~1.6 Ω cm^2 @ 1 kHz) and charge injection capacity (11.7 mC/cm^2 for a 100 ms pulse) into line with those needed for BCI devices. Optimised graphene composites were cast and 3D printed to form freestanding microneedle electrodes, connected using a bioresorbable hyaluronic acid-based backing to create a flexible, multi-channel neural interface. In ongoing work, flat PolyGraph10% electrodes were used to stimulate human neurons in porous 3D hyaluronic acid scaffolds in a stimulation bioreactor prototype, and PolyGraph10% microneedles were used in an electrophysiological setup to investigate the potential of PolyGraph10% for bidirectional recording and stimulation from a brain slice culture.

These findings demonstrate the development of biocompatible, flexible, and versatile graphene composites for BCI devices, with potential for both neural stimulation and recording. An optimal graphene formulation was developed and characterised, followed by its incorporation into composites with PCL. Following treatment to optimise their electrical properties, these composites were applied to the development of a flexible, biocompatible microneedle electrode array for neural interfacing. This research has significant relevance to the BCI space - new, softer materials with versatile processing capabilities are in high demand for advanced devices[430–436,653,654]. Beyond BCIs, the unique properties of PolyGraph composites extend their potential to act as highly conductive, biocompatible materials across a wide range of applications, such as tissue engineering, implantable electronics, and wearable devices.

Chapter 4
Boron Nanoplatelets as an Osteogenic, Anti-Microbial and Mechanically Reinforcing Additive for Biomaterial Scaffolds for Bone Repair

Note

This work forms the basis for the second publication from this PhD, which has been submitted to Advanced Functional Materials for review.

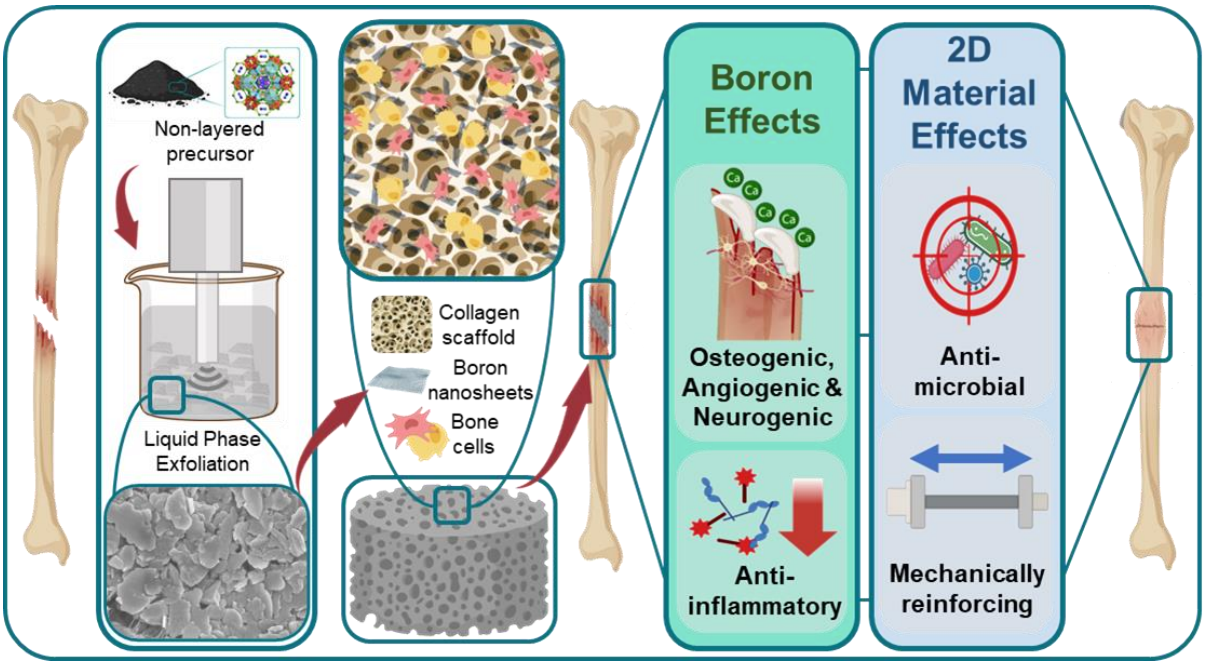

Fig. 4.1 - Boron nanoplatelets allow us to address one of the key requirements of bone tissue engineering therapies – multifunctionality. Bone repair scaffolds must improve osteogenesis, angiogenesis, and neurogenesis, prevent inflammation and infection, and be mechanically similar to bone tissue. 2D boron nanoplatelets allow these requirements to be addressed simultaneously, by opening up properties achievable only as a result of the nanoplatelet morphology, while still taking advantage of the intrinsic biological properties of boron. In this study, we synthesize boron nanoplatelets and combine them with a collagen matrix to form porous scaffolds with osteogenic, angiogenic, neurogenic, anti-inflammatory, and anti-microbial behaviour. This demonstrates the potential of boron as a versatile additive for bone tissue engineering applications.

4.1 Introduction

Developments in the exfoliation of non-layered materials have opened up a wide range of materials for potential exploitation in their two-dimensional (2D) form. For example, boron is a key non-layered trace element in the human body, positively influencing bone health[299–301], osteogenesis[302–307], angiogenesis[308,309] and wound healing[310], among many other biological systems[299,301]. However, research into other dimensionalities of elemental boron has only picked up speed in recent years, as production of 2D nanoplatelets from non-layered boron[114] is not

trivial. In such non-layered materials, the limited spatial anisotropy in the chemical bonding makes exfoliation considerably more challenging, and would be expected to result in relatively low aspect ratio nanoparticles.[148,706] These issues can be countered to a certain extent by careful selection of the material to be exfoliated, as certain crystals exhibit some anisotropy in the bonding strength of their lattice planes. The resultant preferential cleavage can lead to the production of quasi-2D nanoplatelets with somewhat enhanced aspect ratios that can range from as low as 4 to as high as 1400.[129,148] The exact mechanism of this surprising result is highly material dependent and appears to be driven by the formation of cracks at intrinsic defects in a bulk precursor,[129] which then propagate through the material.

In this work, we leverage the dimensionality of recently developed 2D boron nanoplatelets to produce a potent scaffold additive for bone repair. Systemic boron supplementation has been studied[299,305], along with the successful use of boron-containing compounds for bone tissue engineering applications, leading to enhanced bone repair and mineralisation[304,308,311–313]. Boron nanoplatelets, however, have yet to be applied to the repair of large, traumatic bone defects. This is a challenging prospect, since robust osteogenesis, angiogenesis and innervation are required to direct sustainable bone repair[707]. On top of this, the risk of infection[413,708], the inflammatory response of the tissue[709], and the stiffness of the biomaterial[710] must be suitable to direct cell responses. 2D materials are particularly promising for addressing these challenges simultaneously, thanks to their unique properties, such as high surface area-volume ratio[33], sharp edges[38,711], and percolative network effects on the mechanical properties of composites[96,586]. These properties, which arise directly from their 2D nature and are not found in their bulk counterparts, unlock a diverse range of possibilities and applications, from anti-microbial effects[78–81] and drug delivery[82,83], to mechanical reinforcement[24,96,97].

To this end, and building on previous experience in the exfoliation of non-layered materials[9,148] and in the development of 2D nanoparticle composites[87,101,170] from **Chapters 2** and **3**, we aimed to incorporate 2D boron within a macroporous, biocompatible and biodegradable collagen scaffold with proven capacity for bone repair[342,712,713], to extend and enhance the multifunctional pro-regenerative characteristics of the scaffold. Since natural polymers such as collagen excel biologically as scaffold materials[342,714], but often display weaker mechanical properties[342,582], additives such as hydroxyapatite[715,716] and carbon nanomaterials[715,717] are often used to strengthen the material, taking advantage of the preference of mechanosensitive bone cells for stiffer

substrates[718]. To reduce the incidence of expensive osteomyelitic complications[708,719–721], metal ions and chitosan are sometimes used to impart anti-microbial activity[413,722–724]. Beyond these, scaffold-mediated drug and gene delivery is sometimes carried out using nanoparticle carriers[83,725], while osteogenic[405,415,416], angiogenic[415,418], and neurogenic[419] effects are often enhanced by various bioactive ions, materials or growth factors such as Mg^{2+}, hydroxyapatite or BMP-2[405,726,727]. Each of these interventions play an important role in enhancing the benefits of natural polymer scaffolds for bone tissue repair. However, we propose to utilise the multifunctional potential of 2D boron, which can leverage both the effects of elemental boron and the intrinsic effects of 2D materials to address each of the above-mentioned challenges simultaneously, in a single material – we seek to demonstrate that 2D boron is potentially an ideal candidate for a multi-functional additive for bone tissue engineering.

4.1.1 Objectives & Aims

The overall objective of this chapter was to produce biocompatible polymer-stabilised boron nanoplatelets, and to investigate their potential as a multifunctional additive in bone tissue engineering scaffolds, thus demonstrating the broader potential of 2D nanomaterials in tissue engineering. Specifically, the individual aims were to:

1. Synthesise boron nanosheets from a non-layered precursor by liquid phase exfoliation (LPE), characterize their physical and biological characteristics.
2. Fabricate boron-collagen (BColl) composite films and 3D scaffolds by lyophilisation.
3. Investigate the biocompatibility and osteogenic potential of these 3D scaffolds with physiologically relevant bone cells.
4. Demonstrate the functional effects of this material by assessing the anti-microbial, angiogenic, neurogenic and anti-inflammatory effects of boron loading.

4.2 Materials & Methods

4.2.1 Synthesis of 2D boron nanoplatelets

Preparation of inert solvents to prevent boron oxidation

Inert, anhydrous, and deoxygenated solvents were produced by drying, distillation and degassing. The solvent was first dried using molecular sieves for 3 days. The solvent was then distilled to remove impurities. Finally, it was degassed by bubbling nitrogen gas through it for 2 days. The solvent was then stored in the glovebox under an argon atmosphere until use.

Sonic tip exfoliation of boron nanoplatelets

Crystalline boron powder (Stanford Advanced Materials, median particle diameter = 15 μm), stored under an argon atmosphere, and 160 mg of polyvinylpyrrolidone (PVP, M_w = 40 kDa, Sigma Aldrich) were added to 80 mL of anhydrous, degassed *N*-Methyl-2-pyrrolidone (NMP, ACS Reagent, ≥99% purity, Honeywell, USA) in a metal beaker. The mixture was then exfoliated for 8 h at 55% amplitude, on a 6 s/2 s on/off pulse, using a sonic probe (VCX750, Sonics & Materials Inc., USA). Following exfoliation, the material was centrifuged at 1 krpm to cause unexfoliated material to crash out of the dispersion. This sediment was discarded, and the supernatant was subsequently centrifuged at 6 krpm, to remove small impurities and 0D particles from the dispersion[147]. The resulting sediment was redispersed in anhydrous, degassed isopropanol (IPA, HPLC grade, 99.9%, Sigma Aldrich), and washed twice with fresh IPA at 6 krpm to remove excess residual NMP. To slow oxidation, the resulting dispersion was stored under argon in a glovebox (Jacomex, France) until use. For use in biological scaffolds, the material was redispersed in deionised water (18.2 MΩ) by centrifugation at 6 krpm, and washed twice in fresh deionised water to remove traces of IPA. The concentration of the dispersions was assessed by filtration of a known volume of dispersion using a 200 nm filter membrane, followed by weighing.

Cryogenic exfoliation of boron

Cryogenic exfoliation was carried out by submerging a vial of 1 mg/mL boron powder and 1 mg/mL PVP in IPA in in liquid nitrogen for 5 minutes. The material was then immediately placed in a sonic bath, and sonicated at 37 kHz for 1 hour.

4.2.2 Physical characterisation of boron nanoplatelets

Establishing thermal degradation and oxidation properties using thermogravimetric analysis (TGA)

Thermogravimetric analysis was carried out using a Q50 thermogravimetric analyser (TA Instruments, USA). The temperature was ramped from 25 °C to 900 °C, at a ramp rate of 10 °C min^{-1} in air, then held isothermal at 900 °C for 5 min to ensure complete combustion.

Elemental and oxidation analysis using energy-dispersive X-ray spectroscopy (EDX)

EDX analysis was carried out using the secondary electron detector of a Zeiss Ultra FE-SEM (Zeiss, USA), at an accelerating voltage of 5 kV and a working distance of 11 mm. Peak assignment was carried out using INCA software (Oxford Instruments).

Scanning electron microscopy (SEM) for nanoplatelet and scaffold visualization

Where necessary, samples were first gently dehydrated using a Leica critical point dryer. Dry samples were then sputter coated with a 5 nm layer of an 80:20 mixture of gold and palladium using a Cressington 108 auto sputter coater. Imaging was carried out using a Zeiss Ultra FE-SEM using the InLens detector at an accelerating voltage of 5 kV, an aperture size of 30 µm and a working distance of 5 mm, with images acquired at varying magnifications.

Ultraviolet-visible (UV-Vis) spectroscopy

Boron nanoplatelets were first diluted 1:20 in isopropanol. UV-Vis spectroscopy was then carried out in a quartz cuvette (path length 1 mm) using a Perkin-Elmer Lambda 1050+ spectrophotometer and an integrating sphere, to collect information on the scattering, absorption, and extinction spectra, at a wavelength resolution of 2 nm.

Atomic force microscopy (AFM) for establishing nanoplatelet dimensions and morphology

Utilizing a Bruker Multimode 8 microscope, AFM was performed to assess the thickness and lateral dimensions of the flakes. After dilution with isopropanol at a ratio of 1:100, the boron inks were drop-cast onto Si/SiO_2 substrates. Imaging of the samples was carried out using OLTESPA R3 cantilevers in ScanAsyst mode, and statistical data were derived from the analysis of 147 flakes. The lateral dimensions were determined by computing the square root of the product of the flake length and width. Data was analysed using Gwyddion SPM software[656].

Transmission electron microscopy (TEM) for nanoplatelet visualisation

A JEOL 2100 system operating in bright-field mode was used to perform the transmission electron microscopy measurements. Freshly exfoliated boron nanoplatelets, centrifuged between 1 and 6 krpm, was used to prepare the holey carbon TEM grids (400 mesh). 100 µL of the dispersion (concentration of approx. 0.1 mg/mL) was drop-casted on the grids, and vacuum dried at 80 °C in the oven overnight prior to the measurements. Images were acquired at an accelerating voltage of 200 kV.

X-ray diffraction (XRD) for establishing material crystallinity

The powder samples were structurally characterised by performing symmetric $2\theta_\omega$ X-ray diffraction (XRD) scans using a Panalytical X'Pert Pro diffractometer equipped with a Cu K_α source (λ = 1.5406 Å) and a Ni filter to remove K_β peak intensities.

Mechanical testing to identify mechanical reinforcement of natural polymers

Mechanical testing was carried out using a Zwick Z0.5 Proline tensile tester with a 100 N load cell, at a strain rate of 0.01 %/s. Samples were cut into strips (2-4 mm wide), clamped, and tested in a uniaxial strain configuration. The Young's modulus and other mechanical properties were calculated for each sample from the stress-strain curve.

4.2.3 Synthesis of 2D boron/collagen (BColl) nanocomposites

BColl slurry was fabricated by mixing type I collagen (5 mg/mL, milled form, Collagen Solutions) with a 2D boron dispersion in deionised water and acetic acid. The composite slurry was blended (T25 Ultra-Turrax®, VWR) at 15000 rpm for 30 min until homogenous. The composite materials subsequently underwent dehydrothermal (DHT) crosslinking treatment for 24 h at 105 °C under vacuum. For 2D culture, they were cast in square molds and allowed to dry. For 3D culture, porous scaffolds of BColl were produced by lyophilisation - slurries were placed in Teflon molds and freeze dried for 24 h at –40 °C to obtain lyophilized cylindrical scaffolds.

4.2.4 Biocompatibility testing of 2D boron sheets

Ethical declaration for ex vivo experiments

For the experiments using rat mesenchymal stem cells and dorsal root ganglia described below, *ex vivo* tissue was obtained from animals donated as post-mortem byproducts from ongoing

experiments in other groups in the RCSI, in line with our policy of reduction according to the 3Rs of animal research. Rat femora for isolating mesenchymal stem cells were obtained from rats culled under project authorisation number REC202012003, accredited by the Animal Research Ethics Committee of RCSI (RECTH017). Mouse spinal cords used to extract dorsal root ganglia were obtained from animals donated by the Tissue Engineering Research Group. Post-mortem harvesting was carried out under Health Products Regulatory Authority (HPRA) individual license AE19127/I259, with ethical approval from the Animal Research Ethics Committee of RCSI (RECTH017).

Isolation of mesenchymal stem cells (MSCs)

Rat mesenchymal stem and endothelial progenitor cells were isolated from 6–8-week-old male Sprague Dawley as described in Power et al.[728]. Both ends of the femora of the hind legs were clipped to expose the bone marrow, which was then flushed out with rat MSC medium using an 18 G needle and a 12 mL syringe into a petri dish using Dulbecco's Modified Eagle Medium (DMEM) containing: 20% foetal bovine serum (FBS, Biosera, Ireland), 2% penicillin streptomycin (P/s, Sigma Aldrich, USA), 1% non-essential amino acids (NEAA, Thermo Fisher Scientific, USA), 1% GlutaMAX (Thermo Fisher Scientific, USA) and 0.002% Primocin (Sigma, Ireland). The cells were then cultured in 15 mL of media under standard cell culture conditions (37 °C, 5% CO_2) for 24 h. The supernatant was then removed and centrifuged at 300 × g for 5 min.

2D culture of osteoblasts in free suspension with boron nanoplatelets

2D boron was first dispersed in DI water and sterilised by autoclaving. Osteoblastic immortalised cells (MC3T3-E1, American Type Culture Collection, ATCC, Middlesex, UK) were cultured in T175 flasks until needed, then seeded in a 48-well plate, at a density of 1×10^4 cells/well. The cells were supported in growth media consisting of Alpha Modified Eagle Medium (α-MEM, Sigma, Ireland) with 10% fetal bovine serum (FBS, Biosera, Ireland), 1% Penicillin/Streptomycin (P/s, ScienCell, USA) and 1% l-glutamine (l-glut, Sigma, Ireland). The cells were seeded, and left to settle for 24 h, before the treatment was applied. Dispersions of 40 µg/mL and 80 µg/mL of boron nanoplatelets in growth media were made up, and the media on the cells was replaced with 360 µL of fresh treatment media after 24 h of settling. After 24 h and 72 h, 40 µL of Alamar Blue (Invitrogen, UK) was added to measure the cellular metabolic activity, and the cells were incubated at 37 °C for 2 h. Following this, fluorescence was measured

using excitation 535 nm and emission 590 nm with a plate reader (Infinite M Plex, Tecan), to assess the metabolic activity of the cells. The cells were then lysed using lysis buffer (100 mL autoclaved DI water, 0.5 mL Triton X-100, 29 mg EDTA (Ethylenediaminetetraacetic acid), 2.12 g sodium carbonate) and total DNA content was assessed using the Picogreen assay (Invitrogen, UK), which was carried out as per the manufacturer's instructions. For assessment of osteogenesis in 3D, 1% β-glycerophosphate (Sigma, Ireland), 0.5% ascorbic acid (Sigma, Ireland) and 100 nM dexamethasone (Sigma, Ireland) were added to create osteogenic differentiation media.

2D culture of osteoblasts on BColl films

BColl films were fabricated as described above, at loadings of 0 vol%, 0.5 vol%, and 1 vol% boron nanoplatelets in collagen. MC3T3 cells were seeded on 8 mm diameter discs of these films at a density of 2×10^4 cells/film, and allowed to grow for 7 days.

3D culture of osteoblasts and MSCs on BColl scaffolds

BColl scaffolds were fabricated as described above, at loadings of 0 vol%, 0.5 vol%, 1 vol%, 2.5 vol%, and 5 vol%. Scaffolds were sterilised in 70% ethanol for 24 h, followed by washing in PBS (×3, 5 mins). The scaffolds were then immersed in growth media at 37 °C and 5% CO_2 for 24 h. Cells were passaged and seeded at densities of 3×10^5 – 5×10^5 per scaffold. Half of the cells were seeded on each side of the scaffold for 1 hour each, before the wells were flooded with growth media for 24 h. Growth media was exchanged for osteogenic media after 24 hours.

4.2.5 Analysis of boron effect on osteogenesis and bone mineralisation

Alkaline phosphatase (ALP) release quantification to assess osteogenesis

ALP release was analysed using a Sensolyte™ PNPP ALP Assay Kit (Anaspec, USA). Cells (MC3T3 osteoblasts and MSCs) were washed with PBS at the relevant timepoints, and subsequently lysed with ALP lysis buffer. The assay was then carried out according to manufacturer's instructions.

Calcium (Ca^{2+}) release quantification to assess bone mineralisation

Following culture, calcium was extracted from quartered scaffolds using 0.5 M hydrochloric acid (Sigma, Ireland). Calcium release was analysed using a Calcium LiquiColor™ assay (StanBio, USA), according to the manufacturer's instructions.

4.2.6 Histology

Sample preparation

Boron-collagen and collagen-only scaffolds were embedded in sucrose for 48 h, and then sectioned in OCT using a cryostat (Leica Biosystems, UK), into 5 µm thick slices.

Haematoxylin & eosin (H&E) staining to assess matrix deposition

H&E staining was carried out to image the ECM and nuclei present in the sample. The following order was used for staining: Tap water rinse for 5 minutes, haematoxylin for 3 minutes, tap water for 10 minutes, DI water for 5 minutes, eosin for 3 minutes, 3-4 dips in tap water, 15 dips in 95% ethanol, 15 dips 100% ethanol, 15 dips in acetone and 15 dips in xylene substitute. Coverslips were then mounted on the samples using DPX.

Alizarin Red staining to assess calcium deposition

Alizarin Red staining was carried out to image calcium deposition present in the sample. The following order was used for staining: Tap water rinse for 5 minutes, 250 µL of 2% Alizarin Red (Generon, Ireland) per slice for 30 minutes, 5 dips in acetone, 20 dips in 1:1 acetone:xylene substitute solution, xylene substitute for 5 minutes. Coverslips were then mounted on the samples using DPX.

4.2.7 Immunofluorescence staining to assess cellular morphology and proliferation

Cells, on both boron-collagen films and scaffolds, were fixed using 10% formalin (Sigma, Ireland), and stained with phalloidin (Sigma, USA) for the cell membrane, and DAPI (Thermo-Fisher Scientific, USA) for the cell nucleus. The samples, once fixed and stained, were fluorescently imaged using a Zeiss AxioObserver inverted microscope. Infiltration analysis into boron-collagen and collagen scaffolds was carried out by measuring the radial distance from the edge of the scaffold to the furthest infiltrated cell at 15° intervals around the cross-section.

4.2.8 Anti-microbial testing with *S. aureus* and *E. coli*

Staphylococcus aureus *(S. aureus*, Newman) and Escherichia coli *(E. coli)* bacteria were cultured separately for 24 h at 37 °C in brain/heart infusion broth, before 1 mL of bacteria was plated into wells containing sterile boron discs (diameter = 6 mm) at a density of 5×10^5 CFUs/mL. These samples were then cultured for another 24 h at 37 °C. The broth was subsequently removed, and the samples were washed with phosphate buffered saline. Live-dead staining was

carried out with SYTO 9 and propidium iodide (LIVE/DEAD® BacLight™ Bacterial Viability Kit L7007, Thermo Fisher Scientific, USA), according to manufacturer instructions. Imaging was carried out on a Zeiss LSM 710 NLO confocal microscope and analysed using FIJI.

4.2.9 ELISA analysis of MSC paracrine signalling profile on BColl scaffolds

ELISA analysis was carried out using a 19-target multiplex array of rat cytokines (AAR-CYT-1-4, CliniSciences, Ireland). Samples were diluted 1:2 with blocking buffer, and analysis was carried out according to manufacturer's instructions. Densitometry measurements were carried out using FIJI. A blank reading consisting of cell-free media was subtracted from the data.

4.2.10 Neurogenic analysis by dorsal root ganglia (DRG) culture with BColl scaffolds

To assess the ability of the scaffolds to enhance neurogenesis in an *ex vivo* model, dorsal root ganglia (DRGs) from 5-month-old adult female C57 mice (N=9, 385 – 500 g) were seeded onto the scaffolds. DRGs were isolated and dissected using a previously established method[351]. 20-24 DRGs and their roots were dissected from each animal. The roots were then trimmed of their associated nerves using micro-scissors (F.S.T. Cat # 15000-08) and cultured on scaffolds in neurobasal medium with 1% P/s, 1% GlutaMAX and 2% B27 supplement for 14 days.

4.2.11 Statistical analysis

A minimum number of three experimental replicates (N) with at least three technical replicates (n) were used in all assessments. Prior determination of statistical significance, the ROUT method (Q=10%) was used to determine the variance in the population. All data sets were subjected to Kolmogorov–Smirnov test to assess for normality and thereafter the data tested using appropriate parametric (t-test, one- and two-way ANOVA) and non-parametric (Mann-Whitney U, one and two-way Kruskall-Wallis) tests. Post-hoc tests were performed using Tukey's multiple comparisons and Dunnett's correction where needed. All results were plotted with the standard error of mean and were considered significant when $p < 0.05$ and statistical significance was denoted by *: *$p < 0.05$, **$p < 0.01$, ***$p < 0.001$, ****$p < 0.0001$. Significances are relative to control group of timepoint unless stated otherwise. All data were plotted and analysed as means with standard error of the mean while using the software GraphPad Prism (v8.0) and OriginLab 2024.

4.3 Results and Discussion

4.3.1 Synthesis of boron nanoplatelets *(Aim 1)*

Boron is a relatively new member of the two-dimensional material family due to its non-layered nature[729]. As a result, before commencing biological characterisation, optimization of the synthesis protocol was required, in order to both achieve optimal flake yield and quality, and high biocompatibility by means of non-cytotoxic stabilising molecules. This optimisation was carried out along three axes – bulk crystallinity, solvent choice, and exfoliation method. With amorphous boron powder as the precursor, liquid phase exfoliation was carried out in a range of solvents - isopropanol (IPA), ethanol (EtOH) and N-methyl-2-pyrrolidone (NMP). These initial exfoliations failed to yield particles with a 2D morphology, instead yielding 0D nanoparticle dispersions, as seen in **Fig. A3.1 A-C**. This result suggests that the lack of anisotropy in the boron bonding leads to isotropic cleavage, and the subsequent formation of nanoparticles. However, the efficiency of LPE for non-layered materials can be enhanced in similar ways to that of LPE for layered materials. For example, cryogenic treatment can be used to render inter-atomic bonds more brittle, and thus prone to fracture along existing defects during exfoliation[148,157,158].

In order to induce this thermal fracturing, and thus exfoliation along a plane, cryogenic exfoliation in IPA and NMP was then tested. This approach was more successful, yielding a mix of morphologies, including 0D nanoparticles, 1D nanoribbons, and 2D nanoplatelets (**Fig. A3.1 D**). These morphologies potentially arise due to the formation of cracks following cryogenic treatment, which then propagate through the material[148]. However, it was not possible to efficiently separate these morphologies, nor to render the exfoliation more selective for 2D nanoplatelets. Based on these results, we shifted to the use of crystalline boron precursors, which provide crystalline planes along which exfoliation can occur[148], due to intrinsic stacking faults of boron icosahedra in the 3D crystal reducing the cleavage energy along the {001} plane[129].

With this in mind, 2D boron nanoplatelets were ultimately exfoliated successfully from a crystalline precursor in NMP, chosen for its favourable surface tension and solubility parameters[12,142]. As seen in the scanning electron microscopy (SEM) (**Fig. 4.2 A**) and transmission electron microscopy (TEM) (**Fig. 4.2 B**) data, the resulting boron nanoplatelets exhibited a 2D morphology indicative of successful selective exfoliation, which was confirmed by atomic force microscopy (AFM) measurements (**Fig. 4.2 C**). Statistical analysis of these images revealed a broad distribution of nanoplatelet dimensions, with lengths (L) ranging from 50 to 500 nm and thicknesses (t) ranging from 1 to 80 nm (**Fig. 4.2 D**). The nanoplatelet length

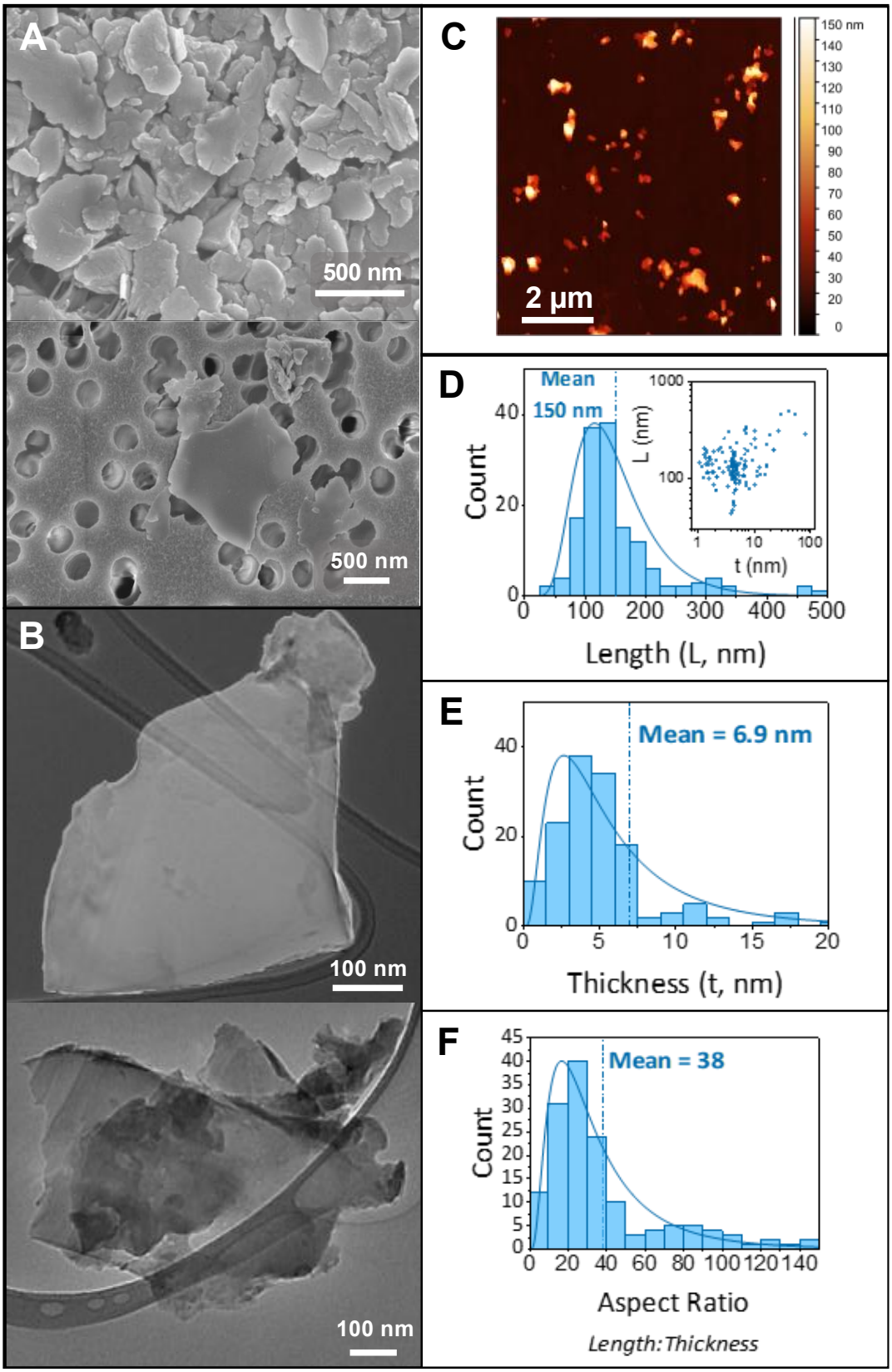

Fig. 4.2 – ***Morphological characterisation of boron nanoplatelets:*** *Scanning electron microscopy (SEM) (**A**, scalebars 500 nm) and transmission electron microscopy (TEM) (**B**, scalebars 100 nm) imaging were used to visualise successful exfoliation of the boron nanoplatelets.* ***C-F)*** *Atomic force microscopy (AFM) imaging (A) of 147 boron nanoplatelets was used to assess the length (D), thickness (E) and aspect ratio (F) distributions of the nanoplatelets, corroborating the 2D morphology seen in the SEM and TEM. Scalebar 2 µm.*

and thickness distributions are shown in **Fig. 4.2 D** and **Fig. 4.2 E** as histograms. The average flake length was measured as 150 ± 6 nm, with an average thickness of 6.9 ± 0.8 nm. Knowledge of nanoplatelet length and thickness allow the calculation of the aspect ratio (AR = $\frac{L}{t}$). The AR distribution is shown in **Fig. 4.2 F** and has a mean of 38. This data gives us an insight to the surface area:volume ratio of our material, which is critical for many applications[730] – for the average nanoplatelet dimensions attained in this work, the surface area:volume ratio is 0.32, >5 times larger than that of the smallest widely commercially available nanoparticles, which have a radius 50 nm[731,732] and a surface area:volume ratio of 0.06 (**Fig. 1.1**). This means more of the material is exposed to the surrounding tissue at any given time, improving the efficiency of the material at delivering intrinsic biological effects[733].

4.3.2 Physical characterisation of boron nanoplatelets *(Aim 1)*

Following the successful exfoliation of boron nanoplatelets, the crystal, thermal and optical properties of the material were established. A primary concern about elemental boron materials is oxidation[138], since it can lead to changes in material properties such as conductivity, surface chemistry and biocompatibility[137,141,734]. To assess the degree of oxidation suffered by the material, thermogravimetric analysis (TGA) and energy-dispersive X-ray spectroscopy (EDX) were carried out. The tendency of the material to oxidise was first observed in TGA data (**Fig. 4.3 A**), which showed that upon heating of the boron under an air atmosphere, the mass increased significantly due to the formation of oxides[138,735,736], with the rate of oxidation increasing rapidly beyond 500 °C. The main oxidation peak (**Fig. 4.3 A, inset**) is centred at 550 °C, consistent with previous reports of the oxidization of boron[737].

EDX (**Fig. 4.3 B**) was then carried out both on samples exfoliated in ambient conditions with commercial solvents, and on samples exfoliated in inert conditions with anhydrous, deoxygenated solvents. Boron exfoliated in both conditions exhibited incomplete oxidation after prolonged storage in ambient and inert conditions, as indicated by comparison with the most common boron oxide, B_2O_3, which would correspond to 60 at% oxygen[738]. This suggests the occurrence of surface oxidation, slowing oxidation of the bulk of the nanoplatelet. Furthermore, these analyses show that the oxidation of the boron primarily occurs during the exfoliation process as a result of dissolved oxygen in the solvents, rather than during storage, as ambient-exfoliated boron that was stored under inert conditions still exhibited a significant amount of oxidation. As a result of these measurements, the standard exfoliation protocol was adapted to use inert, degassed, and anhydrous solvents.

The final characterisation of the boron nanoplatelets was intended to reveal any shifts in crystallinity or optical properties arising after exfoliation. The UV-visible absorption spectrum of a dispersion of boron nanoplatelets exfoliated in anhydrous, degassed NMP is shown in Fig. 4.3 C. We note that the considerable scattering background, typical of nanomaterial dispersions[675], has been removed (Fig. A3.3). The same spectrum has been replotted in the inset, with the absorbance on a log scale, plotted versus photon energy. This graph clearly shows our boron nanoplatelets to be semiconducting, with a bandgap of slightly under 1 eV. This could be consistent with either crystalline boron or amorphous boron which display optical gaps of 0.9 and 0.7 eV respectively[739]. However, our relatively featureless spectrum is more in line with amorphous boron[739]. The increase in absorbance below 250 nm (above 5.1 eV) may arise due to the presence of boron oxide, an insulator with a larger bandgap, around 5.23 eV[740].

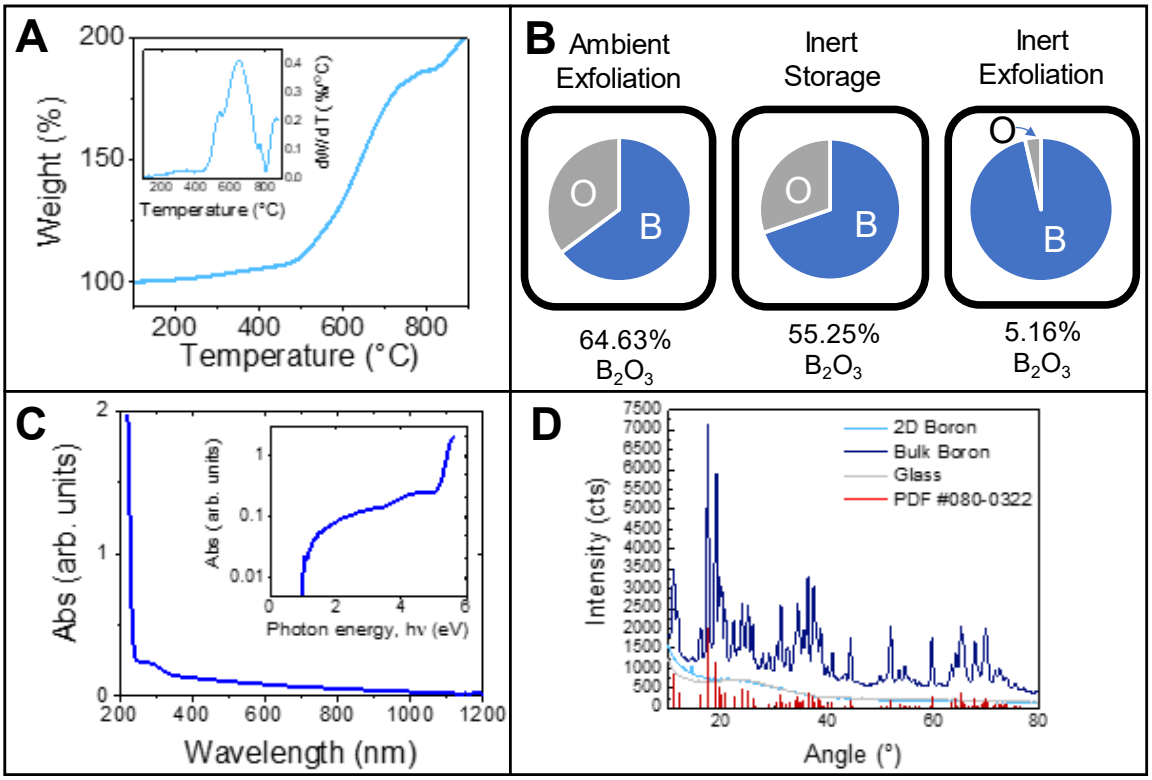

*Fig. 4.3 – **Physical characterisation of boron nanoplatelets: A)** Thermogravimetric analysis (TGA) of boron nanoplatelets in air, with an increase in sample mass with temperature showing oxidation of boron nanoplatelets upon heating. Inset shows derivative of mass loss. **B)** Energy-dispersive X-ray spectroscopy (EDX), used to assess the elemental makeup (atomic %) of the sample under different conditions of exfoliation and storage – exfoliation in anhydrous, deoxygenated solvents was demonstrated to have the largest impact on the prevention of oxidation in the material. **C)** UV-Visible light spectroscopy (UV-Vis) of a boron nanoplatelet dispersion showing absorption spectra typical of a semiconducting nanomaterial. **D)** X-ray diffraction patterns (XRD) used to assess the crystallinity of the starting bulk boron powder and exfoliated boron nanoplatelets, showing a potential shift towards an amorphous allotrope following exfoliation.*

In order to assess whether there was a shift in the crystallinity of the material due to the exfoliation, powder X-ray diffraction (XRD) (**Fig. 4.3 D**) was carried out. The XRD spectrum for the bulk boron precursor is consistent with the crystalline form of β-boron, as shown in the literature[12,741], and matches well with the relevant powder diffraction file from the ICDD database[742] (PDF #080-032). The XRD spectrum for the 2D boron nanoplatelets, on the other hand, is indicative of a shift towards an amorphous allotrope of boron/boron oxide. Such amorphization has been observed previously for LPE of non-layered materials such as red phosphorus[47]. Furthermore, this indicates that no transition to a borophene-like phase occurs. This is consistent with previous work on LPE of crystalline boron precursors[12,130], suggesting that top-down exfoliation of boron leads to the formation of few-layer nanoplatelets consisting of the bulk material, rather than the allotropically distinct borophene phases[743]. Taken together, the physical characterisation of the material shows that we have successfully exfoliated 2D nanoplatelets of amorphous boron, which are suitable for leveraging the benefits of both the intrinsic properties of boron and their 2D morphology.

4.3.3 Fabrication and characterisation of 2D films and 3D scaffolds of BColl (*Aim 2*)

We propose that one important application of our boron nanoplatelets is as a filler material in polymer-based composites. One significant advantage of high aspect ratio nanoplatelets, when compared to quasi-spherical nanoparticles, is their ability to mechanically reinforce polymers[744]. Stiffness is well-established as a key regulator of cellular differentiation[351,718,745–748], and thus mesenchymal stem cells (MSCs) will exhibit different differentiation behaviour on a stiff substrate than a soft substrate. Models such as shear-lag theory[749] and Halpin-Tsai theory[750] clearly show that composite reinforcement depends sensitively on filler particle aspect ratio, with higher aspect ratio particles leading to greater reinforcement. As discussed in Chapter 2, the mechanical properties of collagen are complex due to its fibrillar structure[582,583], and this complexity is compounded when nanomaterial fillers are introduced.

To test the magnitude of mechanical reinforcement and its effect, composite films were fabricated by blending boron nanoplatelets with collagen to form boron-collagen (BColl) slurry, followed by casting into homogenous films of 0, 0.5, 1, 2.5 and 5 vol% boron loading (**Fig. 4.4 A**). Tensile testing was then carried out using thin strips of these BColl films. Examples of stress-strain curves for BColl composites with differing boron volume fractions (V_f) show a clear increase in stress at all strains as the boron loading is increased, a clear sign of reinforcement

(Fig. 4.4 B). While various parameters can be extracted from these stress-strain curves, we focus on the Young's modulus (E, Fig. 4.4 C) and the ultimate tensile strength (UTS, Fig. 4.4 D). In both cases, we see steady increases as the volume fraction is increased, with saturation occurring at a loading of roughly 2.5 vol%, and both parameters undergoing a near doubling in their values on addition of boron. The average Young's modulus of BColl composites was 973 MPa, comparing favourably to the typical stiffness range of trabecular bone, 10 MPa – 3000 MPa[751]. A significant increase was further observed in the initial tensile modulus of the material (Fig. A3.8 A), within the first 0.5% strain, the regime primarily experienced by cells, as well as a trend towards an increase in the toughness (Fig. A3.8 B). These increases render the environment more suitable for osteogenic differentiation, potentially contributing to the increase in osteogenic potential observed for the BColl material.

To understand the reinforcement of the BColl composite films, we analysed the data in Fig. 4.4 C using Halpin-Tsai theory[750]. The Halpin-Tsai equations describe the composite modulus, E, as a function of the filler volume fraction, V_f, the moduli of filler, E_F, and matrix, E_M, as well as the platelet aspect ratio, $\frac{L}{t}$. This particular model is appropriate when nanoplatelets are aligned in the plane of the composite, and has been shown to describe composites of BN nanoplatelets in polymer matrices quite well[752]. It has been shown that applying the approximations that $E_F/E_M >> 1$ and $V_f << 1$, which are appropriate for most nanocomposites, to the basic Halpin-Tsai equation gives the following simplified expression[752]:

$$E \approx \frac{E_F V_f}{\left[\frac{E_F / E_M}{2L/t} + 1\right]} + E_M \qquad \text{(Eq. 4.1)}$$

This equation predicts a linear increase in composite modulus with nanoplatelet volume fraction. We can test the applicability of this equation by plotting its prediction on top of our data using our measured values for E_M (0.64 GPa) and $\frac{L}{t}$ (38), as well as a previously reported value for the stiffness of amorphous boron (E_F = 300 GPa)[753]. This prediction is shown as the solid line in Fig. 4.4 C and matches the data reasonably well, especially at low loadings, where the model is most applicable. This clearly shows that our stiffness results are consistent with theory, confirming that boron nanoplatelets are an appropriate reinforcing material for collagen.

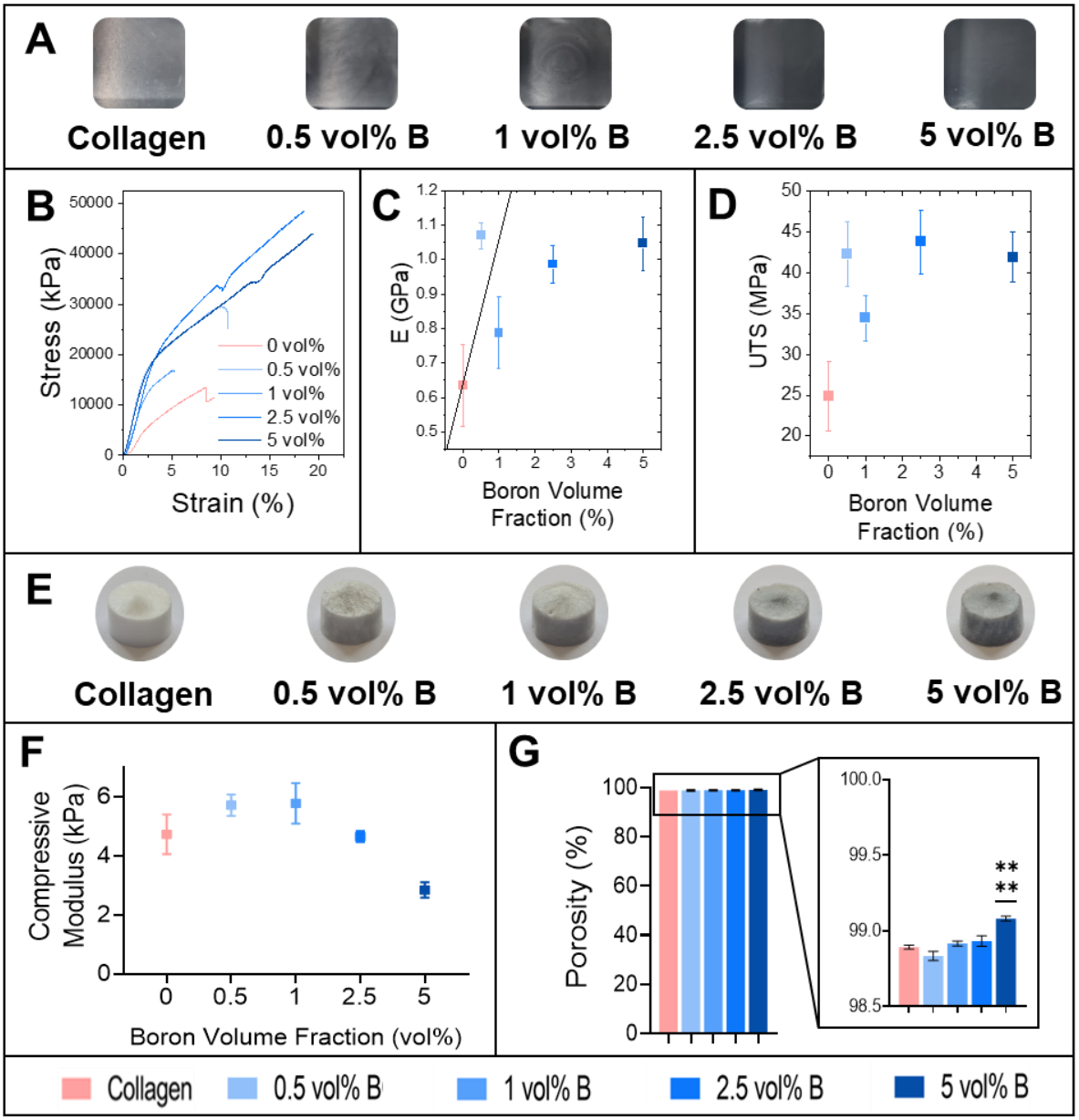

*Fig. 4.4 – **Characterisation of BColl composite films & scaffolds:** **A)** Images of BColl films at each boron loading. **B)** Representative stress-strain curves for BColl composites. **C-D)** Measurement of the Young's modulus (C) and ultimate tensile strength (D) for BColl films, showing significant reinforcement with boron loading. The line in C is a plot of Equation 4.1 using the following values: E_F = 300 GPa, E_M = 0.64 GPa, $\frac{L}{t}$ = 39. **E)** Images of BColl scaffolds at each boron loading. **F)** Compressive modulus testing of BColl scaffolds. **G)** Measurement of the porosity of BColl scaffolds at varying boron loadings, showing a slight increase in porosity for 5 vol% boron loading. Significances: *$p < 0.05$, **$p < 0.01$, ***$p < 0.001$, ****$p < 0.0001$.*

These results imply that boron nanoplatelets are a promising multifunctional composite component for reinforcing the struts of collagen-based tissue engineering scaffolds. To investigate this further, macroporous BColl composite scaffolds (Fig. 4.4 E) were produced by lyophilisation, at boron loadings of 0, 0.5, 1, 2.5 and 5 vol%.

Mechanical testing of these BColl scaffolds to determine compressive modulus revealed a slight trend towards reinforcement at lower boron loadings (Fig. 4.4 F), followed by a drop-off in

modulus, likely to be related to the increased porosity of the higher loading scaffolds (**Fig. 4.4 G**) – this increase was observed for the highest boron loading, and it is posited that it is due to a slight dilution of the collagen slurry caused by the addition of the boron dispersion during synthesis.

4.3.4 Biocompatibility of 2D boron/collagen (BColl) films with bone cells (*Aim 3*)

As with any novel biomaterial additive, it was necessary to establish the biocompatibility of the boron nanoplatelets before proceeding with functional testing, to ensure safe degradation and excretion of the scaffold after implantation. Boron nanoplatelets, stabilised with polyvinylpyrrolidone (PVP), a biosafe polymer[754] for biocompatibility and hydrophilicity, were added to the media of osteoblasts (MC3T3-E1, osteogenic cell line[755]). Cells were grown in suspension with 40 µg/mL and 80 µg/mL of boron for 72 h. Metabolic activity and DNA content analysis (**Fig. 4.5 A**) showed robust proliferation of the cells in the presence of boron, with a significant increase in both measures for 80 µg/mL of boron after 72 h. This indicates that the material is non-cytotoxic and can promote proliferation of bone cells, even in free suspension with high concentrations of the material. This is essential, as during the degradation of BColl scaffolds, boron will be released into the surroundings and must be safely excreted.

Once the biocompatibility of the boron nanoplatelets had been established, to further demonstrate that BColl composite materials were well-tolerated by cells, osteoblasts were grown on the surface of 0, 0.5, and 1 vol% BColl films for 7 days, similar to work in previous chapters assessing the biocompatibility of nanocomposite materials[101]. Metabolic activity and DNA content analysis demonstrated robust proliferation of the cells across the surface of the material (**Fig. 4.5 B**). The cell coverage observed for the BColl materials was significantly higher than that of collagen (**Fig. 4.5 C**), as verified by fluorescent staining of the cells with phalloidin and DAPI, with confluent cell layers forming on the surface of the BColl samples (**Fig. 4.5 D & E**), showing that BColl is not only well-tolerated in a 2D culture environment with bone cells, but that it appears to be enhancing the proliferation and viability of these cells, due to the bioactive effects of boron and its oxides[300,302,420,422]. Various mechanisms that explain ion-mediated enhancement of growth fail to account for boron, which typically does not exist in the B^{3+} form due to the high ionisation energies needed to achieve this state[756], so other research suggests that the release of bio-active ions from the covalent compounds of boron[420] leads to activation of the BMP and MAPK pathways, and subsequent osteogenic and angiogenic effects[300,302,422].

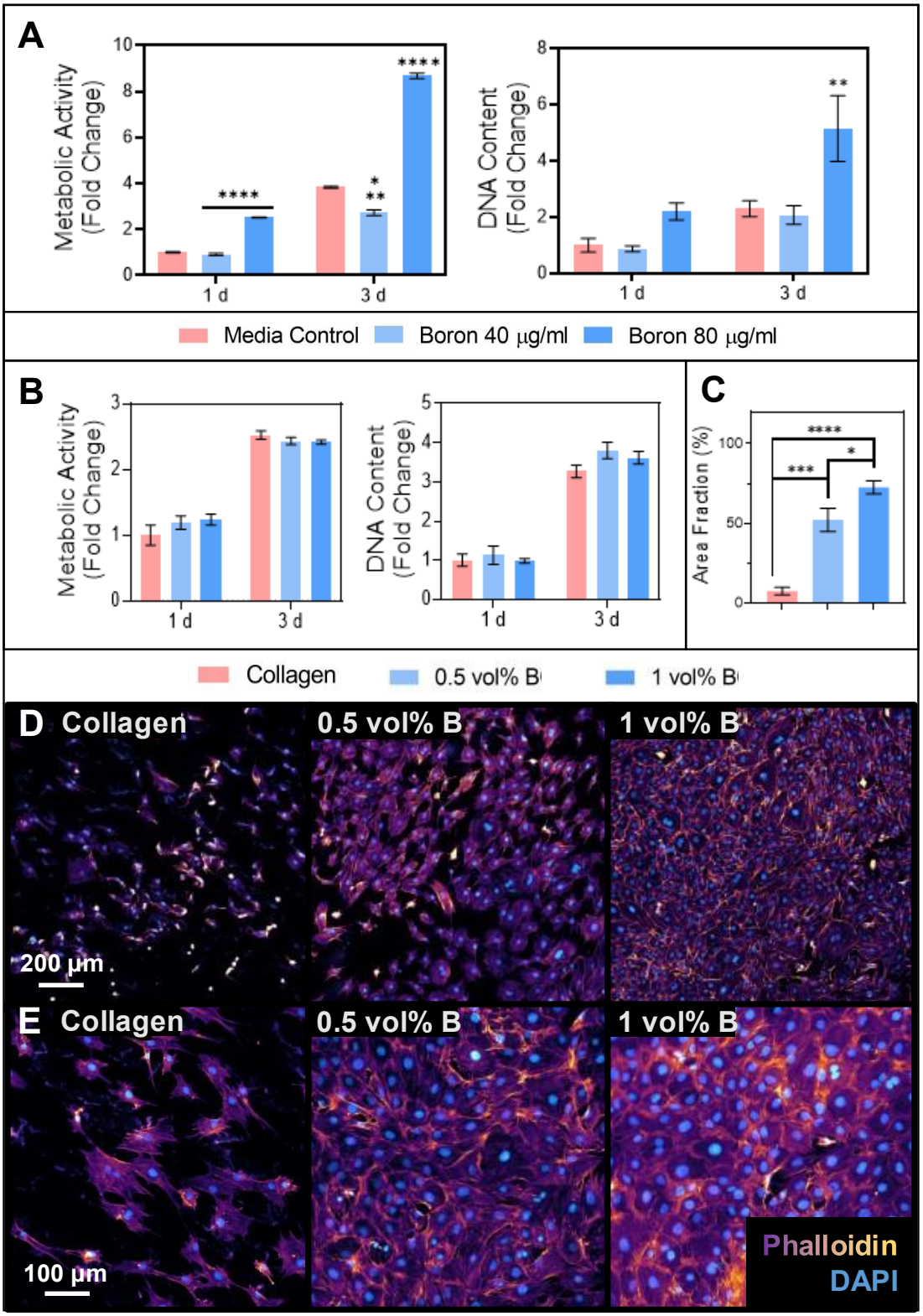

*Fig. 4.5 – **Biological characterisation of boron and BColl films in 2D:** **A)** Metabolic activity and DNA content of osteoblasts in suspension with varying concentrations of boron nanoplatelets, showing robust proliferation, particularly for the highest boron concentration. **B)** Metabolic activity and DNA content of osteoblasts grown on BColl films, showing healthy proliferation in all conditions. **C)** Percentage coverage of osteoblasts grown on BColl films for 7 days, showing a significant increase in coverage for cells grown on BColl films. **D-E)** Cell membrane (phalloidin) and nuclear (DAPI) staining of osteoblasts showed healthy cellular morphology and robust proliferation of cells grown on BColl films for 7 days. Imaged at 10× (D) and 20× (E) magnification. Significances: *$p < 0.05$, **$p < 0.01$, ***$p < 0.001$, ****$p < 0.0001$.*

4.3.5 Analysis of anti-microbial potential of BColl composite films (*Aim 4*)

With the biocompatibility of the boron material confirmed in 2D, focus shifted to testing the anti-microbial activity of the BColl composite, since infection is a key concern during the implantation and lifetime of any scaffold. Escherichia coli (*E. coli*) and Staphylococcus aureus (*S. aureus*) bacteria were cultured on the surface of BColl films for 24 hours, followed by live-dead staining. There was a significant drop in *E. coli* viability at all concentrations of boron tested (**Fig. 4.6 A**). This indicates the potential of the boron to inhibit the growth of gram-negative bacteria on the surface of its composites, addressing a key clinical issue - Masters et al.[719] states that 20% of all trauma-related skeletal infections and 35-55% of those in foot/ankle infections are caused by gram negative bacteria.

However, it is important to note that no anti-microbial effect was observed with *S. aureus* bacteria (**Fig. 4.6 B**). This difference is potentially due to differing interactions of the boron edges with the bacterial membranes of gram-positive (*S. aureus*) vs. gram-negative (*E. coli*) bacteria. Gram-positive bacteria, while possessing more porous membranes and thus less resistance to typical anti-microbial agents, have considerably thicker cell membranes[757] than gram-negative bacteria, which possess a thinner but more complex outer membrane. This thin membrane may be sliced more deeply by sharp nanoplatelets, leading to a greater antimicrobial effect[37,758,759]. This indicates that boron nanoplatelets have the potential to be used in conjunction with a traditional anti-microbial agent, leading to effective inhibition of both bacterial subgroups, as demonstrated previously by Taşaltin et al.[760] Furthermore, adaptations of the boron nanoplatelets, including size selection for smaller, thinner nanoplatelets, or inclusion of nano-needle (~1D) or nano-sword (1D/2D) morphologies may improve the inhibitory effect of boron on bacterial growth.

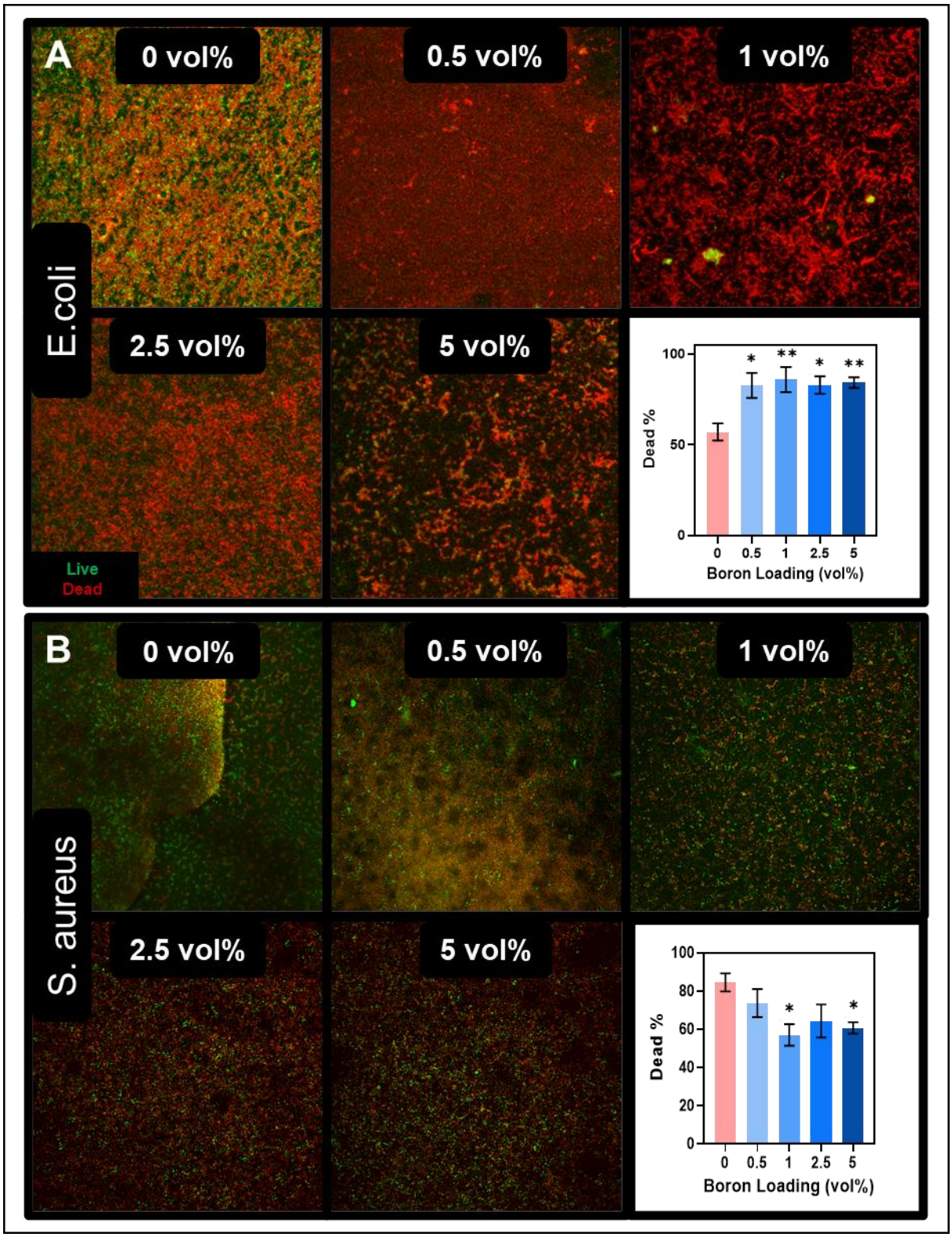

*Fig. 4.6 – **Anti-microbial testing of BColl films:** Anti-microbial testing with BColl films of varying boron loadings ranging from 0–5 vol%, with E. coli **(A)** and S. aureus **(B)** bacteria grown for 24 h, showing significant anti-microbial activity against E. coli bacteria. Live-dead staining coverage was analysed using FIJI. Significances: *$p < 0.05$, **$p < 0.01$, ***$p < 0.001$, ****$p < 0.0001$.*

4.3.6 Biocompatibility and osteogenesis-inducing effect of BColl scaffolds with osteoblasts and mesenchymal stem cells (MSCs) (*Aim 3*)

To demonstrate the potential of BColl in a 3D culture environment, osteoblasts were cultured in BColl scaffolds for 21 days. Both metabolic activity (Fig. 4.7 A) and DNA content analysis (Fig. 4.7 B) showed no significant difference from the control after 21 days, indicating a high degree of biocompatibility of BColl scaffolds with bone cells. The osteogenic potential of the boron was assessed by measuring the release of alkaline phosphatase (ALP), a key enzymatic regulator of bone formation[761], and by the deposition of calcium, indicative of bone mineralisation.

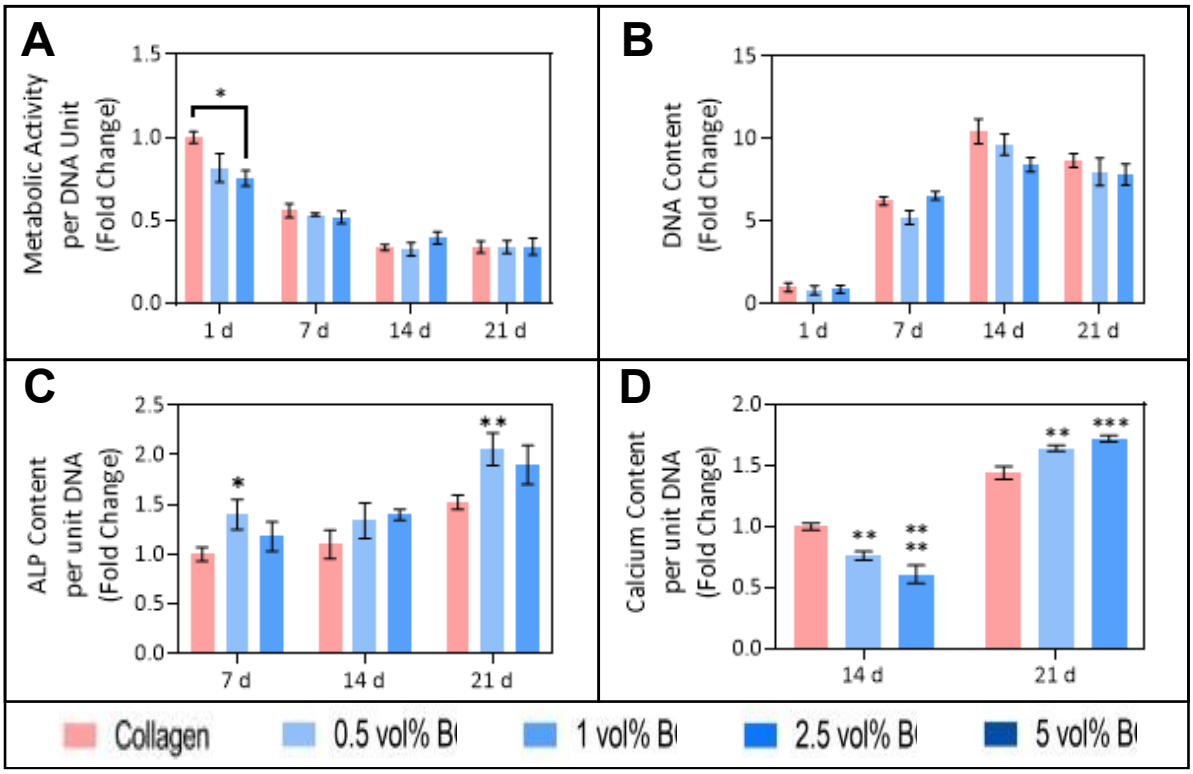

Fig. 4.7 – Assessment of osteogenic effect of BColl scaffolds with a bone cell line: A-B) *Metabolic Activity (A) and DNA content (B) of osteoblasts grown on BColl scaffolds for 21 days, showing high levels of biocompatibility.* ***C)*** *ALP release of osteoblasts on BColl scaffolds, trending towards increased release for BColl scaffolds.* ***D)*** *Calcium release of osteoblasts on BColl scaffolds, showing a significant increase indicative of increased bone mineralisation on BColl scaffolds. Significances: *$p < 0.05$, **$p < 0.01$, ***$p < 0.001$, ****$p < 0.0001$.*

There was a trend towards increased ALP release for the BColl scaffolds at each measured timepoint (Fig. 4.7C) and calcium deposition showed a significant increase at 21 days (Fig. 4.7D), indicative of improved bone mineralisation. This shows that boron supplementation leads to robust proliferation and enhanced osteogenic behaviour in osteoblasts.

While the MC3T3 osteoblast cell line is a good model for osteoblast mineralisation in general, they are not perfect models, with a differing gene expression profile, and variable degrees of mineralisation when compared with the primary osteoblasts they are intended to replicate[762]. For these reasons, we decided to assess the biocompatibility, osteogenic potential, and functional performance of the boron nanomaterial with a more physiologically relevant cell type. For this purpose, mesenchymal stem cells (MSCs) are highly therapeutically relevant, as they are readily differentiated to an osteoblastic lineage by media supplementation, and are used clinically in musculoskeletal applications[763,764]. By culturing MSCs on BColl scaffolds, we are thus able to more accurately model long-term clinical implantation. MSCs were grown on BColl scaffolds for 28 days followed by fluorescent staining and confocal imaging, showing that the cells had proliferated robustly across the BColl scaffolds, and maintained a healthy cellular morphology (**Fig. 4.8 A**). Biocompatibility was assessed by metabolic activity (**Fig. 4.8 B**) and DNA content (**Fig. 4.8 C**) analysis. No significant difference was observed between the boron-treated samples and the collagen-only controls, indicating that the BColl material is well-tolerated even by sensitive MSCs at high concentrations, up to 5 vol%, for extended periods of culture.

The osteogenic potential of these cells was then assessed, as before, by analysing ALP release and measuring calcium deposition. There was no significant difference observed in the ALP release for the BColl samples (**Fig. 4.8 D**) – however, ALP release has a short peak, typically around day 8 as the differentiating cells commit to the osteoblastic lineage[765], and thus it may have been missed by the timepoints analysed. This peak is reflected in the higher per cell expression of ALP for all conditions at days 1 and 7, compared to the later timepoints. As described above, the key indicator of osteogenic potential for any biomaterial is the quantity of calcium deposition. This was measured at days 21 and 28, when MSC-derived osteoblasts had matured sufficiently (**Fig. 4.8 E**). A significant, dose-dependent increase was seen in the calcium deposition for BColl samples when compared with collagen-only scaffolds. This indicates that boron is having a positive effect on the rate of mineralisation, and thus the osteogenic potential of the cells, pointing towards the potential of BColl scaffolds to accelerate bone formation after implantation.

Cross-sections of these scaffolds were stained, and infiltration analysis showed that cells in BColl scaffolds were colonising deeper into the scaffold (**Fig. 4.8 F**). Finally, SEM (**Fig. 4.8 G**) and EDX (**Fig. A3.6**) of these scaffolds showed increased calcium phosphate deposition for

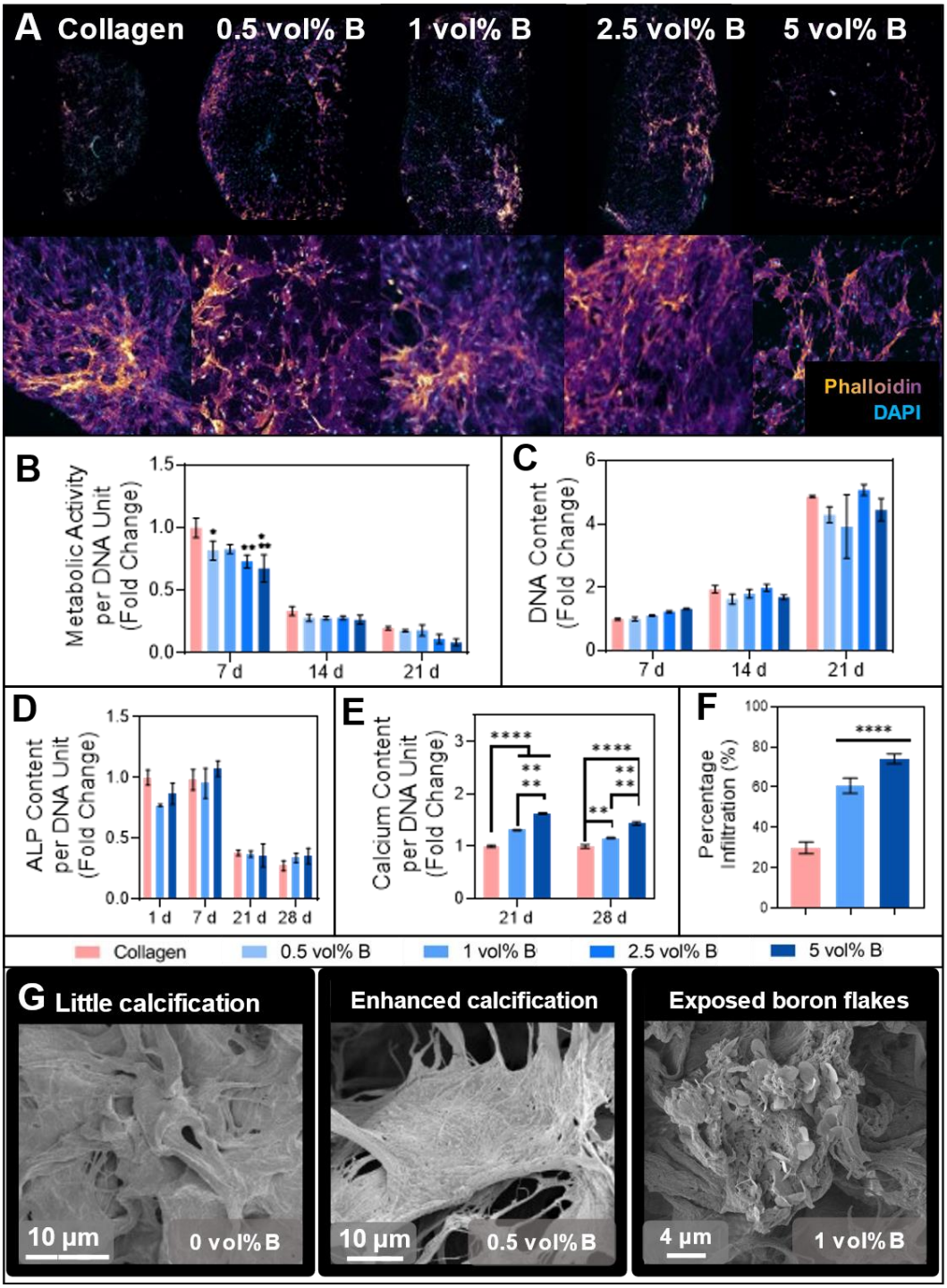

*Fig. 4.8 – **Assessment of osteogenic effect of BColl scaffolds with osteogenically-differentiated mesenchymal stem cells:** **A)** Confocal microscope images of lateral cross sections of BColl scaffolds with MSCs grown in them for 21 days, stained with phalloidin for the cell membrane, and DAPI for the cell nucleus, showing robust cellular proliferation and infiltration of the scaffolds. **B)** Metabolic activity of MSCs on BColl scaffolds and **C)** DNA content of MSCs on BColl scaffolds indicate high levels of biocompatibility. **D)** ALP release of MSCs on BColl scaffolds, showing significant fall-off in release after differentiation is complete. **E)** Calcium release of MSCs on BColl scaffolds, showing significant, dose-dependent increase in calcium deposition and thus bone mineralisation. **F)** Percentage infiltration of MSCs into boron scaffolds measured radially from the geometric centre of the scaffold, showing significant increase in infiltration for boron-containing scaffolds. **G)** SEM imaging showing increased calcification in BColl scaffolds, and exposed boron flakes in the collagen matrix. Significances: $*p < 0.05$, $**p < 0.01$, $***p < 0.001$, $****p < 0.0001$.*

boron containing scaffolds, and further SEM showed areas with exposed boron flakes on the higher loading samples (**Fig. 4.8 G**). While the increase in calcium deposition with boron scaffolds is lower compared to additives like osteoconductive hydroxyapatite[766,767] or expensive osteoinductive growth factors BMP-2[768,769], these scaffolds exhibit both osteoconductive and osteoinductive properties. Additionally, boron scaffolds offer a multifunctional profile, encompassing osteogenic, angiogenic, neurogenic, anti-microbial, mechanically reinforcing, and anti-inflammatory effects—that addresses key challenges in bone repair. Achieving such comprehensive functionality would otherwise require the use of multiple, potentially incompatible additives. Furthermore, although growth factors like BMP-2 provide strong osteoinductive effects, they are associated with several adverse outcomes at high concentrations and high cost when used clinically[770].

4.3.7 Neurogenic assessment of BColl scaffolds with dorsal root ganglia (*Aim 4*)

To assess the impact of boron loading on innervation, a key functional outcome in bone repair, the neurogenic effect of BColl was assessed. Dorsal root ganglia (DRGs) isolated from rats, a model of neuronal tissue that is both aged and injured, and thus particularly difficult to heal, were cultured on the surface of BColl scaffolds for 14 days. Staining and confocal imaging subsequently established that DRGs extended neurites effectively on BColl scaffolds and maintained healthy morphologies (**Fig. 4.9 A**). We next established that the scaffolds led to no cytotoxic or inflammatory effect, by measuring LDH (**Fig. 4.9 B**) and pro-inflammatory TNF-α release (**Fig. 4.9 C**), which showed no significant difference compared to the collagen control scaffolds.

The neurite outgrowth from the DRGs was extracted from these images, showing an increase in the maximum migration distance of DRG neurites on BColl scaffolds (**Fig. 4.9 D**). This was qualitatively confirmed by SEM imaging of the same scaffolds, showing significant neurite outgrowth on BColl scaffolds (**Fig. 4.9 E**). This data shows that boron contributes to a supportive environment for neurogenesis and innervation, a key process in bone regeneration[315,771,772], by employing a highly physiologically relevant tissue explant model.

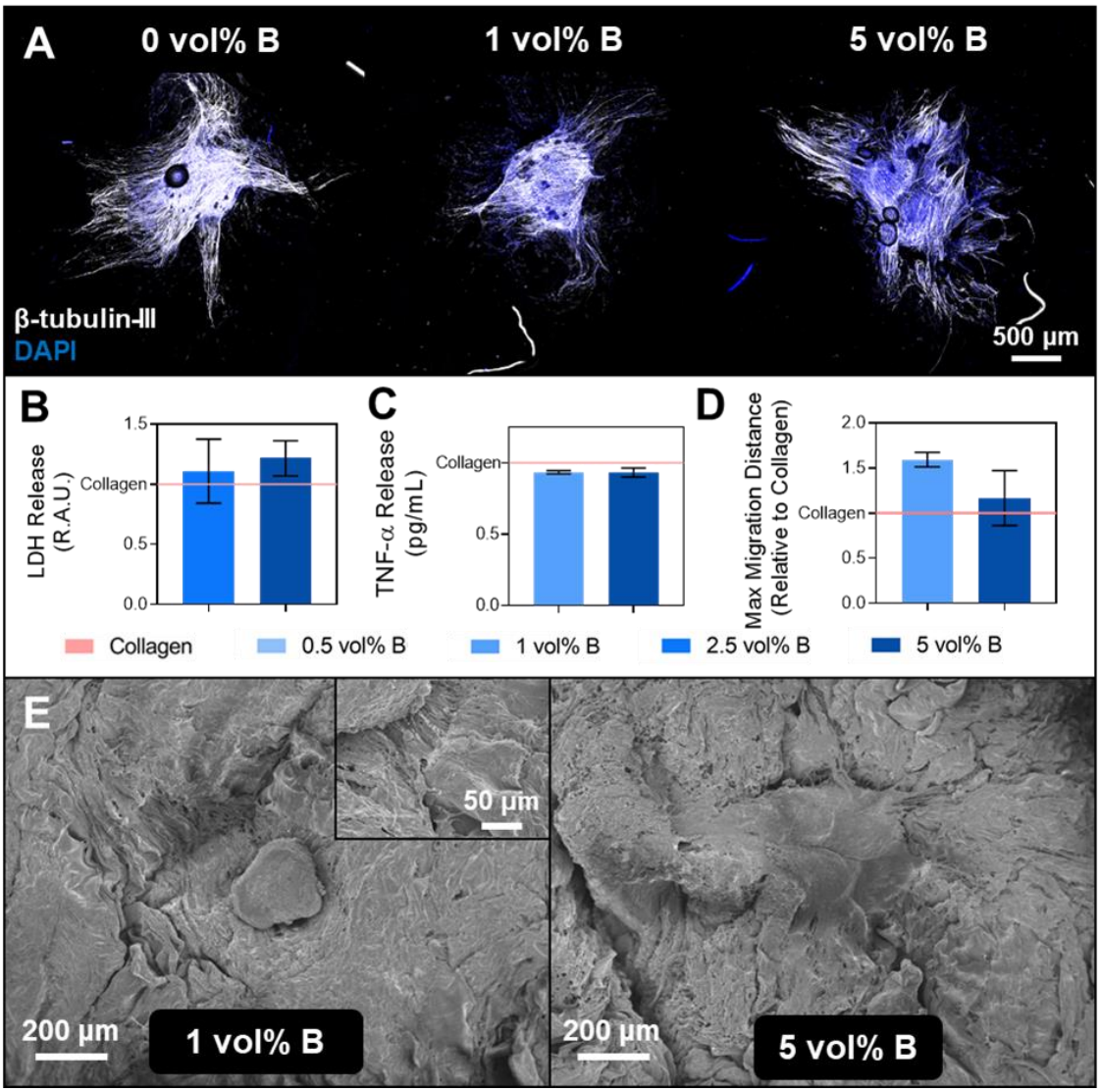

*Fig. 4.9 – **Assessment of neurogenic effect of BColl scaffolds on dorsal root ganglia (DRGs):** **A)** Representative confocal microscopy images of DRGs on surface of scaffolds, stained with β-III-tubulin as a marker of neuronal maturity and for cell morphology, and counter-stained with DAPI for nuclei. **B)** Lactate dehydrogenase (LDH) release was assessed, showing no significant cytotoxicity for BColl scaffolds with DRGs. **C)** Tumour Necrosis Factor alpha (TNF-α) release was assessed to examine the effect of BColl scaffolds on the inflammatory signalling response of DRGs, showing a slight trend towards decreased TNF-α release. **D)** Maximum migration distance of neurites from DRG centre showing a slight increase in migration for BColl scaffolds, measured from confocal images by using NeuriteTracer[773] and FIJI. **E)** SEM images of DRGs growing on BColl scaffolds, with significant neurite outgrowth visible on both samples.*

4.3.8 Angiogenic, immunomodulatory, and neurogenic effect of BColl scaffolds on MSCs (Aim 4)

The final aim of this study was to demonstrate the benefits of boron incorporation for the paracrine release profile of mesenchymal stem cells, a key cell type that modulates bone remodelling *via* cross-talk with other bone cells, and *via* their differentiation into osteoblasts[774]. Effects on the paracrine signalling of these cells can potentially have a downstream impact on the therapeutic efficacy of the scaffold, so a multiplex ELISA array was used to assess the cytokine

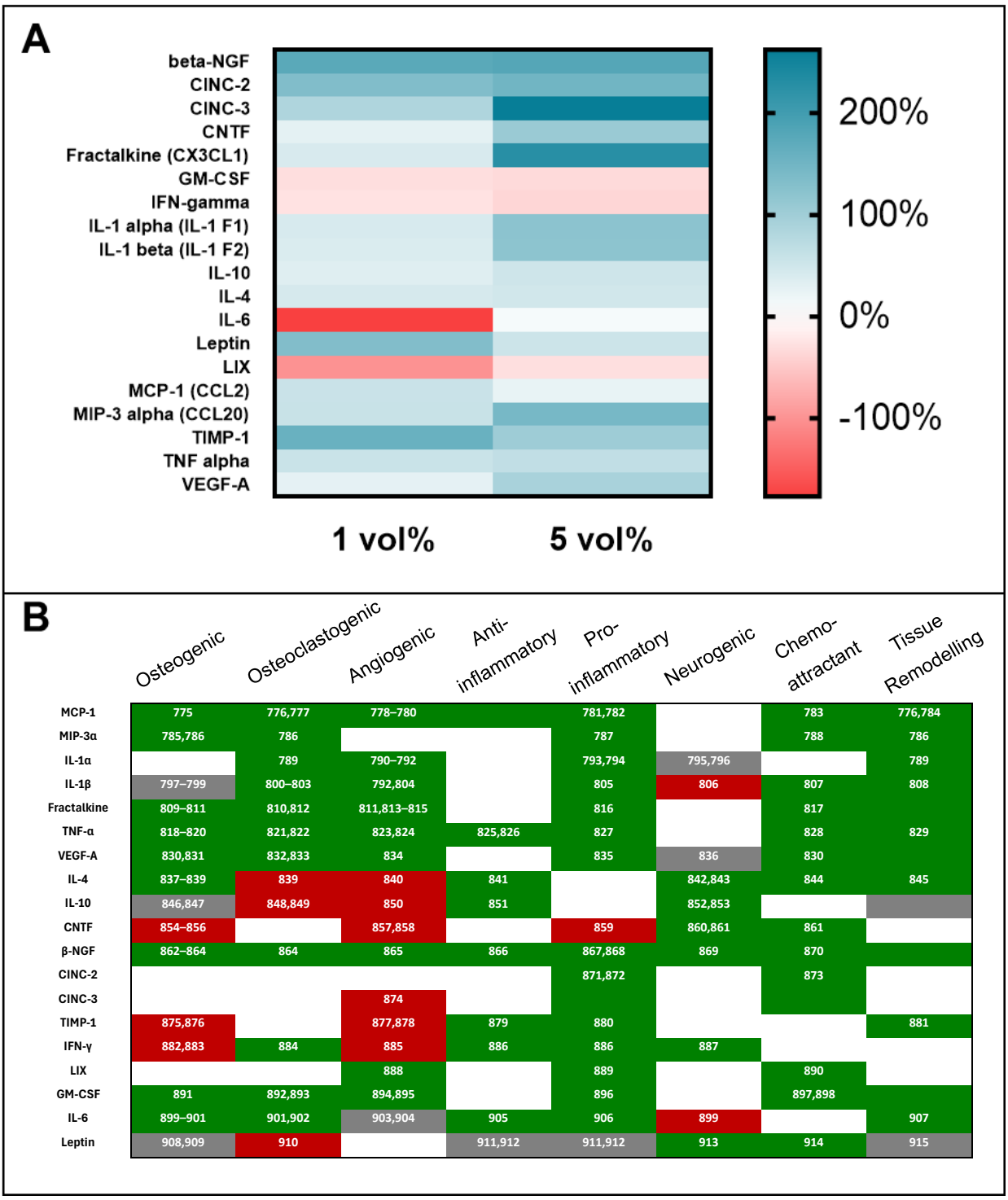

*Fig. 4.10 – **Investigation of paracrine release profile of rMSCs on BColl scaffolds: A)** Assessment of cytokine release profile of rat mesenchymal stem cells using a multiplex ELISA array. Heatmap indicating relative change to collagen-only control. **B)** Matrix detailing the primary effects of each cytokine assessed in the ELISA data. Green corresponds to literature evidence of an effect, grey to contradictory or highly environment-dependent effect, red corresponds to evidence of a negative effect and white corresponds to no evidence for an effect. Numbers are citations.*

release profile of mesenchymal stem cells on the BColl scaffolds at day 7 (Fig. 4.10 A). Of course, many of the cytokines assessed using this array have multiple potential effects, which were assessed by a literature review (Fig. 4.10 B). Firstly, several cytokines can be used to corroborate

the calcium deposition data, indicative of enhanced osteogenic signalling and a more favourable environment for osteoblastic differentiation. Several factors involved in both osteogenesis (monocyte chemoattractant protein-1 (MCP-1 (CCL2)), macrophage inflammatory protein-3 alpha (MIP-3α (CCL20))[786,916]) and osteoclastogenesis (interleukin-1α/β (IL-1α/β)[789,917], fractalkine (CX3CL1)[810,918] and tumor necrosis factor alpha (TNF-α)) were upregulated in BColl scaffolds. We posit that the apparent dose-dependent increase in these osteogenic and osteoclastogenic factors results in a more favourable scaffold environment for infiltrating MSCs, which in turn impacts the rate of osteoblastic differentiation, bone remodelling, and calcium deposition within the scaffold. It is well-established that an increase in osteoblast activity will often be associated with an increase in osteoclast activity, to maintain bone homeostasis[919].

Tissue inhibitor of metalloproteinase 1 (TIMP-1), a cytokine involved in tissue remodelling, is also upregulated in the BColl scaffolds, corroborating the shift towards a supportive environment for bone remodelling. A dose-dependent increase was observed in the expression of angiogenic factors such as vascular endothelial growth factor A (VEGF-A), fractalkine[920] and lipopolysaccharide-induced CXC chemokine (LIX)[888]. This is backed up by a strong trend for enhanced VEGF release from a human ELISA assay on the BColl samples (**Fig. A3.9**). This is a key finding, as vascularisation is an important target in bone regenerating biomaterials[921], and the induction of infiltrating MSCs to a pro-angiogenic phenotype renders the scaffold a more favourable environment for blood vessel formation.

Enhanced vascularisation is not the only non-bone related effect essential for bone repair however – innervation is required for healthy bone repair[419]. Both nerve growth factor-beta (β-NGF) and ciliary neurotrophic factor (CNTF) were upregulated in the BColl scaffolds, indicating an improvement of the neurogenic environment of the scaffold following boron addition, and corroborating the results found with dorsal root ganglia. This is consistent with the literature, where boron-containing compounds have been previously evaluated for their neuroprotective and neuroregenerative effects[315].

Finally, increased anti-inflammatory signalling of MSCs in BColl scaffolds was indicated by downregulation of key inflammatory cytokines interleukin-6 (IL-6), interferon gamma (IFN-γ) and granulocyte-macrophage colony-stimulating factor (GM-CSF), with associated upregulation of anti-inflammatory cytokines such as interleukin-4 (IL-4) and interleukin-10 (IL-10). This is a highly notable result, as nanomaterials often cause inflammatory responses in biological

systems[922]. This anti-inflammatory effect of boron has been observed in previous work[304,923–926], suggesting that boron-mediated immunomodulation may be countering any nanomaterial-induced inflammatory effect. It is worth addressing that many of the cytokines implicated in osteogenesis, osteoclastogenesis, and angiogenesis above are also associated with inflammatory and immune responses from macrophages and other cell types *in vivo*. However, taking the data as a whole, it is clear that boron incorporation in the scaffolds leads to healthy, proliferative cells with a pro-osteogenic paracrine signalling profile. This, coupled with the downregulation of key pro-inflammatory cytokines, makes it significantly more likely that the upregulation of these pleiotropic cytokines is associated with reparative processes.

4.4 Conclusions

This study demonstrates that boron nanoplatelets can be used as a versatile and powerful additive for enhancing the regenerative properties of biomaterial scaffolds for bone repair, thanks to their unique combination of intrinsic and 2D material-specific properties. High aspect ratio 2D boron nanoplatelets, stabilised with polyvinylpyrrolidone, were synthesised using an optimised liquid-phase exfoliation approach. Their biocompatibility was confirmed across a range of exposure conditions and cell types, demonstrating their safety for biomedical applications. Boron increased the osteogenic potential of both osteoblasts and osteogenically differentiated mesenchymal stem cells in long-term 3D scaffold culture. Boron-collagen (BColl) scaffolds also boosted angiogenic, neurogenic and anti-inflammatory cytokine signalling, key targets for regenerative therapies, in addition to increasing neurite migration of neuronal tissue explants on scaffolds. Additionally, the 2D morphology of the nanoplatelets yielded anti-microbial activity against E. coli, and significantly enhanced the tensile modulus, toughness, and strength of collagen. These findings highlight BColl as a versatile composite biomaterial, offering multifunctional benefits for key bone regeneration targets such as mineralisation, angiogenesis, and innervation, along with improved mechanical and antimicrobial properties. In summary, this study employs cutting-edge nanoscience and novel exfoliation techniques to develop biocompatible boron nanoplatelets and BColl composite scaffolds, which represent a promising new treatment for tackling bone repair in orthopaedic, reconstructive, and tissue engineering applications.

"The problem with the future is that it keeps turning into the present."

—

Calvin & Hobbes, Bill Watterson

Chapter 5 Discussion & Future Work

5.1 Overview

The diversity and versatility of 2D materials presents us with a wealth of opportunities for innovative research, but also begs the question – which fields stand to benefit the most from the 2D material revolution? Narrowing down from the broad spectrum of applications discussed in the introduction, we have focused on two main fields in this thesis, both involving the incorporation of 2D materials into biomedical devices and materials. Firstly, tissue engineering is explored in some detail, with **Chapter 2** primarily concerned with neuronal medical devices, and **Chapter 4** investigating bone tissue engineering. In both studies, 2D materials demonstrate their significant potential for enhancing regrowth of tissue following injury. The second field is that of neural interfacing devices, encompassing electrical stimulation of and recording from neurons. This is a primary area of research for **Chapters 2 & 3**, which show the promise of 2D materials and 2D material composites for neural interfacing.

In recent years, scientific interest in the biomedical applications of 2D materials has grown rapidly, although not without roadblocks. The challenge of achieving high-yield exfoliation of 2D materials initially slowed research into their applications – this problem has been addressed by advances in novel exfoliation techniques such as liquid phase exfoliation (LPE)[142]. Furthermore, rendering these materials, which often have innate cytotoxicity either as a result of their composition or dimensionality, sufficiently biocompatible has proved a challenge[198–200]. Much research has therefore been dedicated to the development of biocompatible stabilisers, polymer coatings, and green exfoliation techniques, with the goal of assuaging toxicity concerns[168,174,175,198].

While the upside for these materials is theoretically massive, turning that potential into translatable medical devices and therapies suitable for human patients is far from trivial, with a plethora of advances having been made in recent years to overcome difficulties in fabrication, stability, and performance of 2D nanomaterial-based devices and therapeutics[142,667,927]. Despite these difficulties, 2D nanomaterials are becoming increasingly well positioned for clinical translation, and the treatment modalities they enable and enhance are becoming increasingly

powerful[67,928]. This thesis leverages the revolutionary potential of these materials, and the unique properties they unlock, in biomedicine – specifically focusing on their role in tissue engineering and neural interfacing, enabling the development of highly promising multipotent treatments and devices.

5.2 Collagen/Pristine Graphene as an Electroconductive Interface Material for Neuronal Medical Devices

In **Chapter 2**, we aimed to develop a flexible, biocompatible, and electroconductive substrate for electrical stimulation. This was successfully achieved by optimizing the composition and fabrication of conductive & biocompatible collagen-graphene composites (NeuroGraph), which were subsequently used to deliver electrical stimulation to primary neurons. To further demonstrate the versatility and potential of NeuroGraph for neuronal medical device applications, we fabricated a range of conductive, neural-interfacing structures, including porous scaffolds, microneedle arrays, and 3D circuits for bioelectronics, demonstrating that NeuroGraph constitutes a versatile platform material for electroactive neural interfacing devices.

There has been much progress in fields amenable to the use of 2D materials, informing their future development, unlocking new possibilities, and presenting fresh challenges to overcome. To begin with, tissue engineering is a field that has rapidly matured and continues to progress, with recent innovations including gene therapies[364–366], biomimetic hydrogels[351] and complex multiphase scaffolds[381,929,930]. Each of these innovations has enabled more rapid, more robust, and more physiologically relevant tissue regeneration in important biological systems, from skin to bone. Progress has been made in recent years into the optimal pore size[348–350], matrix composition[346], architecture[357,358] and mechanical properties[351–353] for tissue engineering scaffolds – however, success in clinical translation has been modest, highlighting the need for additives and treatments to further enhance the regrowth induced and supported by these scaffolds. Treatment modalities such as electrical stimulation have shown significant promise in many tissues, as have specialised scaffolds designed to direct and harness electrical stimuli, thus improving their regenerative effect[101,170,377,398,504].

At the core of the challenge in this research is the trade-off between physicochemical properties, biocompatibility, and biodegradability. Materials that are optimal from an electrical or mechanical standpoint may not be (and are often not) the same materials that excel biologically. This is where the focus of this study lay, and where future work building on it will be directed. 2D nanomaterials offer the unique ability to simultaneously leverage the beneficial

physicochemical properties of the filler nanomaterial in a manner that is tunable by the filler loading, while largely maintaining the properties of the matrix, particularly at low loadings. This sets nanomaterial composites apart from metals, conductive polymers, and other bulk materials, which generally do not exhibit the same tunability in their properties. However, taking advantage of these biphasic materials is far from trivial. Composite formation, loading effects, and nanomaterial biocompatibility all play a role in complicating the optimization process.

NeuroGraph effectively navigates these challenges, leveraging the lower stiffness and higher biocompatibility of collagen alongside graphene's electroconductivity to yield soft, conductive (~ 1.5 S/m) composites with low modulus (< 20 MPa), which are otherwise challenging to achieve. Since cells are effectively interfacing with collagen, a well-established biopolymer, concerns around scarring and adverse immunological responses are minimised, as indicated by the proliferation and healthy cellular morphology of multiple neuronal and glial cell types on the surface of the material. This is especially the case when compared to traditional stiff electrode materials such as metals and highly-doped semiconductors, and even to conductive polymers, which as non-biologically native materials must be optimized and assessed independently for their biocompatibility[534,931,932]. NeuroGraph demonstrates the benefits of applying electrical stimulation and conductive materials simultaneously, with a synergistic effect on the neurite outgrowth of primary neurons grown on NeuroGraph substrates. Finally, NeuroGraph exhibits a versatility in processing that sets it apart from traditional materials, which often require complex fabrication techniques to produce devices such as scaffolds and bioelectronic circuits, which are readily achievable with NeuroGraph.

As always, it is worth noting that there are several key limitations of this study. Firstly, while the conductivity of NeuroGraph is similar to neural tissue[933], and sufficiently high to deliver electrical stimulation effectively[101], it is insufficient for low-impedance applications such as bidirectional neural interfaces[526]. The second, and related, limitation is the high graphene loading required to achieve conductivity, due in part to the presence of a thick gelatin layer on the graphene surface – this impacts the mechanical and surface properties of the composite. Work to address these limitations forms the basis of **Chapter 3** and will be discussed in the next section. Finally, more robust optimization of the electrical stimulation parameters across the wide parameter space of frequency, voltage, and duration[377] could further enhance the magnitude of the beneficial effects of electrical stimulation on conductive substrates.

In conclusion, in this study we outlined the development and characterisation of versatile type-I collagen/pristine graphene (NeuroGraph) nanocomposites, that strike the essential balance between physiologically relevant electrical conductivity and neurocompatibility. Combined with its processability into a range of conductive, neural-interfacing structures, including porous scaffolds, microneedle arrays, and 3D printed circuit elements for bioelectronics, this indicates the potential of the soft, conductive NeuroGraph material as a versatile candidate for future neuronal medical devices.

5.3 Biocompatible, Flexible and Electrically Optimised Polymer-Graphene (PolyGraph) Composites for Neural Interfacing Devices

Building on the learnings from **Chapter 2**, we aimed in **Chapter 3** to develop the next generation of biocompatible graphene, and to use it to manufacture graphene composite-based flexible microelectrode arrays for non-scarring bidirectional neural interfaces. This was achieved by developing and characterising the optimal graphene formulation based on biological and electrical parameters, and combining it with polycaprolactone (PCL) to form conductive, processable, and tunable graphene-polymer composites (PolyGraph). The electrochemical properties of PolyGraph were then enhanced using NaOH and AuPd treatment, bringing them into the ranges necessary for effective neural stimulation and recording. As the field of neural interfacing is moving towards higher-resolution electrodes with smaller addressable volumes, we next endeavoured to develop a flexible microneedle-based electrode array. Consisting of individually isolated electrodes and an ECM backing, this device demonstrated that cost-effective, simple fabrication protocols could be used to produce a flexible, biocompatible neural interfacing microelectrode array. Finally, to assess the functional capabilities of this array, an experimental setup for electrical stimulation of neurons was demonstrated in 3D using flat PolyGraph electrodes, and initial recording from a brain slice culture was carried out using sheathed PolyGraph microneedles in an electrophysiological setup. This work is ongoing, and forms the basis of the future work arising from this chapter.

With the global market for bioelectronics forecasted to reach $16-28 billion by 2030[441], positioning PolyGraph in this rapidly rising tide of progress is crucial. To do so, it is worth examining where neural interfacing devices have come from, and where scientists and the public see them heading in the future[441,568,934–937]. From their humble beginnings as low-resolution, non-invasive devices such as EEG, the draw of higher channel count and spatiotemporal resolution, and therefore increased informational quality and therapeutic potential, has driven these devices

to become smaller and more invasive[526,938]. This has, of course, brought its share of trade-offs, with increased invasiveness leading to higher stakes for electrode biocompatibility. To this end, research into electrically conductive materials that are not only flexible, but *soft*, has shown great promise in recent years[486,939–943]. If mechanically stiff and hard materials can be excised from a neural interfacing device entirely, the potential for scarring surrounding any part of the device is considerably lower, yielding more robust, scalable, and long-lived devices[351,450,474,486].

In this landscape, PolyGraph positions itself as a key step along the path to development of electrically, biologically, and mechanically performant nanomaterial composites, allowing advantage to be taken of the properties of both the chosen matrix and the nanomaterial filler. A survey of researchers from academia and industry at the Cambridge Bioelectronics Symposium found that the most important material properties currently lacking in bioelectronics materials are biocompatibility/degradability, flexibility, and stability[441] – PolyGraph makes strides to address each of these concerns, among others.

Firstly, the robust biocompatibility of both the graphene filler and the chosen matrix with multiple neuronal types and physiologically relevant glial cells, along with the increased macro- and micro-flexibility of the overall device, bode well for the long-term biocompatibility of this material *in vivo*. Its amenability to readily accessible and comparatively economical polymer processing techniques such as drop casting and 3D printing signifies its potential for devices ranging from flexible microelectrodes to soft deep brain stimulation electrodes – this robust processability differentiates it from current devices, which often require expensive lithographic processes.

The next key factor is stability – while many materials such as MXenes and polypyrrole are prone to oxidative degradation under physiological conditions, physicochemically inert graphene nanosheets are effectively as stable as the matrix they are combined with. This in turn highlights the importance of the tunability of nanomaterial composites, and the utility of adapting the composite composition based on the required mechanical, electrical and biological properties – this differentiates composite materials from single-phase materials such as metals and conductive polymers, which often require complex treatments and synthesis protocols to effectively tune their properties.

In summary, PolyGraph exhibits a combination of stability, biocompatibility and processability that would be very challenging to achieve with single-phase materials, positioning it as a key candidate for next-generation neural interfaces. The combination of these material properties

with the low-cost, adaptable microelectrode fabrication process employed in this chapter yields a prototype brain-computer interface electrode with both local softness due to the composite material, and device-wide flexibility and conformability due to the flexible backing layer, which shows initial promise for interfacing effectively with neurons as a bidirectional neural interfacing device.

While PolyGraph offers clearly differentiated benefits, there are also limitations worth highlighting, requiring further research. Firstly, the stimulation and recording capabilities of the PolyGraph electrodes have yet to be rigorously demonstrated, due to experimental complexities and delays. This will be addressed in future work, by assessing the capacity of the flat electrodes depicted in **Figure 3.12 A** to enhance neuronal growth in scaffolds, and by using PolyGraph microneedles to both stimulate and record from a murine brain slice *ex vivo* model, using the setup depicted in **Figure 3.12 F**. Next, PolyGraph's electrochemical properties, while firmly in the range required for neural interfacing devices[473,483,691,692,699–702], could be enhanced by further surface treatment optimization, as well as by drawing on insights from existing electrode materials such as platinum, iridium oxide, PEDOT:PSS and MXenes[464,550,691,692,944] to enhance key electrochemical parameters such as the impedance, charge injection capacity and cut-off frequency. This would enable smaller, lower noise, and higher resolution electrodes.

Regarding the mechanical properties of PolyGraph, they are appropriate for microelectrode arrays, which require sufficient stiffness to enable penetration of the target tissue[945] – however, the stiffness of the PCL matrix does not lend itself well to applications requiring ultra-high flexibility and tissue integration. For the same reason, PCL is not an optimal substrate for neuronal growth or stimulation, limiting the potential of this material for use as a stimulation substrate. Both of these issues could be addressed by investigating graphene incorporation in a wider range of matrices, using stiffer materials for tissue penetration, ultra-compliant materials such as hydrogels for minimally invasive implantation[946–948], or even stimuli-responsive polymers to switch between stiff and soft following implantation[949,950]. There are also potential approaches to further enhance the biocompatibility and decrease the foreign body response to PolyGraph – for example, protein coating or biohybridisation with iPSC-derived neurons could be considered[486,951]. Finally, as is the case for all novel biomaterials and implantable devices, extensive *in vivo* testing will be required to establish the behaviour of PolyGraph and its derivative devices under physiological conditions over clinically relevant timeframes, with specific reference to its scarring potential, resolution, and stability of electrical performance.

In conclusion, this study introduces PolyGraph, a multi-phase material combining electroconductive, bio-optimised graphene with a biocompatible polymer. PolyGraph was fabricated into a conductive, non-inflammatory, and flexible microneedle neural interface prototype with potential for both stimulation and recording – key outcomes for successful BCIs. This research has significant relevance to the BCI space – new, softer materials with versatile processing capabilities are in high demand for advanced devices[430–436,653,654]. Beyond BCIs, the unique properties of PolyGraph composites extend their potential to act as highly conductive, biocompatible materials across a diverse range of applications, such as tissue engineering, implantable electronics, and wearable devices.

5.4 Boron Nanoplatelets as an Osteogenic, Anti-Microbial and Mechanically Reinforcing Additive for Biomaterial Scaffolds for Bone Repair

For years, graphene has held a pronounced "first-mover" advantage in the field of 2D materials. Its dominance in the early years of the field was a matter of both necessity, as research into other materials was yet in its infancy, and convenience, as graphene is comparatively easy to produce, and has extraordinary properties – researchers did not find themselves bored by the prospects laid out before them. That being said, graphene cannot do everything, and with advancements in other 2D materials emerging constantly, neglecting to investigate the biomedical applications of at least one such competitor (or compatriot) in this thesis would mean failing to capture the breadth of the field.

To this end, the final objective of this thesis was to produce biocompatible polymer-stabilised boron nanosheets, and demonstrate their potential for applications in bone tissue engineering scaffolds as a multifunctional additive. This was successfully achieved by synthesizing boron nanosheets from a non-layered precursor using liquid phase exfoliation (LPE), followed by their physical and biological characterisation. Following this, 3D scaffolds consisting of boron mixed with collagen (BColl) were fabricated by lyophilisation to produce tailored scaffolds with architecture suitable for bone repair, and their osteogenic potential was assessed with physiologically relevant bone cells. Finally, showcasing of the diverse applications of 2D boron, we demonstrated the anti-microbial, angiogenic, neurogenic and anti-inflammatory effects of 2D boron. In general, this study serves as a reminder of the potential of 2D materials outside of those most commonly used, such as graphene and the transition metal dichalcogenides[67,952].

Tissue engineering in general, and bone tissue engineering specifically, are fields replete with countless additives, techniques, and treatments. In pursuit of the next big treatment, many

materials have been tested – some of which only offer marginal benefits to one singular aspect of tissue regeneration, and which do not possess much promise in the clinic. This study aimed to counter this trend not only by excelling in each functional outcome to a greater extent than the extant bone tissue engineering additives – the likes of hydroxyapatite and bone morphogenic protein-2 (BMP-2) are stiff competition[405,726,727] – but by improving functional outcomes across a wide range of targets, acting as a multipotent additive for bone regeneration. Evidence for this is found in the fact that boron addition provides benefits for osteogenesis and appears to accelerate bone remodelling, while also fostering a more supportive scaffold environment for blood vessel and nerve infiltration. This addresses all three tissues involved in bone regeneration[419,771,865], while demonstrating a reduction in inflammatory paracrine signalling and a shift towards a pro-reparative environment.

Importantly, the high surface area:volume ratio unique to 2D materials means that these effects can be achieved with a smaller amount of additive, simplifying synthesis protocols and reducing the challenge of graceful scaffold degradation. This high surface area:volume ratio could be exploited further, to enable highly efficient drug delivery or gene therapy in bone scaffolds[35,953]. Carrying on, boron further differentiates itself from existing additives by exhibiting the capacity to reduce microbial proliferation, addressing a key concern for traumatic orthopaedic injuries[719].

Finally, the mechanical properties of bone scaffolds are critical, as bone cells are highly mechanosensitive[747,748], rendering the increase in modulus for boron-containing collagen highly significant for regenerative outcomes. Interestingly, the latter two effects arise as a result of the 2D nature of boron nanosheets, rather than being intrinsic properties of boron itself. This draws attention once more to the many benefits of using 2D nanomaterials to achieve properties that would be inaccessible in the bulk.

Future work should bolster the evidence for the functional effects of boron that we have demonstrated, and provide insight into the mechanisms underlying them. For example, robust assessment of the mechanisms underlying angiogenesis and neurogenesis, and of the magnitude of any induced effect, is necessary to establish how boron compares with the literature as regards its functional behaviour. There are also still open questions surrounding the anti-microbial effect of the boron nanosheets – namely, how it may be enhanced by modifications to the morphologies of the nanosheets, and how it differs depending on the strain of bacteria being addressed[37,757–759]. Finally, further *in vitro* and *in vivo* studies should be carried out to examine the potential of these scaffolds in a highly clinically relevant model, such as a critically sized bone defect[403].

In conclusion, this study employs cutting-edge nanoscience and novel exfoliation techniques to demonstrate that biocompatible boron nanosheets can be used as a versatile and powerful additive for enhancing the regenerative properties of biomaterial scaffolds for bone repair, thanks to their unique combination of intrinsic and 2D material-specific properties. BColl offers multifunctional benefits for key bone regeneration targets such as mineralisation, angiogenesis, and innervation, along with improved mechanical and antimicrobial properties, and represents a promising addition to the arsenal of treatments at the disposal of bone tissue engineers for tackling bone repair in orthopaedic, reconstructive, and tissue engineering applications.

5.5 Conclusion

If this thesis demonstrates anything, it should be the concept of balance. Straddling nanomaterial physics and regenerative/augmentative medicine, this work has been shaped by the freedoms and constraints of these fields. Throughout each study, we have balanced biocompatibility with electrical performance, nanomaterial loading with composite properties, device design with processability, and more. The materials developed – NeuroGraph, PolyGraph and BColl – have been tuned for their respective applications: electrical stimulation for neural tissue regeneration, neural interfacing electrodes, and multipotent bone repair scaffolds, each demonstrating the capacity of nanomaterial composites to harness the unique properties of both constituent phases. Graphene was first applied to the challenge of neuronal medical device fabrication, with a focus on enhancing neural growth via electrical stimulation. Electrical stimulation on graphene substrates led to a significant enhancement in neurite outgrowth and cellular morphology, yielding a versatile platform material for electroconductive tissue regeneration. Building on this, our graphene formulation was then further refined for high biocompatibility and conductivity, leading to the development of flexible, biocompatible microelectrode neural interfaces, with enhanced electrical performance. These devices hold significant potential for application to both electrical stimulation therapies and bidirectional neural interfacing. Finally, demonstrating the breadth of possibilities in the field, boron nanosheets were shown to be an effective multifunctional additive for enhancing bone repair by tapping into the innate bioactivity of boron, the distinctive properties of 2D nanomaterials, and the well-established properties of collagen scaffolds.

While we have merely scratched the surface of the vast potential that 2D nanomaterials hold for biomedical applications, the applications investigated here represent a microcosm of the broader challenges and opportunities in the field. The versatility of materials like graphene, boron, and their composites presents a compelling vision for future devices and treatments, smoothing the trade-off between physicochemical and biological properties. Ultimately, refining the scalability and robustness of these composites, while tuning their properties for a wide range of applications, will bring them ever closer to clinical translation. As our appreciation for material behaviour at the nanoscale and the complex interplay between biology, nanomaterials and matrices deepens, these materials could reshape how we view regeneration and augmentation – unlocking a dimension that we could not previously perceive.

Turn

It's the immediate calm after a headwind that gets me
You turn, and suddenly you're free
Each step comes with such ease
You feel foolish for ever struggling

The only reminder, your memory's dregs
Is the dull ache fading in your legs
Your slowing heart rate
And a sense that you are tougher than before

You pass others as they grind along
At best you remember and cheer them on
At worst you forget
And judge them for their pace

Do not forget.
The unseen force, sand-blasted shins
The watering eyes, the fights within
The push for some vague, internal win

Do not forget.
That running back the way you came
You do not come back quite the same
That peace feels so different after pain

Don't forget your legs and lungs they burned
Don't forget each step, each inch you earned
Before the wind, your path, your luck
All turned

Bibliography

1. Abbott EA. *Flatland*. London: Penguin; 1884. 118 p. (Penguin classics).

2. Schaming D, Remita H. *Nanotechnology: from the ancient time to nowadays*. Found Chem. 2015 Oct;17(3):187–205.

3. Murr LE. *Nanoparticulate materials in antiquity: The good, the bad and the ugly*. Materials Characterization. 2009 Apr 1;60(4):261–70.

4. Novoselov KS, Geim AK, Morozov SV, Jiang D, Zhang Y, Dubonos SV, et al. *Electric field in atomically thin carbon films*. Science. 2004 Oct 22;306(5696):666–9.

5. Ouyang J, Feng C, Ji X, Li L, Gutti HK, Kim NY, et al. *2D Monoelemental Germanene Quantum Dots: Synthesis as Robust Photothermal Agents for Photonic Cancer Nanomedicine*. Angewandte Chemie - International Edition. 2019 Sep 16;58(38):13405–10.

6. Dávila ME, Le Lay G. *Silicene: Genesis, remarkable discoveries, and legacy*. Materials Today Advances. 2022 Dec 1;16:100312.

7. Tian R, Coleman JN, Kaur H, Roy A, McCrystall M, Horvath DV, et al. *Production of quasi-2D platelets of nonlayered iron pyrite (FeS_2) by liquid-phase exfoliation for high performance battery electrodes*. ACS Nano. 2020 Oct 27;14(10):13418–32.

8. Nishino H, Fujita T, Yamamoto A, Fujimori T, Fujino A, Ito SI, et al. *Formation Mechanism of Boron-Based Nanosheet through the Reaction of MgB_2 with Water*. Journal of Physical Chemistry C. 2017 May 18;121(19):10587–93.

9. Chen T, Kaur H, McCrystall M, Tian R, Roy A, Smith R, et al. *Liquid phase exfoliation of nonlayered non-van der Waals iron trifluoride (FeF_3) into 2D-platelets for high-capacity lithium storing cathodes*. FlatChem. 2022 May;33:100360.

10. *Why paper cuts hurt so much* [Internet]. [cited 2024 Apr 27]. Available from: https://www.bbc.com/future/article/20160902-why-paper-cuts-hurt-so-much

11. Wang ZQ, Lü TY, Wang HQ, Feng YP, Zheng JC. *Review of borophene and its potential applications*. Frontiers of Physics. 2019;14(3):23403.

12. Zhang F, She L, Jia C, He X, Li Q, Sun J, et al. *Few-layer and large flake size borophene: Preparation with solvothermal-assisted liquid phase exfoliation*. RSC Advances. 2020 Jul 4;10(46):27532–7.

13. Pandey SK, Das R, Mahadevan P. *Layer-Dependent Electronic Structure Changes in Transition Metal Dichalcogenides: The Microscopic Origin*. ACS Omega. 2020 Jun 30;5(25):15169–76.

14. Wei M, Lian J, Zhang Y, Wang C, Wang Y, Xu Z. *Layer-dependent optical and dielectric properties of centimeter-scale $PdSe_2$ films grown by chemical vapor deposition*. npj 2D Mater Appl. 2022 Jan 10;6(1):1–8.

15. Li XL, Han WP, Wu JB, Qiao XF, Zhang J, Tan PH. *Layer-Number Dependent Optical Properties of 2D Materials and Their Application for Thickness Determination*. Advanced Functional Materials. 2017;27(19):1604468.

16. Zhao ZY, Liu QL. *Study of the layer-dependent properties of MoS_2 nanosheets with different crystal structures by DFT calculations*. Catal Sci Technol. 2018 Apr 3;8(7):1867–79.

17. Das S, Robinson JA, Dubey M, Terrones H, Terrones M. *Beyond Graphene: Progress in Novel Two-Dimensional Materials and van der Waals Solids*. Annual Review of Materials Research. 2015;45(1):1–27.

18. Alam S, Asaduzzaman Chowdhury M, Shahid A, Alam R, Rahim A. *Synthesis of emerging two-dimensional (2D) materials – Advances, challenges and prospects*. FlatChem. 2021 Nov 1;30:100305.

19. Zhao M, Casiraghi C, Parvez K. *Electrochemical exfoliation of 2D materials beyond graphene*. Chem Soc Rev. 2024 Mar 18;53(6):3036–64.

20. Knobloch T, Illarionov YY, Ducry F, Schleich C, Wachter S, Müller T, et al. *On the suitability of hBN as an insulator for 2D material-based ultrascaled CMOS devices*. Nat Electron. 2021 Feb 23;4(2):98–108.

21. Kang S, Lee D, Kim J, Capasso A, Kang HS, Park JW, et al. *2D semiconducting materials for electronic and optoelectronic applications: potential and challenge*. 2D Mater. 2020 Feb 14;7(2):022003.

22. Wu F, Tian H, Shen Y, Zhu ZQ, Liu Y, Hirtz T, et al. *High Thermal Conductivity 2D Materials: From Theory and Engineering to Applications*. Advanced Materials Interfaces. 2022;9(21):2200409.

23. Zhang Q, Tao Y, Tang B, Yang J, Liang H, Wang B, et al. *Graphene Quantum Dots with Improved Fluorescence Activity via Machine Learning: Implications for Fluorescence Monitoring*. ACS Applied Nano Materials. 2022 Feb 25;5(2):2728–37.

24. Papageorgiou DG, Kinloch IA, Young RJ. *Mechanical properties of graphene and graphene-based nanocomposites*. Progress in Materials Science. 2017;90:75–127.

25. Coronado E, Dugay ; J. *2D magnetic materials based on molecular/2D hetero structures*. Nature Rev Mater. 2020;5(2):186.

26. He W, Kong L, Zhao W, Yu P. *Atomically Thin 2D van der Waals Magnetic Materials: Fabrications, Structure, Magnetic Properties and Applications*. Coatings 2022, Vol 12, Page 122. 2022 Jan 21;12(2):122.

27. Zeng S, Tang Z, Liu C, Zhou P. *Electronics based on two-dimensional materials: Status and outlook*. Nano Research 2020 14:6. 2020 Jul 13;14(6):1752–67.

28. Tang H, Neupane B, Neupane S, Ruan S, Nepal NK, Ruzsinszky A. *Tunable band gaps and optical absorption properties of bent MoS_2 nanoribbons*. Sci Rep. 2022 Feb 22;12(1):3008.

29. Ma Q, Ren G, Xu K, Ou JZ. *Tunable Optical Properties of 2D Materials and Their Applications*. Advanced Optical Materials. 2021;9(2):2001313.

30. Zhang H. *Introduction: 2D Materials Chemistry*. Chem Rev. 2018 Jul 11;118(13):6089–90.

31. An D, Fu J, Zhang B, Xie N, Nie G, Ågren H, et al. *NIR-II Responsive Inorganic 2D Nanomaterials for Cancer Photothermal Therapy: Recent Advances and Future Challenges*. Advanced Functional Materials. 2021 Jun 10;2101625.

32. Saito Y, Nojima T, Iwasa Y. *Highly crystalline 2D superconductors*. Nat Rev Mater. 2016 Dec 20;2(1):16094.

33. Shanmugam V, Mensah RA, Babu K, Gawusu S, Chanda A, Tu Y, et al. *A Review of the Synthesis, Properties, and Applications of 2D Materials*. Part & Part Syst Charact. 2022 Jun;39(6):2200031.

34. Ronchi RM, Arantes JT, Santos SF. *Synthesis, structure, properties and applications of MXenes: Current status and perspectives*. Ceramics International. 2019 Oct 15;45(15):18167–88.

35. Ouyang J, Rao S, Liu R, Wang L, Chen W, Tao W, et al. *2D materials-based nanomedicine: From discovery to applications*. Advanced Drug Delivery Reviews. 2022 Jun 1;185:114268.

36. Forouzandeh P, Pillai SC. *Two-dimensional (2D) electrode materials for supercapacitors*. Materials Today: Proceedings. 2021 Jan 1;41:498–505.

37. Hou D, Zhou S, Tan X, Yuan D, Yan J, Zeng Q, et al. *2D Materials Kill Bacteria from Within*. Nano Lett, May 24. https://doi.org/10.1021/acs.nanolett.4c00803

38. He J, Zhu X, Qi Z, Wang C, Mao X, Zhu C, et al. *Killing dental pathogens using antibacterial graphene oxide*. ACS Appl Mater Interfaces. 2015 Mar 11;7(9):5605–11.

39. Fu W, John M, Maddumapatabandi TD, Bussolotti F, Yau YS, Lin M, et al. *Toward Edge Engineering of Two-Dimensional Layered Transition-Metal Dichalcogenides by Chemical Vapor Deposition*. ACS Nano. 2023 Sep 12;17(17):16348–68.

40. Wang H, An D, Wang M, Sun L, Li Y, Li H, et al. *Crystalline borophene quantum dots and their derivative boron nanospheres*. Materials Advances, 2021; http://pubs.rsc.org/en/Content/ArticleLanding/2021/MA/D1MA00124H

41. Hadad C, González-Domínguez JM, Armelloni S, Mattinzoli D, Ikehata M, Istif A, et al. *Graphene quantum dots: From efficient preparation to safe renal excretion*. Nano Research. 2021 Mar 1;14(3):674–83.

42. Stanford MG, Rack PD, Jariwala D. *Emerging nanofabrication and quantum confinement techniques for 2D materials beyond graphene*. npj 2D Mater Appl. 2018 Jul 16;2(1):1–15.

43. Kim SJ, Choi K, Lee B, Kim Y, Hong BH. *Materials for Flexible, Stretchable Electronics: Graphene and 2D Materials*. Annual Review of Materials Research. 2015 Jul 1;45:63–84.

44. Moses OA, Gao L, Zhao H, Wang Z, Lawan Adam M, Sun Z, et al. *2D materials inks toward smart flexible electronics*. Materials Today. 2021 Oct 20.

45. Fiori G, Bonaccorso F, Iannaccone G, Palacios T, Neumaier D, Seabaugh A, et al. *Electronics based on two-dimensional materials*. Nature Nanotech. 2014 Oct;9(10):768–79.

46. Hu L, Kim BJ, Ji S, Hong J, Katiyar AK, Ahn JH. *Smart electronics based on 2D materials for wireless healthcare monitoring*. Applied Physics Reviews. 2022 Nov 14;9(4):041308.

47. Kaur H, Konkena B, Gabbett C, Smith R, McCrystall M, Tian R, et al. *Amorphous 2D-Nanoplatelets of Red Phosphorus Obtained by Liquid-Phase Exfoliation Yield High Areal Capacity Na-Ion Battery Anodes*. Advanced Energy Materials. 2022 Dec 23;2203013.

48. Mogulkoc Y, Mogulkoc A, Guler HE, Durgun E. *Design of nanoscale capacitors based on metallic borophene and insulating boron nitride layers*. Physical Review Materials. 2021 Dec 13;5(12):124002.

49. Boland JB, Harvey A, Tian R, Hanlon D, Vega-Mayoral V, Szydlowska B, et al. *Liquid phase exfoliation of MoO_2 nanosheets for lithium ion battery applications*. Nanoscale Advances. 2019 Apr 9;1(4):1560–70.

50. Wang S, Zhao S, Guo X, Wang G, Wang S, Guo X, et al. *2D Material-Based Heterostructures for Rechargeable Batteries*. Advanced Energy Materials. 2021;2100864.

51. Rojaee R, Shahbazian-Yassar R. *Two-Dimensional Materials to Address the Lithium Battery Challenges*. ACS Nano. 2020 Mar 24;14(3):2628–58.

52. Tian R, Alcala N, O'Neill SJK, Horvath DV, Coelho J, Griffin AJ, et al. *Quantifying the Effect of Electronic Conductivity on the Rate Performance of Nanocomposite Battery Electrodes*. ACS Applied Energy Materials. 2020 Mar 23;3(3):2966–74.

53. Yu J, Zhou M, Yang M, Zhang Y, Xu B, Li X, et al. *Pristine and Defective 2D Borophene/Graphene Heterostructure as the Potential Anode of Lithium-Ion Batteries*. Advanced Materials Interfaces. 2022 Feb 25;2102088.

54. Kolosov DA, Glukhova OE. *High-Capacity Ion Batteries Based on Ti_2C MXene and Borophene First Principles Calculations*. Inorganics 2023, Vol 11, Page 95. 2023 Feb 27;11(3):95.

55. Liu L, Zhou M, Li X, Jin L, Su G, Mo Y, et al. *Research Progress in Application of 2D Materials in Liquid-Phase Lubrication System*. Materials, 2018 Jul 30;11(8). Available from: /pmc/articles/PMC6117646/

56. Huang S, Mutyala KC, Sumant AV, Mochalin VN. *Achieving superlubricity with 2D transition metal carbides (MXenes) and MXene/graphene coatings*. Materials Today Advances. 2021 Mar 1;9:100133.

57. Liu L, Zhou M, Jin L, Li L, Mo Y, Su G, et al. *Recent advances in friction and lubrication of graphene and other 2D materials: Mechanisms and applications*. Friction 2019 7:3. 2019 Mar 26;7(3):199–216.

58. Khan K, Tareen AK, Aslam M, Zhang Y, Wang R, Ouyang Z, et al. *Recent advances in two-dimensional materials and their nanocomposites in sustainable energy conversion applications*. Nanoscale. 2019 Nov 21;11(45):21622–78.

59. Gnanasekar P, Kulandaivel J. *Two-Dimensional Materials for Renewable Energy Devices*. digital Encyclopedia of Applied Physics. 2021 Jun 28;1–39.

60. Zafeiratos S. *2D nanomaterials for energy applications: Graphene and beyond*. 2D Nanomaterials for Energy Applications: Graphene and Beyond. 2019 Jan 1;1–337.

61. Deng D, Novoselov KS, Fu Q, Zheng N, Tian Z, Bao X. *Catalysis with two-dimensional materials and their heterostructures*. Nature Nanotech. 2016 Mar;11(3):218–30.

62. Chimene D, Alge DL, Gaharwar AK. *Two-Dimensional Nanomaterials for Biomedical Applications: Emerging Trends and Future Prospects*. Advanced Materials. 2015;27(45):7261–84.

63. Pradeep AV, Satya Prasad SV, Suryam LV, Prasanna Kumari P. *A review on 2D materials for bio-applications*. Materials Today: Proceedings. 2019;19:380–3.

64. Bolotsky A, Butler D, Dong C, Gerace K, Glavin NR, Muratore C, et al. *Two-Dimensional Materials in Biosensing and Healthcare: From in Vitro Diagnostics to Optogenetics and beyond*. ACS Nano. 2019;13(9):9781–810.

65. Cheng L, Wang X, Gong F, Liu T, Liu Z. *2D Nanomaterials for Cancer Theranostic Applications*. Advanced Materials. 2020;32(13):1–23.

66. Wen W, Song Y, Yan X, Zhu C, Du D, Wang S, et al. *Recent advances in emerging 2D nanomaterials for biosensing and bioimaging applications*. Materials Today. 2018 Mar 1;21(2):164–77.

67. Kurapati R, Kostarelos K, Prato M, Bianco A. *Biomedical Uses for 2D Materials Beyond Graphene: Current Advances and Challenges Ahead*. Advanced Materials. 2016 Aug 3;28(29):6052–74.

68. Kumar P, Li Z, Wong SL. *Functionalized Transition Metal Dichalcogenide-Based Nanomaterials for Biomedical Applications*. Biomedical Applications of Functionalized Nanomaterials: Concepts, Development and Clinical Translation. Elsevier Inc.; 2018. 289–314 p. https://doi.org/10.1016/B978-0-323-50878-0.00010-0

69. Ménard-Moyon C, Bianco A, Kalantar-Zadeh K. *Two-Dimensional Material-Based Biosensors for Virus Detection*. ACS Sensors. 2020 Nov 23;5(12):3739–69.

70. Catania F, Marras E, Giorcelli M, Jagdale P, Lavagna L, Tagliaferro A, et al. *A review on recent advancements of graphene and graphene-related materials in biological applications*. Applied Sciences (Switzerland). 2021;11(2):1–21.

71. Jeong WY, Kang MS, Lee H, Lee JH, Kim J, Han DW, et al. *Recent Trends in Photoacoustic Imaging Techniques for 2D Nanomaterial-Based Phototherapy*. Biomedicines. 2021;9(1):80.

72. Zheng Y, Hong X, Wang J, Feng L, Fan T, Guo R, et al. *2D Nanomaterials for Tissue Engineering and Regenerative Nanomedicines: Recent Advances and Future Challenges*. Advanced Healthcare Materials. 2021 Jan 29;2001743.

73. Sreenilayam SP, Ul Ahad I, Nicolosi V, Brabazon D. *Mxene materials based printed flexible devices for healthcare, biomedical and energy storage applications*. Materials Today. 2021 Feb 5; https://linkinghub.elsevier.com/retrieve/pii/S136970212030376X

74. Huang J, Li Z, Mao Y, Li Z. *Progress and biomedical applications of MXenes*. Nano Select. 2021 Feb 20;nano.202000309.

75. Meng Q, Tian R, Long H, Wu X, Lai J, Zharkova O, et al. *Capturing Cytokines with Advanced Materials: A Potential Strategy to Tackle COVID-19 Cytokine Storm.* Advanced materials (Deerfield Beach, Fla). 2021 Apr 10;e2100012.

76. Zhang J, Liu D, Zhou G, Shen S. *Application of nanomaterials in tissue engineering*. Progress in Chemistry. 2010 Nov 26;22(11):2232–7.

77. Martín C, Kostarelos K, Prato M, Bianco A. *Biocompatibility and biodegradability of 2D materials: Graphene and beyond*. Chemical Communications. 2019 May 9;55(39):5540–6.

78. Jayakumar A, Mathew S, Radoor S, Kim JT, Rhim JW, Siengchin S. *Recent advances in two-dimensional nanomaterials: properties, antimicrobial, and drug delivery application of nanocomposites*. Materials Today Chemistry. 2023 Jun 1;30:101492.

79. Singhwane A, Chaturvedi K, Mohapatra RK, Srivastava AK, Verma S. *Mxene-Based Composite Materials as Antibacterial Agents for Healthcare Applications*. In: Mahapatra DM, Singh L, editors. ACS Symposium Series. Washington, DC: American Chemical Society; 2023. p. 1–17. https://pubs.acs.org/doi/abs/10.1021/bk-2023-1443.ch001

80. Valentini F, Calcaterra A, Ruggiero V, Pichichero E, Martino A, Iosi F, et al. *Functionalized Graphene Derivatives: Antibacterial Properties and Cytotoxicity*. Journal of Nanomaterials. 2019.

81. Zhao J, Huang S, Ravisankar P, Zhu H. *Two-Dimensional Nanomaterials for Photoinduced Antibacterial Applications*. ACS Applied Bio Materials. 2020 Nov 23;3(12):8188–210.

82. Pourmadadi M, Rahmani E, Eshaghi MM, Shamsabadipour A, Ghotekar S, Rahdar A, et al. *Graphitic carbon nitride (g-C_3N_4) as a new carrier for drug delivery applications: A review*. Journal of Drug Delivery Science and Technology. 2022 Nov 28;104001.

83. Kazemi N, Bakhshandeh B, Dehghani Z, Naghizadeh MM. *Nanobiomaterials in drug delivery: from science to applications*. Polym Bull. 2023 Oct 6; https://link.springer.com/10.1007/s00289-023-05006-x

84. Liu M, Fernandes DCC, Saleeba ZSSL, Hurt RH. *Controlled Release of Molecular Intercalants from Two-Dimensional Nanosheet Films*. ACS Nano. 2021 Dec 6;11:acsnano.1c07888.

85. Tabish TA, Narayan RJ. *Crossing the blood–brain barrier with graphene nanostructures*. Materials Today. 2021 Sep; https://linkinghub.elsevier.com/retrieve/pii/S1369702121002996

86. Niu Y, Li J, Gao J, Ouyang X, Cai L, Xu Q. *Two-dimensional quantum dots for biological applications*. Nano Research 2021. 2021 Sep 4;1–20.

87. Costard LS, Kelly DC, Power RN, Hobbs C, Jaskaniec S, Nicolosi V, et al. *Layered double hydroxide as a potent non-viral vector for nucleic acid delivery using gene-activated scaffolds for tissue regeneration applications*. Pharmaceutics. 2020 Dec 16;12(12):1–24.

88. Davis R, Urbanowski RA, Gaharwar AK. *2D Layered Nanomaterials for Therapeutics Delivery*. Current Opinion in Biomedical Engineering. 2021 Jul 2;100319.

89. An J, Gou Y, Yang C, Hu F, Wang C. *Synthesis of a biocompatible gelatin functionalized graphene nanosheets and its application for drug delivery*. Materials Science and Engineering C. 2013 Jul 1;33(5):2827–37.

90. Zhang S, Liu C, Zhang G, Chen Y, Shang F, Xia Q, et al. *Full review: The progress and developing trends of nanosheet-based sensing applications*. Coordination Chemistry Reviews. 2021 Apr 15;433:213742.

91. Garg M, Gupta A, Sharma AL, Singh S. *Advancements in 2D Materials Based Biosensors for Oxidative Stress Biomarkers*. ACS Applied Bio Materials. 2021 Aug 3;acsabm.1c00625.

92. Yildiz G, Bolton-Warberg M, Awaja F. *Graphene and graphene oxide for bio-sensing: general properties and the effects of graphene ripples*. Acta Biomaterialia. 2021 Jul 5; https://linkinghub.elsevier.com/retrieve/pii/S1742706121004293

93. Song Y, Wang M, Akkineni S, Yang W, Hettige JJ, Jin H, et al. *Highly Bright and Photostable Two-Dimensional Nanomaterials Assembled from Sequence-Defined Peptoids*. ACS Materials Letters. 2021 Mar 22;46:420–7.

94. Gazzi A, Fusco L, Khan A, Bedognetti D, Zavan B, Vitale F, et al. *Photodynamic therapy based on graphene and MXene in cancer theranostics*. Frontiers in Bioengineering and Biotechnology. 2019 Oct 25;7:295.

95. Sajjadi M, Nasrollahzadeh M, Jaleh B, Jamalipour Soufi G, Iravani S. *Carbon-based nanomaterials for targeted cancer nanotherapy: recent trends and future prospects*. Journal of Drug Targeting. 2021 Feb 10;1–78.

96. Papageorgiou DG, Li Z, Liu M, Kinloch IA, Young RJ. *Mechanisms of mechanical reinforcement by graphene and carbon nanotubes in polymer nanocomposites*. Nanoscale. 2020;12(4):2228–67.

97. May P, Khan U, O'Neill A, Coleman JN. *Approaching the theoretical limit for reinforcing polymers with graphene*. Journal of Materials Chemistry. 2012 Jan 28;22(4):1278–82.

98. Castro Neto AH, Guinea F, Peres NMR, Novoselov KS, Geim AK. *The electronic properties of graphene*. Rev Mod Phys. 2009 Jan 14;81(1):109–62.

99. Krukiewicz K, Britton J, Więcławska D, Skorupa M, Fernandez J, Sarasua JR, et al. *Electrical percolation in extrinsically conducting, poly(ε-decalactone) composite neural interface materials*. Scientific Reports. 2021 Dec 14;11(1):1295.

100. Marsden AJ, Papageorgiou DG, Vallés C, Liscio A, Palermo V, Bissett MA, et al. *Electrical percolation in graphene-polymer composites*. 2D Materials. 2018 Jun 1;5(3):032003.

101. Maughan J, Gouveia PJ, Gonzalez JG, Leahy LM, Woods I, O'Connor C, et al. *Collagen/pristine graphene as an electroconductive interface material for neuronal medical device applications*. Applied Materials Today. 2022 Dec 1;29:101629.

102. Kireev D, Kutagulla S, Hong J, Wilson MN, Ramezani M, Kuzum D, et al. *Atomically thin bioelectronics*. Nat Rev Mater. 2024 Oct 31;1–17.

103. Palmieri V, Palmieri V, Spirito MD, Spirito MD, Papi M, Papi M. *Graphene-based scaffolds for tissue engineering and photothermal therapy*. Nanomedicine. 2020 Jun 1;15(14):1411–7.

104. Dias D, Vale AC, Cunha EPF, C. Paiva M, Reis RL, Vaquette C, et al. *3D-printed cryomilled poly(ε-caprolactone)/graphene composite scaffolds for bone tissue regeneration*. Journal of Biomedical Materials Research - Part B Applied Biomaterials. 2020 Nov 25;jbm.b.34761.

105. Xavier Mendes A, Moraes Silva S, O'Connell CD, Duchi S, Quigley AF, Kapsa RMI, et al. *Enhanced Electroactivity, Mechanical Properties, and Printability through the Addition of Graphene Oxide to Photo-Cross-linkable Gelatin Methacryloyl Hydrogel*. ACS Biomaterials Science & Engineering. 2021 May 6;acsbiomaterials.0c01734.

106. Domínguez-Bajo A, González-Mayorga A, López-Dolado E, Serrano MC. *Graphene-Derived Materials Interfacing the Spinal Cord: Outstanding in Vitro and in Vivo Findings*. Frontiers in Systems Neuroscience. 2017 Sep 27;11. Available from: /pmc/articles/PMC5649236/?report=abstract

107. Geim AK. *Graphene: Status and Prospects*. Science. 2009 Jun 19;324(5934):1530–4.

108. Georgakilas V, Otyepka M, Bourlinos AB, Chandra V, Kim N, Kemp KC, et al. *Functionalization of Graphene: Covalent and Non-Covalent Approaches, Derivatives and Applications*. Chem Rev. 2012 Nov 14;112(11):6156–214.

109. Mbayachi VB, Ndayiragije E, Sammani T, Taj S, Mbuta ER, khan A ullah. *Graphene synthesis, characterization and its applications: A review*. Results in Chemistry. 2021 Jan 1;3:100163.

110. Pop E, Varshney V, Roy AK. *Thermal properties of graphene: Fundamentals and applications*. MRS Bull. 2012 Dec;37(12):1273–81.

111. Mohan VB, Brown R, Jayaraman K, Bhattacharyya D. *Characterisation of reduced graphene oxide: Effects of reduction variables on electrical conductivity*. Materials Science and Engineering: B. 2015 Mar 1;193(C):49–60.

112. Wang Y, Chen Y, Lacey SD, Xu L, Xie H, Li T, et al. *Reduced graphene oxide film with record-high conductivity and mobility*. Materials Today. 2018 Mar 1;21(2):186–92.

113. Lee JU, Yoon D, Cheong H. *Estimation of Young's modulus of graphene by Raman spectroscopy*. Nano Lett. 2012 Sep 12;12(9):4444–8.

114. E. Housecroft C, G. Sharpe A. *Inorganic Chemistry* [Internet]. Pearson; 2018. Available from: https://chem.libretexts.org/Bookshelves/Inorganic_Chemistry/Map%3A_Inorganic_Chemistry_(Housecroft)/13%3A_The_Group_13_Elements/13.04%3A_The_Elements/13.4B%3A_Structures_of_the_Elements

115. Woods WG. *An introduction to boron: history, sources, uses, and chemistry*. Environ Health Perspect. 1994 Nov;102 Suppl 7(Suppl 7):5–11.

116. Kharita MH, Yousef S, AlNassar M. *Review on the addition of boron compounds to radiation shielding concrete*. Progress in Nuclear Energy. 2011 Mar 1;53(2):207–11.

117. Widom M, Mihalkovič M. *Symmetry-broken crystal structure of elemental boron at low temperature*. Phys Rev B. 2008 Feb 25;77(6):064113.

118. Kumar P, Singh G, Bahadur R, Li Z, Zhang X, Sathish CI, et al. *The rise of borophene*. Progress in Materials Science. 2024 Dec 1;146:101331.

119. Xie SY, Wang Y, Li XB. *Flat Boron: A New Cousin of Graphene*. Advanced Materials. 2019 Sep 17;31(36):1900392.

120. Kaneti YV, Benu DP, Xu X, Yuliarto B, Yamauchi Y, Golberg D. *Borophene: Two-dimensional Boron Monolayer: Synthesis, Properties, and Potential Applications*. Chemical Reviews. 2021 Nov 3;acs.chemrev.1c00233.

121. Mannix AJ, Zhou XF, Kiraly B, Wood JD, Alducin D, Myers BD, et al. *Synthesis of borophenes: Anisotropic, two-dimensional boron polymorphs*. Science. 2015 Dec 18;350(6267):1513–6.

122. Feng B, Zhang J, Zhong Q, Li W, Li S, Li H, et al. *Experimental realization of two-dimensional boron sheets*. Nature Chemistry. 2016 Jun 1;8(6):563–8.

123. Kiraly B, Liu X, Wang L, Zhang Z, Mannix AJ, Fisher BL, et al. *Borophene Synthesis on Au(111)*. ACS Nano. 2019 Apr 23;13(4):3816–22.

124. Wu R, Drozdov IK, Eltinge S, Zahl P, Ismail-Beigi S, Božović I, et al. *Large-area single-crystal sheets of borophene on Cu(111) surfaces*. Nature Nanotech. 2019 Jan;14(1):44–9.

125. Wu R, Gozar A, Božović I. *Large-area borophene sheets on sacrificial Cu(111) films promoted by recrystallization from subsurface boron*. npj Quantum Mater. 2019 Aug 2;4(1):1–6.

126. Ranjan P, Sahu TK, Bhushan R, Yamijala SSRKC, Late DJ, Kumar P, et al. *Freestanding Borophene and Its Hybrids*. Advanced Materials. 2019 Jul 5;31(27):1900353.

127. Lin H, Shi H, Wang Z, Mu Y, Li S, Zhao J, et al. *Scalable Production of Freestanding Few-Layer β_{12}-Borophene Single Crystalline Sheets as Efficient Electrocatalysts for Lithium−Sulfur Batteries*. ACS Nano. 2021 Sep 22;15(11):17327–36.

128. Chahal S, Ranjan P, Motlag M, Yamijala SSRKC, Late DJ, Sadki EHS, et al. *Borophene via Micromechanical Exfoliation*. Advanced Materials. 2021 Jul 16;2102039.

129. Chung JY, Yuan Y, Mishra TP, Joseph C, Canepa P, Ranjan P, et al. *Structure and exfoliation mechanism of two-dimensional boron nanosheets*. Nat Commun. 2024 Jul 20;15(1):6122.

130. Li H, Jing L, Liu W, Lin J, Tay RY, Tsang SH, et al. *Scalable Production of Few-Layer Boron Sheets by Liquid-Phase Exfoliation and Their Superior Supercapacitive Performance*. ACS Nano. 2018 Feb 27;12(2):1262–72.

131. Fan Q, Choi C, Yan C, Liu Y, Qiu J, Hong S, et al. *High-yield production of few-layer boron nanosheets for efficient electrocatalytic N2 reduction*. Chem Commun. 2019 Apr 4;55(29):4246–9.

132. Ji X, Kong N, Wang J, Li W, Xiao Y, Gan ST, et al. *A Novel Top-Down Synthesis of Ultrathin 2D Boron Nanosheets for Multimodal Imaging-Guided Cancer Therapy*. Advanced Materials. 2018 Sep 6;30(36). https://pubmed.ncbi.nlm.nih.gov/30019786/

133. Wang X, Liang J, You Q, Zhu J, Fang F, Xiang Y, et al. *Bandgap Engineering of Hydroxy-Functionalized Borophene for Superior Photo-Electrochemical Performance*. Angewandte Chemie International Edition. 2020;59(52):23559–63.

134. Ma D, Zhao J, Xie J, Zhang F, Wang R, Wu L, et al. *Ultrathin boron nanosheets as an emerging two-dimensional photoluminescence material for bioimaging*. Nanoscale Horiz. 2020 Mar 30;5(4):705–13.

135. Ma C, Yin P, Khan K, Tareen AK, Huang R, Du J, et al. *Broadband Nonlinear Photonics in Few-Layer Borophene*. Small. 2021;17(7):2006891.

136. Najiya KPP, Konnola R, Sreena TS, Solomon S, Gopchandran KG. *Liquid phase exfoliation of few-layer borophene with high hole mobility for low-power electronic devices*. Inorganic Chemistry Communications. 2024 Aug 8;112962.

137. Lei X, Zatsepin AF, Boukhvalov DW. *Chemical instability of free-standing boron monolayers and properties of oxidized borophene sheets*. Physica E: Low-Dimensional Systems and Nanostructures. 2020 Jun 1;120:114082.

138. Jain A, Joseph K, Anthonysamy S, Gupta GS. *Kinetics of oxidation of boron powder*. Thermochimica Acta. 2011;514:67–73.

139. Liu X, Rahn M, Ruan Q, Yakobson BI, Hersam MC. *Probing borophene oxidation at the atomic scale*. Nanotechnology. 2022 Feb 18; https://iopscience.iop.org/article/10.1088/1361-6528/ac56bd

140. Li Q, Kolluru VSC, Rahn MS, Schwenker E, Li S, Hennig RG, et al. *Synthesis of borophane polymorphs through hydrogenation of borophene*. Science. 2021 Mar 12;371(6534):1143–8.

141. Lherbier A, Botello-Méndez AR, Charlier JC. *Electronic and optical properties of pristine and oxidized borophene*. 2D Mater. 2016 Oct 5;3(4):045006.

142. Hernandez Y, Nicolosi V, Lotya M, Blighe FM, Sun Z, De S, et al. *High-yield production of graphene by liquid-phase exfoliation of graphite*. Nature Nanotechnology. 2008 Sep 5;3(9):563–8.

143. Achee TC, Sun W, Hope JT, Quitzau SG, Sweeney CB, Shah SA, et al. *High-yield scalable graphene nanosheet production from compressed graphite using electrochemical exfoliation*. Sci Rep. 2018 Sep 28;8(1):14525.

144. Nicolosi V, Chhowalla M, Kanatzidis MG, Strano MS, Coleman JN. *Liquid exfoliation of layered materials*. Science. 2013;340(6139).

145. Hu CX, Shin Y, Read O, Casiraghi C. *Dispersant-assisted liquid-phase exfoliation of 2D materials beyond graphene*. Nanoscale. 2021;13(2):460–84.

146. Shin Y, Vranic S, Just-Baringo X, Gali SM, Kisby T, Chen Y, et al. *Stable, concentrated, biocompatible, and defect-free graphene dispersions with positive charge*. Nanoscale. 2020 Jun 21;12(23):12383–94.

147. Backes C, Szydłowska BM, Harvey A, Yuan S, Vega-Mayoral V, Davies BR, et al. *Production of highly monolayer enriched dispersions of liquid-exfoliated nanosheets by liquid cascade centrifugation*. ACS Nano. 2016;10(1):1589–601.

148. Kaur H, Coleman JN, Kaur H, Coleman J. *Liquid-phase Exfoliation of Nonlayered non-van der Waals Crystals into Nanoplatelets*. Advanced Materials. 2022 Apr 25;2202164.

149. Cai Z, Liu B, Zou X, Cheng HM. *Chemical Vapor Deposition Growth and Applications of Two-Dimensional Materials and Their Heterostructures*. Chem Rev. 2018 Jul 11;118(13):6091–133.

150. Yu J, Li J, Zhang W, Chang H. *Synthesis of high quality two-dimensional materials via chemical vapor deposition*. Chem Sci. 2015;6(12):6705–16.

151. Bhowmik S, Govind Rajan A. *Chemical vapor deposition of 2D materials: A review of modeling, simulation, and machine learning studies*. iScience. 2022 Mar;25(3):103832.

152. Shen J, He Y, Wu J, Gao C, Keyshar K, Zhang X, et al. *Liquid Phase Exfoliation of Two-Dimensional Materials by Directly Probing and Matching Surface Tension Components*. Nano Lett. 2015 Aug 12;15(8):5449–54.

153. Li Z, Young RJ, Backes C, Zhao W, Zhang X, Zhukov AA, et al. *Mechanisms of Liquid-Phase Exfoliation for the Production of Graphene*. ACS Nano. 2020 Sep 22;14(9):10976–85.

154. Huo C, Yan Z, Song X, Zeng H. *2D materials via liquid exfoliation: a review on fabrication and applications*. Science Bulletin. 2015 Dec;60(23):1994–2008.

155. Wang H, Jiao Y, Wu B, Wang D, Hu Y, Liang F, et al. *Exfoliated 2D Layered and Nonlayered Metal Phosphorous Trichalcogenides Nanosheets as Promising Electrocatalysts for CO_2 Reduction*. Angewandte Chemie International Edition. 2023;62(17):e202217253.

156. Zhang X, Deng J, Yan J, Song Y, Mo Z, Qian J, et al. *Cryo-mediated liquid-phase exfoliated 2D BP coupled with 2D C_3N_4 to photodegradate organic pollutants and simultaneously generate hydrogen*. Applied Surface Science. 2019 Oct 1;490:117–23.

157. Ouyang J, Zhang L, Li L, Chen W, Tang Z, Ji X, et al. *Cryogenic Exfoliation of 2D Stanene Nanosheets for Cancer Theranostics*. 123AD; https://doi.org/10.1007/s40820-021-00619-1

158. Zhang C, Xu Y, Lu P, Wei C, Zhu C, Yao H, et al. *Cryogenic Exfoliation of Non-layered Magnesium into Two-Dimensional Crystals*. Angewandte Chemie International Edition. 2019 Jun 24;58(26):8814–8.

159. Wang Y, Liu Y, Zhang J, Wu J, Xu H, Wen X, et al. *Cryo-mediated exfoliation and fracturing of layered materials into 2D quantum dots*. Science Advances. 2017 Dec 15;3(12):e1701500.

160. Yang M, Schoop LM. *Friends not Foes: Exfoliation of Non-van der Waals Materials*. Acc Chem Res. 2024 Aug 16; https://doi.org/10.1021/acs.accounts.4c00295

161. Hernandez Y, Lotya M, Rickard D, Bergin SD, Coleman JN. *Measurement of Multicomponent Solubility Parameters for Graphene Facilitates Solvent Discovery*. Langmuir. 2010 Mar 2;26(5):3208–13.

162. Cunningham G, Lotya M, Cucinotta CS, Sanvito S, Bergin SD, Menzel R, et al. *Solvent exfoliation of transition metal dichalcogenides: Dispersibility of exfoliated nanosheets varies only weakly between compounds*. ACS Nano. 2012 Apr 24;6(4):3468–80.

163. Hanlon D, Backes C, Doherty E, Cucinotta CS, Berner NC, Boland C, et al. *Liquid exfoliation of solvent-stabilized few-layer black phosphorus for applications beyond electronics*. Nature Communications 2015 6:1. 2015 Oct 15;6(1):1–11.

164. Vega-Mayoral V, Tian R, Kelly AG, Griffin A, Harvey A, Borrelli M, et al. *Solvent exfoliation stabilizes TiS_2 nanosheets against oxidation, facilitating lithium storage applications*. Nanoscale. 2019 Mar 28;11(13):6206–16.

165. Griffin A, Nisi K, Pepper J, Harvey A, Szydłowska BM, Coleman JN, et al. *Effect of Surfactant Choice and Concentration on the Dimensions and Yield of Liquid-Phase-Exfoliated Nanosheets*. Chemistry of Materials. 2020 Apr 14;32(7):2852–62.

166. Lotya M, King PJ, Khan U, De S, Coleman JN. *High-concentration, surfactant-stabilized graphene dispersions*. ACS Nano. 2010 Jun 22;4(6):3155–62.

167. *Toxicity of N-Methyl-2-pyrrolidone (NMP): Teratogenic, Subchronic, and Two-Year Inhalation Studies | Toxicological Sciences | Oxford Academic*. https://oxfordjournals.org/toxsci/article-abstract/9/2/222/1637803

168. Shin Y, Just-Baringo X, Boyes M, Panigrahi A, Zarattini M, Chen Y, et al. *Enhanced liquid phase exfoliation of graphene in water using an insoluble bis-pyrene stabiliser*. Faraday Discuss. 2021;227:46–60.

169. Koczkur KM, Mourdikoudis S, Polavarapu L, Skrabalak SE. *Polyvinylpyrrolidone (PVP) in nanoparticle synthesis*. Dalton Trans. 2015 Oct 13;44(41):17883–905.

170. Ryan AJ, Kearney CJ, Shen N, Khan U, Kelly AG, Probst C, et al. *Electroconductive Biohybrid Collagen/Pristine Graphene Composite Biomaterials with Enhanced Biological Activity*. Advanced Materials. 2018 Apr 12;30(15):1706442.

171. Duthen S, Rochat C, Kleiber D, Violleau F, Daydé J, Raynaud C, et al. *Physicochemical characterization and study of molar mass of industrial gelatins by AsFlFFFUV/ MALS and chemometric approach*. PLoS ONE. 2018 Oct 1;13(10). Available from: /pmc/articles/PMC6177121/?report=abstract

172. Knappe P, Bienert R, Weidner S, Thünemann AF. *Characterization of poly(*N-*vinyl-2-pyrrolidone)s with broad size distributions*. Polymer. 2010 Apr 6;51(8):1723–7.

173. Glanzer S, Pulido SA, Tutz S, Wagner GE, Kriechbaum M, Gubensäk N, et al. *Structural and Functional Implications of the Interaction between Macrolide Antibiotics and Bile Acids*. Chemistry – A European Journal. 2015;21(11):4350–8.

174. Kurakula M, Rao GSNK. *Pharmaceutical assessment of polyvinylpyrrolidone (PVP): As excipient from conventional to controlled delivery systems with a spotlight on COVID-19 inhibition*. Journal of Drug Delivery Science and Technology. 2020 Dec;60:102046.

175. Bahadur R, Singh B, Rai D, Srivastava R. *Influence of PEGylation on WS_2 Nanosheets and Its Application in Photothermal Therapy*. ACS Appl Bio Mater. 2023 Oct 28;acsabm.3c00506.

176. Garcia JR, O'Suilleabhain D, Kaur H, Coleman JN. *A Simple Model Relating Gauge Factor to Filler Loading in Nanocomposite Strain Sensors*. ACS Applied Nano Materials. 2021 Mar 26;4(3):2876–86.

177. Young RJ, Liu M, Kinloch IA, Li S, Zhao X, Vallés C, et al. *The mechanics of reinforcement of polymers by graphene nanoplatelets*. Composites Science and Technology. 2018 Jan 18;154:110–6.

178. Kelly AG, O'Suilleabhain D, Gabbett C, Coleman JN. *The electrical conductivity of solution-processed nanosheet networks*. Nature Reviews Materials 2021. 2021 Nov 9;1–18.

179. Wu S, Ladani RB, Zhang J, Bafekrpour E, Ghorbani K, Mouritz AP, et al. *Aligning multilayer graphene flakes with an external electric field to improve multifunctional properties of epoxy nanocomposites*. Carbon. 2015 Nov 1;94:607–18.

180. Boden A, Boerner B, Kusch P, Firkowska I, Reich S. *Nanoplatelet size to control the alignment and thermal conductivity in copper-graphite composites*. Nano Letters. 2014 Jun 11;14(6):3640–4.

181. compositematerialshub.com. *Rule of mixtures in composite materials* [Internet]. Composite Materials Hub. 2024 [cited 2025 Mar 19]. Available from: https://compositematerialshub.com/rule-of-mixtures/

182. Chen Q, Gong S, Moll J, Zhao D, Kumar SK, Colby RH. *Mechanical Reinforcement of Polymer Nanocomposites from Percolation of a Nanoparticle Network*. ACS Macro Lett. 2015 Apr 21;4(4):398–402.

183. Baxter SC, Burrows BJ, Fralick BS. *Mechanical percolation in nanocomposites: Microstructure and micromechanics*. Probabilistic Engineering Mechanics. 2016 Apr 1;44:35–42.

184. Sweeney J, Ward IM. *Mechanical Properties of Solid Polymers*.

185. Maccabi A, Shin A, Namiri NK, Bajwa N, John MS, Taylor ZD, et al. *Quantitative characterization of viscoelastic behavior in tissue-mimicking phantoms and ex vivo animal tissues*. PLoS ONE. 2018 Jan 26;13(1):e0191919.

186. Huang D, Huang Y, Xiao Y, Yang X, Lin H, Feng G, et al. *Viscoelasticity in natural tissues and engineered scaffolds for tissue reconstruction*. Acta Biomaterialia. 2019 Oct 1;97:74–92.

187. Wang L, Wang C, Wu S, Fan Y, Li X. *Influence of the mechanical properties of biomaterials on degradability, cell behaviors and signaling pathways: current progress and challenges*. Biomater Sci. 2020 May 19;8(10):2714–33.

188. Elosegui-Artola A, Gupta A, Najibi AJ, Seo BR, Garry R, Tringides CM, et al. *Matrix viscoelasticity controls spatiotemporal tissue organization*. Nat Mater. 2023 Jan;22(1):117–27.

189. Health C for D and R. *Classify Your Medical Device* [Internet]. FDA. FDA; 2023 [cited 2024 Aug 1]. Available from: https://www.fda.gov/medical-devices/overview-device-regulation/classify-your-medical-device

190. *Medical devices | European Medicines Agency (EMA)* [Internet]. 2019 [cited 2024 Aug 1]. Available from: https://www.ema.europa.eu/en/human-regulatory-overview/medical-devices

191. Kuroda C, Ajima K, Ueda K, Sobajima A, Yoshida K, Kamanaka T, et al. *Isolated lymphatic vessel lumen perfusion system for assessing nanomaterial movements and nanomaterial-induced responses in lymphatic vessels*. Nano Today. 2021 Feb;36:101018.

192. Moore C, Movia D, Smith RJ, Hanlon D, Lebre F, Lavelle EC, et al. *Industrial grade 2D molybdenum disulphide (MoS_2): an* in vitro *exploration of the impact on cellular uptake, cytotoxicity, and inflammation*. 2D Mater. 2017 Apr 3;4(2):025065.

193. Li J, Wang X, Mei KC, Chang CH, Jiang J, Liu X, et al. *Lateral size of graphene oxide determines differential cellular uptake and cell death pathways in Kupffer cells, LSECs, and hepatocytes*. Nano Today. 2021 Apr 1;37:101061.

194. Ou L, Song B, Liang H, Liu J, Feng X, Deng B, et al. *Toxicity of graphene-family nanoparticles: a general review of the origins and mechanisms*. Part Fibre Toxicol. 2016 Dec;13(1):57.

195. Jasim DA, Newman L, Rodrigues AF, Vacchi IA, Lucherelli MA, Lozano N, et al. *The impact of graphene oxide sheet lateral dimensions on their pharmacokinetic and tissue distribution profiles in mice*. J Control Release. 2021 Oct 10;338:330–40.

196. Jasim DA, Ménard-Moyon C, Bégin D, Bianco A, Kostarelos K. *Tissue distribution and urinary excretion of intravenously administered chemically functionalized graphene oxide sheets*. Chemical Science. 2015 Jul 1;6(7):3952–64.

197. Fan T, Yan L, He S, Hong Q, Ai F, He S, et al. *Biodistribution, degradability and clearance of 2D materials for their biomedical applications*. Chemical Society Reviews. 2022; https://pubs.rsc.org/en/content/articlehtml/2022/cs/d1cs01070k

198. Naikoo GA, Arshad F, Almas M, Hassan IU, Pedram MZ, Aljabali AAA, et al. *2D materials, synthesis, characterization and toxicity: A critical review*. Chemico-Biological Interactions. 2022 Aug 7;110081.

199. Song SJ, Shin YC, Lee HU, Kim B, Han DW, Lim D. *Dose- and Time-Dependent Cytotoxicity of Layered Black Phosphorus in Fibroblastic Cells*. Nanomaterials. 2018 Jun;8(6):408.

200. Bavorova H, Svadlakova T, Fiala Z, Pisal R, Mokry J. *The Dose- and Time-Dependent Cytotoxic Effect of Graphene Nanoplatelets: In Vitro and In Vivo Study*. Nanomaterials. 2022 Jun;12(12):1978.

201. Liu Y, Zhu S, Gu Z, Chen C, Zhao Y. *Toxicity of manufactured nanomaterials*. Particuology. 2022 Oct 1;69:31–48.

202. Tan E, Li BL, Ariga K, Lim CT, Garaj S, Leong DT. *Toxicity of Two-Dimensional Layered Materials and Their Heterostructures*. Bioconjugate Chemistry. 2019 Sep 18;30(9):2287–99.

203. Wang K, Ruan J, Song H, Zhang J, Wo Y, Guo S, et al. *Biocompatibility of Graphene Oxide*. Nanoscale Res Lett. 2011 Dec;6(1):8.

204. Chang Y, Yang ST, Liu JH, Dong E, Wang Y, Cao A, et al. *In vitro toxicity evaluation of graphene oxide on A549 cells*. Toxicol Lett. 2011 Feb 5;200(3):201–10.

205. Liao KH, Lin YS, Macosko CW, Haynes CL. *Cytotoxicity of Graphene Oxide and Graphene in Human Erythrocytes and Skin Fibroblasts*. ACS Appl Mater Interfaces. 2011 Jul 27;3(7):2607–15.

206. Shaw ZL, Kuriakose S, Cheeseman S, Dickey MD, Genzer J, Christofferson AJ, et al. *Antipathogenic properties and applications of low-dimensional materials*. Nature Communications. 2021 Dec 23;12(1):3897.

207. Dallavalle M, Calvaresi M, Bottoni A, Melle-Franco M, Zerbetto F. *Graphene Can Wreak Havoc with Cell Membranes*. ACS Publications. American Chemical Society; 2015. https://pubs.acs.org/doi/abs/10.1021/am508938u

208. Rasool K, Helal M, Ali A, Ren CE, Gogotsi Y, Mahmoud KA. *Antibacterial Activity of $Ti_3C_2T_x$ MXene*. ACS Nano. 2016 Mar 22;10(3):3674–84.

209. Jasim DA, Boutin H, Fairclough M, Ménard-Moyon C, Prenant C, Bianco A, et al. *Thickness of functionalized graphene oxide sheets plays critical role in tissue accumulation and urinary excretion: A pilot PET/CT study*. Applied Materials Today. 2016 Sep 1;4:24–30.

210. Choi HS, Liu W, Misra P, Tanaka E, Zimmer JP, Itty Ipe B, et al. *Renal clearance of quantum dots*. Nat Biotechnol. 2007 Oct;25(10):1165–70.

211. Tencer J, Frick IM, Öquist BW, Alm P, Rippe B. *Size-selectivity of the glomerular barrier to high molecular weight proteins: Upper size limitations of shunt pathways*. Kidney International. 1998 Mar;53(3):709–15.

212. Ogawara K ichi, Yoshida M, Higaki K, Toshikiro Kimura, Shiraishi K, Nishikawa M, et al. *Hepatic uptake of polystyrene microspheres in rats: Effect of particle size on intrahepatic distribution*. Journal of Controlled Release. 1999 May 1;59(1):15–22.

213. Cao T, You P, Zhou X, Luo J, Xu X, Zhou Z, et al. *Visualization of size-dependent tumour retention of PEGylated nanographene oxide via SPECT imaging*. J Mater Chem B. 2016 Oct 5;4(39):6446–53.

214. Yin X, Zhang S, Wen L, Su J, Huang J, Duan G, et al. *Nonmonotonic Relationship between the Oxidation State of Graphene-Based Materials and Its Cell Membrane Damage Effects*. ACS Applied Materials & Interfaces. 2022 Jun 24; https://pubs.acs.org/doi/full/10.1021/acsami.2c03520

215. Duch MC, Budinger GRS, Liang YT, Soberanes S, Urich D, Chiarella SE, et al. *Minimizing Oxidation and Stable Nanoscale Dispersion Improves the Biocompatibility of Graphene in the Lung*. Nano Lett. 2011 Dec 14;11(12):5201–7.

216. Li R, Guiney LM, Chang CH, Mansukhani ND, Ji Z, Wang X, et al. *Surface Oxidation of Graphene Oxide Determines Membrane Damage, Lipid Peroxidation, and Cytotoxicity in Macrophages in a Pulmonary Toxicity Model*. ACS Nano. 2018 Feb 27;12(2):1390–402.

217. Gurunathan S, Arsalan Iqbal M, Qasim M, Park CH, Yoo H, Hwang JH, et al. *Evaluation of Graphene Oxide Induced Cellular Toxicity and Transcriptome Analysis in Human Embryonic Kidney Cells*. Nanomaterials (Basel). 2019 Jul 2;9(7):969.

218. Gurunathan S, Kim JH. *Synthesis, toxicity, biocompatibility, and biomedical applications of graphene and graphene-related materials*. International Journal of Nanomedicine. 2016 May 5;11:1927–45.

219. Feng W, Wang J, Li B, Liu Y, Xu D, Cheng K, et al. *Graphene oxide leads to mitochondrial-dependent apoptosis by activating ROS-p53-mPTP pathway in intestinal cells*. The International Journal of Biochemistry & Cell Biology. 2022 May 1;146:106206.

220. Nanda SS, An SSA, Yi DK. *Oxidative stress and antibacterial properties of a graphene oxide-cystamine nanohybrid*. Int J Nanomedicine. 2015 Jan 12;10:549–56.

221. Pulingam T, Thong KL, Appaturi JN, Lai CW, Leo BF. *Mechanistic actions and contributing factors affecting the antibacterial property and cytotoxicity of graphene oxide*. Chemosphere. 2021 Oct 1;281:130739.

222. Zhang W, Yan L, Li M, Zhao R, Yang X, Ji T, et al. *Deciphering the underlying mechanisms of oxidation-state dependent cytotoxicity of graphene oxide on mammalian cells*. Toxicology Letters. 2015 Sep 2;237(2):61–71.

223. Hou Y, Wang W, Bartolo P. *The effect of graphene and graphene oxide induced reactive oxygen species on polycaprolactone scaffolds for bone cancer applications*. Materials Today Bio. 2023 Nov;100886.

224. Pelin M, Fusco L, Martín C, Sosa S, Frontiñán-Rubio J, González-Domínguez JM, et al. *Graphene and graphene oxide induce ROS production in human HaCaT skin keratinocytes: the role of xanthine oxidase and NADH dehydrogenase*. Nanoscale. 2018 Jul 5;10(25):11820–30.

225. Bendali A, Hess LH, Seifert M, Forster V, Stephan AF, Garrido JA, et al. *Purified Neurons can Survive on Peptide-Free Graphene Layers*. Advanced Healthcare Materials. 2013;2(7):929–33.

226. Adeel M, Bilal M, Rasheed T, Sharma A, Iqbal HMN. *Graphene and graphene oxide: Functionalization and nano-bio-catalytic system for enzyme immobilization and biotechnological perspective*. International Journal of Biological Macromolecules. 2018 Dec 1;120:1430–40.

227. Guo Z, Chakraborty S, Monikh A, Varsou DD, Chetwynd AJ, Afantitis A, et al. *Surface Functionalization of Graphene-Based Materials: Biological Behavior, Toxicology, and Safe-By-Design Aspects*. Advanced Biology. 2021 Sep 1;5(9):2100637.

228. Wang Y, Li Z, Wang J, Li J, Lin Y. *Graphene and graphene oxide: biofunctionalization and applications in biotechnology*. Trends in Biotechnology. 2011 May 1;29(5):205–12.

229. Metwally S, Stachewicz U. *Surface potential and charges impact on cell responses on biomaterials interfaces for medical applications*. Materials Science and Engineering: C. 2019 Nov 1;104:109883.

230. Mei K, Costa PM, Kreuzer M, Al-Jamal KT. *Interpreting 2D Materials Bio-Nano Interactions: Influence of Aggregation Status, Protein Corona, Cell Culture Media, and Cell Types*. Advanced Materials Interfaces. 2021 Aug 12;2100251.

231. Murugadoss S, Brassinne F, Sebaihi N, Petry J, Cokic SM, Van Landuyt KL, et al. *Agglomeration of titanium dioxide nanoparticles increases toxicological responses in vitro and in vivo*. Particle and Fibre Toxicology. 2020 Feb 26;17(1):10.

232. Li J, Chen C, Xia T. *Understanding Nanomaterial-Liver Interactions to Facilitate the Development of Safer Nanoapplications*. Adv Mater. 2022 Mar;34(11):e2106456.

233. Tsoi KM, MacParland SA, Ma XZ, Spetzler VN, Echeverri J, Ouyang B, et al. *Mechanism of hard nanomaterial clearance by the liver*. Nat Mater. 2016 Nov;15(11):1212–21.

234. Zhao H, Li L, Zhan H, Chu Y, Sun B. *Mechanistic Understanding of the Engineered Nanomaterial-Induced Toxicity on Kidney*. Journal of Nanomaterials. 2019;2019(1):2954853.

235. Dattani R. *Femoral osteolysis following total hip replacement*. Postgrad Med J. 2007 May;83(979):312–6.

236. Lind G, Linsmeier CE, Schouenborg J. *The density difference between tissue and neural probes is a key factor for glial scarring*. Scientific Reports. 2013 Oct 15;3. Available from: /pmc/articles/PMC3796741/

237. Vianello F, Cecconello A, Magro M. *Toward the Specificity of Bare Nanomaterial Surfaces for Protein Corona Formation*. International Journal of Molecular Sciences. 2021 Jan;22(14):7625.

238. Aljabali AA, Obeid MA, Bashatwah RM, Serrano-Aroca Á, Mishra V, Mishra Y, et al. *Nanomaterials and Their Impact on the Immune System*. International Journal of Molecular Sciences. 2023 Jan;24(3):2008.

239. Lin S, Mortimer M, Chen R, Kakinen A, Riviere JE, Davis TP, et al. *NanoEHS beyond Toxicity – Focusing on Biocorona*. Environ Sci Nano. 2017 Jul 1;7(4):1433–54.

240. Li X, Wang L, Fan Y, Feng Q, Cui F zhai. *Biocompatibility and Toxicity of Nanoparticles and Nanotubes*. Journal of Nanomaterials. 2012;2012(1):548389.

241. Becker H, Herzberg F, Schulte A, Kolossa-Gehring M. *The carcinogenic potential of nanomaterials, their release from products and options for regulating them*. International Journal of Hygiene and Environmental Health. 2011 Jun 1;214(3):231–8.

242. Hou WC, Westerhoff P, D. Posner J. *Biological accumulation of engineered nanomaterials: a review of current knowledge*. Environmental Science: Processes & Impacts. 2013;15(1):103–22.

243. Wang B, He X, Zhang Z, Zhao Y, Feng W. *Metabolism of Nanomaterials in Vivo: Blood Circulation and Organ Clearance*. Acc Chem Res. 2013 Mar 19;46(3):761–9.

244. Malakar A, Kanel SR, Ray C, Snow DD, Nadagouda MN. *Nanomaterials in the environment, human exposure pathway, and health effects: A review*. Science of The Total Environment. 2021 Mar 10;759:143470.

245. Poon W, Zhang YN, Ouyang B, Kingston BR, Wu JLY, Wilhelm S, et al. *Elimination Pathways of Nanoparticles*. ACS Nano. 2019 May 28;13(5):5785–98.

246. Liu Z, Davis C, Cai W, He L, Chen X, Dai H. *Circulation and long-term fate of functionalized, biocompatible single-walled carbon nanotubes in mice probed by Raman spectroscopy*. Proceedings of the National Academy of Sciences. 2008 Feb 5;105(5):1410–5.

247. Phillips E, Penate-Medina O, Zanzonico PB, Carvajal RD, Mohan P, Ye Y, et al. *Clinical translation of an ultrasmall inorganic optical-PET imaging nanoparticle probe*. Science translational medicine. 2014 Oct 29;6(260):260ra149.

248. Liu J, Cui L, Losic D. *Graphene and graphene oxide as new nanocarriers for drug delivery applications*. Acta Biomater. 2013 Dec;9(12):9243–57.

249. Yang K, Feng L, Shi X, Liu Z. *Nano-graphene in biomedicine: theranostic applications*. Chem Soc Rev. 2013;42(2):530–47.

250. Liu C, Wong HM, Yeung KWK, Tjong SC. *Novel Electrospun Polylactic Acid Nanocomposite Fiber Mats with Hybrid Graphene Oxide and Nanohydroxyapatite Reinforcements Having Enhanced Biocompatibility*. Polymers. 2016 Aug;8(8):287.

251. Yang K, Zhang S, Zhang G, Sun X, Lee ST, Liu Z. *Graphene in Mice: Ultrahigh In Vivo Tumor Uptake and Efficient Photothermal Therapy*. Nano Lett. 2010 Sep;10(9):3318–23.

252. Robinson JT, Tabakman SM, Liang Y, Wang H, Casalongue HS, Daniel V, et al. *Ultrasmall Reduced Graphene Oxide with High Near-Infrared Absorbance for Photothermal Therapy*. J Am Chem Soc. 2011 May 4;133(17):6825–31.

253. Zhang L, Xia J, Zhao Q, Liu L, Zhang Z. *Functional Graphene Oxide as a Nanocarrier for Controlled Loading and Targeted Delivery of Mixed Anticancer Drugs*. Small. 2010 Feb 22;6(4):537–44.

254. Carpio IEM, Santos CM, Wei X, Rodrigues DF. *Toxicity of a polymer–graphene oxide composite against bacterial planktonic cells, biofilms, and mammalian cells*. Nanoscale. 2012 Jul 12;4(15):4746–56.

255. Mei L, Zhu S, Yin W, Chen C, Nie G, Gu Z, et al. *Two-dimensional nanomaterials beyond graphene for antibacterial applications: current progress and future perspectives*. Theranostics. 2020;10(2):757.

256. Li B, Luo Y, Zheng Y, Liu X, Tan L, Wu S. *Two-dimensional antibacterial materials*. Progress in Materials Science. 2022 Oct 1;130:100976.

257. Teixeira-Santos R, Belo S, Vieira R, Mergulhão FJM, Gomes LC. *Graphene-Based Composites for Biomedical Applications: Surface Modification for Enhanced Antimicrobial Activity and Biocompatibility*. Biomolecules. 2023 Oct 24;13(11):1571.

258. Rastogi SK, Raghavan G, Yang G, Cohen-Karni T. *Effect of Graphene on Nonneuronal and Neuronal Cell Viability and Stress*. Nano Letters. 2017 May 10;17(5):3297–301.

259. Lebre F, Boland JB, Gouveia P, Gorman AL, Lundahl MLE, I Lynch R, et al. *Pristine graphene induces innate immune training*. Nanoscale. 2020;12(20):11192–200.

260. Agarwal G, Kumar N, Srivastava A. *Highly elastic, electroconductive, immunomodulatory graphene crosslinked collagen cryogel for spinal cord regeneration*. 2020. https://doi.org/10.1016/j.msec.2020.111518

261. Pok S, Vitale F, Eichmann SL, Benavides OM, Pasquali M, Jacot JG. *Biocompatible carbon nanotube-chitosan scaffold matching the electrical conductivity of the heart*. ACS Nano. 2014 Oct 28;8(10):9822–32.

262. Uz M, Donta M, Mededovic M, Sakaguchi DS, Mallapragada SK. *Development of Gelatin and Graphene-Based Nerve Regeneration Conduits Using Three-Dimensional*

(3D) Printing Strategies for Electrical Transdifferentiation of Mesenchymal Stem Cells. Industrial and Engineering Chemistry Research. 2019 May 8;58(18):7421–7.

263. Liao C, Li Y, Tjong SC. *Graphene Nanomaterials: Synthesis, Biocompatibility, and Cytotoxicity*. Int J Mol Sci. 2018 Nov 12;19(11):3564.

264. Syama S, Mohanan PV. *Safety and biocompatibility of graphene: A new generation nanomaterial for biomedical application*. International Journal of Biological Macromolecules. 2016 May 1;86:546–55.

265. Kostarelos K. *Translating graphene and 2D materials into medicine*. Nature Reviews Materials. 2016;1(11):1–2.

266. Bitounis D, Ali-Boucetta H, Hong BH, Min D, Kostarelos K. *Prospects and Challenges of Graphene in Biomedical Applications*. Advanced Materials. 2013 Apr 24;25(16):2258–68.

267. Green R, Abidian MR. *Conducting Polymers for Neural Prosthetic and Neural Interface Applications*. Advanced materials (Deerfield Beach, Fla). 2015 Dec 9;27(46):7620.

268. Wellman SM, Eles JR, Ludwig KA, Seymour JP, Michelson NJ, McFadden WE, et al. *A Materials Roadmap to Functional Neural Interface Design*. Advanced Functional Materials. 2018 Mar 21;28(12):1701269.

269. Rauti R, Medelin M, Newman L, Vranic S, Reina G, Bianco A, et al. *Graphene Oxide Flakes Tune Excitatory Neurotransmission in Vivo by Targeting Hippocampal Synapses*. Nano Letters. 2019 May 8;19(5):2858–70.

270. Yang JW, Chen CY, Yu ZY, Chung JHY, Liu X, Wu CY, et al. *An electroactive hybrid biointerface for enhancing neuronal differentiation and axonal outgrowth on bio-subretinal chip*. Materials Today Bio. 2022 Mar 1;14:100253.

271. Lu Y, Liu X, Kuzum D. *Graphene-based neurotechnologies for advanced neural interfaces*. Current Opinion in Biomedical Engineering. 2018 Jun 1;6:138–47.

272. Fabbro A, Scaini D, León V, Vázquez E, Cellot G, Privitera G, et al. *Graphene-Based interfaces do not alter target nerve cells*. ACS Nano. 2016;10(1):615–23.

273. Ciesielski A, Samorì P. *Graphene via sonication assisted liquid-phase exfoliation*. Chemical Society Reviews. 2013 Dec 2;43(1):381–98.

274. Sattar T. *Current Review on Synthesis, Composites and Multifunctional Properties of Graphene*. Top Curr Chem (Z). 2019 Apr;377(2):10.

275. Chwalibog A, Sawosz E, Jaworski S, Kutwin M, Hotowy A, Wierzbicki M, et al. *Toxicity of pristine graphene in experiments in a chicken embryo model*. IJN. 2014 Aug;3913.

276. Li Y, Liu Y, Fu Y, Wei T, Le Guyader L, Gao G, et al. *The triggering of apoptosis in macrophages by pristine graphene through the MAPK and TGF-beta signaling pathways*. Biomaterials. 2012 Jan;33(2):402–11.

277. Veliev F, Briançon-Marjollet A, Bouchiat V, Delacour C. *Impact of crystalline quality on neuronal affinity of pristine graphene*. Biomaterials. 2016 Apr;86:33–41.

278. Bei H, Yang Y, Zhang Q, Tian Y, Luo X, Yang M, et al. *Graphene-Based Nanocomposites for Neural Tissue Engineering*. Molecules. 2019 Feb 13;24(4):658.

279. Kostarelos K, Novoselov KS. *Exploring the interface of graphene and biology*. Science. 2014 Apr 18;344(6181):261–3.

280. Li N, Zhang X, Song Q, Su R, Zhang Q, Kong T, et al. *The promotion of neurite sprouting and outgrowth of mouse hippocampal cells in culture by graphene substrates*. Biomaterials. 2011 Dec;32(35):9374–82.

281. Park SY, Park J, Sim SH, Sung MG, Kim KS, Hong BH, et al. *Enhanced Differentiation of Human Neural Stem Cells into Neurons on Graphene*. Advanced Materials. 2011;23(36):H263–7.

282. He Z, Zhang S, Song Q, Li W, Liu D, Li H, et al. *The structural development of primary cultured hippocampal neurons on a graphene substrate*. Colloids and Surfaces B: Biointerfaces. 2016 Oct 1;146:442–51.

283. Tang M, Song Q, Li N, Jiang Z, Huang R, Cheng G. *Enhancement of electrical signaling in neural networks on graphene films*. Biomaterials. 2013 Sep;34(27):6402–11.

284. Nair S, Varma P, Kandasubramanian B. *Unlocking the Potential of Graphene-Based Nanocomposites in Neurogenesis*. Biomedical Materials & Devices. 2024 Jul 29; https://doi.org/10.1007/s44174-024-00214-z

285. Convertino D, Fabbri F, Mishra N, Mainardi M, Cappello V, Testa G, et al. *Graphene Promotes Axon Elongation through Local Stall of Nerve Growth Factor Signaling Endosomes*. Nano Lett. 2020 May 13;20(5):3633–41.

286. Zhang Z, Klausen LH, Chen M, Dong M. *Electroactive Scaffolds for Neurogenesis and Myogenesis: Graphene-Based Nanomaterials*. Small. 2018 Nov 28;14(48):1801983.

287. Lee JS, Lipatov A, Ha L, Shekhirev M, Andalib MN, Sinitskii A, et al. *Graphene substrate for inducing neurite outgrowth*. Biochem Biophys Res Commun. 2015 May 1;460(2):267–73.

288. Moschetta M, Lee J, Rodrigues J, Podestà A, Varvicchio O, Son J, et al. *Hydrogenated Graphene Improves Neuronal Network Maturation and Excitatory Transmission*. Advanced Biology. 2021;2000177:2000177.

289. Gobbi M, Orgiu E, Samorì P. *When 2D Materials Meet Molecules: Opportunities and Challenges of Hybrid Organic/Inorganic van der Waals Heterostructures*. Advanced Materials. 2018 May;30(18):1706103.

290. Capasso A, Rodrigues J, Moschetta M, Buonocore F, Faggio G, Messina G, et al. *Interactions between Primary Neurons and Graphene Films with Different Structure and Electrical Conductivity*. Advanced Functional Materials. 2021;31(11):2005300.

291. Akinwande D, Tao L, Yu Q, Lou X, Peng P, Kuzum D. *Large-Area Graphene Electrodes: Using CVD to facilitate applications in commercial touchscreens, flexible*

nanoelectronics, and neural interfaces. IEEE Nanotechnology Mag. 2015 Sep;9(3):6–14.

292. Convertino D, Luin S, Marchetti L, Coletti C. *Peripheral Neuron Survival and Outgrowth on Graphene*. Front Neurosci. 2018 Jan 22;12. https://www.frontiersin.org/journals/neuroscience/articles/10.3389/fnins.2018.00001/full

293. Carey T, Alhourani A, Tian R, Seyedin S, Arbab A, Maughan J, et al. *Cyclic production of biocompatible few-layer graphene ink with in-line shear-mixing for inkjet-printed electrodes and Li-ion energy storage*. npj 2D Materials and Applications 2022 6:1. 2022 Jan 12;6(1):1–11.

294. Mauro GD, Rauti R, Casani R, Chimowa G, Galibert AM, Flahaut E, et al. *Tuning the Reduction of Graphene Oxide Nanoflakes Differently Affects Neuronal Networks in the Zebrafish*. Nanomaterials. 2021;2021(9):2161.

295. Bellier N, Baipaywad P, Ryu N, Lee JY, Park H. *Recent biomedical advancements in graphene oxide- and reduced graphene oxide-based nanocomposite nanocarriers*. Biomaterials Research 2022 26:1. 2022 Nov 26;26(1):1–23.

296. Lebre F, Hanlon D, Boland JB, Coleman J, Lavelle EC. *Exfoliation in Endotoxin-Free Albumin Generates Pristine Graphene with Reduced Inflammatory Properties*. Advanced Biosystems. 2018;2(12):1800102.

297. Ławkowska K, Pokrywczyńska M, Koper K, Kluth LA, Drewa T, et al. *Application of Graphene in Tissue Engineering of the Nervous System*. International Journal of Molecular Sciences 2022, Vol 23, Page 33. 2021 Dec 21;23(1):33.

298. Ni F, Chen Y, Wang Z, Zhang X, Gao F, Shao Z, et al. *Graphene derivative based hydrogels in biomedical applications*. J Tissue Eng. 2024 Jan;15:20417314241282131.

299. Pizzorno L. *Nothing Boring About Boron*. Integrative Medicine: A Clinician's Journal. 2015;14(4):35.

300. Rico P, Rodrigo-Navarro A, Sánchez Pérez L, Salmeron-Sanchez M, Rico P, Salmerón-Sánchez M. *Boron induces osteogenesis by stimulating NaBC1 in cooperation with BMPR1A*. Available from: https://doi.org/10.1101/2020.03.17.995001

301. Penland JG. *Dietary Boron, Brain Function, and Cognitive Performance*. Environmental Health Perspectives. 1994;102.

302. Yin C, Jia X, Zhao Q, Zhao Z, Wang J, Zhang Y, et al. *Transcription factor 7-like 2 promotes osteogenic differentiation and boron-induced bone repair via lipocalin 2*. Materials Science and Engineering C. 2020 May 1;110.

303. Uysal T, Ustdal A, Sonmez MF, Ozturk F. *Stimulation of Bone Formation by Dietary Boron in an Orthopedically Expanded Suture in Rabbits*. The Angle Orthodontist. 2009 Sep 1;79(5):984–90.

304. Balasubramanian P, Büttner T, Miguez Pacheco V, Boccaccini AR. *Boron-containing bioactive glasses in bone and soft tissue engineering*. Journal of the European Ceramic Society. 2018 Mar 1;38(3):855–69.

305. Rondanelli M, Faliva MA, Peroni G, Infantino V, Gasparri C, Iannello G, et al. *Pivotal role of boron supplementation on bone health: A narrative review*. Journal of Trace Elements in Medicine and Biology. 2020 Dec 1;62:126577.

306. Ying X, Cheng S, Wang W, Lin Z, Chen Q, Zhang W, et al. *Effect of boron on osteogenic differentiation of human bone marrow stromal cells*. Biological trace element research. 2011 Dec;144(1–3):306–15.

307. Szczodra A, Houaoui A, Agniel R, Sicard L, Miettinen S, Massera J, et al. *Boron substitution in silicate bioactive glass scaffolds to enhance bone differentiation and regeneration*. Acta Biomaterialia. 2024 Aug 2; https://www.sciencedirect.com/science/article/pii/S1742706124004367

308. Balasubramanian P, Hupa L, Jokic B, Detsch R, Grünewald A, Boccaccini AR. *Angiogenic potential of boron-containing bioactive glasses: in vitro study*. J Mater Sci. 2017 Aug 1;52(15):8785–92.

309. Decker S, Arango-Ospina M, Rehder F, Moghaddam A, Simon R, Merle C, et al. *In vitro and in ovo impact of the ionic dissolution products of boron-doped bioactive silicate glasses on cell viability, osteogenesis and angiogenesis*. Scientific Reports. 2022 Dec;12(1).

310. Nzietchueng RM, Dousset B, Franck P, Benderdour M, Nabet P, Hess K. *Mechanisms implicated in the effects of boron on wound healing*. Journal of Trace Elements in Medicine and Biology. 2002 Jan 1;16(4):239–44.

311. Xia L, Ma W, Zhou Y, Gui Z, Yao A, Wang D, et al. *Stimulatory Effects of Boron Containing Bioactive Glass on Osteogenesis and Angiogenesis of Polycaprolactone: In Vitro Study*. BioMed Research International. 2019 Mar 18;2019:e8961409.

312. Gümüşderelioğlu M, Tunçay EÖ, Kaynak G, Demirtaş TT, Aydın ST, Hakkı SS. *Encapsulated boron as an osteoinductive agent for bone scaffolds*. J Trace Elem Med Biol. 2015;31:120–8.

313. Pazarçeviren AE, Tezcaner A, Keskin D, Kolukısa ST, Sürdem S, Evis Z. *Boron-doped Biphasic Hydroxyapatite/β-Tricalcium Phosphate for Bone Tissue Engineering*. Biol Trace Elem Res. 2021 Mar 1;199(3):968–80.

314. Ri CC, Mf CR, D RV, T PC, F TC, Ir S, et al. *Boron-Containing Compounds for Prevention, Diagnosis, and Treatment of Human Metabolic Disorders*. Biol Trace Elem Res. 2023 May;201(5):2222–39.

315. Barrón-González M, Montes-Aparicio AV, Cuevas-Galindo ME, Orozco-Suárez S, Barrientos R, Alatorre A, et al. *Boron-containing compounds on neurons: Actions and potential applications for treating neurodegenerative diseases*. Journal of Inorganic Biochemistry. 2023 Jan;238:112027.

316. Ali F, S Hosmane N, Zhu Y. *Boron Chemistry for Medical Applications*. Molecules. 2020 Feb 13;25(4):828.

317. Chatterjee S, Tripathi NM, Bandyopadhyay A. *The modern role of boron as a 'magic element' in biomedical science: chemistry perspective*. Chem Commun. 2021 Dec 16;57(100):13629–40.

318. Grams RJ, Santos WL, Scorei IR, Abad-García A, Rosenblum CA, Bita A, et al. *The Rise of Boron-Containing Compounds: Advancements in Synthesis, Medicinal Chemistry, and Emerging Pharmacology*. Chem Rev. 2024 Feb 21;acs.chemrev.3c00663.

319. Dong M, Zhou S, Xue X, Feng X, Sayyed M, Khandaker MU, et al. *The potential use of boron containing resources for protection against nuclear radiation*. Radiat Phys Chem. 2021 Nov;188:109601.

320. Qi P, Chen Q, Tu D, Yao S, Zhang Y, Wang J, et al. *The potential role of borophene as a radiosensitizer in boron neutron capture therapy (BNCT) and particle therapy (PT)*. Biomaterials Science. 2020;8(10):2778–85.

321. Duo Y, Xie Z, Wang L, Mahmood Abbasi N, Yang T, Li Z, et al. *Borophene-based biomedical applications: Status and future challenges*. Coordination Chemistry Reviews. 2021 Jan 15;427:213549.

322. Fu Z, Williams GR, Niu S, Wu J, Gao F, Zhang X, et al. *Functionalized boron nanosheets as an intelligent nanoplatform for synergistic low-temperature photothermal therapy and chemotherapy*. Nanoscale. 2020 Jul 21;12(27):14739–50.

323. Malouff TD, Seneviratne DS, Ebner DK, Stross WC, Waddle MR, Trifiletti DM, et al. *Boron Neutron Capture Therapy: A Review of Clinical Applications*. Front Oncol. 2021 Feb 26;11:601820.

324. Hou C, Tai G, Liu Y, Liu R, Liang X, Wu Z, et al. *Borophene pressure sensing for electronic skin and human-machine interface*. Nano Energy. 2022 Mar 26;107189.

325. Nangare SN, Khan ZG, Patil AG, Patil PO. *Design of monoelemental based two dimensional nanoarchitectures for therapeutic, chemical sensing and in vitro diagnosis applications: A case of borophene*. Journal of Molecular Structure. 2022 May 26;133387.

326. Gungor S, Tasaltin C, Gurol I, Baytemir G, Karakus S, Tasaltin N. *Copper phthalocyanine-borophene nanocomposite-based non-enzymatic electrochemical urea biosensor*. Appl Phys A-Mater Sci Process. 2022 Jan;128(1):89.

327. Coghi PS, Zhu Y, Xie H, Hosmane NS, Zhang Y. *Organoboron Compounds: Effective Antibacterial and Antiparasitic Agents*. Molecules. 2021 May 31;26(11):3309.

328. Koldemir-Gündüz M, Aydin HE, Berikten D, Kaymak G, Köse DA, Arslantaş A. *Synthesis of New Boron Derived Compounds; Anticancer, Antioxidant and Antimicrobial Effect in Vitro Glioblastoma Tumor Model*. J Korean Neurosurg Soc. 2021 Nov;64(6):864–72.

329. Celebi O, Celebi D, Baser S, Aydın E, Rakıcı E, Uğraş S, et al. *Antibacterial Activity of Boron Compounds Against Biofilm-Forming Pathogens*. Biol Trace Elem Res. 2024 Jan 1;202(1):346–59.

330. Han M, Zhu L, Mo J, Wei W, Yuan B, Zhao J, et al. *Protein Corona and Immune Responses of Borophene: A Comparison of Nanosheet-Plasma Interface with Graphene and Phosphorene*. ACS Applied Bio Materials. 2020 Jul 20;3(7):4220–9.

331. *Worldwide cancer data | World Cancer Research Fund International* [Internet]. WCRF International. [cited 2024 Jul 28]. Available from: https://www.wcrf.org/cancer-trends/worldwide-cancer-data/

332. He C, Feng P, Hao M, Tang Y, Wu X, Cui W, et al. *Nanomaterials in Antibacterial Photodynamic Therapy and Antibacterial Sonodynamic Therapy*. Advanced Functional Materials:2402588.

333. Li N. *Recent Advances in Photothermal Therapy at Near-Infrared-II Based on 2D MXenes*. 2023;

334. Einafshar E, Ghorbani A. *Advances in Black Phosphorus Quantum Dots for Cancer Research: Synthesis, Characterization, and Applications*. Top Curr Chem (Z). 2024 Jul 15;382(3):25.

335. Shao J, Xie H, Huang H, Li Z, Sun Z, Xu Y, et al. *Biodegradable black phosphorus-based nanospheres for in vivo photothermal cancer therapy*. Nature Communications. 2016 Sep 30;7(1):1–13.

336. Li X, Wang Y, Liu T, Zhang Y, Wang C, Xie B. *Ultrasmall graphene oxide for combination of enhanced chemotherapy and photothermal therapy of breast cancer*. Colloids and Surfaces B: Biointerfaces. 2023 May 1;225:113288.

337. Shavanova K, Bakakina Y, Burkova I, Shtepliuk I, Viter R, Ubelis A, et al. *Application of 2D Non-Graphene Materials and 2D Oxide Nanostructures for Biosensing Technology*. Sensors. 2016 Feb;16(2):223.

338. Sinha A, Dhanjai, Zhao H, Huang Y, Lu X, Chen J, et al. *MXene: An emerging material for sensing and biosensing*. TrAC Trends in Analytical Chemistry. 2018 Aug 1;105:424–35.

339. Krishnan SK, Singh E, Singh P, Meyyappan M, Nalwa HS. *A review on graphene-based nanocomposites for electrochemical and fluorescent biosensors*. RSC Adv. 2019 Mar 15;9(16):8778–881.

340. Nurunnabi M, McCarthy JR. *Biomedical applications of graphene and 2D nanomaterials* [Internet]. Biomedical Applications of Graphene and 2D Nanomaterials. Amsterdam : Elsevier,; 2019 [cited 2020 Sep 23]. 1–383 p. Available from: https://stella.catalogue.tcd.ie/iii/encore/record/C__Rb18136645__Sgraphene biomedical__Orightresult__U__X2?lang=eng&suite=cobalt

341. Langer R, Vacanti JP. *Tissue Engineering*. Science. 1993;260(5110):920–6.

342. O'Brien FJ. *Biomaterials & scaffolds for tissue engineering*. Materials Today. 2011 Mar 1;14(3):88–95.

343. Lanza R, Langer R, Vacanti JP, Atala A. *Principles of Tissue Engineering*. Academic Press; 2020. 1679 p.

344. Ikada Y. *Challenges in tissue engineering*. J R Soc Interface. 2006 Oct 22;3(10):589–601.

345. Liu J, Chi J, Wang K, Liu X, Liu J, Gu F. *Full-thickness wound healing using 3D bioprinted gelatin-alginate scaffolds in mice: a histopathological study*. International Journal of Clinical and Experimental Pathology.

346. Mao AS, Mooney DJ. *Regenerative medicine: Current therapies and future directions*. Proceedings of the National Academy of Sciences. 2015 Nov 24;112(47):14452–9.

347. Hench L, Jones J. *Biomaterials, Artificial Organs and Tissue Engineering*. Elsevier; 2005. 298 p.

348. Yadav P, Beniwal G, Saxena KK. *A review on pore and porosity in tissue engineering*. Materials Today: Proceedings. 2021 Jan 1;44:2623–8.

349. Murphy CM, Haugh MG, O'Brien FJ. *The effect of mean pore size on cell attachment, proliferation and migration in collagen–glycosaminoglycan scaffolds for bone tissue engineering*. Biomaterials. 2010 Jan 1;31(3):461–6.

350. O'Brien FJ, Harley BA, Yannas IV, Gibson LJ. *The effect of pore size on cell adhesion in collagen-GAG scaffolds*. Biomaterials. 2005 Feb 1;26(4):433–41.

351. Woods I, O'Connor C, Frugoli L, Kerr S, Gonzalez JG, Stasiewicz M, et al. *Biomimetic Scaffolds for Spinal Cord Applications Exhibit Stiffness-dependent Immunomodulatory and Neurotrophic Characteristics*. Advanced Healthcare Materials. 2021 Nov 16;2101663.

352. Breuls RGM, Jiya TU, Smit TH. *Scaffold Stiffness Influences Cell Behavior: Opportunities for Skeletal Tissue Engineering*. Open Orthop J. 2008 May 29;2:103–9.

353. Yi B, Xu Q, Liu W. *An overview of substrate stiffness guided cellular response and its applications in tissue regeneration*. Bioact Mater. 2021 Dec 25;15:82–102.

354. Saberi A, Jabbari F, Zarrintaj P, Saeb MR, Mozafari M. *Electrically Conductive Materials: Opportunities and Challenges in Tissue Engineering*. Biomolecules. 2019 Sep 4;9(9):448.

355. Metwally S, Stachewicz U. *Surface potential and charges impact on cell responses on biomaterials interfaces for medical applications*. Materials Science and Engineering: C. 2019 Nov 1;104:109883.

356. Dave K, Gomes VG. *Interactions at scaffold interfaces: Effect of surface chemistry, structural attributes and bioaffinity*. Materials Science and Engineering: C. 2019 Dec 1;105:110078.

357. Xie J, Shen H, Yuan G, Lin K, Su J. *The effects of alignment and diameter of electrospun fibers on the cellular behaviors and osteogenesis of BMSCs*. Materials Science and Engineering: C. 2021 Jan 1;120:111787.

358. Subramony SD, Dargis BR, Castillo M, Azeloglu EU, Tracey MS, Su A, et al. *The Guidance of Stem Cell Differentiation by Substrate Alignment and Mechanical Stimulation*. Biomaterials. 2013 Mar;34(8):1942–53.

359. Batool F, Özçelik H, Stutz C, Gegout PY, Benkirane-Jessel N, Petit C, et al. *Modulation of immune-inflammatory responses through surface modifications of biomaterials to*

promote bone healing and regeneration. J Tissue Eng. 2021 Oct 26;12:20417314211041428.

360. Alvarez MM, Liu JC, Trujillo-de Santiago G, Cha BH, Vishwakarma A, Ghaemmaghami AM, et al. *Delivery strategies to control inflammatory response: Modulating M1–M2 polarization in tissue engineering applications*. Journal of Controlled Release. 2016 Oct 28;240:349–63.

361. Salerno A, Cesarelli G, Pedram P, Netti PA. *Modular Strategies to Build Cell-Free and Cell-Laden Scaffolds towards Bioengineered Tissues and Organs*. J Clin Med. 2019 Nov 1;8(11):1816.

362. Oliveira ÉR, Nie L, Podstawczyk D, Allahbakhsh A, Ratnayake J, Brasil DL, et al. *Advances in Growth Factor Delivery for Bone Tissue Engineering*. Int J Mol Sci. 2021 Jan 18;22(2):903.

363. Lee K, Silva EA, Mooney DJ. *Growth factor delivery-based tissue engineering: general approaches and a review of recent developments*. Journal of The Royal Society Interface. 2010 Aug 18;8(55):153–70.

364. Dang JM, Leong KW. *Natural polymers for gene delivery and tissue engineering*. Advanced Drug Delivery Reviews. 2006 Jul 7;58(4):487–99.

365. Hosseinkhani H, Domb AJ, Sharifzadeh G, Nahum V. *Gene Therapy for Regenerative Medicine*. Pharmaceutics. 2023 Mar 6;15(3):856.

366. Zhang X, Godbey WT. *Viral vectors for gene delivery in tissue engineering*. Advanced Drug Delivery Reviews. 2006 Jul 7;58(4):515–34.

367. Nguyen EP, De Carvalho Castro Silva C, Merkoçi A. *Recent advancement in biomedical applications on the surface of two-dimensional materials: From biosensing to tissue engineering*. Nanoscale. 2020 Oct 7;12(37):19043–67.

368. Kwee BJ, Mooney DJ. *Biomaterials for Skeletal Muscle Tissue Engineering*. Current opinion in biotechnology. 2017 Oct 1;47:16.

369. Koons GL, Diba M, Mikos AG. *Materials design for bone-tissue engineering*. Nature Reviews Materials 2020 5:8. 2020 Jun 8;5(8):584–603.

370. Nguyen AH, Marsh P, Schmiess-Heine L, Burke PJ, Lee A, Lee J, et al. *Cardiac tissue engineering: state-of-the-art methods and outlook*. Journal of Biological Engineering 2019 13:1. 2019 Jun 28;13(1):1–21.

371. Scott L, Elídóttir K, Jeevaratnam K, Jurewicz I, Lewis R. *Electrical stimulation through conductive scaffolds for cardiomyocyte tissue engineering: Systematic review and narrative synthesis*. Annals of the New York Academy of Sciences. 2022 Jun 8; Available from: https://onlinelibrary.wiley.com/doi/10.1111/nyas.14812

372. Boni R, Ali A, Shavandi A, Clarkson AN. *Current and novel polymeric biomaterials for neural tissue engineering*. Journal of Biomedical Science 2018 25:1. 2018 Dec 20;25(1):1–21.

373. Bradbury EJ, Burnside ER. *Moving beyond the glial scar for spinal cord repair*. Nature Communications. 2019;10(1):1–15.

374. Lopes B, Sousa P, Alvites R, Branquinho M, Sousa AC, Mendonça C, et al. *Peripheral Nerve Injury Treatments and Advances: One Health Perspective*. Int J Mol Sci. 2022 Jan 14;23(2):918.

375. Li R, Li D hui, Zhang H yu, Wang J, Li X kun, Xiao J. *Growth factors-based therapeutic strategies and their underlying signaling mechanisms for peripheral nerve regeneration*. Acta Pharmacol Sin. 2020 Oct;41(10):1289–300.

376. Patel S, Athirasala A, Menezes PP, Ashwanikumar N, Zou T, Sahay G, et al. *Messenger RNA Delivery for Tissue Engineering and Regenerative Medicine Applications*. Tissue Eng Part A. 2019 Jan 1;25(1–2):91–112.

377. Bertucci C, Koppes R, Dumont C, Koppes A. *Neural responses to electrical stimulation in 2D and 3D in vitro environments*. Brain Research Bulletin. 2019 Oct 1;152:265–84.

378. Gaudin R, Knipfer C, Henningsen A, Smeets R, Heiland M, Hadlock T. *Approaches to Peripheral Nerve Repair: Generations of Biomaterial Conduits Yielding to Replacing Autologous Nerve Grafts in Craniomaxillofacial Surgery*. BioMed Research International. 2016;2016(1):3856262.

379. Rotshenker S. *Wallerian degeneration: the innate-immune response to traumatic nerve injury*. Journal of Neuroinflammation. 2011 Aug 30;8(1):109.

380. Huang C, Ouyang Y, Niu H, He N, Ke Q, Jin X, et al. *Nerve guidance conduits from aligned nanofibers: improvement of nerve regeneration through longitudinal nanogrooves on a fiber surface*. ACS Appl Mater Interfaces. 2015 Apr 8;7(13):7189–96.

381. Ryan AJ, Lackington WA, Hibbitts AJ, Matheson A, Alekseeva T, Stejskalova A, et al. *A Physicochemically Optimized and Neuroconductive Biphasic Nerve Guidance Conduit for Peripheral Nerve Repair*. Advanced Healthcare Materials. 2017;6(24):1–13.

382. Zhao Y, Liu Y, Lu C, Sun D, Kang S, Wang X, et al. *Reduced Graphene Oxide Fibers Combined with Electrical Stimulation Promote Peripheral Nerve Regeneration*. IJN. 2024 Mar;Volume 19:2341–57.

383. Xu H, Li R, Li Y, He Q, Yan X, Shu T, et al. *Preparation and Characterization of Poly Lactic Acid/Graphene Oxide/Nerve Growth Factor Scaffold with Electrical Stimulation for Peripheral Nerve Regeneration in vitro*. Journal Wuhan University of Technology, Materials Science Edition. 2020 Dec 1;35(6):1149–61.

384. Lackington WA, Ryan AJ, O'Brien FJ. *Advances in Nerve Guidance Conduit-Based Therapeutics for Peripheral Nerve Repair*. ACS Biomater Sci Eng. 2017 Jul 10;3(7):1221–35.

385. Hibbitts AJ, Kočí Z, Kneafsey S, Matsiko A, Žilić L, Dervan A, et al. *Multi-Factorial Nerve Guidance Conduit Engineering Improves Outcomes in Inflammation, Angiogenesis and Large Defect Nerve Repair*. Matrix Biology. 2022 Jan 13; Available from: https://linkinghub.elsevier.com/retrieve/pii/S0945053X22000026

386. Kwon SG, Kwon YW, Lee TW, Park GT, Kim JH. *Recent advances in stem cell therapeutics and tissue engineering strategies*. Biomaterials Research. 2018 Dec 19;22(1):36.

387. Wang A, Tang Z, Park IH, Zhu Y, Patel S, Daley GQ, et al. *Induced Pluripotent Stem Cells for Neural Tissue Engineering*. Biomaterials. 2011 Aug;32(22):5023–32.

388. Yi S, Zhang Y, Gu X, Huang L, Zhang K, Qian T, et al. *Application of stem cells in peripheral nerve regeneration*. Burns Trauma. 2020 Feb 27;8:tkaa002.

389. Miller RH. *The promise of stem cells for neural repair*. Brain Research. 2006 May 26;1091(1):258–64.

390. Doblado LR, Martínez-Ramos C, Pradas MM. *Biomaterials for Neural Tissue Engineering*. Front Nanotechnol. 2021 Apr 26; https://www.frontiersin.org/journals/nanotechnology/articles/10.3389/fnano.2021.643507/full

391. Bennett J, Das JM, Emmady PD. *Spinal Cord Injuries*. In: StatPearls [Internet]. Treasure Island (FL): StatPearls Publishing; 2024 [cited 2024 Aug 5]. Available from: http://www.ncbi.nlm.nih.gov/books/NBK560721/

392. Ahuja CS, Wilson JR, Nori S, Kotter MRN, Druschel C, Curt A, et al. *Traumatic spinal cord injury*. Nat Rev Dis Primers. 2017 Apr 27;3(1):1–21.

393. Silver J. *The glial scar is more than just astrocytes*. Exp Neurol. 2016 Dec;286:147–9.

394. Silver J. *CNS Regeneration: Only on One Condition*. Current Biology. 2009 Jun 9;19(11):R444–6.

395. Cregg JM, DePaul MA, Filous AR, Lang BT, Tran A, Silver J. *Functional regeneration beyond the glial scar*. Exp Neurol. 2014 Mar;253:197–207.

396. Chin JS, Milbreta U, Becker DL, Chew SY. *Targeting connexin 43 expression via scaffold mediated delivery of antisense oligodeoxynucleotide preserves neurons, enhances axonal extension, reduces astrocyte and microglial activation after spinal cord injury*. J Tissue Eng. 2023 Feb 10;14:20417314221145789.

397. Cronin M, Anderson PN, Cook JE, Green CR, Becker DL. *Blocking connexin43 expression reduces inflammation and improves functional recovery after spinal cord injury*. Molecular and Cellular Neuroscience. 2008 Oct;39(2):152–60.

398. Leahy LM, Woods I, Gutierrez-Gonzalez J, Maughan J, O'Connor C, Stasiewicz M, et al. *Electrostimulation via a 3D-printed, biomimetic, neurotrophic, electroconductive scaffold for the promotion of axonal regrowth after spinal cord injury*. Materials Today. 2024 Aug 28. https://www.sciencedirect.com/science/article/pii/S136970212400155X

399. Koffler J, Zhu W, Qu X, Platoshyn O, Dulin JN, Brock J, et al. *Biomimetic 3D-printed scaffolds for spinal cord injury repair*. Nature Medicine. 2019;25(2):263–9.

400. Sousa JPM, Stratakis E, Mano J, Marques PAAP. *Anisotropic 3D scaffolds for spinal cord guided repair: Current concepts*. Biomaterials Advances. 2023 Feb 23;213353.

401. Serafin A, Rubio MC, Carsi M, Ortiz-Serna P, Sanchis MJ, Garg AK, et al. *Electroconductive PEDOT nanoparticle integrated scaffolds for spinal cord tissue repair*. Biomaterials Research. 2022 Nov 22;26(1):63.

402. Chen K, Yu W, Zheng G, Xu Z, Yang C, Wang Y, et al. *Biomaterial-based regenerative therapeutic strategies for spinal cord injury*. NPG Asia Mater. 2024 Jan 19;16(1):1–29.

403. Schmitz JP, Hollinger JO. *The critical size defect as an experimental model for craniomandibulofacial nonunions*. Clin Orthop Relat Res. 1986 Apr;(205):299–308.

404. kumari S, Divakar S, Srivastava P, Singh BN, Mishra A. *Generation of Graphene oxide and nano-bioglass based scaffold for Bone tissue regeneration*. Biomedical Materials. 2022 Sep 16; https://iopscience.iop.org/article/10.1088/1748-605X/ac92b4

405. Pantulap U, Arango-Ospina M, Boccaccini AR. *Bioactive glasses incorporating less-common ions to improve biological and physical properties*. J Mater Sci: Mater Med. 2022 Jan;33(1):3.

406. Qi X, Huang Y, Han D, Zhang J, Cao J, Jin X, et al. *Three-dimensional poly (ε-caprolactone)/hydroxyapatite/collagen scaffolds incorporating bone marrow mesenchymal stem cells for the repair of bone defects*. Biomed Mater. 2016 Mar;11(2):025005.

407. Strunk T, Nawaz Q, Damiani C, Boccaccini A. *3D-printability of composite scaffolds based on PCL and bioactive glass nanoparticles for bone tissue engineering applications*.

408. Jeong J, Kim JH, Shim JH, Hwang NS, Heo CY. *Bioactive calcium phosphate materials and applications in bone regeneration*. Biomaterials Research. 2019 Jan 14;23(1):4.

409. Ghassemi T, Shahroodi A, Ebrahimzadeh MH, Mousavian A, Movaffagh J, Moradi A. *Current Concepts in Scaffolding for Bone Tissue Engineering*. Arch Bone Jt Surg. 2018 Mar;6(2):90–9.

410. Zhang Z, Hao Z, Xian C, Fang Y, Cheng B, Wu J, et al. *Neuro-Bone Tissue Engineering: Multiple potential translational strategies between nerve and bone*. Acta Biomaterialia. 2022 Sep 16; http://www.ncbi.nlm.nih.gov/pubmed/36116724

411. Chen S, Zhou X, Li T, He C. *Vascularization and Innervation for Bone Tissue Engineering*. Acc Mater Res. 2024 Jul 24; https://doi.org/10.1021/accountsmr.4c00165

412. Sadowska JM, Power RachaelN, Genoud KJ, Matheson A, González-Vázquez A, Costard L, et al. *A Multifunctional Scaffold for Bone Infection Treatment by Delivery of microRNA Therapeutics Combined With Antimicrobial Nanoparticles*. Advanced Materials. 2024;36(6):2307639.

413. Sadowska JM, Genoud KJ, Kelly DJ, Brien FJO. *Bone biomaterials for overcoming antimicrobial resistance : Advances in non- antibiotic antimicrobial approaches for regeneration of infected osseous tissue*. Materials Today. 2021 Mar 1;46:136–54.

414. Johnson CT, García AJ. *Scaffold-based Anti-infection Strategies in Bone Repair*. Ann Biomed Eng. 2015 Mar;43(3):515–28.

415. *Applications of Bioactive Ions in Bone Regeneration*. Chinese Journal of Dental Research. 2019 Jun 17;22(2):93–104.

416. Iqbal N, Pant T, Rohra N, Goyal A, Lawrence M, Dey A, et al. *Nanobiotechnology in Bone Tissue Engineering Applications: Recent Advances and Future Perspectives*. Applied Biosciences. 2023 Nov 15;2(4):617–38.

417. O'Neill E, Awale G, Daneshmandi L, Umerah O, Lo KWH. *The roles of ions on bone regeneration*. Drug Discovery Today. 2018 Apr 1;23(4):879–90.

418. Sadowska JM, Ziminska M, Ferreira C, Matheson A, Balouch A, Bogle J, et al. *Development of miR-26a-activated scaffold to promote healing of critical-sized bone defects through angiogenic and osteogenic mechanisms*. Biomaterials. 2023 Nov;122398.

419. Wang L, Pang Y, Tang Y, Wang X, Zhang D, Zhang X, et al. *A biomimetic piezoelectric scaffold with sustained Mg2+ release promotes neurogenic and angiogenic differentiation for enhanced bone regeneration*. Bioactive Materials. 2022 Nov 29; https://linkinghub.elsevier.com/retrieve/pii/S2452199X22004686

420. Alexandra S, Coelho R, Almeida JC, Unalan I, Detsch R, Margarida I, et al. *Cellular Response to Sol−Gel Hybrid Materials Releasing Boron and Calcium Ions*. ACS Biomaterials Science & Engineering. 2021; https://dx.doi.org/10.1021/acsbiomaterials.0c01546

421. Ellakwa TE, Ellakwa A, Abu-Khadra AS, Gomaa HM, El-Taib Heakal F, El-Sayed Ellakwa D. *Reviewing and exploring boron oxide's role in bioactive glasses: a synthesis of modeling and applications*. J Aust Ceram Soc. 2024 Oct 17; https://doi.org/10.1007/s41779-024-01103-w

422. Park M, Li Q, Shcheynikov N, Zeng W, Muallem S. *NaBC1 is a ubiquitous electrogenic Na+ -coupled borate transporter essential for cellular boron homeostasis and cell growth and proliferation*. Mol Cell. 2004 Nov 5;16(3):331–41.

423. Berger H. *Über das Elektrenkephalogramm des Menschen*. Archiv f Psychiatrie. 1929 Dec 1;87(1):527–70.

424. Ji B, Sun F, Guo J, Zhou Y, You X, Fan Y, et al. *Brainmask: an ultrasoft and moist micro-electrocorticography electrode for accurate positioning and long-lasting recordings*. Microsyst Nanoeng. 2023 Oct 10;9(1):126.

425. Lo YT, Jiang L, Woodington B, Middya S, Braendlein M, Lam J, et al. *Recording of single-unit activities with flexible micro-electrocorticographic array in rats for decoding of whole-body navigation*. J Neural Eng. 2024 Jul 10; https://iopscience.iop.org/article/10.1088/1741-2552/ad618c

426. Shokoueinejad M, Park DW, Jung YH, Brodnick SK, Novello J, Dingle A, et al. *Progress in the Field of Micro-Electrocorticography*. Micromachines (Basel). 2019 Jan 17;10(1):62.

427. Xie K, Zhang S, Dong S, Li S, Yu C, Xu K, et al. *Portable wireless electrocorticography system with a flexible microelectrodes array for epilepsy treatment*. Sci Rep. 2017 Aug 10;7(1):7808.

428. Kaiju T, Doi K, Yokota M, Watanabe K, Inoue M, Ando H, et al. *High Spatiotemporal Resolution ECoG Recording of Somatosensory Evoked Potentials with Flexible Micro-Electrode Arrays*. Front Neural Circuits. 2017 Apr 11; https://www.frontiersin.org/journals/neural-circuits/articles/10.3389/fncir.2017.00020/full

429. Li X, Song Y, Xiao G, He E, Xie J, Dai Y, et al. *PDMS–Parylene Hybrid, Flexible Micro-ECoG Electrode Array for Spatiotemporal Mapping of Epileptic Electrophysiological Activity from Multicortical Brain Regions*. ACS Applied Bio Materials. 2021 Oct 9;acsabm.1c00923.

430. Li J, Ma Y, Huang D, Wang Z, Zhang Z, Ren Y, et al. *High-Performance Flexible Microneedle Array as a Low-Impedance Surface Biopotential Dry Electrode for Wearable Electrophysiological Recording and Polysomnography*. Nano-Micro Letters 2022 14:1. 2022 Jun 14;14(1):1–22.

431. Wang X, Qiu W, Lu C, Jiang Z, Hou C, Li Y, et al. *Fabrication of Flexible and Conductive Microneedle Array Electrodes from Silk Fibroin by Mesoscopic Engineering*. Advanced Functional Materials. n/a(n/a):2311535.

432. Zhu H. *Implanted Electrodes and Microneedle Array Electrodes for the Neuromodulation*. Vol. 2022, Highlights in Science, Engineering and Technology IPIIS. 2022.

433. Zhao Z, Li X, He F, Wei X, Lin S, Xie C. *Parallel, minimally-invasive implantation of ultra-flexible neural electrode arrays*. J Neural Eng. 2019 Jun;16(3):035001.

434. van Daal R, Kraft M, Kloosterman F, Aarts A. *Ultra-flexible high-density electrode arrays for chronic deep brain neural interfacing*. 2023. Available from: https://lirias.kuleuven.be/4084109

435. Horváth C, Csikós K, Árkossy B, Klein E, Ruther P, Ulbert I, et al. *Polymer-based laminar probes with an ultra-long flexible spiral-shaped cable for in vivo neural recordings*. Sensors and Actuators B: Chemical. 2024 Oct 15;417:136220.

436. Musk E, Neuralink. *An Integrated Brain-Machine Interface Platform With Thousands of Channels*. Journal of Medical Internet Research. 2019 Oct 31;21(10):e16194.

437. *Will we ever control the world with our minds?* [Internet]. [cited 2024 Sep 5]. Available from: https://www.bbc.com/future/article/20190814-will-we-ever-control-the-world-with-our-minds

438. Duffy C. *First Neuralink human trial subject can control a computer mouse with brain implant, Elon Musk says | CNN Business* [Internet]. CNN. 2024 [cited 2024 Sep 8]. Available from: https://www.cnn.com/2024/02/20/tech/first-neuralink-human-subject-computer-mouse-elon-musk/index.html

439. Drew L. *The ethics of brain–computer interfaces*. Nature. 2019 Jul 25;571(7766):S19–21.

440. Illes J, Hossain S. *Neuroethics: Anticipating the Future*. Oxford University Press; 2017. 693 p.

441. *Materials for Bioelectronics in Healthcare* [Internet]. Henry Royce Institute. [cited 2024 Oct 2]. Available from: https://www.royce.ac.uk/collaborate/roadmapping-landscaping/materials-for-bioelectronics-in-healthcare/

442. Zeng Q, Li X, Zhang S, Deng C, Wu T. *Think big, see small—A review of nanomaterials for neural interfaces*. Nano Select. 2021 Nov 14; Available from: https://onlinelibrary.wiley.com/doi/full/10.1002/nano.202100256

443. Wang M, Mi G, Shi D, Bassous N, Hickey D, Webster TJ. *Nanotechnology and Nanomaterials for Improving Neural Interfaces*. Advanced Functional Materials. 2018;28(12):1700905.

444. Faisal SN, Iacopi F. *Thin-Film Electrodes Based on Two-Dimensional Nanomaterials for Neural Interfaces*. ACS Applied Nano Materials. 2022 Jul 28; Available from: https://pubs-acs-org.elib.tcd.ie/doi/full/10.1021/acsanm.2c03056

445. Wu N, Wan S, Su S, Huang H, Dou G, Sun L. *Electrode materials for brain–machine interface: A review*. InfoMat. 2021 Aug 11;inf2.12234.

446. Fattahi P, Yang G, Kim G, Abidian MR. *A Review of Organic and Inorganic Biomaterials for Neural Interfaces*. Advanced Materials. 2014 Mar 26;26(12):1846–85.

447. Otte E, Vlachos A, Asplund M. *Engineering strategies towards overcoming bleeding and glial scar formation around neural probes*. Cell Tissue Res. 2022;387(3):461–77.

448. Polikov VS, Tresco PA, Reichert WM. *Response of brain tissue to chronically implanted neural electrodes*. Journal of Neuroscience Methods. 2005 Oct 15;148(1):1–18.

449. Salatino JW, Ludwig KA, Kozai TDY, Purcell EK. *Glial responses to implanted electrodes in the brain*. Nat Biomed Eng. 2017 Nov;1(11):862–77.

450. Schulte J, Ashouri D, Stieglitz T. *The Longevity of Neural Interfaces—Mechanical Oscillation of Thin Film Metal-Based Neural Electrodes Determine Stability During Electrical Stimulation*. Adv Funct Materials. 2023 Dec 2;2310130.

451. Luan L, Robinson JT, Aazhang B, Chi T, Yang K, Li X, et al. *Recent Advances in Electrical Neural Interface Engineering: Minimal Invasiveness, Longevity, and Scalability*. 2020; Available from: https://doi.org/10.1016/j.neuron.2020.10.011

452. Redolfi Riva E, Micera S. *Progress and challenges of implantable neural interfaces based on nature-derived materials*. Bioelectronic Medicine. 2021 Dec 27;7(1):6.

453. Chamanzar M, Malekoshoaraie M, Wu B, Krahe D, Ahmed Z, Pupa S, et al. *Fully flexible implantable neural probes for electrophysiology recording and controlled neurochemical modulation*. Research Square; 2023 Sep. Available from: https://www.researchsquare.com/article/rs-3322010/v1

454. Cho Y, Park S, Lee J, Yu KJ. *Emerging Materials and Technologies with Applications in Flexible Neural Implants: A Comprehensive Review of Current Issues with Neural Devices*. Advanced Materials. 2021 May 29;2005786.

455. Cho KW, Sunwoo SH, Hong YJ, Koo JH, Kim JH, Baik S, et al. *Soft Bioelectronics Based on Nanomaterials*. Chemical Reviews. 2021 Dec 28;acs.chemrev.1c00531.

456. Peñas-Núñez SJ, Mecerreyes D, Criado-Gonzalez M. *Recent Advances and Developments in Injectable Conductive Polymer Gels for Bioelectronics*. ACS Appl Bio Mater. 2024 Feb 16;acsabm.3c01224.

457. Yang M, Chen P, Qu X, Zhang F, Ning S, Ma L, et al. *Robust Neural Interfaces with Photopatternable, Bioadhesive, and Highly Conductive Hydrogels for Stable Chronic Neuromodulation*. ACS Nano. 2023 Jan 11; https://pubs.acs.org/doi/full/10.1021/acsnano.2c04606

458. Go GT, Lee Y, Seo DG, Lee TW. *Organic Neuro-Electronics: From Neural Interface to Neuroprosthetics*. Advanced Materials. 2022 Aug 4;2201864.

459. Bettucci O, Matrone GM, Santoro F. *Conductive Polymer-Based Bioelectronic Platforms toward Sustainable and Biointegrated Devices: A Journey from Skin to Brain across Human Body Interfaces*. Advanced Materials Technologies. 2021 Jul;2100293.

460. Zhou J, Vijayavenkataraman S. *3D-printable conductive materials for tissue engineering and biomedical applications*. 2021; Available from: https://doi.org/10.1016/j.bprint.2021.e00166

461. Inal S. *Turning tissues into conducting matter*. Science. 2023 Feb 24;379(6634):758–9.

462. Zhu M, Wang H, Li S, Liang X, Zhang M, Dai X, et al. *Flexible Electrodes for In Vivo and In Vitro Electrophysiological Signal Recording*. Advanced Healthcare Materials. 2021 May 29;2100646.

463. Kostarelos K, Vincent M, Hebert C, Garrido JA. *Graphene in the Design and Engineering of Next-Generation Neural Interfaces*. Advanced Materials. 2017 Nov 13;29(42).

464. Driscoll N, Richardson AG, Maleski K, Anasori B, Adewole O, Lelyukh P, et al. *Two-Dimensional Ti_3C_2 MXene for High-Resolution Neural Interfaces*. ACS Nano. 2018 Oct 23;12(10):10419–29.

465. Halim A, Qu KY, Zhang XF, Huang NP. *Recent Advances in the Application of Two-Dimensional Nanomaterials for Neural Tissue Engineering and Regeneration*. ACS Biomaterials Science & Engineering. 2021 Jul 22;acsbiomaterials.1c00490.

466. Kotov NA, Winter JO, Clements IP, Jan E, Timko BP, Campidelli S, et al. *Nanomaterials for Neural Interfaces*. Advanced Materials. 2009 Oct 26;21(40):3970–4004.

467. Han J, Choi J, Jeong H, Park D, Cheong E, Sung J, et al. *Impact of Impedance Levels on Recording Quality in Flexible Neural Probes*. Sensors. 2024 Jan;24(7):2300.

468. Negi S, Bhandari R, Solzbacher F. *A novel technique for increasing charge injection capacity of neural electrodes for efficacious and safe neural stimulation*. Annual International Conference of the IEEE Engineering in Medicine and Biology Society IEEE Engineering in Medicine and Biology Society Annual International Conference. 2012;2012:5142–5.

469. Teixeira HJ, Dias C, Veloso RC, Apolinário A, Ventura J. *Tuning PEDOT:PSS low-impedance thin films with high charge injection for microelectrodes applications*. Progress in Organic Coatings. 2022;168:106894.

470. Bonfrate V, Manno D, Serra A, Salvatore L, Sannino A, Buccolieri A, et al. *Enhanced electrical conductivity of collagen films through long-range aligned iron oxide nanoparticles*. Journal of Colloid and Interface Science. 2017 Sep 1;501:185–91.

471. Marianiová D, Lapčík L. *Electrical conductivity measurements of hyaluronic acid and collagen*. Colloid Polym Sci. 1993 Feb 1;271(2):143–7.

472. Bramini M, Alberini G, Colombo E, Chiacchiaretta M, DiFrancesco ML, Maya-Vetencourt JF, et al. *Interfacing graphene-based materials with neural cells*. Frontiers in Systems Neuroscience. 2018 Apr 11;12:12.

473. Boehler C, Carli S, Fadiga L, Stieglitz T, Asplund M. *Tutorial: guidelines for standardized performance tests for electrodes intended for neural interfaces and bioelectronics*. Nat Protoc. 2020 Nov;15(11):3557–78.

474. Wang Y, Yang X, Zhang X, Wang Y, Pei W. *Implantable intracortical microelectrodes: reviewing the present with a focus on the future*. Microsystems & Nanoengineering 2023 9:1. 2023 Jan 5;9(1):1–17.

475. Wijeratne K, Ail U, Brooke R, Vagin M, Liu X, Fahlman M, et al. *Bulk electronic transport impacts on electron transfer at conducting polymer electrode–electrolyte interfaces*. Proc Natl Acad Sci USA. 2018 Nov 20;115(47):11899–904.

476. Seker E, Berdichevsky Y, Begley MR, Reed ML, Staley KJ, Yarmush ML. *The fabrication of low-impedance nanoporous gold multiple-electrode arrays for neural electrophysiology studies*. Nanotechnology. 2010 Mar 26;21(12):125504.

477. Kappenman ES, Luck SJ. *The effects of electrode impedance on data quality and statistical significance in ERP recordings*. Psychophysiology. 2010 Mar; https://onlinelibrary.wiley.com/doi/10.1111/j.1469-8986.2010.01009.x

478. Castagnola V, Descamps E, Lecestre A, Dahan L, Remaud J, Nowak LG, et al. *Parylene-based flexible neural probes with PEDOT coated surface for brain stimulation and recording*. Biosensors and Bioelectronics. 2015 May 15;67:450–7.

479. Steins H, Mierzejewski M, Brauns L, Stumpf A, Kohler A, Heusel G, et al. *A flexible protruding microelectrode array for neural interfacing in bioelectronic medicine*. Microsyst Nanoeng. 2022 Dec 22;8(1):1–15.

480. Erdey-Grúz T, Volmer M. *Zur Theorie der Wasserstoff Überspannung*. Zeitschrift für Physikalische Chemie. 1930 Sep 1;150A(1):203–13.

481. Zheng J, Tan G, Shan P, Liu T, Hu J, Feng Y, et al. *Understanding Thermodynamic and Kinetic Contributions in Expanding the Stability Window of Aqueous Electrolytes*. Chem. 2018 Dec 13;4(12):2872–82.

482. Cogan SF, Ludwig KA, Welle CG, Takmakov P. *Tissue damage thresholds during therapeutic electrical stimulation*. J Neural Eng. 2016 Apr;13(2):021001.

483. Cisnal A, Fraile JC, Pérez-Turiel J, Muñoz-Martinez V, Müller C, Ihmig FR. *A Measurement Setup and Automated Calculation Method to Determine the Charge Injection Capacity of Implantable Microelectrodes*. Sensors (Basel, Switzerland). 2018 Dec 1; Available from: /pmc/articles/PMC6308657/

484. W I. *The chronaxie time and its practical importance*. Pacing and clinical electrophysiology : PACE. 1980 May. https://pubmed.ncbi.nlm.nih.gov/6160523/

485. Rattay F, Paredes LP, Leao RN. *Strength–duration relationship for intra- versus extracellular stimulation with microelectrodes*. Neuroscience. 2012 Jul 12;214(5):1–13.

486. Rochford AE, Carnicer-Lombarte A, Curto VF, Malliaras GG, Barone DG. *When Bio Meets Technology: Biohybrid Neural Interfaces*. Advanced Materials. 2020 Apr 13;32(15):1903182.

487. Alwahab NSA. *Engineering Hydrogel-coated Neural Interfaces for Chronic Deep Brain Recording*. 2023. https://infoscience.epfl.ch/record/302110

488. Moshayedi P, Ng G, Kwok JCF, Yeo GSH, Bryant CE, Fawcett JW, et al. *The relationship between glial cell mechanosensitivity and foreign body reactions in the central nervous system*. Biomaterials. 2014 Apr 1;35(13):3919–25.

489. Marinval N, Chew SY. *Mechanotransduction assays for neural regeneration strategies: A focus on glial cells*. APL Bioeng. 2021 Apr 30;5(2):021505.

490. Pathak MM, Nourse JL, Tran T, Hwe J, Arulmoli J, Le DTT, et al. *Stretch-activated ion channel Piezo1 directs lineage choice in human neural stem cells*. Proc Natl Acad Sci U S A. 2014 Nov 11;111(45):16148–53.

491. Lourenço T, Paes de Faria J, Bippes CA, Maia J, Lopes-da-Silva JA, Relvas JB, et al. *Modulation of oligodendrocyte differentiation and maturation by combined biochemical and mechanical cues*. Sci Rep. 2016 Feb 16;6:21563.

492. Adewole DO, Serruya MD, Wolf JA, Cullen DK. *Bioactive Neuroelectronic Interfaces*. Frontiers in Neuroscience. 2019 Mar 29;13:269.

493. Lotti F, Ranieri F, Vadalà G, Zollo L, Di Pino G. *Invasive intraneural interfaces: Foreign body reaction issues*. Frontiers in Neuroscience. 2017 Sep 6;11(SEP):497.

494. Jeong YC, Eol Lee H, Shin A, Kim DG, Jae Lee K, Kim D, et al. *Progress in Brain-Compatible Interfaces with Soft Nanomaterials*. Advanced Materials. 2020 Sep 1;32(35):1907522.

495. Lee M, Shim HJ, Choi C, Kim DH. *Soft High-Resolution Neural Interfacing Probes: Materials and Design Approaches*. Nano Lett. 2019 May 8;19(5):2741–9.

496. Liu Y, McGuire AF, Lou HY, Li TL, Tok JBH, Cui B, et al. *Soft conductive micropillar electrode arrays for biologically relevant electrophysiological recording*. Proc Natl Acad Sci USA. 2018 Nov 13;115(46):11718–23.

497. Manousiouthakis E, Park J, Hardy JG, Lee JY, Schmidt CE. *Towards the translation of electroconductive organic materials for regeneration of neural tissues*. Acta Biomaterialia. 2022 Feb 1;139:22–42.

498. Spencer AR, Primbetova A, Koppes AN, Koppes RA, Fenniri H, Annabi N. *Electroconductive Gelatin Methacryloyl-PEDOT:PSS Composite Hydrogels: Design, Synthesis, and Properties*. ACS Biomaterials Science and Engineering. 2018 May 14;4(5):1558–67.

499. Dong R, Ma PX, Guo B. *Conductive biomaterials for muscle tissue engineering*. Biomaterials. 2020 Jan 1;229:119584.

500. Wu Y, Wang L, Hu T, Ma PX, Guo B. *Conductive micropatterned polyurethane films as tissue engineering scaffolds for Schwann cells and PC12 cells*. Journal of Colloid and Interface Science. 2018 May 15;518:252–62.

501. Lind G, Linsmeier CE, Thelin J, Schouenborg J. *Gelatine-embedded electrodes - A novel biocompatible vehicle allowing implantation of highly flexible microelectrodes*. Journal of Neural Engineering. 2010 Aug;7(4).

502. Shen W, Karumbaiah L, Liu X, Saxena T, Chen S, Patkar R, et al. *Extracellular matrix-based intracortical microelectrodes: Toward a microfabricated neural interface based on natural materials*. Microsystems and Nanoengineering. 2015;1.

503. Vitale F, Shen W, Driscoll N, Burrell JC, Richardson AG, Adewole O, et al. *Biomimetic extracellular matrix coatings improve the chronic biocompatibility of microfabricated subdural microelectrode arrays*. PLoS ONE. 2018 Nov 1;13(11).

504. Asaro GA, Solazzo M, Suku M, Spurling D, Genoud K, Gonzalez JG, et al. *MXene functionalized collagen biomaterials for cardiac tissue engineering driving iPSC-derived cardiomyocyte maturation*. npj 2D Materials and Applications 2023 7:1. 2023 Jun 27;7(1):1–13.

505. Fabbri R, Saracino E, Treossi E, Zamboni R, Palermo V, Benfenati V. *Graphene glial-interfaces: challenges and perspectives*. Nanoscale. 2021 Mar 4;13(8):4390–407.

506. Fabbri R, Scidà A, Kovtun A, Candini A, Kirdajova D, Spennato D, et al. *Graphene-Glial interfaces for the selective modulation of brain signaling*. Adv Healthc Mater. 2018;6:1801139.

507. Lattanzi W, Dixon DT, Gomillion CT. *Conductive Scaffolds for Bone Tissue Engineering: Current State and Future Outlook*. Journal of Functional Biomaterials 2022, Vol 13, Page 1. 2021 Dec 21;13(1):1.

508. Por Hajrezaei S, Haghbin Nazarpak M, Hojjati Emami S, Shahryari E. *Biocompatible and Electroconductive Nanocomposite Scaffolds with Improved Piezoelectric Response for Bone Tissue Engineering*. Fernández-García M, editor. International Journal of Polymer Science. 2022 Apr 25;2022:1–10.

509. Zhang W, Luo Y, Xu J, Guo C, Shi J, Li L, et al. *The Possible Role of Electrical Stimulation in Osteoporosis: A Narrative Review*. Medicina 2023, Vol 59, Page 121. 2023 Jan 8;59(1):121.

510. Zhao H, Liu C, Liu Y, Ding Q, Wang T, Li H, et al. *Harnessing electromagnetic fields to assist bone tissue engineering*. Stem Cell Research & Therapy 2023 14:1. 2023 Jan 11;14(1):1–22.

511. Zhang X, Wang T, Zhang Z, Liu H, Li L, Wang A, et al. *Electrical stimulation system based on electroactive biomaterials for bone tissue engineering*. Materials Today. 2023 Jul 17; https://linkinghub.elsevier.com/retrieve/pii/S1369702123002043

512. Dixon DT, Gomillion CT. *3D-Printed conductive polymeric scaffolds with direct current electrical stimulation for enhanced bone regeneration*. Journal of Biomedical Materials Research Part B: Applied Biomaterials. 2023;111(7):1351–64.

513. Zhou Z, Zheng J, Meng X, Wang F. *Effects of Electrical Stimulation on Articular Cartilage Regeneration with a Focus on Piezoelectric Biomaterials for Articular Cartilage Tissue Repair and Engineering*. International Journal of Molecular Sciences 2023, Vol 24, Page 1836. 2023 Jan 17;24(3):1836.

514. Katoh K. *Effects of Electrical Stimulation of the Cell: Wound Healing, Cell Proliferation, Apoptosis, and Signal Transduction*. Medical Sciences. 2023 Mar. https://www.ncbi.nlm.nih.gov/pmc/articles/PMC9944882/

515. Yu X, Wu G, Cai P, Ding Y, Cui J, Wu J, et al. *Carbon Fiber-Mediated Electrospinning Scaffolds Can Conduct Electricity for Repairing Defective Tendon*. ACS Appl Mater Interfaces. 2024 Sep 17. https://doi.org/10.1021/acsami.4c12245

516. Zarrintaj P, Manouchehri S, Ahmadi Z, Saeb MR, Urbanska AM, Kaplan DL, et al. *Agarose-based biomaterials for tissue engineering*. Carbohydrate Polymers. 2018 May 1;187:66–84.

517. Zhao S, Mehta AS, Zhao M. *Biomedical applications of electrical stimulation*. Cell Mol Life Sci. 2020 Jan 23;77(14):2681–99.

518. Chen C, Bai X, Ding Y, Lee IS. *Electrical stimulation as a novel tool for regulating cell behavior in tissue engineering*. Biomaterials Research 2019 23:1. 2019 Dec 5;23(1):1–12.

519. Ye H, Hendee J, Ruan J, Zhirova A, Ye J, Dima M. *Neuron matters: neuromodulation with electromagnetic stimulation must consider neurons as dynamic identities*. Journal of NeuroEngineering and Rehabilitation. 2022 Nov 3;19(1):116.

520. Rattay F. *The basic mechanism for the electrical stimulation of the nervous system*. Vol. 89, Neuroscience. 1999 p. 335–46.

521. Madison DV, Malenka RC, Nicoll RA. *Mechanisms Underlying Long-Term Potentiation of Synaptic Transmission*. Annu Rev Neurosci. 1991 Mar;14(1):379–97.

522. Farokhi M, Mottaghitalab F, Saeb MR, Shojaei S, Zarrin NK, Thomas S, et al. *Conductive Biomaterials as Substrates for Neural Stem Cells Differentiation towards Neuronal Lineage Cells*. Macromolecular Bioscience. 2021 Jan 1;21(1).

523. Choi I, Kwon GH, Lee S, Nam CS. *Functional Electrical Stimulation Controlled by Motor Imagery Brain-Computer Interface for Rehabilitation*. Brain Sci. 2020 Aug 2;10(8):512.

524. Jovanovic LI, Popovic MR, Marquez-Chin C. *KITE-BCI: A brain-computer interface system for functional electrical stimulation therapy*. J Spinal Cord Med. 44(Suppl 1):S203–14.

525. Furlan JC, Pakosh M, Craven BC, Popovic MR. *Insights on the Potential Mechanisms of Action of Functional Electrical Stimulation Therapy in Combination With Task-Specific Training: A Scoping Review*. Neuromodulation: Technology at the Neural Interface. 2021 May 24;ner.13403.

526. Hong G, Lieber CM. *Novel electrode technologies for neural recordings*. Nat Rev Neurosci. 2019 Jun;20(6):330–45.

527. Drongelen W van. *Signal Processing for Neuroscientists*. Academic Press; 2018. 742 p.

528. Tang-Schomer MD. *3D axon growth by exogenous electrical stimulus and soluble factors*. Brain Research. 2018 Jan 1;1678:288–96.

529. Purves D, Augustine GJ, Fitzpatrick D, Katz LC, LaMantia AS, McNamara JO, et al. *The Refractory Period*. In: Neuroscience 2nd edition. Sinauer Associates; 2001. Available from: https://www.ncbi.nlm.nih.gov/books/NBK11146/

530. Neudorfer C, Chow C, Boutet A, Loh A, Germann J, Elias GJB, et al. *Kilohertz-frequency stimulation of the nervous system: a review of underlying mechanisms*. Brain Stimulation. 2021 May 1;14(3):513–30.

531. Mohan UR, Watrous AJ, Miller JF, Lega BC, Sperling MR, Worrell GA, et al. *The effects of direct brain stimulation in humans depend on frequency, amplitude, and white-matter proximity*. Brain Stimulation. 2020 Sep 1;13(5):1183–95.

532. Nguyen HT, Sapp S, Wei C, Chow JK, Nguyen A, Coursen J, et al. *Electric field stimulation through a biodegradable polypyrrole-co-polycaprolactone substrate enhances neural cell growth*. Journal of Biomedical Materials Research Part A. 2014;102(8):2554–64.

533. Agrawal L, Vimal SK, Barzaghi P, Takashi S, Terenzio M. *Biodegradable and electrically conductive melanin-Poly (3-hydroxybutyrate) 3D fibrous scaffolds for neural tissue engineering applications*. Macromolecular Bioscience. 2022 Sep 17;2200315.

534. Zhao Y, Liang Y, Ding S, Zhang K, Mao H quan, Yang Y. *Application of conductive PPy/SF composite scaffold and electrical stimulation for neural tissue engineering*. Biomaterials. 2020 Oct 1;255:120164.

535. McCreery DB, Agnew WF, Yuen TGH, Bullara L. *Charge density and charge per phase as cofactors in neural injury induced by electrical stimulation*. IEEE Transactions on Biomedical Engineering. 1990 Oct;37(10):996–1001.

536. McCreery DB, Agnew WF, Bullara LA. *The Effects of Prolonged Intracortical Microstimulation on the Excitability of Pyramidal Tract Neurons in the Cat*. Annals of Biomedical Engineering. 2002 Jan 1;30(1):107–19.

537. Abiri R, Borhani S, Sellers EW, Jiang Y, Zhao X. *A comprehensive review of EEG-based brain–computer interface paradigms*. J Neural Eng. 2019 Jan;16(1):011001.

538. Christopher deCharms R. *Applications of real-time fMRI*. Nat Rev Neurosci. 2008 Sep;9(9):720–9.

539. Xie Y, Peng Y, Guo J, Liu M, Zhang B, Yin L, et al. *Materials and devices for high-density, high-throughput micro-electrocorticography arrays*. Fundamental Research. 2024 Feb 28. https://www.sciencedirect.com/science/article/pii/S2667325824000402

540. Hong JH, Lee JY, Dutta A, Yoon SL, Cho YU, Kim K, et al. *Monolayer, Open-Mesh, Pristine PEDOT:PSS-based Conformal Brain Implants for Fully MRI-Compatible Neural Interfaces*. Biosensors and Bioelectronics. 2024 May 28;116446.

541. Hong G, Yang X, Zhou T, Lieber CM. *Mesh electronics: a new paradigm for tissue-like brain probes*. Current Opinion in Neurobiology. 2018 Jun 1;50:33–41.

542. *g.tec medical engineering GmbH | Brain-Computer Interface & Neurotechnology* [Internet]. g.tec medical engineering GmbH. [cited 2024 Sep 5]. Available from: https://www.gtec.at/

543. *Neuralink — Pioneering Brain Computer Interfaces* [Internet]. [cited 2024 Sep 5]. Available from: https://neuralink.com/

544. Medtronic. *Deep Brain Stimulation Systems - Activa Platform* [Internet]. [cited 2024 Sep 5]. Available from: https://europe.medtronic.com/xd-en/healthcare-professionals/products/neurological/deep-brain-stimulation-systems/activa-platform.html

545. Liu J, Fu TM, Cheng Z, Hong G, Zhou T, Jin L, et al. *Syringe-injectable electronics*. Nature Nanotech. 2015 Jul;10(7):629–36.

546. Veitinger S, DeRose J, Greb C. *What is the Patch-Clamp Technique?* 2023 May 4 [cited 2024 Sep 5]; Available from: https://www.leica-microsystems.com/science-lab/life-science/the-patch-clamp-technique/

547. *Neuropixels | Janelia Research Campus* [Internet]. [cited 2024 Sep 1]. Available from: https://www.janelia.org/open-science/neuropixels

548. igeneve.com. *Mission* [Internet]. inbrain-neuroelectronics. [cited 2024 Sep 6]. Available from: https://inbrain-neuroelectronics.com/

549. *Utah Array, Electrodes | Products* [Internet]. Blackrock Neurotech. [cited 2024 Sep 6]. Available from: https://blackrockneurotech.com/products/utah-array/

550. Bianchi M, Guzzo S, Lunghi A, Greco P, Pisciotta A, Murgia M, et al. *Synergy of Nanotopography and Electrical Conductivity of PEDOT/PSS for Enhanced Neuronal Development*. ACS Appl Mater Interfaces. 2023 Dec 13;

551. Perkucin I. *Soft Electronic Materials Inspired by Biologic Derivatives for use in Neural Regenerative Applications*. 2022.

552. Li YM, Ji Y, Meng YX, Kim YJ, Lee H, Kurian AG, et al. *Neural Tissue-Like, not Supraphysiological, Electrical Conductivity Stimulates Neuronal Lineage Specification through Calcium Signaling and Epigenetic Modification*. Advanced Science. 2400586.

553. Zarrintaj P, Zangene E, Manouchehri S, Amirabad LM, Baheiraei N, Hadjighasem MR, et al. *Conductive biomaterials as nerve conduits: Recent advances and future challenges*. Applied Materials Today. 2020 Sep 1;20:100784.

554. Malarkey EB, Fisher KA, Bekyarova E, Liu W, Haddon RC, Parpura V. *Conductive Single-Walled Carbon Nanotube Substrates Modulate Neuronal Growth*. Nano Lett. 2009 Jan;9(1):264–8.

555. Rajnicek AM, Zhao Z, Moral-Vico J, Cruz AM, McCaig CD, Casañ-Pastor N. *Controlling Nerve Growth with an Electric Field Induced Indirectly in Transparent Conductive Substrate Materials*. Advanced Healthcare Materials. 2018;7(17):1800473.

556. Kotwal A, Schmidt CE. *Electrical stimulation alters protein adsorption and nerve cell interactions with electrically conducting biomaterials*. Biomaterials. 2001 May 1;22(10):1055–64.

557. Guo R, Zhang S, Xiao M, Qian F, He Z, Li D, et al. *Accelerating bioelectric functional development of neural stem cells by graphene coupling: Implications for neural interfacing with conductive materials*. Biomaterials. 2016 Nov 1;106:193–204.

558. Ghasemi-Mobarakeh L, Prabhakaran MP, Morshed M, Nasr-Esfahani MH, Baharvand H, Kiani S, et al. *Application of conductive polymers, scaffolds and electrical stimulation for nerve tissue engineering*. J Tissue Eng Regen Med. 2011 Apr;5(4):e17–35.

559. Feng Y, Yu Z, Liu H, Guan L, Yang X, Zvyagin AV, et al. *Biomimicking 3D soft scaffold combined with electrical stimulation to manipulate neural stem cell differentiation for guidance spinal cord injury repair*. Materials Today. 2023 Nov;S1369702123003401.

560. Han F, Ma X, Zhai Y, Cui L, Yang L, Zhu Z, et al. *Strategy for Designing a Cell Scaffold to Enable Wireless Electrical Stimulation for Enhanced Neuronal Differentiation of Stem Cells*. Advanced Healthcare Materials. 2021;10(11):2100027.

561. Ferguson M, Sharma D, Ross D, Zhao F. *A Critical Review of Microelectrode Arrays and Strategies for Improving Neural Interfaces*. Advanced Healthcare Materials. 2019 Oct 1;8(19):1900558.

562. Kaushik R. *Neuralink and Brain-Machine Interfaces: A Review*. Science and Technology. 2021;10(02).

563. Ferro MD, Proctor CM, Gonzalez A, Jayabal S, Zhao E, Gagnon M, et al. *NeuroRoots, a bio-inspired, seamless brain machine interface for long-term recording in delicate brain regions*. AIP Advances. 2024 Aug 7;14(8):085109.

564. Canales A, Park S, Kilias A, Anikeeva P. *Multifunctional Fibers as Tools for Neuroscience and Neuroengineering*. Acc Chem Res. 2018 Apr 17;51(4):829–38.

565. Garwood IC, Major AJ, Antonini MJ, Correa J, Lee Y, Sahasrabudhe A, et al. *Multifunctional fibers enable modulation of cortical and deep brain activity during cognitive behavior in macaques*. Science Advances. 2023 Oct 6;9(40):eadh0974.

566. Rochford AE, Carnicer-Lombarte A, Kawan M, Jin A, Hilton S, Curto VF, et al. *Functional neurological restoration of amputated peripheral nerve using biohybrid regenerative bioelectronics*. Science Advances. 2023 Mar 22;9(12). Available from: https://www.science.org/doi/10.1126/sciadv.add8162

567. Wang Y, Liu S, Wang H, Zhao Y, Zhang XD. *Neuron devices: emerging prospects in neural interfaces and recognition*. Microsyst Nanoeng. 2022 Dec 7;8(1):1–13.

568. Valeriani D, Santoro F, Ienca M. *The present and future of neural interfaces*. Front Neurorobot. 2022 Oct 11. www.frontiersin.org/journals/neurorobotics/articles/10.3389/fnbot.2022.953968/full

569. Geddes LA. *The first stimulators-reviewing the history of electrical stimulation and the devices crucial to its development*. IEEE Engineering in Medicine and Biology Magazine. 1994 Aug;13(4):532–42.

570. Sahni D, Jea A, Mata JA, Marcano DC, Sivaganesan A, Berlin JM, et al. *Biocompatibility of pristine graphene for neuronal interface*. J Neurosurg: Pediatrics. 2013;11:575–83.

571. Sayadi JJ, Sayadi L, Satteson E, Chopan M. *Nerve injury and repair in a ketogenic milieu: A systematic review of traumatic injuries to the spinal cord and peripheral nervous tissue*. Raoul C, editor. PloS one. 2021 Jan 4;16(1):e0244244.

572. Wang S, Wen X, Fan Z, Ding X, Wang Q, Liu Z, et al. *Research advancements on nerve guide conduits for nerve injury repair*. Reviews in the Neurosciences. 2024 Mar 25 https://www.degruyter.com/document/doi/10.1515/revneuro-2023-0093/html

573. Liu H, Feng Y, Che S, Guan L, Yang X, Zhao Y, et al. *An Electroconductive Hydrogel Scaffold with Injectability and Biodegradability to Manipulate Neural Stem Cells for Enhancing Spinal Cord Injury Repair*. Biomacromolecules. 2022 Dec 13 https://pubs.acs.org/doi/full/10.1021/acs.biomac.2c00920

574. Serafin A, Culebras M, Oliveira JM, Koffler J, Collins MN. *3D printable electroconductive gelatin-hyaluronic acid materials containing polypyrrole nanoparticles for electroactive tissue engineering*. Advanced Composites and Hybrid Materials 2023 6:3. 2023 May 20;6(3):1–14.

575. Yang Y, Deng Y, Xu S, Liu Y, Liang W, Zhang K, et al. *PPy/SWCNTs-Modified Microelectrode Array for Learning and Memory Model Construction through Electrical Stimulation and Detection of In Vitro Hippocampal Neuronal Network*. ACS Applied Bio Materials. 2023 Apr 18. https://pubs.acs.org/doi/full/10.1021/acsabm.3c00105

576. Xu S, Deng Y, Luo J, He E, Liu Y, Zhang K, et al. *High-Throughput PEDOT:PSS/PtNPs-Modified Microelectrode Array for Simultaneous Recording and Stimulation of Hippocampal Neuronal Networks in Gradual Learning Process*. ACS Applied Materials & Interfaces. 2022 Mar 16;acsami.1c23170.

577. Haugh MG, Jaasma MJ, O'Brien FJ. *The effect of dehydrothermal treatment on the mechanical and structural properties of collagen-GAG scaffolds*. J Biomed Mater Res A. 2009 May;89(2):363–9.

578. Stansley B, Post J, Hensley K. *A comparative review of cell culture systems for the study of microglial biology in Alzheimer's disease*. Journal of Neuroinflammation. 2012 May 31;9(1):115.

579. Corradin SB, Mauël J, Donini SD, Quattrocchi E, Ricciardi-Castagnoli P. *Inducible nitric oxide synthase activity of cloned murine microglial cells*. Glia. 1993 Mar;7(3):255–62.

580. Nistor PA, May PW, Tamagnini F, Randall AD, Caldwell MA. *Long-term culture of pluripotent stem-cell-derived human neurons on diamond--A substrate for neurodegeneration research and therapy*. Biomaterials. 2015 Aug;61:139–49.

581. Krieger KJ, Bertollo N, Dangol M, Sheridan JT, Lowery MM, O'Cearbhaill ED. *Simple and customizable method for fabrication of high-aspect ratio microneedle molds using low-cost 3D printing*. Microsyst Nanoeng. 2019 Sep 9;5(1):1–14.

582. Fratzl P, Misof K, Zizak I, Rapp G, Amenitsch H, Bernstorff S. *Fibrillar Structure and Mechanical Properties of Collagen*. Journal of Structural Biology. 1998 Jan 1;122(1):119–22.

583. Wenger MPE, Bozec L, Horton MA, Mesquida P. *Mechanical Properties of Collagen Fibrils*. Biophysical Journal. 2007 May 25;93(4):1255.

584. Xu B, Li H, Zhang Y. *Understanding the viscoelastic behavior of collagen matrices through relaxation time distribution spectrum*. Biomatter. 2013 Apr 1;3(3):e24651.

585. Bose S, Li S, Mele E, Silberschmidt VV. *Dry vs. wet: Properties and performance of collagen films. Part II. Cyclic and time-dependent behaviours*. Journal of the Mechanical Behavior of Biomedical Materials. 2020 Dec 1;112:104040.

586. Papageorgiou DG, Kinloch IA, Young RJ. *Graphene/elastomer nanocomposites*. Carbon. 2015 Oct 11;95:460–84.

587. Akhtar R, Sherratt MJ, Cruickshank JK, Derby B. *Characterizing the elastic properties of tissues*. Mater Today (Kidlington). 2011 Mar;14(3):96–105.

588. Kozai TDY, Catt K, Li X, Gugel ZV, Olafsson VT, Vazquez AL, et al. *Mechanical failure modes of chronically implanted planar silicon-based neural probes for laminar recording*. Biomaterials. 2015 Jan;37:25–39.

589. Kourgiantaki A, Tzeranis DS, Karali K, Georgelou K, Bampoula E, Psilodimitrakopoulos S, et al. *Neural stem cell delivery via porous collagen scaffolds promotes neuronal differentiation and locomotion recovery in spinal cord injury*. npj Regenerative Medicine 2020 5:1. 2020 Jun 15;5(1):1–14.

590. Kholkhoev BC, Buinov AS, Makotchenko VG, Fedorov VE, Timashev PS, Burdukovskii VF. *Electrically conductive composites of collagen and graphene*. Russian Chemical Bulletin. 2018;67(7):1316–8.

591. Koessler L, Colnat-Coulbois S, Cecchin T, Hofmanis J, Dmochowski JP, Norcia AM, et al. *In-vivo measurements of human brain tissue conductivity using focal electrical current injection through intracerebral multicontact electrodes*. Hum Brain Mapp. 2017 Feb;38(2):974–86.

592. Biazar E, Heidari M, Asefnejad A, Montazeri N. *The relationship between cellular adhesion and surface roughness in polystyrene modified by microwave plasma radiation*. Int J Nanomedicine. 2011;6:631–9.

593. Zareidoost A, Yousefpour M, Ghaseme B, Amanzadeh A. *The relationship of surface roughness and cell response of chemical surface modification of titanium*. J Mater Sci Mater Med. 2012 Jun;23(6):1479–88.

594. Brunetti V, Maiorano G, Rizzello L, Sorce B, Sabella S, Cingolani R, et al. *Neurons sense nanoscale roughness with nanometer sensitivity*. Proceedings of the National Academy of Sciences. 2010 Apr 6;107(14):6264–9.

595. Cai S, Wu C, Yang W, Liang W, Yu H, Liu L. *Recent advance in surface modification for regulating cell adhesion and behaviors*. Nanotechnology Reviews. 2020 Jan 1;9(1):971–89.

596. Gentile F, Tirinato L, Battista E, Causa F, Liberale C, di Fabrizio EM, et al. *Cells preferentially grow on rough substrates*. Biomaterials. 2010 Oct;31(28):7205–12.

597. Carnicer-Lombarte A, Chen ST, Malliaras GG, Barone DG. *Foreign Body Reaction to Implanted Biomaterials and Its Impact in Nerve Neuroprosthetics*. Front Bioeng Biotechnol. 2021;9:622524.

598. Halassa MM, Haydon PG. *Integrated Brain Circuits: Astrocytic Networks Modulate Neuronal Activity and Behavior*. Annu Rev Physiol. 2010 Mar 17;72:335–55.

599. Gao Z, Zhu Q, Zhang Y, Zhao Y, Cai L, Shields CB, et al. *Reciprocal modulation between microglia and astrocyte in reactive gliosis following the CNS injury*. Mol Neurobiol. 2013 Dec;48(3):690–701.

600. Bellver-Landete V, Bretheau F, Mailhot B, Vallières N, Lessard M, Janelle ME, et al. *Microglia are an essential component of the neuroprotective scar that forms after spinal cord injury*. Nat Commun. 2019 Jan 31;10(1):518.

601. Sridharan R, Cavanagh B, Cameron AR, Kelly DJ, O'Brien FJ. *Material stiffness influences the polarization state, function and migration mode of macrophages*. Acta Biomaterialia. 2019 Apr 15;89:47–59.

602. Mendonça MCP, Soares ES, de Jesus MB, Ceragioli HJ, Irazusta SP, Batista ÂG, et al. *Reduced graphene oxide: nanotoxicological profile in rats*. J Nanobiotechnology. 2016 Jun 24;14(1):53.

603. Bramini M, Chiacchiaretta M, Armirotti A, Rocchi A, Kale DD, Martin C, et al. *An Increase in Membrane Cholesterol by Graphene Oxide Disrupts Calcium Homeostasis in Primary Astrocytes*. Small. 2019 Apr;15(15):e1900147.

604. Durso M, I. Borrachero-Conejo A, Bettini C, Treossi E, Scidà A, Saracino E, et al. *Biomimetic graphene for enhanced interaction with the external membrane of astrocytes*. Journal of Materials Chemistry B. 2018;6(33):5335–42.

605. Chiacchiaretta M, Bramini M, Rocchi A, Armirotti A, Giordano E, Vázquez E, et al. *Graphene Oxide Upregulates the Homeostatic Functions of Primary Astrocytes and Modulates Astrocyte-to-Neuron Communication*. Nano Lett. 2018 Sep 12;18(9):5827–38.

606. Gottipati MK, Kalinina I, Bekyarova E, Haddon RC, Parpura V. *Chemically Functionalized Water-Soluble Single-Walled Carbon Nanotubes Modulate Morpho-Functional Characteristics of Astrocytes*. Nano Lett. 2012 Sep 12;12(9):4742–7.

607. Matejuk A, Ransohoff RM. *Crosstalk Between Astrocytes and Microglia: An Overview*. Front Immunol. 2020 Jul 16. www.frontiersin.org/journals/immunology/articles/10.3389/fimmu.2020.01416/full

608. Liddelow SA, Barres BA. *Reactive Astrocytes: Production, Function, and Therapeutic Potential*. Immunity. 2017 Jun 20;46(6):957–67.

609. Tang Y, Le W. *Differential Roles of M1 and M2 Microglia in Neurodegenerative Diseases*. Mol Neurobiol. 2016 Mar;53(2):1181–94.

610. Zhou K, Motamed S, Thouas GA, Bernard CC, Li D, Parkington HC, et al. *Graphene Functionalized Scaffolds Reduce the Inflammatory Response and Supports Endogenous Neuroblast Migration when Implanted in the Adult Brain*. PLOS ONE. 2016 Mar 15;11(3):e0151589.

611. Song Q, Jiang Z, Li N, Liu P, Liu L, Tang M, et al. *Anti-inflammatory effects of three-dimensional graphene foams cultured with microglial cells*. Biomaterials. 2014;35(25):6930–40.

612. Yang Z, Pan Y, Chen T, Li L, Zou W, Liu D, et al. *Cytotoxicity and Immune Dysfunction of Dendritic Cells Caused by Graphene Oxide*. Front Pharmacol. 2020;11:1206.

613. Ledeboer A, Brevé JJP, Wierinckx A, van der Jagt S, Bristow AF, Leysen JE, et al. *Expression and regulation of interleukin-10 and interleukin-10 receptor in rat astroglial and microglial cells*. Eur J Neurosci. 2002 Oct;16(7):1175–85.

614. Szostak KM, Grand L, Constandinou TG. *Neural interfaces for intracortical recording: Requirements, fabrication methods, and characteristics*. Frontiers in Neuroscience. 2017 Dec 7;11(DEC):665.

615. Cui H, Xie X, Xu S, Chan LLH, Hu Y. *Electrochemical characteristics of microelectrode designed for electrical stimulation*. BioMedical Engineering Online. 2019 Aug 1;18(1):1–14.

616. Zhang Q, Esrafilzadeh D, Crook JM, Kapsa R, Stewart EM, Tomaskovic-Crook E, et al. *Electrical Stimulation Using Conductive Polymer Polypyrrole Counters Reduced Neurite Outgrowth of Primary Prefrontal Cortical Neurons from NRG1-KO and DISC1-LI Mice*. Sci Rep. 2017 Feb 15;7(1):42525.

617. Tang-Schomer MD. *3D axon growth by exogenous electrical stimulus and soluble factors*. Brain Research. 2018 Jan 1;1678:288–96.

618. Kumar PJ, Adams RD, Harkins AB, Engeberg ED, Willits RK. *Stimulation Frequency Alters the Dorsal Root Ganglion Neurite Growth and Directionality In Vitro*. IEEE Transactions on Biomedical Engineering. 2016 Jun;63(6):1257–68.

619. Rd F. *Effects of ion channel activity on development of dorsal root ganglion neurons*. Journal of Neurobiology. 1998 Oct;37(1). https://pubmed.ncbi.nlm.nih.gov/9777739/

620. Pemberton JM, Pogmore JP, Andrews DW. *Neuronal cell life, death, and axonal degeneration as regulated by the BCL-2 family proteins*. Cell Death Differ. 2021 Jan;28(1):108–22.

621. Najafi MF, Zahri S, Vahedi F, Toosi LE, Ariaee N. *Which form of collagen is suitable for nerve cell culture?* Neural Regeneration Research. 2013;8(23):2165.

622. Deng WS, Ma K, Liang B, Liu XY, Xu HY, Zhang J, et al. *Collagen scaffold combined with human umbilical cord-mesenchymal stem cells transplantation for acute complete spinal cord injury*. Neural Regeneration Research. 2020 Sep 1;15(9):1686–700.

623. Xiang Z, Liu J, Lee C. *A flexible three-dimensional electrode mesh: An enabling technology for wireless brain–computer interface prostheses*. Microsystems & Nanoengineering 2016 2:1. 2016 May 23;2(1):1–8.

624. Yan D, Jiman A, Ratze D, Huang S, Parizi S, Welle E, et al. *Microneedle Penetrating Array with Axon-Sized Dimensions for Cuff-less Peripheral Nerve Interfacing*. International IEEE/EMBS Conference on Neural Engineering, NER. 2019 May 16;2019-March:827–30.

625. Murr LE. *A Metallographic Review of 3D Printing/Additive Manufacturing of Metal and Alloy Products and Components*. Metallogr Microstruct Anal. 2018 Apr 1;7(2):103–32.

626. Flack JA, Sharma KD, Xie JY. *Delving into the recent advancements of spinal cord injury treatment: a review of recent progress*. Neural Regen Res. 2021 Jul 8;17(2):283–91.

627. Bettinger CJ, Ecker M, Yoshida Kozai TD, Malliaras GG, Meng E, Voit W. *Recent advances in neural interfaces - Materials chemistry to clinical translation*. MRS Bulletin. 2020 Aug 1;45(8):655–68.

628. Shen H, Fan C, You Z, Xiao Z, Zhao Y, Dai J. *Advances in Biomaterial-Based Spinal Cord Injury Repair*. Advanced Functional Materials. 2022;32(13):2110628.

629. Frank JA, Antonini MJ, Anikeeva P. *Next-generation interfaces for studying neural function*. Nat Biotechnol. 2019 Sep;37(9):1013–23.

630. Zhang M, Tang Z, Liu X, Van der Spiegel J. *Electronic neural interfaces*. Nat Electron. 2020 Apr;3(4):191–200.

631. Jackson AF, Bolger DJ. *The neurophysiological bases of EEG and EEG measurement: A review for the rest of us*. Psychophysiology. 2014 Nov;51(11):1061–71.

632. Teplan M. *Fundamentals of EEG Measurement*. Measurement Science Review. 2002;2.

633. Värbu K, Muhammad N, Muhammad Y. *Past, Present, and Future of EEG-Based BCI Applications*. Sensors. 2022 Jan;22(9):3331.

634. Hinterberger T, Weiskopf N, Veit R, Wilhelm B, Betta E, Birbaumer N. *An EEG-driven brain-computer interface combined with functional magnetic resonance imaging (fMRI)*. IEEE Transactions on Biomedical Engineering. 2004 Jun;51(6):971–4.

635. Sorger B, Goebel R. *Chapter 21 - Real-time fMRI for brain-computer interfacing*. In: Ramsey NF, Millán J del R, editors. Handbook of Clinical Neurology. Elsevier; 2020. p. 289–302. (Brain-Computer Interfaces; vol. 168). Available from: https://www.sciencedirect.com/science/article/pii/B9780444639349000214

636. Sridharan A, Rajan SD, Muthuswamy J. *Long-term changes in the material properties of brain tissue at the implant–tissue interface*. J Neural Eng. 2013 Oct;10(6):066001.

637. Fernández-Merino MJ, Paredes JI, Villar-Rodil S, Guardia L, Solís-Fernández P, Salinas-Torres D, et al. *Investigating the influence of surfactants on the stabilization of aqueous reduced graphene oxide dispersions and the characteristics of their composite films*. Carbon. 2012 Aug 1;50(9):3184–94.

638. Seredych M, Maleski K, Mathis TS, Gogotsi Y. *Delamination of MXenes using bovine serum albumin*. Colloids and Surfaces A: Physicochemical and Engineering Aspects. 2022 May 20;641:128580.

639. Kumar CV, Pattammattel A. *Chapter Eleven - BioGraphene: Direct Exfoliation of Graphite in a Kitchen Blender for Enzymology Applications*. Methods in Enzymology. Academic Press; 2016. p. 225–44. (Rational Design of Enzyme-Nanomaterials; vol. 571). https://www.sciencedirect.com/science/article/pii/S007668791600121X

640. Shin Y, Vranic S, Just-Baringo X, Gali SM, Kisby T, Chen Y, et al. *Stable, concentrated, biocompatible, and defect-free graphene dispersions with positive charge*. Nanoscale. 2020 Jun 18;12(23):12383–94.

641. Kurakula M, Rao GSNK. *Pharmaceutical assessment of polyvinylpyrrolidone (PVP): As excipient from conventional to controlled delivery systems with a spotlight on COVID-19 inhibition*. Journal of Drug Delivery Science and Technology. 2020 Dec;60:102046.

642. Yu H, Wang B, Zhou S, Zhu M, Chen W, Chen H, et al. *Polyvinylpyrrolidone functionalization induces deformable structure of graphene oxide nanosheets for lung-targeting delivery*. Nano Today. 2021 Jun 1;38:101151.

643. Bourlinos AB, Georgakilas V, Zboril R, Steriotis TA, Stubos AK, Trapalis C. *Aqueous-phase exfoliation of graphite in the presence of polyvinylpyrrolidone for the production of water-soluble graphenes*. Solid State Communications. 2009 Dec 1;149(47–48):2172–6.

644. Wajid AS, Das S, Irin F, Ahmed HST, Shelburne JL, Parviz D, et al. *Polymer-stabilized graphene dispersions at high concentrations in organic solvents for composite production*. Carbon. 2012 Feb 1;50(2):526–34.

645. Malikmammadov E, Tanir TE, Kiziltay A, Hasirci V, Hasirci N. *PCL and PCL-based materials in biomedical applications*. Journal of Biomaterials Science, Polymer Edition. 2018 Jun 13;29(7–9):863–93.

646. Yang X, Wang Y, Zhou Y, Chen J, Wan Q. *The Application of Polycaprolactone in Three-Dimensional Printing Scaffolds for Bone Tissue Engineering*. Polymers (Basel). 2021 Aug 17;13(16):2754.

647. Karbalaei Akbari M, Siraj Lopa N, Shahriari M, Najafzadehkhoee A, Galusek D, Zhuiykov S. *Functional Two-Dimensional Materials for Bioelectronic Neural Interfacing*. Journal of Functional Biomaterials. 2023 Jan;14(1):35.

648. Gou S, Yang S, Cheng Y, Yang S, Liu H, Li P, et al. *Applications of 2D Nanomaterials in Neural Interface*. Int J Mol Sci. 2024 Aug 7;25(16):8615.

649. Viana D, Walston ST, Masvidal-Codina E, Illa X, Rodríguez-Meana B, Del Valle J, et al. *Nanoporous graphene-based thin-film microelectrodes for in vivo high-resolution neural recording and stimulation*. Nat Nanotechnol. 2024 Jan 11; https://www.nature.com/articles/s41565-023-01570-5

650. Yan D, Jiman A, Ratze D, Huang S, Parizi S, Welle E, et al. *Microneedle Penetrating Array with Axon-Sized Dimensions for Cuff-less Peripheral Nerve Interfacing*. In: 2019 9th International IEEE/EMBS Conference on Neural Engineering (NER). 2019. p. 827–30. https://ieeexplore.ieee.org/document/8717097

651. Shih JJ, Krusienski DJ, Wolpaw JR. *Brain-Computer Interfaces in Medicine*. Mayo Clinic Proceedings. 2012 Mar;87(3):268.

652. Mudgal SK, Sharma SK, Chaturvedi J, Sharma A. *Brain computer interface advancement in neurosciences: Applications and issues*. Interdisciplinary Neurosurgery. 2020 Jun 1;20:100694.

653. Schiavone G, Kang X, Fallegger F, Gandar J, Courtine G, Lacour SP. *Guidelines to Study and Develop Soft Electrode Systems for Neural Stimulation*. Neuron. 2020 Oct 28;108(2):238–58.

654. Hyakumura T, Aregueta-Robles U, Duan W, Villalobos J, Adams WK, Poole-Warren L, et al. *Improving Deep Brain Stimulation Electrode Performance in vivo Through Use of Conductive Hydrogel Coatings*. Front Neurosci. 2021 Nov 5;15. www.frontiersin.org/journals/neuroscience/articles/10.3389/fnins.2021.761525/full

655. Backes C, Szydłowska BM, Harvey A, Yuan S, Vega-Mayoral V, Davies BR, et al. *Production of highly monolayer enriched dispersions of liquid-exfoliated nanosheets by liquid cascade centrifugation*. ACS Nano. 2016 Jan 26;10(1):1589–601.

656. Nečas D, Klapetek P. *Gwyddion: an open-source software for SPM data analysis*. Central European Journal of Physics. 2012;10(1):181–8.

657. Nistor PA, May PW, Tamagnini F, Randall AD, Caldwell MA. *Long-term culture of pluripotent stem-cell-derived human neurons on diamond - A substrate for neurodegeneration research and therapy*. Biomaterials. 2015;61:139–49.

658. McComish SF, Caldwell MA. *Generation of defined neural populations from pluripotent stem cells*. Philosophical Transactions of the Royal Society B: Biological Sciences. 2018;373(1750).

659. Crompton LA, McComish SF, Stathakos P, Cordero-Llana O, Lane JD, Caldwell MA. *Efficient and scalable generation of human ventral midbrain astrocytes from human-induced pluripotent stem cells*. Journal of Visualized Experiments. 2021;(176):1–19.

660. Serio A, Bilican B, Barmada SJ, Ando DM, Zhao C, Siller R, et al. *Astrocyte pathology and the absence of non-cell autonomy in an induced pluripotent stem cell model of TDP-43 proteinopathy*. Proceedings of the National Academy of Sciences. 2013;110(12):4697–702.

661. Cahill EM, O'Cearbhaill ED. *Toward Biofunctional Microneedles for Stimulus Responsive Drug Delivery*. Bioconjug Chem. 2015 Jul 15;26(7):1289–96.

662. Uddin MdE, Kuila T, Nayak GC, Kim NH, Ku BC, Lee JH. *Effects of various surfactants on the dispersion stability and electrical conductivity of surface modified graphene*. Journal of Alloys and Compounds. 2013 Jun 15;562:134–42.

663. Htwe YZN, Mariatti M. *Surfactant-assisted water-based graphene conductive inks for flexible electronic applications*. Journal of the Taiwan Institute of Chemical Engineers. 2021 Aug 1;125:402–12.

664. Li YM, Ji Y, Meng YX, Kim YJ, Lee H, Kurian AG, et al. *Neural Tissue-Like, not Supraphysiological, Electrical Conductivity Stimulates Neuronal Lineage Specification through Calcium Signaling and Epigenetic Modification*. Advanced Science. n/a(n/a):2400586.

665. Northrop JH. *Comparative hydrolysis of gelatin by pepsin, trypsin, acid, and alkali*. Journal of General Physiology. 1921 Sep 20;4(1):57–71.

666. Suk JS, Xu Q, Kim N, Hanes J, Ensign LM. *PEGylation as a strategy for improving nanoparticle-based drug and gene delivery*. Adv Drug Deliv Rev. 2016 Apr 1;99(Pt A):28–51.

667. Hu CX, Read O, Shin Y, Chen Y, Wang J, Boyes M, et al. *Effects of Lateral Size, Thickness, and Stabilizer Concentration on the Cytotoxicity of Defect-Free Graphene Nanosheets: Implications for Biological Applications*. ACS Applied Nano Materials. 2022 Sep 12; https://pubs.acs.org/doi/full/10.1021/acsanm.2c02403

668. Veronese FM, Mero A. *The impact of PEGylation on biological therapies*. BioDrugs. 2008;22(5):315–29.

669. Mohan VB, Nieuwoudt M, Jayaraman K, Bhattacharyya D. *Quantification and analysis of Raman spectra of graphene materials*. Graphene Technol. 2017 Dec 1;2(3):47–62.

670. Bianchi V, Carey T, Viti L, Li L, Linfield EH, Davies AG, et al. *Terahertz saturable absorbers from liquid phase exfoliation of graphite*. Nat Commun. 2017 Jun 15;8:15763.

671. Paton KR, Varrla E, Backes C, Smith RJ, Khan U, O'Neill A, et al. *Scalable production of large quantities of defect-free few-layer graphene by shear exfoliation in liquids*. Nature Materials. 2014;13(6):624–30.

672. Rubio N, Au H, Coulter GO, Guetaz L, Gebel G, Mattevi C, et al. *Effect of graphene flake size on functionalisation: quantifying reaction extent and imaging locus with single Pt atom tags*. Chem Sci. 2021;12(44):14907–19.

673. Çiplak Z, Karabudak Yildiz N, Çalimli A. *Investigation of Graphene/Ag Nanocomposites Synthesis Parameters for Two Different Synthesis Methods*. Fullerenes, Nanotubes and Carbon Nanostructures. 2014 Sep 10;23:361–70.

674. Hidayah NMS, Liu WW, Lai CW, Noriman NZ, Khe CS, Hashim U, et al. *Comparison on graphite, graphene oxide and reduced graphene oxide: Synthesis and characterization*. 2017. p. 150002. https://pubs.aip.org/aip/acp/article/965987

675. Wang X, Cao Y. *Characterizations of absorption, scattering, and transmission of typical nanoparticles and their suspensions*. Journal of Industrial and Engineering Chemistry. 2020 Feb;82:324–32.

676. Duncan TV. *Release of Engineered Nanomaterials from Polymer Nanocomposites: the Effect of Matrix Degradation*. ACS Appl Mater Interfaces. 2015 Jan 14;7(1):20–39.

677. Ragaert K, Cardon L, Baere ID, Degrieck J. *Bulk mechanical properties of thermoplastic poly-ε-caprolactone.*

678. Eshraghi S, Das S. *Mechanical and microstructural properties of polycaprolactone scaffolds with one-dimensional, two-dimensional, and three-dimensional orthogonally oriented porous architectures produced by selective laser sintering*. Acta Biomater. 2010 Jul;6(7):2467–76.

679. Noel J. *Review of the properties of gold material for MEMS membrane applications*. IET Circuits, Devices & Systems. 2016 Feb 8;10.

680. Callister WD, Rethwisch DG. *Materials science and engineering: an introduction: SI Version*. 10th edition, global edition. Hoboken: Wiley; 2020. 834 p.

681. Hopcroft MA, Nix WD, Kenny TW. *What is the Young's Modulus of Silicon?* Journal of Microelectromechanical Systems. 2010 Apr;19(2):229–38.

682. Lee JY. *Individual and combinatorial effects of stiffness and electrical conductivity on host-immune responses to conductive hydrogels*. 2023;

683. Stauffer D, Aharony A. *Introduction To Percolation Theory: Second Edition*. 2nd ed. London: Taylor & Francis; 2017. 192 p.

684. Khan T, Irfan MS, Ali M, Dong Y, Ramakrishna S, Umer R. *Insights to low electrical percolation thresholds of carbon-based polypropylene nanocomposites*. Carbon. 2021 May 1;176:602–31.

685. Meloni M, Large MJ, Miguel J, Domínguez G, Victor-román S, Fratta G, et al. *Explosive percolation yields highly-conductive polymer nanocomposites*. Nature Communications 2022 13:1. 2022 Nov 11;13(1):1–9.

686. Choi HJ, Kim MS, Ahn D, Yeo SY, Lee S. *Electrical percolation threshold of carbon black in a polymer matrix and its application to antistatic fibre*. Sci Rep. 2019 Apr 19;9(1):6338.

687. Kumar S, Bose S, Chatterjee K. *Amine-functionalized multiwall carbon nanotubes impart osteoinductive and bactericidal properties in poly(ε-caprolactone) composites*. RSC Adv. 2014 Apr 24;4(37):19086–98.

688. Capuani S, Malgir G, Chua CYX, Grattoni A. *Advanced strategies to thwart foreign body response to implantable devices*. Bioeng Transl Med. 2022 Mar 2;7(3):e10300.

689. Gori M, Vadalà G, Giannitelli SM, Denaro V, Di Pino G. *Biomedical and Tissue Engineering Strategies to Control Foreign Body Reaction to Invasive Neural Electrodes*. Front Bioeng Biotechnol. 2021 May 25;9:659033.

690. Tomiyasu H, Shikata H, Takao K, Asanuma N, Taruta S, Park YY. *An aqueous electrolyte of the widest potential window and its superior capability for capacitors*. Sci Rep. 2017 Mar 21;7(1):45048.

691. Wilks SJ, Richardson-Burn SM, Hendricks JL, Martin D, Otto KJ. *Poly(3,4-ethylene dioxythiophene) (PEDOT) as a micro-neural interface material for electrostimulation*. Front Neuroeng. 2009 Jun 9: www.frontiersin.org/journals/neuroengineering/articles/10.3389/neuro.16.007.2009

692. Zeng Q, Yu S, Fan Z, Huang Y, Song B, Zhou T. *Nanocone-Array-Based Platinum-Iridium Oxide Neural Microelectrodes: Structure, Electrochemistry, Durability and Biocompatibility Study*. Nanomaterials. 2022 Jan;12(19):3445.

693. Kumsa DW, Bhadra N, Hudak EM, Kelley SC, Untereker DF, Mortimer JT. *Electron transfer processes occurring on platinum neural stimulating electrodes: a tutorial on the i(Ve) profile*. J Neural Eng. 2016 Aug;13(5):052001.

694. Gupta D, Singh AK, Kar N, Dravid A, Bellare J. *Modelling and optimization of NaOH-etched 3-D printed PCL for enhanced cellular attachment and growth with minimal loss of mechanical strength*. Materials Science and Engineering: C. 2019 May 1;98:602–11.

695. Schneider M, Fritzsche N, Puciul-Malinowska A, Baliś A, Mostafa A, Bald I, et al. *Surface Etching of 3D Printed Poly(lactic acid) with NaOH: A Systematic Approach*. Polymers. 2020 Jul 30;12:1711.

696. Zhou ZX, Chen YR, Zhang JY, Jiang D, Yuan FZ, Mao ZM, et al. *Facile Strategy on Hydrophilic Modification of Poly(ε-caprolactone) Scaffolds for Assisting Tissue-Engineered Meniscus Constructs In Vitro*. Front Pharmacol. 2020 May 1;11:471.

697. Zhao C, Zheng W. *A Review for Aqueous Electrochemical Supercapacitors*. Front Energy Res. 2015 May 8. https://www.frontiersin.org/journals/energy-research/articles/10.3389/fenrg.2015.00023/full

698. Höflinger G. *Brief Introduction to Coating Technology for Electron Microscopy*. 2013 Aug 28; Available from: https://www.leica-microsystems.com/science-lab/life-science/brief-introduction-to-coating-technology-for-electron-microscopy/

699. Dijk G, Ruigrok HJ, O'Connor RP. *PEDOT:PSS-Coated Stimulation Electrodes Attenuate Irreversible Electrochemical Events and Reduce Cell Electropermeabilization*. Advanced Materials Interfaces. 2021 Sep 9;2100214.

700. Ganji M, Tanaka A, Gilja V, Halgren E, Dayeh SA. *Scaling Effects on the Electrochemical Stimulation Performance of Au, Pt, and PEDOT:PSS Electrocorticography Arrays*. Advanced Functional Materials. 2017 Nov 10;27(42).

701. Weiland JD, Anderson DJ, Humayun MS. *In vitro electrical properties for iridium oxide versus titanium nitride stimulating electrodes*. IEEE Transactions on Biomedical Engineering. 2002 Dec;49(12):1574–9.

702. Harris AR, Newbold C, Carter P, Cowan R, Wallace GG. *Measuring the effective area and charge density of platinum electrodes for bionic devices*. J Neural Eng. 2018 May;15(4):046015.

703. Tran KTM, Nguyen TD. *Lithography-based methods to manufacture biomaterials at small scales*. Journal of Science: Advanced Materials and Devices. 2017 Mar 1;2(1):1–14.

704. Pérez Davila S, González Rodríguez L, Chiussi S, Serra J, González P. *How to Sterilize Polylactic Acid Based Medical Devices?* Polymers (Basel). 2021 Jun 28;13(13):2115.

705. Haj Hosseini N, Hoffmann R, Kisban S, Stieglitz T, Paul O, Ruther P. *Comparative study on the insertion behavior of cerebral microprobes*. In: 2007 29th Annual International Conference of the IEEE Engineering in Medicine and Biology Society. Lyon: IEEE; 2007. p. 4711–4. http://ieeexplore.ieee.org/document/4353391/

706. Wang F, Wang Z, Shifa TA, Wen Y, Wang F, Zhan X, et al. *Two-Dimensional Non-Layered Materials: Synthesis, Properties and Applications*. Adv Funct Materials. 2017 May;27(19):1603254.

707. Amini AR, Laurencin CT, Nukavarapu SP. *Bone Tissue Engineering: Recent Advances and Challenges*. Crit Rev Biomed Eng. 2012;40(5):363–408.

708. Vallet-Regí M, Lozano D, González B, Izquierdo-Barba I. *Biomaterials against Bone Infection*. Advanced Healthcare Materials. 2020;9(13):2000310.

709. Mountziaris PM, Mikos AG. *Modulation of the Inflammatory Response for Enhanced Bone Tissue Regeneration*. Tissue Eng Part B Rev. 2008 Jun;14(2):179–86.

710. Mullen CA, Vaughan TJ, Billiar KL, McNamara LM. *The Effect of Substrate Stiffness, Thickness, and Cross-Linking Density on Osteogenic Cell Behavior*. Biophys J. 2015 Apr 7;108(7):1604–12.

711. Ye S, Shao K, Li Z, Guo N, Zuo Y, Li Q, et al. *Antiviral Activity of Graphene Oxide: How Sharp Edged Structure and Charge Matter*. ACS Appl Mater Interfaces. 2015 Sep 30;7(38):21571–9.

712. Amirrah IN, Lokanathan Y, Zulkiflee I, Wee MFMR, Motta A, Fauzi MB. *A Comprehensive Review on Collagen Type I Development of Biomaterials for Tissue Engineering: From Biosynthesis to Bioscaffold*. Biomedicines. 2022 Sep 16;10(9):2307.

713. C D, Y L. *Application of Collagen Scaffold in Tissue Engineering: Recent Advances and New Perspectives*. Polymers. 2016 Feb 4;8(2). https://pubmed.ncbi.nlm.nih.gov/30979136/

714. Yannas IV, Lee E, Orgill DP, Skrabut EM, Murphy GF. *Synthesis and characterization of a model extracellular matrix that induces partial regeneration of adult mammalian skin.* Proceedings of the National Academy of Sciences. 1989 Feb;86(3):933–7.

715. Saurav S, Sharma P, Kumar A, Tabassum Z, Girdhar M, Mamidi N, et al. *Harnessing Natural Polymers for Nano-Scaffolds in Bone Tissue Engineering: A Comprehensive Overview of Bone Disease Treatment*. Curr Issues Mol Biol. 2024 Jan 5;46(1):585–611.

716. Feroz S, Muhammad N, Ullah R, Nishan U, Cathro P, Dias G. *Mechanical properties, and in vitro biocompatibility assessment of biomimetic dual layered keratin/ hydroxyapatite scaffolds*. Front Bioeng Biotechnol. 2023 Dec 15. https://www.frontiersin.org/journals/bioengineering-and-biotechnology/articles/10.3389/fbioe.2023.1304147/full

717. Eivazzadeh-Keihan R, Maleki A, de la Guardia M, Bani MS, Chenab KK, Pashazadeh-Panahi P, et al. *Carbon based nanomaterials for tissue engineering of bone: Building*

new bone on small black scaffolds: A review. Journal of Advanced Research. 2019 Jul 1;18:185–201.

718. Zhang T, Lin S, Shao X, Zhang Q, Xue C, Zhang S, et al. *Effect of matrix stiffness on osteoblast functionalization*. Cell Proliferation. 2017 Jun;50(3):e12338.

719. Masters EA, Ricciardi BF, Bentley KL de M, Moriarty TF, Schwarz EM, Muthukrishnan G. *Skeletal infections: microbial pathogenesis, immunity and clinical management*. Nat Rev Microbiol. 2022 Jul;20(7):385–400.

720. O'Connor O, Thahir A, Krkovic M. *How Much Does an Infected Fracture Cost?* Arch Bone Jt Surg. 2022 Feb;10(2):135–40.

721. Norris BL, Vanderkarr M, Sparks C, Chitnis AS, Ray B, Holy CE. *Treatments, cost and healthcare utilization of patients with segmental bone defects*. Injury. 2021 Oct 1;52(10):2935–40.

722. Cabral CSD, De Melo-Diogo D, Ferreira P, Moreira AF, Correia IJ. *Reduced graphene oxide–reinforced tricalcium phosphate/gelatin/chitosan light-responsive scaffolds for application in bone regeneration*. International Journal of Biological Macromolecules. 2024 Jan;129210.

723. Wang J, Liu M, Yang C, Pan Y, Ji S, Han N, et al. *Biomaterials for bone defect repair: Types, mechanisms and effects*. Int J Artif Organs. 2024 Jan 2;03913988231218884.

724. Khodabandehloo AH, Pourmadadi M, Shamsabadipour A, Langari H, Manicum AL, Rahdar A, et al. *Two-dimensional materials for bone tissue engineering*. Journal of the American Ceramic Society. 2023 May 11; https://onlinelibrary.wiley.com/doi/full/10.1111/jace.19185

725. Bai L, Tao G, Feng M, Xie Y, Cai S, Peng S, et al. *Hydrogel Drug Delivery Systems for Bone Regeneration*. Pharmaceutics. 2023 Apr 25;15(5):1334.

726. Ielo I, Calabrese G, De Luca G, Conoci S. *Recent Advances in Hydroxyapatite-Based Biocomposites for Bone Tissue Regeneration in Orthopedics*. Int J Mol Sci. 2022 Aug 27;23(17):9721.

727. Halloran D, Durbano HW, Nohe A. *Bone Morphogenetic Protein-2 in Development and Bone Homeostasis*. J Dev Biol. 2020 Sep 13;8(3):19.

728. Power RN, Cavanagh BL, Dixon JE, Curtin CM, O'Brien FJ. *Development of a Gene-Activated Scaffold Incorporating Multifunctional Cell-Penetrating Peptides for pSDF-1α Delivery for Enhanced Angiogenesis in Tissue Engineering Applications*. International Journal of Molecular Sciences. 2022 Jan;23(3):1460.

729. Yang M, Jin H, Sun Z, Gui R. *Monoelemental two-dimensional boron nanomaterials beyond theoretical simulations: From experimental preparation, functionalized modification to practical applications*. Advances in Colloid and Interface Science. 2022 Jun 1;304:102669.

730. Navya PN, Daima HK. *Rational engineering of physicochemical properties of nanomaterials for biomedical applications with nanotoxicological perspectives*. Nano Converg. 2016 Feb 1;3:1.

731. American Elements. *Boron Nanoparticles / Nanopowder* [Internet]. American Elements. 2024 [cited 2024 Feb 9]. Available from: https://www.americanelements.com/boron-nanoparticles-nanopowder-7440-42-8

732. Nanografi. *Boron (B) Nanopowder/Nanoparticles* [Internet]. Nanografi. 2024 [cited 2024 Feb 9]. Available from: https://nanografi.com/nanoparticles/boron-b-nanopowder-nanoparticles-aps-100-nm-purity-99-55/

733. Farahmandghavi F, Imani M, Hajiesmaeelian F. *Silicone matrices loaded with levonorgestrel particles: Impact of the particle size on drug release*. Journal of Drug Delivery Science and Technology. 2019 Feb 1;49:132–42.

734. Wang Y, Fan J, Trenary M. *Surface Chemistry of Boron Oxidation. 1. Reactions of Oxygen and Water with Boron Films Grown on Ta(110)*. Chem Mater. 1993;5:192–8.

735. Ojha PK, Maji R, Karmakar S. *Effect of crystallinity on droplet regression and disruptive burning characteristics of nanofuel droplets containing amorphous and crystalline boron nanoparticles*. Combustion and Flame. 2018 Feb;188:412–27.

736. Rizzo HF. *Oxidation of Boron at Temperatures between 400 and 1300°C in Air*. In: Kohn JA, Nye WF, Gaulé GK, editors. Boron Synthesis, Structure, and Properties. Boston, MA: Springer US; 1960. p. 175–89.

737. He Z cheng, Wu J jun. *Research on the oxidation process of micro-boron below the melting point temperature*. Acta Astronautica. 2024 Dec 1;225:67–76.

738. Briggs M. *Boron Oxides, Boric Acid, and Borates*. Kirk-Othmer Encyclopedia of Chemical Technology. 2023.

739. Feldman C. *AMORPHOUS SEMICONDUCTORS*.

740. Lin S, Gu J, Zhang H, Wang Y, Chen Z. *Porous hexagonal boron oxide monolayer with robust wide band gap: A computational study*. FlatChem. 2018 May 1;9:27–32.

741. Sartinska L, Kasumov A, Koval A, Frolov G. *Properties of Composite Powder Based on Boron Nitride Prepared under Concentrated Light*. Condensed Matter. 2022 Jun 11;7(2):42.

742. Gates-Rector S, Blanton T. *The Powder Diffraction File: a quality materials characterization database*. Powder Diffraction. 2019 Dec;34(4):352–60.

743. Sun X, Liu X, Yin J, Yu J, Li Y, Hang Y, et al. *Two-Dimensional Boron Crystals: Structural Stability, Tunable Properties, Fabrications and Applications*. Advanced Functional Materials. 2017;27(19):1603300.

744. Young RJ, Kinloch IA, Gong L, Novoselov KS. *The mechanics of graphene nanocomposites: A review*. Composites Science and Technology. 2012 Jul 23;72(12):1459–76.

745. Li S, Dong C, Lv Y. *Magnetic liquid metal scaffold with dynamically tunable stiffness for bone tissue engineering*. Biomaterials Advances. 2022 Aug 1;139:212975.

746. Lian JB, Stein GS. *Concepts of Osteoblast Growth and Differentiation: Basis for Modulation of Bone Cell Development and Tissue Formation*. Critical Reviews in Oral Biology & Medicine. 1992 Apr;3(3):269–305.

747. Gao S, Chen B, Gao M, Xu Y, Yang X, Yang C, et al. *Substrate Stiffness of Bone Microenvironment Controls Functions of Pre-Osteoblasts and Fibroblasts In Vitro*. Biomimetics. 2023 Aug 4;8(4):344.

748. Witkowska-Zimny M, Walenko K, Wrobel E, Mrowka P, Mikulska A, Przybylski J. *Effect of substrate stiffness on the osteogenic differentiation of bone marrow stem cells and bone-derived cells*. Cell Biol Int. 2013 Jun;37(6):608–16.

749. Hull D, Clyne TW. *An Introduction to Composite Materials*. 2nd ed. Cambridge: Cambridge University Press; 1996. (Cambridge Solid State Science Series). Available from: https://www.cambridge.org/core/books/an-introduction-to-composite-materials/E42355260EDA500515C567390271E995

750. Harris B. *ENGINEERING COMPOSITE MATERIALS*.

751. Morgan EF, Unnikrisnan GU, Hussein AI. *Bone Mechanical Properties in Healthy and Diseased States*. Annu Rev Biomed Eng. 2018 Jun 4;20:119–43.

752. Jan R, May P, Bell AP, Habib A, Khan U, Coleman JN. *Enhancing the mechanical properties of BN nanosheet–polymer composites by uniaxial drawing*. Nanoscale. 2014 Apr 10;6(9):4889–95.

753. Maita JM, Song G, Colby M, Lee SW. *Atomic arrangement and mechanical properties of chemical-vapor-deposited amorphous boron*. Materials & Design. 2020 Aug 1;193:108856.

754. Liu X, Xu Y, Wu Z, Chen H. *Poly(N-vinylpyrrolidone)-Modified Surfaces for Biomedical Applications*. Macromolecular Bioscience. 2013;13(2):147–54.

755. Sudo H, Kodama HA, Amagai Y, Yamamoto S, Kasai S. *In vitro differentiation and calcification in a new clonal osteogenic cell line derived from newborn mouse calvaria.* The Journal of cell biology. 1983 Jan 1;96(1):191–8.

756. *CRC Handbook of Chemistry and Physics: A Ready-Reference of Chemical and Physical Data, 85th ed Edited by David R. Lide (National Institute of Standards and Technology). CRC Press LLC: Boca Raton, FL. 2004. 2712 pp. $139.99. ISBN 0-8493-0485-7.* J Am Chem Soc. 2005 Mar 1;127(12):4542–4542.

757. Mai-Prochnow A, Clauson M, Hong J, Murphy AB. *Gram positive and Gram negative bacteria differ in their sensitivity to cold plasma*. Sci Rep. 2016 Dec 9;6(1):38610.

758. Xu Y, Liu X, Zheng Y, Li C, Kwok Yeung KW, Cui Z, et al. *Ag_3PO_4 decorated black urchin-like defective TiO_2 for rapid and long-term bacteria-killing under visible light*. Bioactive Materials. 2021 Jun 1;6(6):1575–87.

759. Shao X, Fang Z, Li M, Zou W, Wang Q, Zhang C, et al. *Graphene Oxide Nanosheets Induce Mitochondrial Fragmentation by Cutting through Membrane*. ACS Materials Letters. 2023 Jul 29;27:2308–16.

760. Taşaltın N, Güllülü S, Karakuş S. *Dual-role of β borophene nanosheets as highly effective antibacterial and antifungal agent*. Inorganic Chemistry Communications. 2022 Feb 1;136:109150.

761. Vimalraj S. *Alkaline phosphatase: Structure, expression and its function in bone mineralization*. Gene. 2020 Sep;754:144855.

762. Hwang PW, Horton JA. *Variable osteogenic performance of MC3T3-E1 subclones impacts their utility as models of osteoblast biology*. Sci Rep. 2019 Jun 5;9(1):8299.

763. Zaminy A, Ragerdi Kashani I, Barbarestani M, Hedayatpour A, Mahmoudi R, Farzaneh Nejad A. *Osteogenic differentiation of rat mesenchymal stem cells from adipose tissue in comparison with bone marrow mesenchymal stem cells: melatonin as a differentiation factor*. Iran Biomed J. 2008 Jul;12(3):133–41.

764. Stamnitz S, Klimczak A. *Mesenchymal Stem Cells, Bioactive Factors, and Scaffolds in Bone Repair: From Research Perspectives to Clinical Practice*. Cells. 2021 Jul 29;10(8):1925.

765. Castano-Izquierdo H. *Pre-culture period of mesenchymal stem cells in osteogenic media influences their in vivo bone forming potential*. 2006;

766. Ryan AJ, Gleeson JP, Matsiko A, Thompson EM, O'Brien FJ. *Effect of different hydroxyapatite incorporation methods on the structural and biological properties of porous collagen scaffolds for bone repair*. J Anat. 2015 Dec;227(6):732–45.

767. Kane RJ, Weiss-Bilka HE, Meagher MJ, Liu Y, Gargac JA, Niebur GL, et al. *Hydroxyapatite reinforced collagen scaffolds with improved architecture and mechanical properties*. Acta Biomaterialia. 2015 Apr 15;17:16–25.

768. Li C, Vepari C, Jin HJ, Kim HJ, Kaplan DL. *Electrospun silk-BMP-2 scaffolds for bone tissue engineering*. Biomaterials. 2006 Jun 1;27(16):3115–24.

769. Geng Y, Duan H, Xu L, Witman N, Yan B, Yu Z, et al. *BMP-2 and VEGF-A modRNAs in collagen scaffold synergistically drive bone repair through osteogenic and angiogenic pathways*. Commun Biol. 2021 Jan 19;4:82.

770. James AW, LaChaud G, Shen J, Asatrian G, Nguyen V, Zhang X, et al. *A Review of the Clinical Side Effects of Bone Morphogenetic Protein-2*. Tissue Eng Part B Rev. 2016 Aug;22(4):284–97.

771. Sun W, Ye B, Chen S, Zeng L, Lu H, Wan Y, et al. *Neuro–bone tissue engineering: emerging mechanisms, potential strategies, and current challenges*. Bone Res. 2023 Dec 20;11(1):65.

772. Alcaide M, Taylor A, Fjorback M, Zachar V, Pennisi CP. *Boron-Doped Nanocrystalline Diamond Electrodes for Neural Interfaces: In vivo Biocompatibility Evaluation*. Front Neurosci. 2016 Mar 8.
https://www.journal.frontiersin.org/Article/10.3389/fnins.2016.00087/abstract

773. Pool M, Thiemann J, Bar-Or A, Fournier AE. *NeuriteTracer: a novel ImageJ plugin for automated quantification of neurite outgrowth*. J Neurosci Methods. 2008 Feb 15;168(1):134–9.

774. Knight MN, Hankenson KD. *Mesenchymal Stem Cells in Bone Regeneration*. Adv Wound Care (New Rochelle). 2013 Jul;2(6):306–16.

775. Toya M, Zhang N, Tsubosaka M, Kushioka J, Gao Q, Li X, et al. *CCL2 promotes osteogenesis by facilitating macrophage migration during acute inflammation*. Front Cell Dev Biol. 2023 Jun 30. https://www.frontiersin.org/articles/10.3389/fcell.2023.1213641

776. Mulholland BS, Forwood MR, Morrison NA. *Monocyte Chemoattractant Protein-1 (MCP-1/CCL2) Drives Activation of Bone Remodelling and Skeletal Metastasis*. Curr Osteoporos Rep. 2019 Dec 1;17(6):538–47.

777. Siddiqui JA, Le Henaff C, Johnson J, He Z, Rifkin DB, Partridge NC. *Osteoblastic monocyte chemoattractant protein-1 (MCP-1) mediation of parathyroid hormone's anabolic actions in bone implicates TGF-β signaling*. Bone. 2021 Feb;143:115762.

778. Lien MY, Chang AC, Tsai HC, Tsai MH, Hua CH, Cheng SP, et al. *Monocyte Chemoattractant Protein 1 Promotes VEGF-A Expression in OSCC by Activating ILK and MEK1/2 Signaling and Downregulating miR-29c*. Front Oncol. 2020 Nov 27 https://www.frontiersin.org/journals/oncology/articles/10.3389/fonc.2020.592415/full

779. Hong KH, Ryu J, Han KH. *Monocyte chemoattractant protein-1-induced angiogenesis is mediated by vascular endothelial growth factor-A*. Blood. 2005 Feb 15;105(4)

780. Niu J, Azfer A, Zhelyabovska O, Fatma S, Kolattukudy PE. *Monocyte chemotactic protein (MCP)-1 promotes angiogenesis via a novel transcription factor, MCP-1-induced protein (MCPIP)*. J Biol Chem. 2008 May 23;283(21):14542–51.

781. Cranford TL, Enos RT, Velázquez KT, McClellan JL, Davis JM, Singh UP, et al. *Role of MCP-1 on Inflammatory Processes and Metabolic Dysfunction Following High-Fat Feedings in the FVB/N Strain*. Int J Obes (Lond). 2016 May;40(5):844–51.

782. Becker LC. *Yin and Yang of MCP-1*. Circulation Research. 2005 Apr 29;96(8):812–4.

783. Deshmane SL, Kremlev S, Amini S, Sawaya BE. *Monocyte Chemoattractant Protein-1 (MCP-1): An Overview*. J Interferon Cytokine Res. 2009 Jun;29(6):313–26.

784. Jürgensen HJ, Silva LM, Krigslund O, van Putten S, Madsen DH, Behrendt N, et al. *CCL2/MCP-1 signaling drives extracellular matrix turnover by diverse macrophage subsets*. Matrix Biol Plus. 2019 Feb;1:100003.

785. Doucet M, Jayaraman S, Swenson E, Tusing B, Weber KL, Kominsky SL. *CCL20/CCR6 Signaling Regulates Bone Mass Accrual in Mice*. Journal of Bone and Mineral Research. 2016 Jul 1;31(7):1381–90.

786. Lisignoli G, Piacentini A, Cristino S, Grassi F, Cavallo C, Cattini L, et al. *CCL20 chemokine induces both osteoblast proliferation and osteoclast differentiation: Increased levels of CCL20 are expressed in subchondral bone tissue of rheumatoid arthritis patients*. Journal Cellular Physiology. 2007 Mar;210(3):798–806.

787. Izadpanah A, Dwinell MB, Eckmann L, Varki NM, Kagnoff MF. *Regulated MIP-3alpha/CCL20 production by human intestinal epithelium: mechanism for modulating*

mucosal immunity. Am J Physiol Gastrointest Liver Physiol. 2001 Apr;280(4):G710-719.

788. Aziz N, Detels R, Chang LC, Butch AW. *Macrophage Inflammatory Protein-3 Alpha (MIP-3α)/CCL20 in HIV-1-Infected Individuals*. J AIDS Clin Res. 2016 Jul;7(7):587.

789. Lee YM, Fujikado N, Manaka H, Yasuda H, Iwakura Y. *IL-1 plays an important role in the bone metabolism under physiological conditions*. International Immunology. 2010 Oct 1;22(10):805–16.

790. Salven P, Hattori K, Heissig B, Rafii S. *Interleukin-1alpha promotes angiogenesis in vivo via VEGFR-2 pathway by inducing inflammatory cell VEGF synthesis and secretion*. FASEB J. 2002 Sep;16(11):1471–3.

791. Naldini A, Carraro F. *Role of Inflammatory Mediators in Angiogenesis*. CDTIA. 2005 Feb 1;4(1):3–8.

792. Voronov E, Carmi Y, Apte RN. *The role IL-1 in tumor-mediated angiogenesis*. Front Physiol. 2014 Mar 28. https://www.frontiersin.org/journals/physiology/articles/10.3389/fphys.2014.00114

793. Malik A, Kanneganti TD. *Function and regulation of IL-1α in inflammatory diseases and cancer*. Immunol Rev. 2018 Jan;281(1):124–37.

794. Guo C, Yang XG, Wang F, Ma XY. *IL-1α induces apoptosis and inhibits the osteoblast differentiation of MC3T3-E1 cells through the JNK and p38 MAPK pathways*. International Journal of Molecular Medicine. 2016 Jul 1;38(1):319–27.

795. Salmeron KE, Maniskas ME, Edwards DN, Wong R, Rajkovic I, Trout A, et al. *Interleukin 1 alpha administration is neuroprotective and neuro-restorative following experimental ischemic stroke*. Journal of Neuroinflammation. 2019 Nov 14;16(1):222.

796. Murray KN, Parry-Jones AR, Allan SM. *Interleukin-1 and acute brain injury*. Front Cell Neurosci. 2015 Feb 6;9:18.

797. Wang H, Ni Z, Yang J, Li M, Liu L, Pan X, et al. *IL-1β promotes osteogenic differentiation of mouse bone marrow mesenchymal stem cells via the BMP/Smad pathway within a certain concentration range*. Exp Ther Med. 2020 Oct;20(4):3001–8.

798. Lacey DC, Simmons PJ, Graves SE, Hamilton JA. *Proinflammatory cytokines inhibit osteogenic differentiation from stem cells: implications for bone repair during inflammation*. Osteoarthritis and Cartilage. 2009 Jun 1;17(6):735–42.

799. Mao C y, Wang Y g, Zhang X, Zheng X y, Tang T t, Lu E y. *Double-edged-sword effect of IL-1β on the osteogenesis of periodontal ligament stem cells via crosstalk between the NF-κB, MAPK and BMP/Smad signaling pathways*. Cell Death Dis. 2016 Jul;7(7):e2296.

800. Wei S, Kitaura H, Zhou P, Ross FP, Teitelbaum SL. *IL-1 mediates TNF-induced osteoclastogenesis*. J Clin Invest. 2005 Feb 1;115(2):282–90.

801. Ma T, Miyanishi K, Suen A, Epstein NJ, Tomita T, Smith RL, et al. *Human interleukin-1-induced murine osteoclastogenesis is dependent on RANKL, but independent of TNF-α*. Cytokine. 2004 May 7;26(3):138–44.

802. Kim JH, Jin HM, Kim K, Song I, Youn BU, Matsuo K, et al. *The mechanism of osteoclast differentiation induced by IL-1*. J Immunol. 2009 Aug 1;183(3):1862–70.

803. Otsuka Y, Kondo T, Aoki H, Goto Y, Kawaguchi Y, Waguri-Nagaya Y, et al. *IL-1β promotes osteoclastogenesis by increasing the expression of IGF2 and chemokines in non-osteoclastic cells*. Journal of Pharmacological Sciences. 2023 Jan 1;151(1):1–8.

804. Fahey E, Doyle SL. *IL-1 Family Cytokine Regulation of Vascular Permeability and Angiogenesis*. Frontiers in Immunology. 2019;10. https://www.ncbi.nlm.nih.gov/pmc/articles/PMC6603210/

805. Ren K, Torres R. *Role of interleukin-1β during pain and inflammation*. Brain Res Rev. 2009 Apr;60(1):57–64.

806. Koo JW, Duman RS. *IL-1beta is an essential mediator of the antineurogenic and anhedonic effects of stress*. Proc Natl Acad Sci U S A. 2008 Jan 15;105(2):751–6.

807. Hunninghake GW, Glazier AJ, Monick MM, Dinarello CA. *Interleukin-1 is a chemotactic factor for human T-lymphocytes*. Am Rev Respir Dis. 1987 Jan;135(1)

808. Dodds RA, Merry K, Littlewood A, Gowen M. *Expression of mRNA for IL1 beta, IL6 and TGF beta 1 in developing human bone and cartilage.* J Histochem Cytochem. 1994 Jun 1;42(6):733–44.

809. Xiao J, Dong H, Wu Y, Tian W, Liu L. *Gene Expression Profiling of Cx3cl1 in Bone Marrow Mesenchymal Stem Cells by Osteogenic Induction*. OMICS: A Journal of Integrative Biology. 2009 Aug;13(4):337–43.

810. Koizumi K, Saitoh Y, Minami T, Takeno N, Tsuneyama K, Miyahara T, et al. *Role of CX3CL1/Fractalkine in Osteoclast Differentiation and Bone Resorption*. The Journal of Immunology. 2009 Dec 15;183(12):7825–31.

811. Yang T, Guo L, Chen L, Li J, Li Q, Pi Y, et al. *A novel role of FKN/CX3CR1 in promoting osteogenic transformation of VSMCs and atherosclerotic calcification*. Cell Calcium. 2020 Nov 1;91:102265.

812. Kuboi Y, Kuroda Y, Ohkuro M, Motoi S, Tomimori Y, Yasuda H, et al. *The Fractalkine-CX3CR1 Axis Regulates Non-inflammatory Osteoclastogenesis by Enhancing Precursor Cell Survival*. JBMR Plus. 2022 Sep 22;6(10):e10680.

813. Szewczyk G, Pyzlak M, Pankiewicz K, Szczerba E, Stangret A, Szukiewicz D, et al. *The potential association between a new angiogenic marker fractalkine and a placental vascularization in preeclampsia*. Arch Gynecol Obstet. 2021 Aug 1;304(2):365–76.

814. Kim JA, Kwak JY, Eunjung Y, Lee J, Park Y, Broxmeyer HE. *Fractalkine/CX3CR1 Signaling Promotes Angiogenic Potentials in CX3CR1 Expressing Monocytes*. Blood. 2016 Dec 2;128(22):2507.

815. Volin MV, Woods JM, Amin MA, Connors MA, Harlow LA, Koch AE. *Fractalkine: a novel angiogenic chemokine in rheumatoid arthritis*. Am J Pathol. 2001 Oct;159(4):1521–30.

816. Jones BA, Beamer M, Ahmed S. *Fractalkine/CX3CL1: A Potential New Target for Inflammatory Diseases*. Mol Interv. 2010 Oct;10(5):263–70.

817. Wojdasiewicz P, Poniatowski ŁA, Kotela A, Deszczyński J, Kotela I, Szukiewicz D. *The Chemokine CX3CL1 (Fractalkine) and its Receptor CX3CR1: Occurrence and Potential Role in Osteoarthritis*. Arch Immunol Ther Exp (Warsz). 2014;62(5):395–403.

818. Daniele S, Natali L, Giacomelli C, Campiglia P, Novellino E, Martini C, et al. *Osteogenesis Is Improved by Low Tumor Necrosis Factor Alpha Concentration through the Modulation of Gs-Coupled Receptor Signals*. Mol Cell Biol. 2017 Mar 31;37(8):e00442-16.

819. Mo Q, Zhang W, Zhu A, Backman LJ, Chen J. *Regulation of osteogenic differentiation by the pro-inflammatory cytokines IL-1β and TNF-α: current conclusions and controversies*. Human Cell. 2022 Jul 1;35(4):957–71.

820. Hess K, Ushmorov A, Fiedler J, Brenner RE, Wirth T. *TNFα promotes osteogenic differentiation of human mesenchymal stem cells by triggering the NF-κB signaling pathway*. Bone. 2009 Aug 1;45(2):367–76.

821. Lam J, Takeshita S, Barker JE, Kanagawa O, Ross FP, Teitelbaum SL. *TNF-α induces osteoclastogenesis by direct stimulation of macrophages exposed to permissive levels of RANK ligand*. J Clin Invest. 2000 Dec 15;106(12):1481–8.

822. Luo G, Li F, Li X, Wang ZG, Zhang B. *TNF-α and RANKL promote osteoclastogenesis by upregulating RANK via the NF-κB pathway*. Mol Med Rep. 2018 May;17(5):6605–11.

823. Fajardo LF, Kwan HH, Kowalski J, Allisont AC. *Dual Role of Tumor Necrosis Factor-a in Angiogenesis*. The American Journal of Pathology. 1992;140(3).

824. Leibovich SJ, Polverini PJ, Shepard HM, Wiseman DM, Shively V, Nuseir N. *Macrophage-induced angiogenesis is mediated by tumour necrosis factor-α*. Nature. 1987 Oct;329(6140):630–2.

825. Zakharova M, Ziegler HK. *Paradoxical Anti-Inflammatory Actions of TNF-α: Inhibition of IL-12 and IL-23 via TNF Receptor 1 in Macrophages and Dendritic Cells1*. The Journal of Immunology. 2005 Oct 15;175(8):5024–33.

826. Masli S, Turpie B. *Anti-inflammatory effects of tumour necrosis factor (TNF)-α are mediated via TNF-R2 (p75) in tolerogenic transforming growth factor-β-treated antigen-presenting cells*. Immunology. 2009 May;127(1):62.

827. van Loo G, Bertrand MJM. *Death by TNF: a road to inflammation*. Nat Rev Immunol. 2023 May;23(5):289–303.

828. Torrente Y, Fahime EE, Caron NJ, Del Bo R, Belicchi M, Pisati F, et al. *Tumor Necrosis Factor-α (TNF-α) Stimulates Chemotactic Response in Mouse Myogenic Cells*. Cell Transplant. 2003 Jan;12(1):91–100.

829. Glass GE, Chan JK, Freidin A, Feldmann M, Horwood NJ, Nanchahal J. *TNF-α promotes fracture repair by augmenting the recruitment and differentiation of muscle-derived stromal cells*. Proc Natl Acad Sci U S A. 2011 Jan 25;108(4):1585–90.

830. Mayr-Wohlfart U, Waltenberger J, Hausser H, Kessler S, Günther KP, Dehio C, et al. *Vascular endothelial growth factor stimulates chemotactic migration of primary human osteoblasts*. Bone. 2002 Mar;30(3):472–7.

831. Hu K, Olsen BR. *The roles of vascular endothelial growth factor in bone repair and regeneration*. Bone. 2016 Oct;91:30–8.

832. Aldridge SE, Lennard TWJ, Williams JR, Birch MA. *Vascular endothelial growth factor receptors in osteoclast differentiation and function*. Biochem Biophys Res Commun. 2005 Sep 30;335(3):793–8.

833. Kim HR, Kim KW, Kim BM, Cho ML, Lee SH. *The Effect of Vascular Endothelial Growth Factor on Osteoclastogenesis in Rheumatoid Arthritis*. PLoS One. 2015 Apr 20;10(4):e0124909.

834. Verheul HMW, Pinedo HM. *The Role of Vascular Endothelial Growth Factor (VEGF) in Tumor Angiogenesis and Early Clinical Development of VEGFReceptor Kinase Inhibitors*. Clinical Breast Cancer. 2000 Sep 1;1:S80–4.

835. Reinders MEJ, Sho M, Izawa A, Wang P, Mukhopadhyay D, Koss KE, et al. *Proinflammatory functions of vascular endothelial growth factor in alloimmunity*. J Clin Invest. 2003 Dec 1;112(11):1655–65.

836. Shen SW, Duan CL, Chen XH, Wang YQ, Sun X, Zhang QW, et al. *Neurogenic effect of VEGF is related to increase of astrocytes transdifferentiation into new mature neurons in rat brains after stroke*. Neuropharmacology. 2016 Sep 1;108:451–61.

837. Li D, Li X, Zhang J, Tang Z, Tian A. *The immunomodulatory effect of IL-4 accelerates bone substitute material-mediated osteogenesis in aged rats via NLRP3 inflammasome inhibition*. Front Immunol. 2023 Apr 20. www.frontiersin.org/journals/immunology/articles/10.3389/fimmu.2023.1121549/full

838. Zhang J, Shi H, Zhang N, Hu L, Jing W, Pan J. *Interleukin-4-loaded hydrogel scaffold regulates macrophages polarization to promote bone mesenchymal stem cells osteogenic differentiation via TGF-β1/Smad pathway for repair of bone defect*. Cell Prolif. 2020 Oct;53(10):e12907.

839. Yamada A, Takami M, Kawawa T, Yasuhara R, Zhao B, Mochizuki A, et al. *Interleukin-4 inhibition of osteoclast differentiation is stronger than that of interleukin-13 and they are equivalent for induction of osteoprotegerin production from osteoblasts*. Immunology. 2007 Apr;120(4):573–9.

840. Volpert OV, Fong T, Koch AE, Peterson JD, Waltenbaugh C, Tepper RI, et al. *Inhibition of Angiogenesis by Interleukin 4*. J Exp Med. 1998 Sep 21;188(6):1039–46.

841. Woodward EA, Prêle CM, Nicholson SE, Kolesnik TB, Hart PH. *The anti-inflammatory effects of interleukin-4 are not mediated by suppressor of cytokine signalling-1 (SOCS1)*. Immunology. 2010 Sep;131(1):118–27.

842. Pan D, Schellhardt L, Acevedo-Cintron JA, Hunter D, Snyder-Warwick AK, Mackinnon SE, et al. *IL-4 expressing cells are recruited to nerve after injury and promote regeneration*. Experimental Neurology. 2022 Jan 1;347:113909.

843. Daines JM, Schellhardt L, Wood MD. *The role of the IL-4 signaling pathway in traumatic nerve injuries*. Neurorehabil Neural Repair. 2021 May;35(5):431–43.

844. Villar MTA, Douglass JA, Heusser C, Bradding P, Holgate ST, Church MK. *The Chemoattractant Properties of Interleukin-4*. In: Lindley IJD, Westwick J, Kunkel S, editors. The Chemokines: Biology of the Inflammatory Peptide Supergene Family II. Boston, MA: Springer US; 1993. p. 191–191. Available from: https://doi.org/10.1007/978-1-4615-2952-1_26

845. Bosurgi L, Cao YG, Cabeza-Cabrerizo M, Tucci A, Hughes LD, Kong Y, et al. *Macrophage function in tissue repair and remodeling requires IL-4 or IL-13 with apoptotic cells*. Science. 2017 Jun 9;356(6342):1072–6.

846. Yuan L, You H, Qin N, Zuo W. *Interleukin-10 Modulates the Metabolism and Osteogenesis of Human Dental Pulp Stem Cells*. Cellular Reprogramming. 2021 Oct;23(5):270–6.

847. Van Vlasselaer P, Borremans B, Van Den Heuvel R, Van Gorp U, de Waal Malefyt R. *Interleukin-10 inhibits the osteogenic activity of mouse bone marrow*. Blood. 1993 Oct 15;82(8):2361–70.

848. Mohamed SGK, Sugiyama E, Shinoda K, Taki H, Hounoki H, Abdel-Aziz HO, et al. *Interleukin-10 inhibits RANKL-mediated expression of NFATc1 in part via suppression of c-Fos and c-Jun in RAW264.7 cells and mouse bone marrow cells*. Bone. 2007 Oct 1;41(4):592–602.

849. Evans KE, Fox SW. *Interleukin-10 inhibits osteoclastogenesis by reducing NFATc1 expression and preventing its translocation to the nucleus*. BMC Cell Biol. 2007 Jan 19;8:4.

850. Dace DS, Khan AA, Kelly J, Apte RS. *Interleukin-10 promotes pathological angiogenesis by regulating macrophage response to hypoxia during development*. PLoS One. 2008;3(10):e3381.

851. Steen EH, Wang X, Balaji S, Butte MJ, Bollyky PL, Keswani SG. *The Role of the Anti-Inflammatory Cytokine Interleukin-10 in Tissue Fibrosis*. Adv Wound Care (New Rochelle). 2020 Apr 1;9(4):184–98.

852. Patilas C, Varsamos I, Galanis A, Vavourakis M, Zachariou D, Marougklianis V, et al. *The Role of Interleukin-10 in the Pathogenesis and Treatment of a Spinal Cord Injury*. Diagnostics. 2024 Jan;14(2):151.

853. Li J, Wang P, Zhou T, Jiang W, Wu H, Zhang S, et al. *Neuroprotective effects of interleukin 10 in spinal cord injury*. Front Mol Neurosci. 2023 Jul 10 https://www.frontiersin.org/articles/10.3389/fnmol.2023.1214294

854. McGregor NE, Poulton IJ, Walker EC, Pompolo S, Quinn JMW, Martin TJ, et al. *Ciliary neurotrophic factor inhibits bone formation and plays a sex-specific role in bone growth and remodeling*. Calcif Tissue Int. 2010 Mar;86(3):261–70.

855. Amarasekara DS, Kim S, Rho J. *Regulation of Osteoblast Differentiation by Cytokine Networks*. International Journal of Molecular Sciences. 2021 Jan;22(6):2851.

856. Yong J, Gröger S, von Bremen J, Ruf S. *Ciliary Neurotrophic Factor (CNTF) Inhibits In Vitro Cementoblast Mineralization and Induces Autophagy, in Part by STAT3/ERK Commitment*. Int J Mol Sci. 2022 Aug 18;23(16):9311.

857. Bucher F, Aguilar E, Marra KV, Rapp J, Arnold J, Diaz-Aguilar S, et al. *CNTF Prevents Development of Outer Retinal Neovascularization Through Upregulation of CxCl10*. Invest Ophthalmol Vis Sci. 2020 Aug 3;61(10):20.

858. Bucher F, Buehler AD, Martin G, Schlunck GR, Agostini H, Stahl A. *Ciliary neurotrophic factor (CNTF) reduces neovascularization in the mouse-model of oxygen-induced retinopathy*. Investigative Ophthalmology & Visual Science. 2014 Apr 30;55(13):5408.

859. Lin HW, Jain MR, Li H, Levison SW. *Ciliary neurotrophic factor (CNTF) plus soluble CNTF receptor α increases cyclooxygenase-2 expression, PGE2 release and interferon-γ-induced CD40 in murine microglia*. J Neuroinflammation. 2009 Mar 6;6:7.

860. Rockenstein E, Ubhi K, Doppler E, Novak P, Moessler H, Li B, et al. *Regional comparison of the neurogenic effects of CNTF-derived peptides and cerebrolysin in AβPP transgenic mice*. J Alzheimers Dis. 2011;27(4):743–52.

861. Cen LP, Luo JM, Zhang CW, Fan YM, Song Y, So KF, et al. *Chemotactic effect of ciliary neurotrophic factor on macrophages in retinal ganglion cell survival and axonal regeneration*. Invest Ophthalmol Vis Sci. 2007 Sep;48(9):4257–66.

862. Rivera KO, Russo F, Boileau RM, Tomlinson RE, Miclau T, Marcucio RS, et al. *Local injections of β-NGF accelerates endochondral fracture repair by promoting cartilage to bone conversion*. Sci Rep. 2020 Dec 17;10:22241.

863. Yang S, Cheng J, Man C, Jiang L, Long G, Zhao W, et al. *Effects of exogenous nerve growth factor on the expression of BMP-9 and VEGF in the healing of rabbit mandible fracture with local nerve injury*. Journal of Orthopaedic Surgery and Research. 2021 Jan 21;16(1):74.

864. Hemingway F, Taylor R, Knowles HJ, Athanasou NA. *RANKL-independent human osteoclast formation with APRIL, BAFF, NGF, IGF I and IGF II*. Bone. 2011 Apr 1;48(4):938–44.

865. Chen WH, Mao CQ, Zhuo LL, Ong JL. *Beta-nerve growth factor promotes neurogenesis and angiogenesis during the repair of bone defects*. Neural Regen Res. 2015 Jul;10(7):1159–65.

866. Prencipe G, Minnone G, Strippoli R, De Pasquale L, Petrini S, Caiello I, et al. *Nerve Growth Factor Downregulates Inflammatory Response in Human Monocytes through TrkA*. The Journal of Immunology. 2014 Apr 1;192(7):3345–54.

867. Terracina S, Ferraguti G, Tarani L, Fanfarillo F, Tirassa P, Ralli M, et al. *Nerve Growth Factor and Autoimmune Diseases*. Curr Issues Mol Biol. 2023 Nov 10;45(11):8950–73.

868. Minnone G, De Benedetti F, Bracci-Laudiero L. *NGF and Its Receptors in the Regulation of Inflammatory Response*. Int J Mol Sci. 2017 May 11;18(5):1028.

869. Skaper SD. *Nerve growth factor: a neuroimmune crosstalk mediator for all seasons*. Immunology. 2017;151(1):1–15.

870. Sawada J, Itakura A, Tanaka A, Furusaka T, Matsuda H. *Nerve growth factor functions as a chemoattractant for mast cells through both mitogen-activated protein kinase and phosphatidylinositol 3-kinase signaling pathways*. Blood. 2000 Mar 15;95(6):2052–8.

871. Nakagawa H, Shiota S, Takano K, Shibata F, Kato H. *Cytokine-Induced Neutrophil Chemoattractant (CINC)-2 α, a Novel Member of Rat GRO/CINCs, is a Predominant Chemokine Produced by Lipopolysaccharide-Stimulated Rat Macrophages in Culture*. Biochemical and Biophysical Research Communications. 1996 Mar 27;220(3):945–8.

872. Nakagawa H, Komorita N, Shibata F, Ikesue A, Konishi K, Fujioka M, et al. *Identification of cytokine-induced neutrophil chemoattractants (CINC), rat GRO/CINC-2 alpha and CINC-2 beta, produced by granulation tissue in culture: purification, complete amino acid sequences and characterization.* Biochem J. 1994 Jul 15;301(Pt 2):545–50.

873. Takano K, Nakagawa H. *Contribution of cytokine-induced neutrophil chemoattractant CINC-2 and CINC-3 to neutrophil recruitment in lipopolysaccharide-induced inflammation in rats*. Inflamm Res. 2001 Oct;50(10):503–8.

874. Jenkins J, Wagner E. *Angiogenesis in the Ischemic Rat Lung*. J Vis Exp. 2013 Feb 8;(72):50217.

875. Liang T, Gao W, Zhu L, Ren J, Yao H, Wang K, et al. *TIMP-1 inhibits proliferation and osteogenic differentiation of hBMSCs through Wnt/β-catenin signaling*. Biosci Rep. 2019 Jan 8;39(1):BSR20181290.

876. Egea V, Zahler S, Rieth N, Neth P, Popp T, Kehe K, et al. *Tissue inhibitor of metalloproteinase-1 (TIMP-1) regulates mesenchymal stem cells through let-7f microRNA and Wnt/β-catenin signaling*. Proceedings of the National Academy of Sciences. 2012 Feb 7;109(6):E309–16.

877. Reed MJ, Koike T, Sadoun E, Sage EH, Puolakkainen P. *Inhibition of TIMP1 enhances angiogenesis in vivo and cell migration in vitro*. Microvasc Res. 2003 Jan;65(1):9–17.

878. Sang QXA. *Complex role of matrix metalloproteinases in angiogenesis*. Cell Res. 1998 Sep;8(3):171–7.

879. Lee EJ, Kim HS. *The anti-inflammatory role of tissue inhibitor of metalloproteinase-2 in lipopolysaccharide-stimulated microglia*. J Neuroinflammation. 2014 Jun 27;11:116.

880. Schoeps B, Frädrich J, Krüger A. *Cut loose TIMP-1: an emerging cytokine in inflammation*. Trends in Cell Biology. 2023 May 1;33(5):413–26.

881. Cabral-Pacheco GA, Garza-Veloz I, Castruita-De la Rosa C, Ramirez-Acuña JM, Perez-Romero BA, Guerrero-Rodriguez JF, et al. *The Roles of Matrix Metalloproteinases and Their Inhibitors in Human Diseases*. Int J Mol Sci. 2020 Dec 20;21(24):9739.

882. Lai JH, Hsu YP, Yang CH, Chen YH, Liu CC, Chen SK. *Interferon-gamma regulates the levels of bone formation effectors in a stage-dependent manner*. Mol Biol Rep. 2022 Dec;49(12):12007–15.

883. Dighe AS, Yang S, Madhu V, Balian G, Cui Q. *Interferon gamma and T cells inhibit osteogenesis induced by allogeneic mesenchymal stromal cells*. J Orthop Res. 2013 Feb;31(2):227–34.

884. Gao Y, Grassi F, Ryan MR, Terauchi M, Page K, Yang X, et al. *IFN-gamma stimulates osteoclast formation and bone loss in vivo via antigen-driven T cell activation*. J Clin Invest. 2007 Jan;117(1):122–32.

885. Sato N, Nariuchi H, Tsuruoka N, Nishihara T, Beitz JG, Calabresi P, et al. *Actions of TNF and IFN-gamma on angiogenesis in vitro*. J Invest Dermatol. 1990 Dec;95(6 Suppl):85S-89S.

886. Mühl H, Pfeilschifter J. *Anti-inflammatory properties of pro-inflammatory interferon-gamma*. Int Immunopharmacol. 2003 Sep;3(9):1247–55.

887. Yuan X, He F, Zheng F, Xu Y, Zou J. *Interferon-gamma Facilitates Neurogenesis by Activating Wnt/β-catenin Cell Signaling Pathway via Promotion of STAT1 Regulation of the β-Catenin Promoter*. Neuroscience. 2020 Nov 10;448:219–33.

888. Moldobaeva A, Baek A, Eldridge L, Wagner EM. *Differential activity of pro-angiogenic CXC chemokines*. Microvascular Research. 2010 Jul 1;80(1):18–22.

889. Chandrasekar B, Melby PC, Sarau HM, Raveendran M, Perla RP, Marelli-Berg FM, et al. *Chemokine-cytokine cross-talk. The ELR+ CXC chemokine LIX (CXCL5) amplifies a proinflammatory cytokine response via a phosphatidylinositol 3-kinase-NF-kappa B pathway*. J Biol Chem. 2003 Feb 14;278(7):4675–86.

890. Rovai LE, Herschman HR, Smith JB. *The murine neutrophil-chemoattractant chemokines LIX, KC, and MIP-2 have distinct induction kinetics, tissue distributions, and tissue-specific sensitivities to glucocorticoid regulation in endotoxemia*. J Leukoc Biol. 1998 Oct;64(4):494–502.

891. Roseren F, Pithioux M, Robert S, Balasse L, Guillet B, Lamy E, et al. *Systemic Administration of G-CSF Accelerates Bone Regeneration and Modulates Mobilization of Progenitor Cells in a Rat Model of Distraction Osteogenesis*. Int J Mol Sci. 2021 Mar 28;22(7):3505.

892. Ruef N, Dolder S, Aeberli D, Seitz M, Balani D, Hofstetter W. *Granulocyte-macrophage colony-stimulating factor-dependent CD11c-positive cells differentiate into active osteoclasts*. Bone. 2017 Apr;97:267–77.

893. Nomura K, Kuroda S, Yoshikawa H, Tomita T. *Inflammatory osteoclastogenesis can be induced by GM-CSF and activated under TNF immunity*. Biochemical and Biophysical Research Communications. 2008 Mar 21;367(4):881–7.

894. Zhao J, Chen L, Shu B, Tang J, Zhang L, Xie J, et al. *Granulocyte/macrophage colony-stimulating factor influences angiogenesis by regulating the coordinated expression of VEGF and the Ang/Tie system*. PLoS One. 2014;9(3):e92691.

895. Wallner S, Peters S, Pitzer C, Resch H, Bogdahn U, Schneider A. *The Granulocyte-colony stimulating factor has a dual role in neuronal and vascular plasticity*. Front Cell Dev Biol. 2015 Aug 7. https://www.frontiersin.org/articles/10.3389/fcell.2015.00048

896. Bhattacharya P, Budnick I, Singh M, Thiruppathi M, Alharshawi K, Elshabrawy H, et al. *Dual Role of GM-CSF as a Pro-Inflammatory and a Regulatory Cytokine: Implications for Immune Therapy*. J Interferon Cytokine Res. 2015 Aug 1;35(8):585–99.

897. Khajah M, Millen B, Cara DC, Waterhouse C, McCafferty DM. *Granulocyte-macrophage colony-stimulating factor (GM-CSF): a chemoattractive agent for murine leukocytes in vivo*. J Leukoc Biol. 2011 Jun;89(6):945–53.

898. Gomez-Cambronero J, Horn J, Paul CC, Baumann MA. *Granulocyte-Macrophage Colony-Stimulating Factor Is a Chemoattractant Cytokine for Human Neutrophils: Involvement of the Ribosomal p70 S6 Kinase Signaling Pathway 1*. The Journal of Immunology. 2003 Dec 15;171(12):6846–55.

899. Park YT, Lee SM, Kou X, Karabucak B. *The Role of Interleukin 6 in Osteogenic and Neurogenic Differentiation Potentials of Dental Pulp Stem Cells*. J Endod. 2019 Nov;45(11):1342–8.

900. Huang RL, Sun Y, Ho CK, Liu K, Tang QQ, Xie Y, et al. *IL-6 potentiates BMP-2-induced osteogenesis and adipogenesis via two different BMPR1A-mediated pathways*. Cell Death Dis. 2018 Feb 2;9(2):1–15.

901. McGregor NE, Murat M, Elango J, Poulton IJ, Walker EC, Crimeen-Irwin B, et al. *IL-6 exhibits both cis- and trans-signaling in osteocytes and osteoblasts, but only trans-signaling promotes bone formation and osteoclastogenesis*. J Biol Chem. 2019 May 10;294(19):7850–63.

902. Udagawa N, Takahashi N, Katagiri T, Tamura T, Wada S, Findlay DM, et al. *Interleukin (IL)-6 induction of osteoclast differentiation depends on IL-6 receptors expressed on osteoblastic cells but not on osteoclast progenitors.* The Journal of experimental medicine. 1995 Nov 1;182(5):1461–8.

903. Cohen T, Nahari D, Cerem LW, Neufeld G, Levi BZ. *Interleukin 6 Induces the Expression of Vascular Endothelial Growth Factor (∗)*. Journal of Biological Chemistry. 1996 Jan 12;271(2):736–41.

904. Gopinathan G, Milagre C, Pearce OMT, Reynolds LE, Hodivala-Dilke K, Leinster DA, et al. *Interleukin-6 Stimulates Defective Angiogenesis*. Cancer Res. 2015 Aug 1;75(15):3098–107.

905. Xing Z, Gauldie J, Cox G, Baumann H, Jordana M, Lei XF, et al. *IL-6 is an antiinflammatory cytokine required for controlling local or systemic acute inflammatory responses.* J Clin Invest. 1998 Jan 15;101(2):311–20.

906. Tanaka T, Narazaki M, Kishimoto T. *IL-6 in Inflammation, Immunity, and Disease*. Cold Spring Harb Perspect Biol. 2014 Oct;6(10):a016295.

907. Pedroza M, Schneider DJ, Karmouty-Quintana H, Coote J, Shaw S, Corrigan R, et al. *Interleukin-6 contributes to inflammation and remodeling in a model of adenosine mediated lung injury*. PLoS One. 2011;6(7):e22667.

908. Włodarski K, Włodarski P. *Leptin as a modulator of osteogenesis*. Ortop Traumatol Rehabil. 2009;11(1):1–6.

909. Ducy P, Amling M, Takeda S, Priemel M, Schilling AF, Beil FT, et al. *Leptin Inhibits Bone Formation through a Hypothalamic Relay: A Central Control of Bone Mass*. Cell. 2000 Jan 21;100(2):197–207.

910. Holloway WR, Collier FM, Aitken CJ, Myers DE, Hodge JM, Malakellis M, et al. *Leptin inhibits osteoclast generation*. J Bone Miner Res. 2002 Feb;17(2):200–9.

911. Bernotiene E, Palmer G, Gabay C. *The role of leptin in innate and adaptive immune responses*. Arthritis Research & Therapy. 2006 Jul 28;8(5):217.

912. Dessie G, Ayelign B, Akalu Y, Shibabaw T, Molla MD. *Effect of Leptin on Chronic Inflammatory Disorders: Insights to Therapeutic Target to Prevent Further Cardiovascular Complication*. DMSO. 2021 Jul 17;14:3307–22.

913. Calió ML, Mosini AC, Marinho DS, Salles GN, Massinhani FH, Ko GM, et al. *Leptin enhances adult neurogenesis and reduces pathological features in a transgenic mouse model of Alzheimer's disease*. Neurobiology of Disease. 2021 Jan 1;148:105219.

914. Montecucco F, Bianchi G, Gnerre P, Bertolotto M, Dallegri F, Ottonello L. *Induction of neutrophil chemotaxis by leptin: crucial role for p38 and Src kinases*. Ann N Y Acad Sci. 2006 Jun;1069:463–71.

915. Motyl KJ, Rosen CJ. *Understanding leptin-dependent regulation of skeletal homeostasis*. Biochimie. 2012 Oct;94(10):2089–96.

916. Mulholland BS, Forwood MR, Morrison NA. *Monocyte Chemoattractant Protein-1 (MCP-1/CCL2) Drives Activation of Bone Remodelling and Skeletal Metastasis*. Curr Osteoporos Rep. 2019 Dec;17(6):538–47.

917. Nguyen L, Dewhirst FE, Hauschka PV, Stashenko P. *Interleukin-1 beta stimulates bone resorption and inhibits bone formation in vivo*. Lymphokine Cytokine Res. 1991 Apr;10(1–2):15–21.

918. Kuboi Y, Kuroda Y, Ohkuro M, Motoi S, Tomimori Y, Yasuda H, et al. *The FRACTALKINE-CX3CR1 Axis Regulates Non-inflammatory Osteoclastogenesis by Enhancing Precursor Cell Survival*. JBMR Plus. 2022 Oct;6(10):e10680.

919. Rodan GA. *Bone homeostasis*. Proc Natl Acad Sci U S A. 1998 Nov 10;95(23):13361–2.

920. Marchica V, Toscani D, Corcione A, Bolzoni M, Storti P, Vescovini R, et al. *Bone Marrow CX3CL1/Fractalkine is a New Player of the Pro-Angiogenic Microenvironment in Multiple Myeloma Patients*. Cancers. 2019 Mar 6;11(3):321.

921. Hankenson KD, Dishowitz M, Gray C, Schenker M. *Angiogenesis in Bone Regeneration*. Injury. 2011 Jun;42(6):556–61.

922. Padmanabhan J, Kyriakides TR. *Nanomaterials, Inflammation and Tissue Engineering*. Wiley Interdiscip Rev Nanomed Nanobiotechnol. 2015 May;7(3):355–70.

923. Zheng K, Fan Y, Torre E, Balasubramanian P, Taccardi N, Cassinelli C, et al. *Incorporation of Boron in Mesoporous Bioactive Glass Nanoparticles Reduces Inflammatory Response and Delays Osteogenic Differentiation*. Particle and Particle Systems Characterization. 2020 Jul 1;37(7).

924. Nielsen FH, Meacham SL. *Growing Evidence for Human Health Benefits of Boron:* Journal of Evidence-Based Integrative Medicine. 2011 May 9;16(3):169–80.

925. Zheng K, Niu W, Lei B, Boccaccini AR. *Immunomodulatory bioactive glasses for tissue regeneration*. Acta Biomaterialia. 2021 Oct 1;133:168–86.

926. Lu X, Li K, Xie Y, Qi S, Shen Q, Yu J, et al. *Improved osteogenesis of boron incorporated calcium silicate coatings via immunomodulatory effects*. Journal of Biomedical Materials Research Part A. 2019 Jan 1;107(1):12–24.

927. May P, Khan U, Hughes JM, Coleman JN. *Role of solubility parameters in understanding the steric stabilization of exfoliated two-dimensional nanosheets by adsorbed polymers*. Journal of Physical Chemistry C. 2012;116(20):11393–400.

928. Murali A, Lokhande G, Deo KA, Brokesh A, Gaharwar AK. *Emerging 2D Nanomaterials for Biomedical Applications*. Mater Today (Kidlington). 2021 Nov;50:276–302.

929. Liu P, Li M, Yu H, Fang H, Yin J, Zhu D, et al. *Biphasic CK2.1-coated β-glycerophosphate chitosan/LL37-modified layered double hydroxide chitosan composite scaffolds enhance coordinated hyaline cartilage and subchondral bone regeneration*. Chemical Engineering Journal. 2021 Mar 27;129531.

930. Montalbano G, Calore AR, Vitale-Brovarone C. *Extrusion 3D printing of a multiphase collagen-based material: An optimized strategy to obtain biomimetic scaffolds with high shape fidelity*. Journal of Applied Polymer Science. 2023;e53593.

931. Sordini L, Garrudo FFF, Rodrigues CAV, Linhardt RJ, Cabral JMS, Ferreira FC, et al. *Effect of Electrical Stimulation Conditions on Neural Stem Cells Differentiation on Cross-Linked PEDOT:PSS Films*. Frontiers in Bioengineering and Biotechnology. 2021 Feb 12;9.

932. Chen YC, Lin YF, Liu CT, Liu YC, Lin MH, Lan GY, et al. *Facilitation of Osteogenic Differentiation of hASCs on PEDOT:PSS/MXene Composite Sponge with Electrical Stimulation*. ACS Applied Polymer Materials. 2023 Jun 7 https://pubs.acs.org/doi/full/10.1021/acsapm.3c00146

933. Li YM, Ji Y, Meng YX, Kim YJ, Lee H, Kurian AG, et al. *Neural Tissue-Like, not Supraphysiological, Electrical Conductivity Stimulates Neuronal Lineage Specification through Calcium Signaling and Epigenetic Modification*. Advanced Science. n/a(n/a):2400586.

934. McGlynn E, Nabaei V, Ren E, Galeote-Checa G, Das R, Curia G, et al. *The Future of Neuroscience: Flexible and Wireless Implantable Neural Electronics*. Advanced Science. 2021 Mar 9;2002693.

935. Mim HTR, Haque M, Khan Promon S. *Neural implants: A review of current trends and future perspectives Author 1: Halima-Tul-Rokeya Mim*. 2022; Available from: www.preprints.org

936. Wilson M, Ramezani M, Kim J, Kuzum D. *The Future of Holistic Neural Interfaces: 2D Materials, Neuromorphic Computing, and Computational Co-Design*. 2022 International Electron Devices Meeting (IEDM). 2022 Dec 3;29.5.1-29.5.4.

937. *Precision Neurotechnologies* [Internet]. ARIA. [cited 2024 Oct 2]. Available from: https://www.aria.org.uk/precision-neurotechnologies/

938. *https://www.aria.org.uk/wp-content/uploads/2023/12/ARIA-Precisely-interfacing-with-the-human-brain-v1.0.pdf* [Internet]. [cited 2024 Oct 2]. Available from: https://www.aria.org.uk/wp-content/uploads/2023/12/ARIA-Precisely-interfacing-with-the-human-brain-v1.0.pdf

939. Barshutina MN, Kirichenko SO, Wodolajsky VA, Lopachev AV, Barshutin SN, Gorsky OV, et al. *PDMS-CNT composite for soft bioelectronic neuronal implants*. Composites Part B: Engineering. 2022 Sep 30;110286.

940. Cao B, Huang Y, Chen L, Jia W, Li D, Jiang Y. *Soft Bioelectronics for Diagnostic and Therapeutic Applications in Neurological Diseases*. Biosensors and Bioelectronics. 2024 May 11;116378.

941. Chen C, Sun X, Peng H. *The Rise of Soft Neural Electronics*. Giant. 2021 Aug 21;100075.

942. Lee M, Shim HJ, Choi C, Kim DH. *Soft High-Resolution Neural Interfacing Probes: Materials and Design Approaches*. Nano Lett. 2019 May 8;19(5):2741–9.

943. Kim M, Lee H, Nam S, Kim DH, Cha GD. *Soft Bioelectronics Using Nanomaterials and Nanostructures for Neuroengineering*. Acc Chem Res. 2024 May 16 https://doi.org/10.1021/acs.accounts.4c00163

944. Dijk G, Pas J, Markovic K, Scancar J, O'Connor RP. *PEDOT:PSS-coated platinum electrodes for neural stimulation*. APL Bioengineering. 2023 Dec 1;7(4):046117.

945. Aldawood FK, Andar A, Desai S. *A Comprehensive Review of Microneedles: Types, Materials, Processes, Characterizations and Applications*. Polymers. 2021 Aug;13(16). https://www.ncbi.nlm.nih.gov/pmc/articles/PMC8400269/

946. Abidian MR, Daneshvar ED, Egeland BM, Kipke DR, Cederna PS, Urbanchek MG. *Hybrid Conducting Polymer-Hydrogel Conduits for Axonal Growth and Neural Tissue Engineering*. Advanced Healthcare Materials. 2012 Nov 1;1(6):762–7.

947. Cheng S, Zhu R, Xu X. *Hydrogels for next generation neural interfaces*. Commun Mater. 2024 Jun 12;5(1):1–9.

948. Han M, Yildiz E, Kaleli HN, Karaz S, Eren GO, Dogru-Yuksel IB, et al. *Tissue-like Optoelectronic Neural Interface Enabled by PEDOT:PSS Hydrogel for Cardiac and Neural Stimulation*. Advanced Healthcare Materials. 2021 Dec 30;2102160.

949. Montero de Espinosa L, Meesorn W, Moatsou D, Weder C. *Bioinspired Polymer Systems with Stimuli-Responsive Mechanical Properties*. Chem Rev. 2017 Oct 25;117(20):12851–92.

950. Mao Png Z, Wang CG, Chuan Yeo JC, Cheng Lee JJ, Erdeanna Surat'man N, Lin Tan Y, et al. *Stimuli-responsive structure–property switchable polymer materials*. Molecular Systems Design & Engineering. 2023;8(9):1097–129.

951. Boulingre M, Portillo-Lara R, Green RA. *Biohybrid neural interfaces: improving the biological integration of neural implants*. Chem Commun. 2023;10.1039.D3CC05006H.

952. Derakhshi M, Daemi S, Shahini P, Habibzadeh A, Mostafavi E, Ashkarran AA. *Functional Biomaterials Two-Dimensional Nanomaterials beyond Graphene for Biomedical Applications*. 2022 [cited 2022 Mar 15]; Available from: https://doi.org/10.3390/jfb13010027

953. Wang X, Han X, Li C, Chen Z, Huang H, Chen J, et al. *2D Materials for Bone Therapy*. Advanced Drug Delivery Reviews. 2021 Sep;113970.

Appendices

Appendix 1 – Additional Figures for Chapter 2

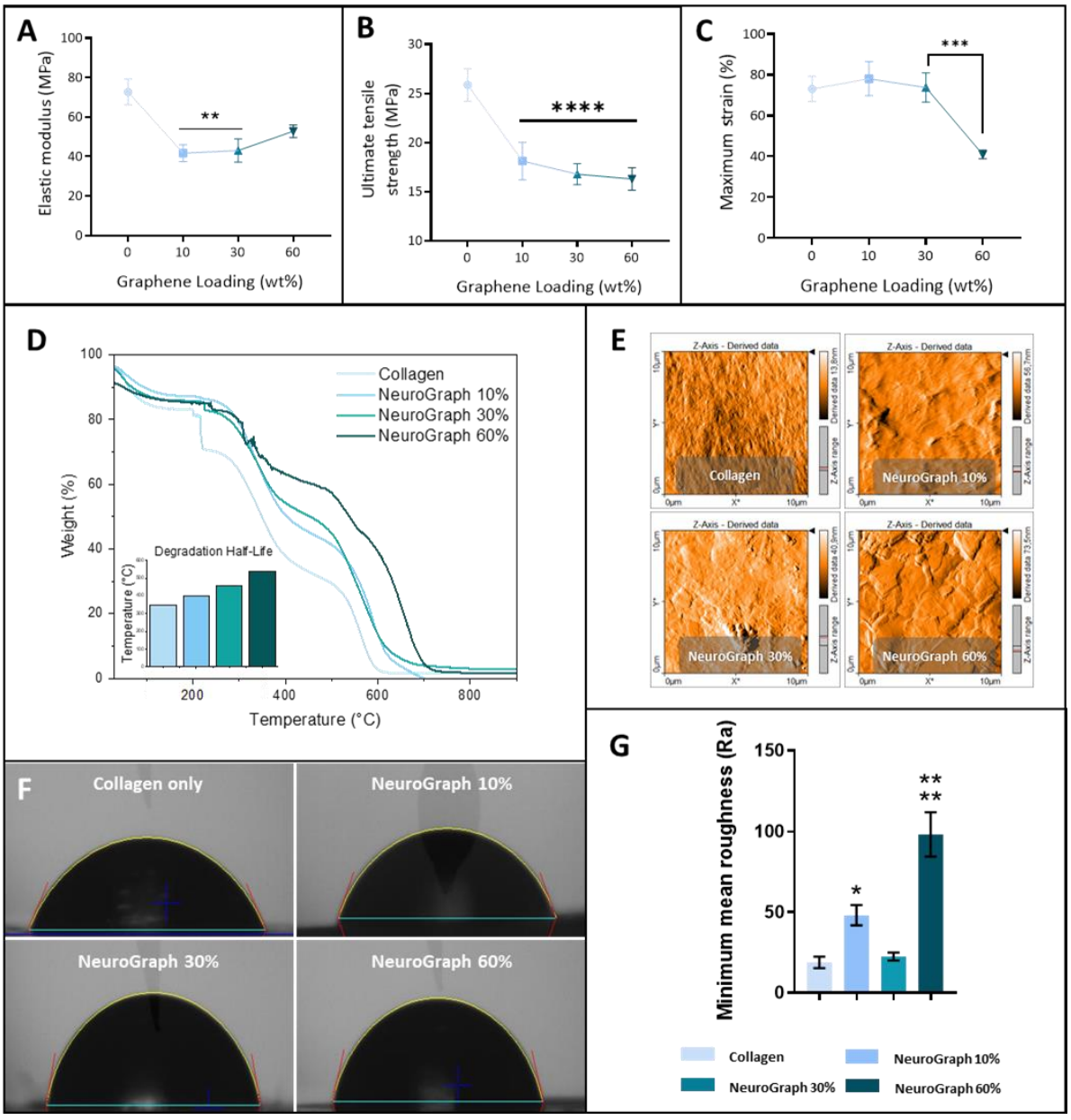

Fig. A1.1 – ***Characterization of bulk physical properties of collagen/pristine graphene (NeuroGraph) composite films: A-C)*** *Assessment of the maximum elastic modulus in the linear elastic region of the stress-strain curve (A), ultimate tensile strength (B), and maximum strain (C) of the hydrated films, as a function of pG loading and obtained by stress-strain measurements.* ***D)*** *Thermogravimetric analysis of NeuroGraph films under an O_2 atmosphere, with inset chart showing the temperature at which half of the sample is degraded.* ***E)*** *AFM images derived from z-axis scans for collagen only, 10%, 30%, and 60% NeuroGraph samples.* ***F)*** *Contact angle goniometric images for collagen only, 10%, 30%, and 60% NeuroGraph samples.* ***G)*** *Assessment of surface topographic features of NeuroGraph films, namely minimum line roughness, through AFM. * Denotes statistical significance: *$p < 0.05$, **$p < 0.01$, ***$p < 0.001$, ****$p < 0.0001$.*

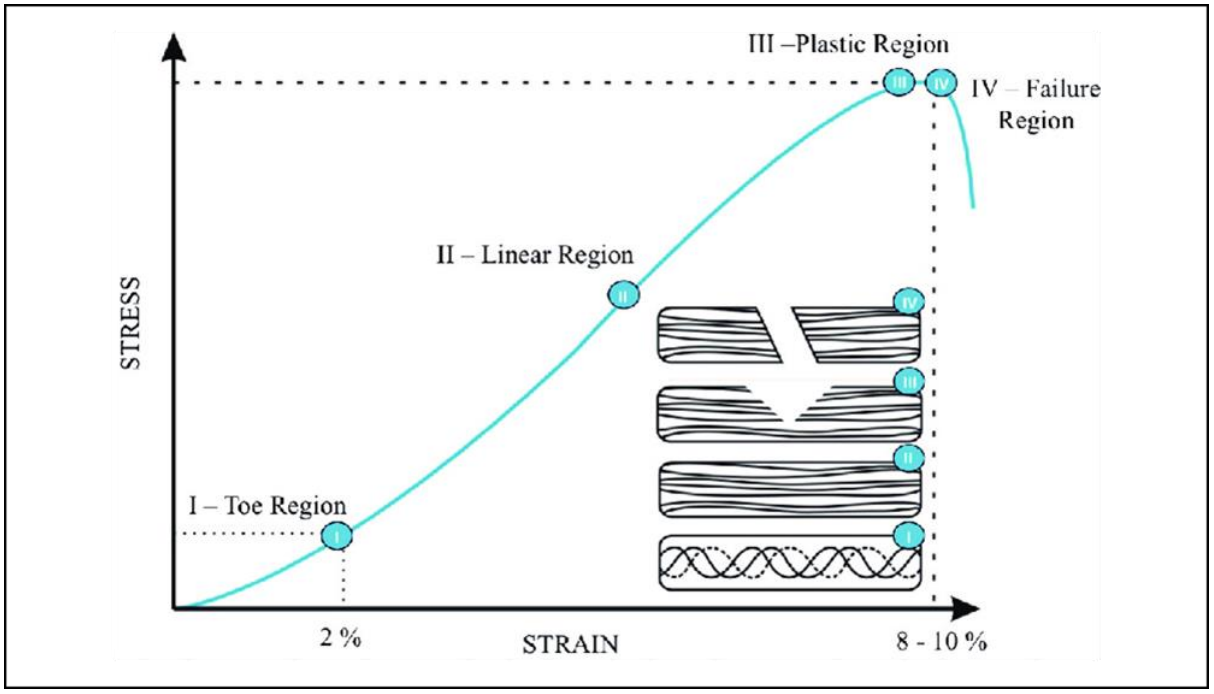

*Fig. A1.2 – **Stress-strain curve for collagen:** Diagram illustrating typical stress-strain curve for collagen, adapted from Robi K, Jakob N, Matevz K, Matjaz V (2013). Chapter 2: The Physiology of Sports Injuries and Repair Processes. In Hamlin M (Ed.), ISBN: 978-953-51-1031-6, InTech, DOI: 10.5772/54234.*

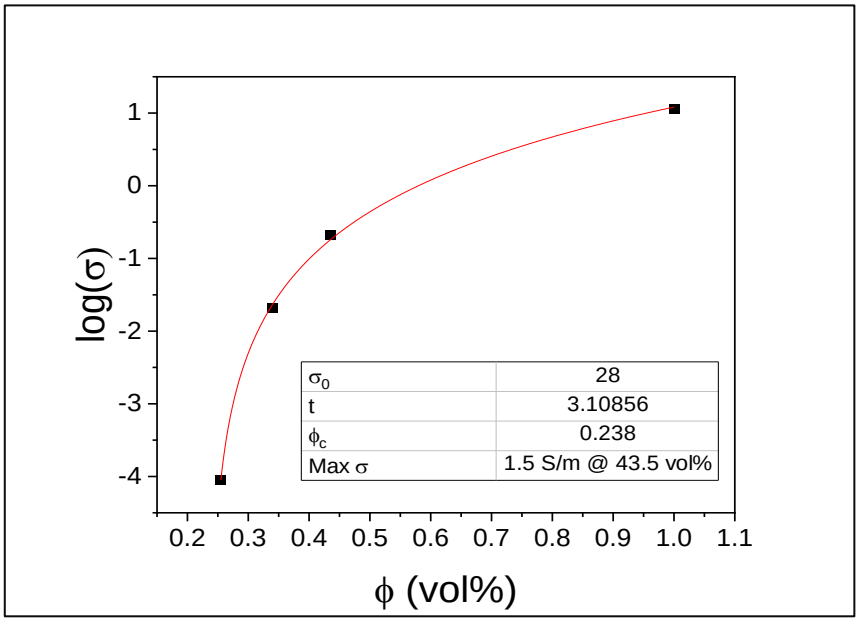

*Fig. A1.3 – **Percolation curve of collagen-graphene composites**: Percolation curve for collagen-graphene composites, indicating percolation onset at 23.8 vol%, with a maximum conductivity achieved at 60 vol%, before composite mechanical properties began to degrade. σ = Conductivity, ϕ = Volume fraction of filler, σ_0 = Conductivity of filler, t = Percolation exponent, ϕ_c = Percolation threshold.*

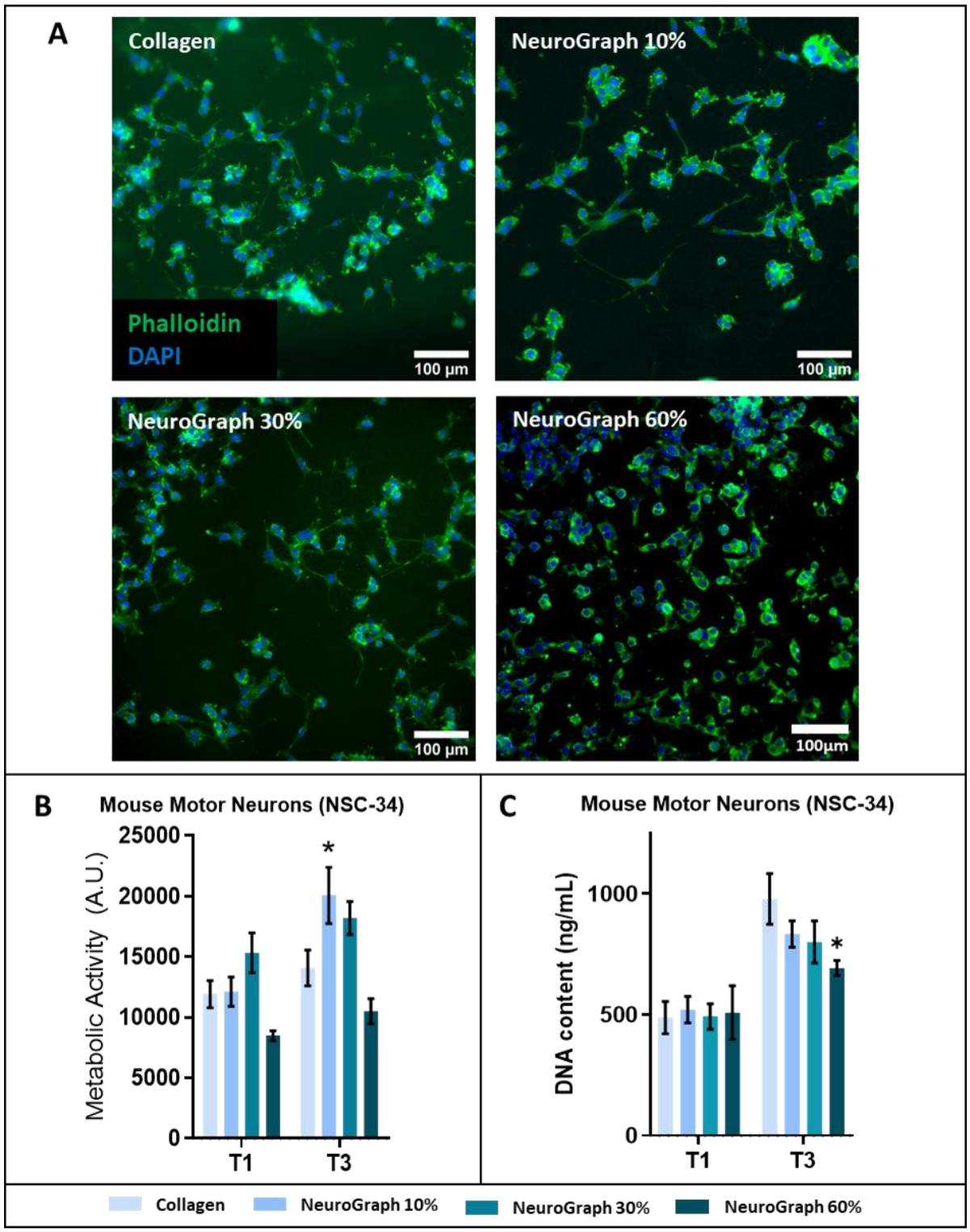

*Fig. A1.4 – **Further characterization of neuro-compatibility of collagen/pristine graphene films: A)** NSC-34 neurons grown for 3 days on collagen and composites films immunostained with β-tubulin III exhibited typical neuronal morphologies with no differences between the groups. **B)** Assessment of metabolic activity and **C)** DNA content of neurons grown on the films at 1 and 3 days after seeding showed similar values for both parameters across all groups. Scalebar = 100 µm. *p< 0.05.*

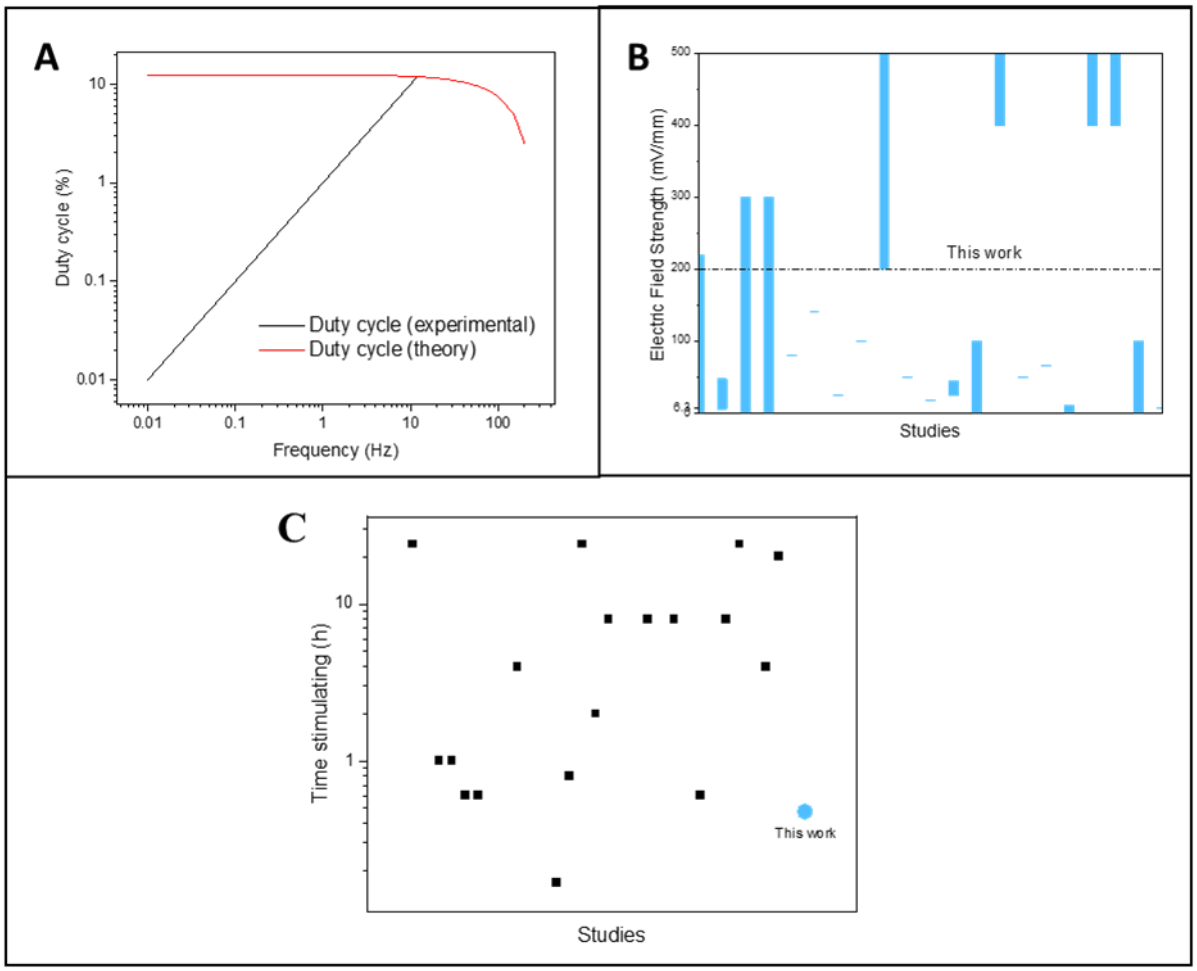

*Fig. A1.5 – **Optimisation of electrical stimulation parameters for spinal cord neurons:** **A)** Duty cycle calculations, based on limitations of IonOptix stimulation device. **B)** Review of electric field strength (Bertucci et al.[377]) in comparison to value used in this work. **C)** Review of time spent stimulating (Bertucci et al.[377]) compared to parameters used in this work.*

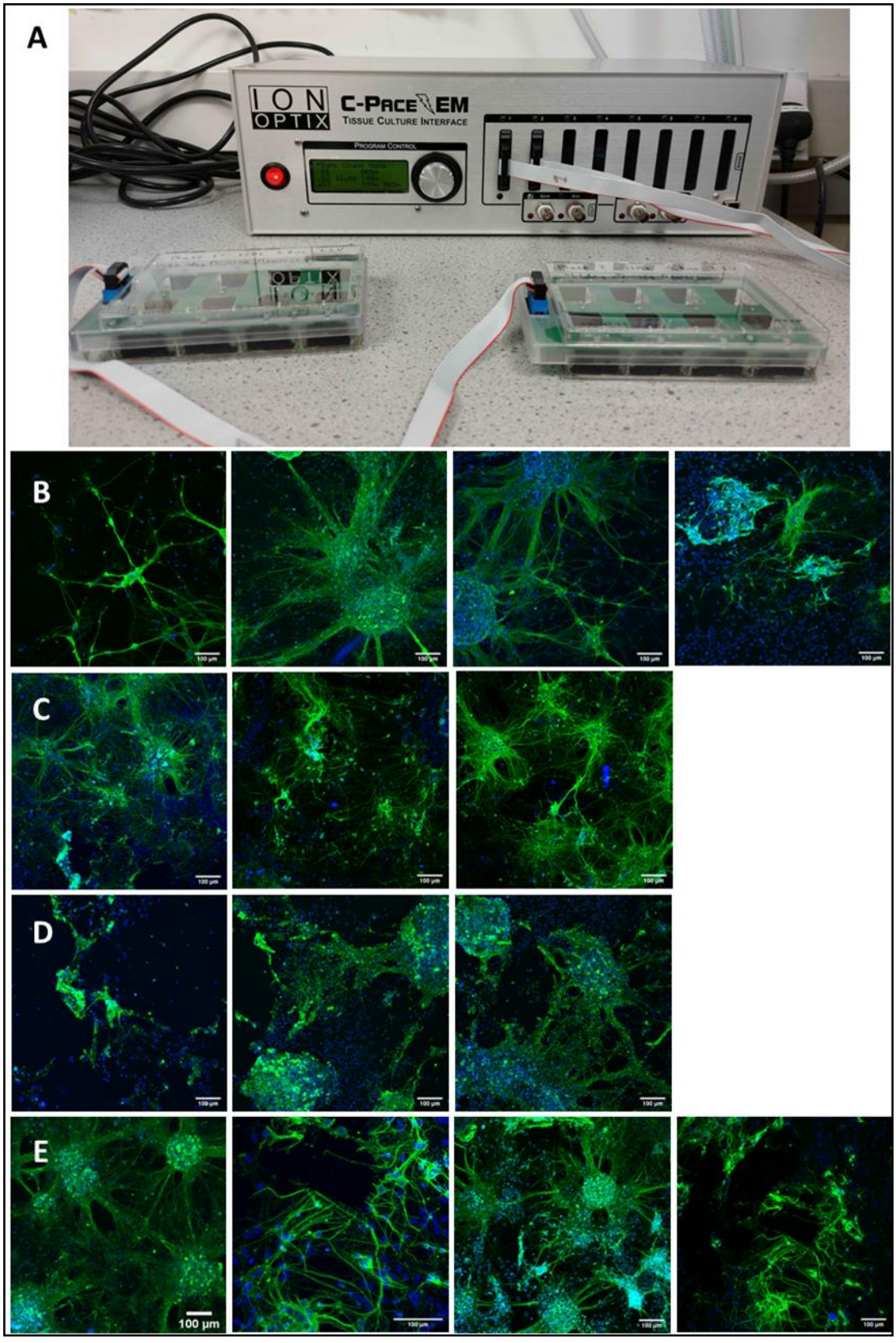

Fig. A1.6 – ***Further electrical stimulation data: A)*** *Image of the IonOptix electrical stimulation rig used for stimulation in this study, with electrodes in plates shown.* ***B-E)*** *Representative images of mouse primary cortical neurons on collagen without stimulation (B), NeuroGraph without stimulation (C), collagen after stimulation (D), and NeuroGraph after stimulation (E). All cells stained with β-III-tubulin and DAPI and taken at 10× magnification. Scalebars 100 µm.*

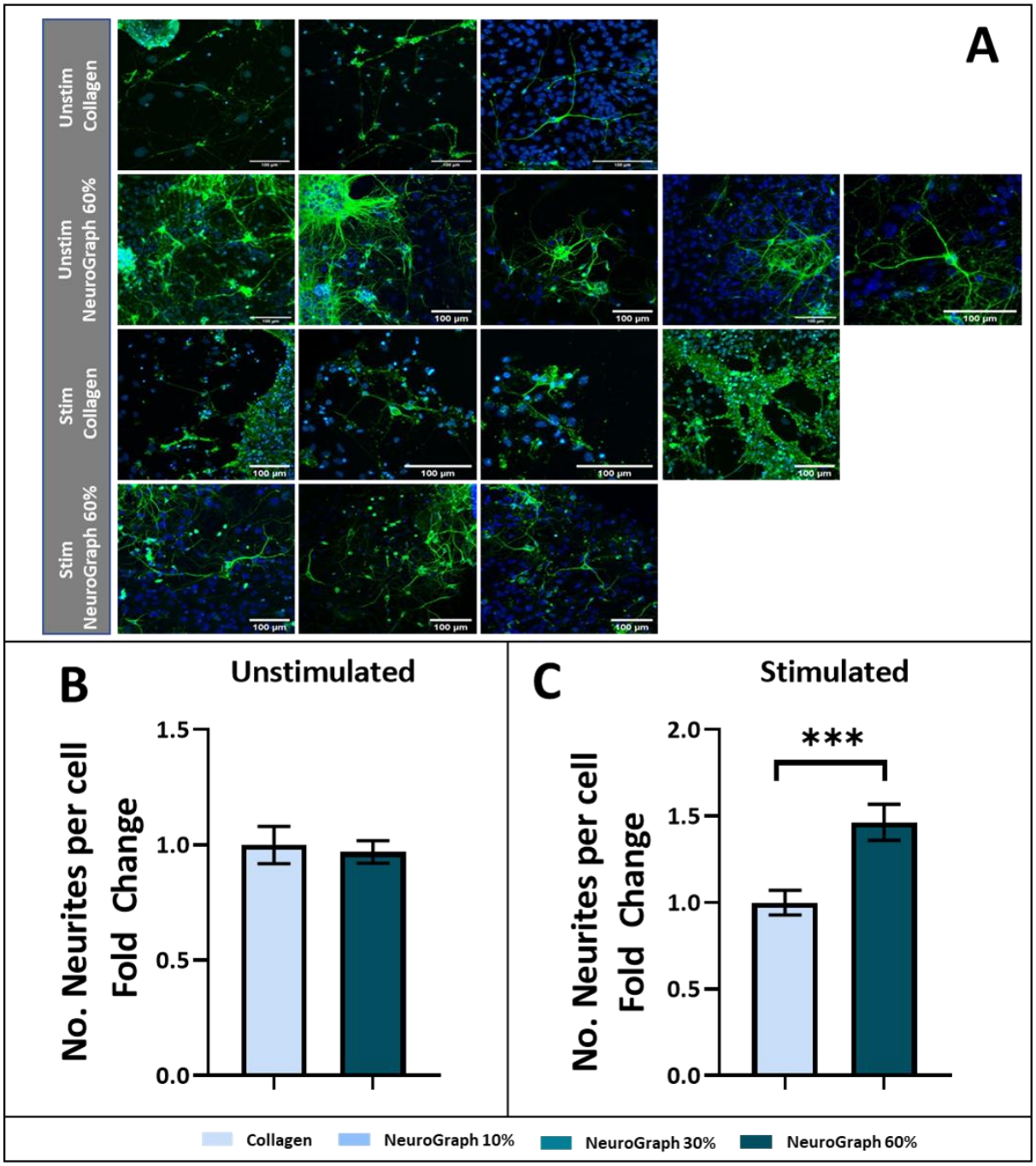

*Fig. A1.7 – **Further electrical stimulation data: A)** Representative images of mouse primary cortical neurons on NeuroGraph 60% after stimulation, collagen after stimulation, NeuroGraph without stimulation, and collagen without stimulation. All cells stained with β-III-tubulin and DAPI and taken at 20× magnification. **B-C)** Number of neurites per cell for unstimulated (B) and stimulated (C) mouse primary cortical neurons on collagen and NeuroGraph60%. * Denotes statistical significance: ***p<0.001. Scalebars 100 µm.*

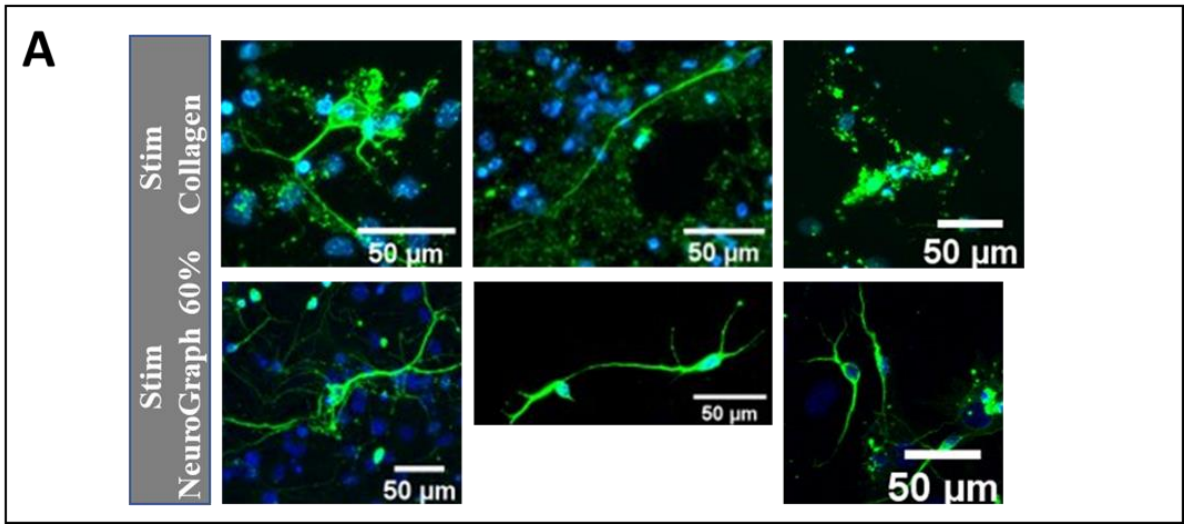

Fig. A1.8 – ***Higher magnification electrical stimulation images: A)*** *Representative images of mouse primary cortical neurons on NeuroGraph60% and collagen after stimulation. All cells stained with β-III-tubulin and DAPI and taken at 20× magnification and zoomed in to focus on individual neurons.*

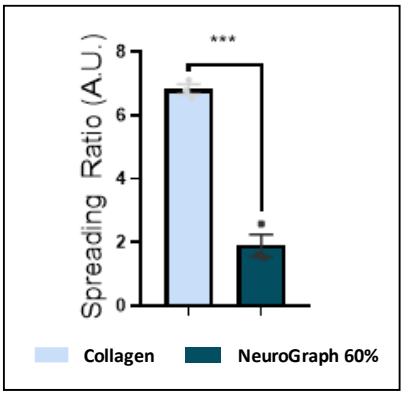

Fig. A1.9 – Printability of NeuroGraph: Spreading ratio data for 12 mg/mL collagen and NeuroGraph60% slurries extrusion printed at 4°C. * Denotes statistical significance: ***p<0.001.

```
%Elastic Modulus by percent strain
clear all
close all
clc

%Written by Jessica Perez, Pedro Jose Gouveia, Javier Gutierrez Gonzalez,
%Gabriel Costa and Jack Maughan

% Input:
% Excel files: files containing stress and strain of the sample that underwent uniaxial tensile testing. This code can do
% multiple files in one run.
% Note: The resulting file will contain the results of all the files that are inputted. You can input them in forms of
% conditions but it is not necessary as the excel file exported has the data labelled by the sample name

%Output:
% (1) Figure that contains a subplot of 3 graphs
%     (I) Stress vs Strain curve of data with the line of the elastic
%         modulus in red
%     (II) Slope vs Strain
%     (III) Rsquare vs Strain
% (2) Excel sheet named 'ElasticModulusResults.xlsx'. It contains the following data for all the samples analyzed in one run.
%     (I) 'R2': Rsquared of elastic modulus line
%     (II) 'Elastic Modulus': slope of best fit line i.e. the elastic modulus
%     (III) 'Tensile Strength': max stress i.e. tensile strength
%     (IV) 'Strain': the strain at max stress

%% Elastic Modulus MATLAB code
%This is to prompt how many times you will run the code i.e. how many files you want to analyse.
prompt= 'How many samples will be analysed? (Input number in Command Window): ';
s=input(prompt);

for i=1:s
%Extracting  data from excel file
prompt= 'Select the file of the sample/condition '
[filename, pathname] = uigetfile('*.*', 'Select file');
data=xlsread(filename);
index=size(data,1);

%Two options here. Read carefully and comment the one you don't need and uncomment the one that you do need
%(1) There is data in the first column of wall thickness
strain=data(9:index,3); %for sheets where data starts on 7th row 4th column
stress=data(9:index,4); %for sheets where data starts on 7th row 3rd column
%(2) There is no data in the first column of wall thickness making it 3 columns instead of 4 in the data array
%strain=data(7:index,4); %for sheets where data starts on 7th row 4th column
%stress=data(7:index,3); %for sheets where data starts on 7th row 3rd column
SMmax = max(stress); %max stress or tensile strength
SSmax = strain(find(stress == SMmax,1)); % strain for tensile strength

% Define length of the slope which you want to calculate Elastic Modulus for:
   % window size with fraction of datapoints
   winsz = 10; % in percentage
   sampint = 2; % position a sliding window every sample interval
   szdata = length(strain); % get full size of datapoints
   % get initial and final positions of each sliding window
%Used to find the maximum elastic modulus in the linear region of the curve
   %posI = 0:sampint:(floor(max(strain)-winsz)); % initial pos every 2% % -winsz makes sure the vector stops at max(strain) -
winsz%, so that a winsz window fits
   %posF = posI + winsz; % final pos for 5% windows
%Used to find the elastic modulus in the first 10% of the stress-strain curve
   posI = 0;
   posF = 10;
   GetData = [];
   %% Select input data:
   tic
```

```
    for nwin = 1:length(posI)
      initpoint = min(find(strain >= posI(nwin)));
      endpoint  = min(find(strain >= posF(nwin)));
            datax = strain(initpoint:endpoint);
      datay = stress(initpoint:endpoint);
      [p S] = polyfit(datax,datay,1);   % p returns 2 coefficients fitting r = a_1 * x + a_2
      Rsq = 1 - (S.normr/norm(datay - mean(datay)))^2; % check that polyfit returns R2 by doing this
      GetData.b(nwin) = p(2); %p is from polyfit and in this calculates the y intercept of the line that will be tangent line that
will be seen in the graph
      GetData.m(nwin) = p(1); %p is from polyfit and in this calculates slope
      GetData.Rsq(nwin) = Rsq; %Rsq from equating using S info from polyfit
      GetData.centre(nwin) = mean(strain([initpoint endpoint]));
      GetData.initpoint(nwin)=initpoint;
      GetData.endpoint(nwin)=endpoint;
    end
    timefun = toc;
    maxm = max(GetData.m);
    cmmax = min(find(GetData.m == maxm)); % first max m centre
%These commands gets all the data that is relevant for the maximum slope
    GetData.mmax = GetData.m(cmmax);
    GetData.Rmmax = GetData.Rsq(cmmax);
    GetData.bmmax = GetData.b(cmmax);
    GetData.initpointmmax=GetData.initpoint(cmmax);
    GetData.endpointmmax=GetData.endpoint(cmmax);
%makes matrix of the data relevant to the max m to be used to export the data into an excel sheet
m1=GetData.mmax;
b1=GetData.bmmax;
ip=GetData.initpointmmax;
ep=GetData.endpointmmax;
EMgraph_x=transpose(linspace(strain(ip),strain(ep),1000));
EMgraph_y=(m1.*EMgraph_x)+b1; %this calculates the numbers for your y-axis i.e. strain from the equation y=mx+b
figure;
    subplot(3,1,1)
    plot(strain, stress, 'b', 'LineWidth', 1.5);hold on;
    plot(EMgraph_x,EMgraph_y,'r','LineWidth',1.5);hold on;
    plot(SSmax,SMmax,'ro');hold on;
    title('Stress (y) vs Strain (x)')
    subplot(3,1,2)
    plot(GetData.centre, GetData.m, 'r', 'LineWidth', 1.5)
    title('Slope')
    subplot(3,1,3)
    plot(GetData.centre, GetData.Rsq, 'k', 'LineWidth', 1.5)
    title('Rsquared for Linear Fit')
    newfilename = erase(filename,".xlsx"); %deletes extension .xlsx, if the excel sheet is different extesion, change this
    saveas (gcf,newfilename,'jpeg'); %saves the figure as a jpeg with the filename
R2(i)=GetData.Rmmax;
m(i)=GetData.mmax;
b(i)=GetData.bmmax;
str(i)=string(newfilename); %this makes a matrix with the filename so that it can show which sample corresponds to the data
SS(i)=SSmax;
SM(i)=SMmax;
end
R2=transpose(R2);
m=transpose(m);
str=transpose(str);
SM=transpose(SM);
SS=transpose(SS);
output=[str R2 m SM SS]; %all output data that comes from the code
h={'Sample','R2', 'Elastic modulus', 'Ultimate Tensile Strength', 'Maximum Strain (%)'};
q=[h;num2cell(output)];
filename='ElasticModulusResults.xlsx'; %name of file that will be exported
xlswrite(filename, q);
```

Fig. A1.10 – MATLAB code for calculating the Young's modulus for a stress-strain curve

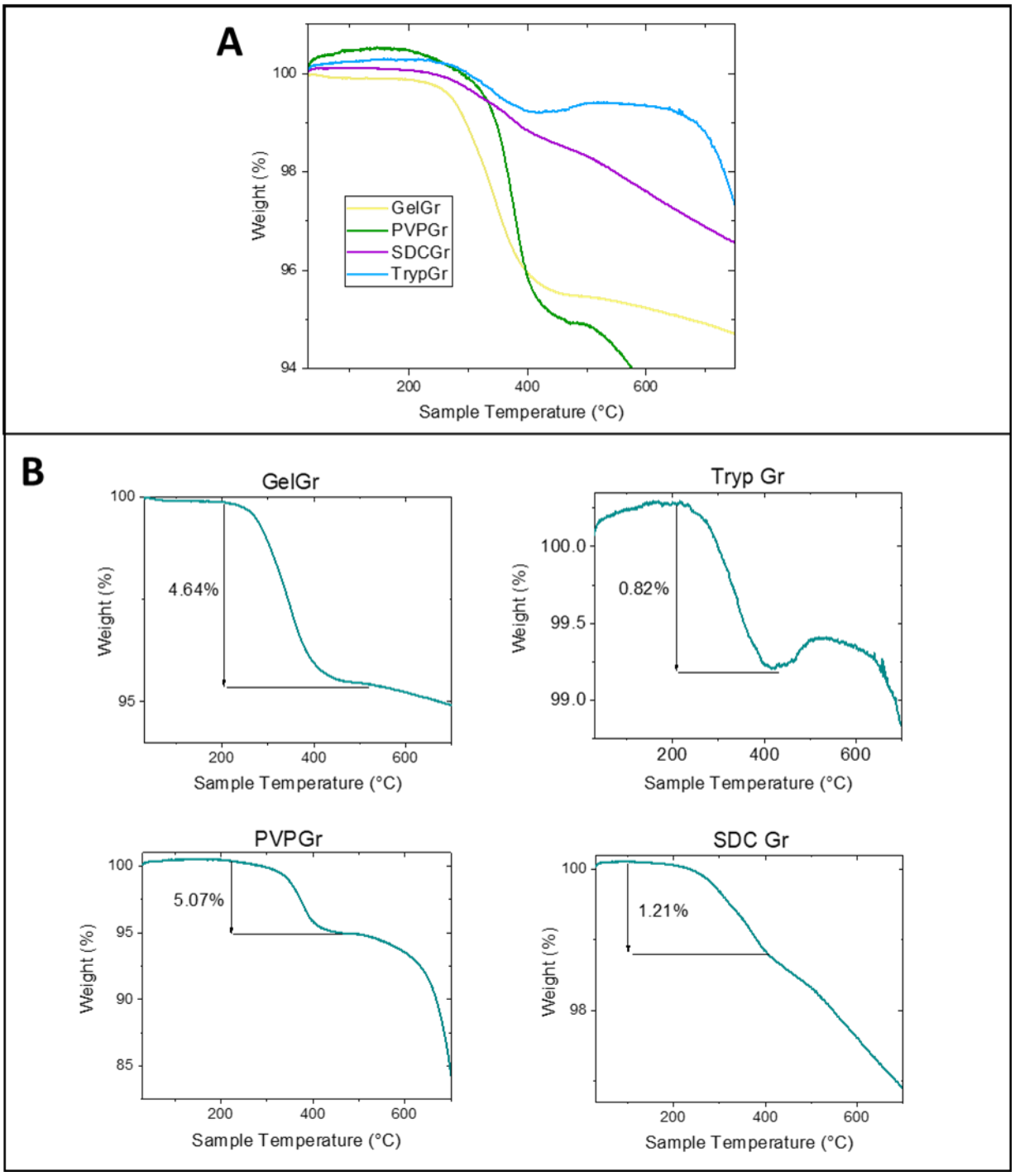

Fig. A2.1 – ***Nitrogen TGA of graphene candidates:*** *Thermogravimetric analysis carried out under nitrogen on graphene samples (A), with individual traces shown in B for GelGr, TrypGr, PVPGr and SDCGr.*

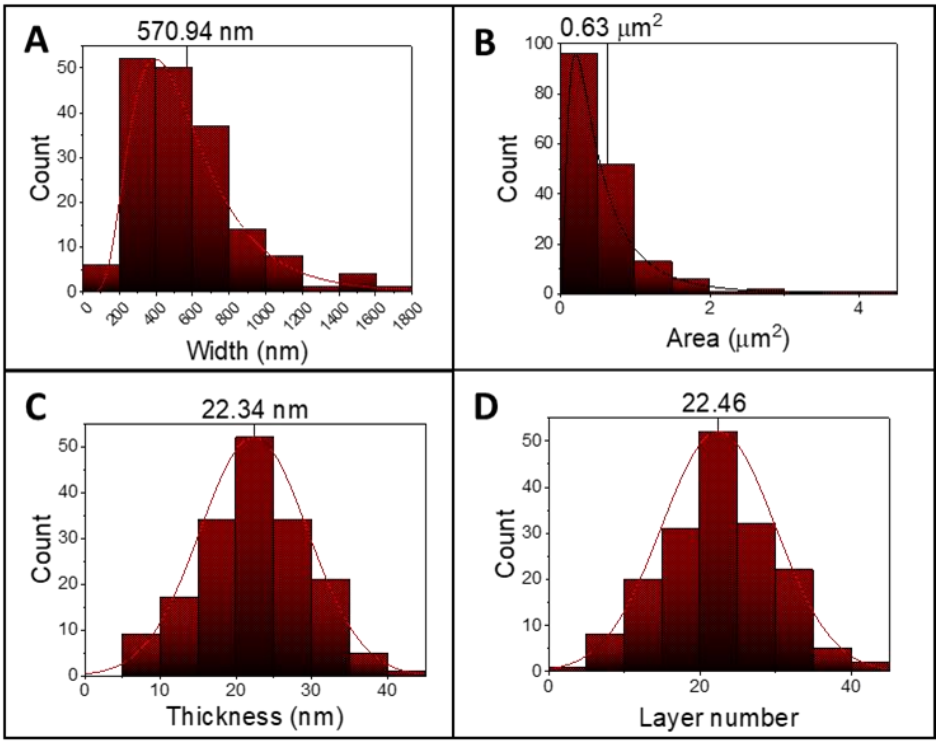

Fig. A2.2 – ***AFM analysis for PVPGr nanosheets:*** *Histograms of* ***A)*** *Nanosheet width* ***B)*** *Nanosheet area* ***C)*** *Nanosheet thickness and* ***D)*** *Layer number.*

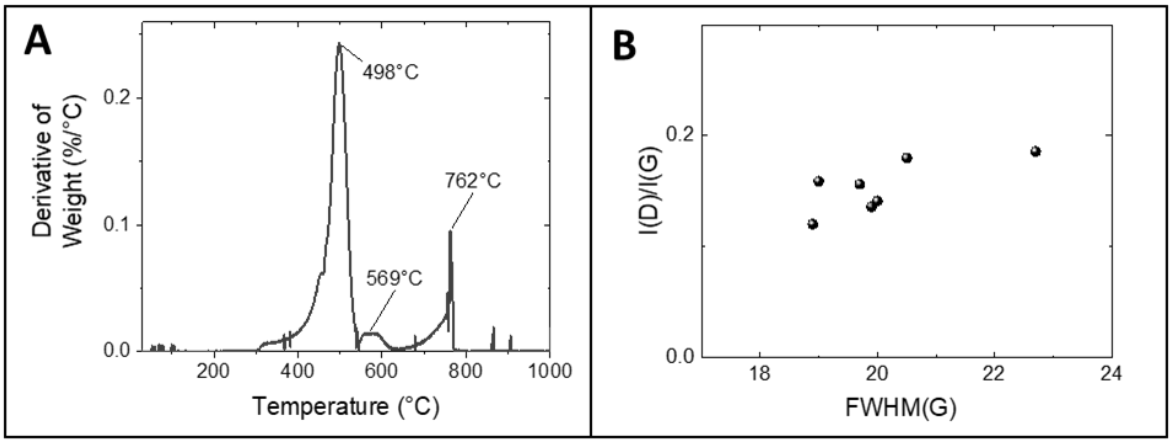

Fig. A2.3 – ***Further physical characterisation of PVPGr and PolyGraph:*** ***A)*** *Derivative of TGA spectrum for PVPGr/PCL 10vol%, showing peaks in decomposition corresponding to PCL (~500 °C) and PVPGr (~750 °C) respectively.* ***B)*** *Raman statistics for PVPGr, with the lack of correlation between the* I_D/I_G *ratio and the full-width-half-maximum (FWHM) of the G peak indicating a defect-free basal plane.*

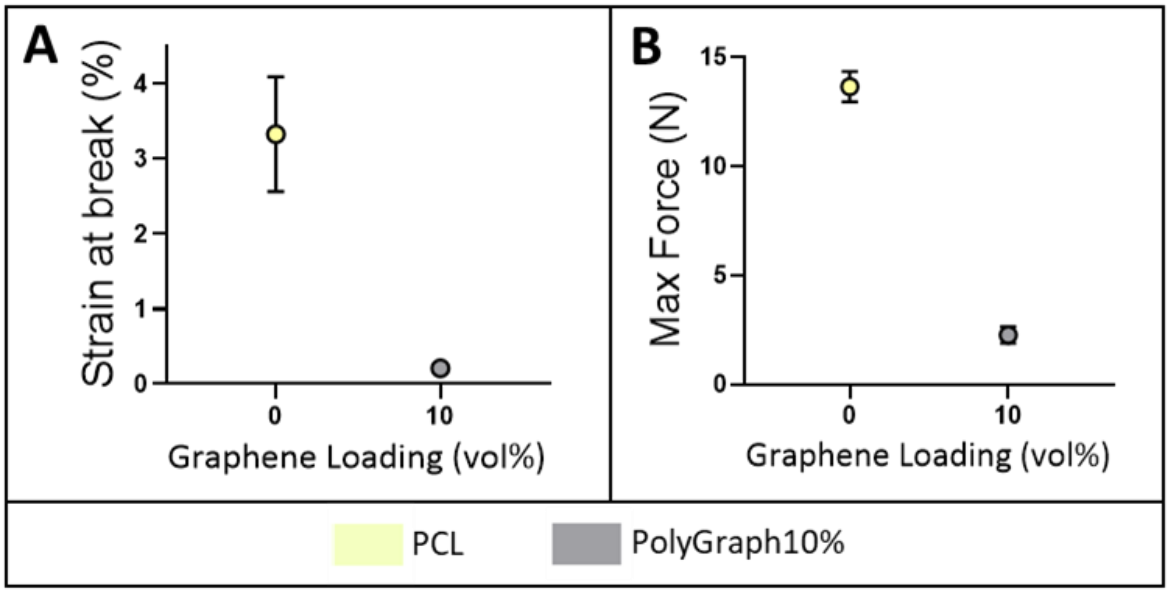

*Fig. A2.4 – **Mechanical testing of PolyGraph:** **A)** Strain at break and **B)** maximum force measurements for PCL and PolyGraph10%, showing a decrease in ductility due to addition of graphene.*

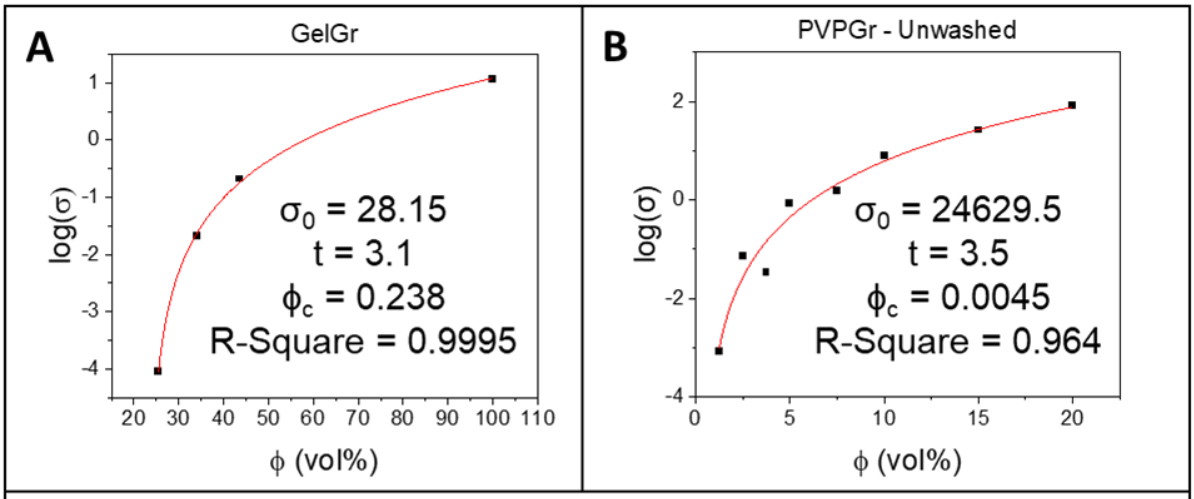

C

Composite	σ_0	t	ϕ_c	Max σ
Collagen/GelGr	28.1 ± 6.0	3.1 ± 0.2	0.238 ± 0.003	1.5 S/m at 43.5 vol%
PCL/PVPGr Washed	52105 ± 74498	3.1 ± 0.7	0.0145 ± 0.007	228.1 S/m at 20 vol%
PCL/PVPGr Unwashed	24630 ± 39830	3.5 ± 0.7	0.0045 ± 0.005	81 S/m at 20 vol%

*Fig. A2.5 – **Percolation curves:** Percolation curves (A-B) and fitting parameters (C) for GelGr (A) and PVPGr without washing (B), showing significant improvements in electrical properties for PolyGraph compared to Collagen/GelGr, and a significant improvement of the electrical performance following washing of excess polymer stabiliser from the graphene material.*

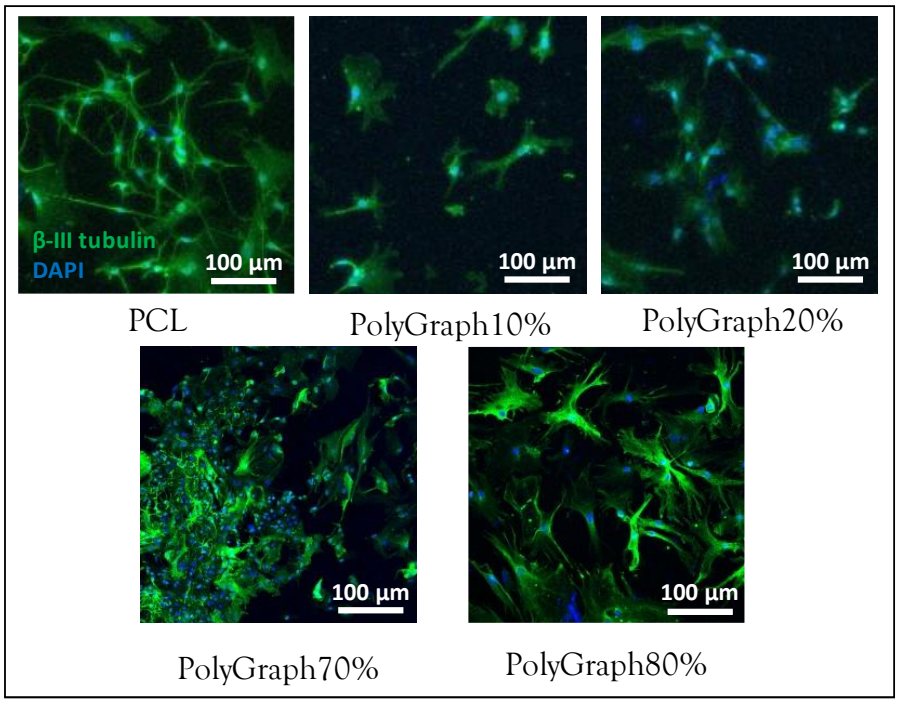

*Fig. A2.6 – **Mouse primary cortical neurons grown on PolyGraph substrates:** Mouse primary neurons grown on the surface of PolyGraph composites for 14 days imaged using confocal microscopy following staining with β-tubulin III for neuronal morphology and DAPI for nuclei. Robust proliferation across the surface indicated biocompatibility with sensitive, physiologically relevant cells.*

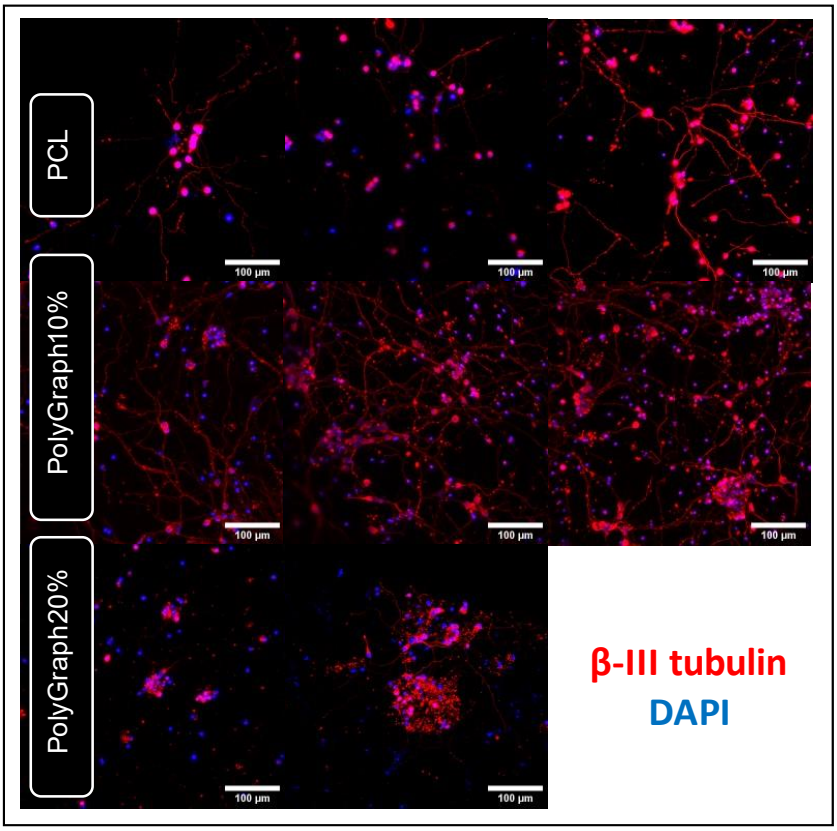

*Fig. A2.7 – **iPSC neurons on PolyGraph:** iPSC neurons grown on PolyGraph for 14 days, imaged by confocal microscopy following staining with β-III tubulin for the neuronal cell body and DAPI for the cell nucleus. Scalebars are 100 µm.*

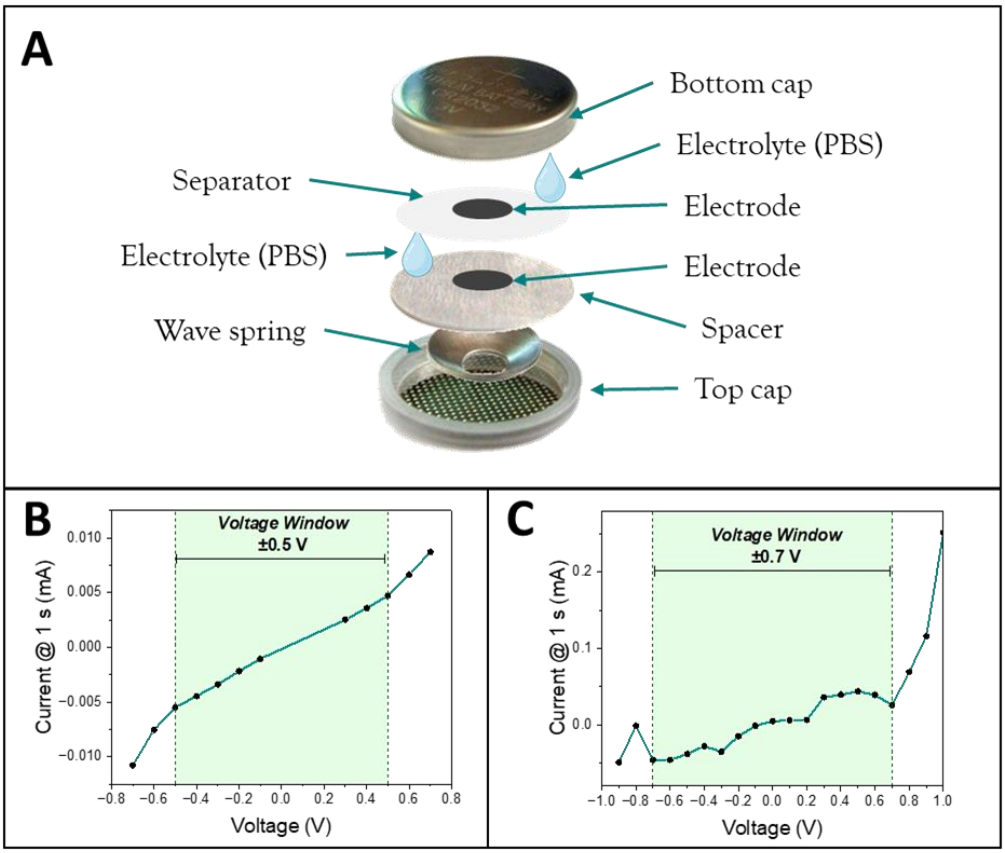

Fig. A2.8 – ***Electrical characterisation of PVPGr and PolyGraph composites: A)*** *Schematic of two-electrode coin cell setup used for electrochemical characterisation.* ***B)*** *Current at 1s from chronoamperometry, showing the potential window of untreated PolyGraph at ±0.5 V.* ***C)*** *Current at 1s from chronoamperometry, showing the potential window of the AuPd + NaOH treated PolyGraph at ~±0.7 V.*

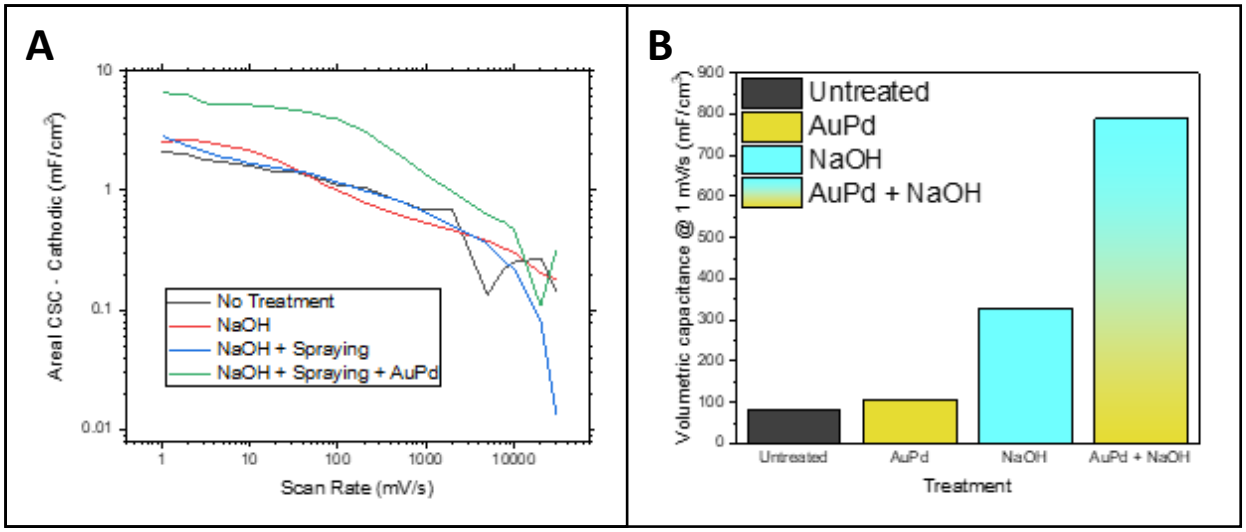

Fig. A2.9 – ***Charge storage capacity for composites treated by spray coating: A)*** *Impact of graphene spray coating and AuPd coating on charge storage capacity of PolyGraph composites.* ***B)*** *Volumetric capacitance of PolyGraph composites following surface treatments.*

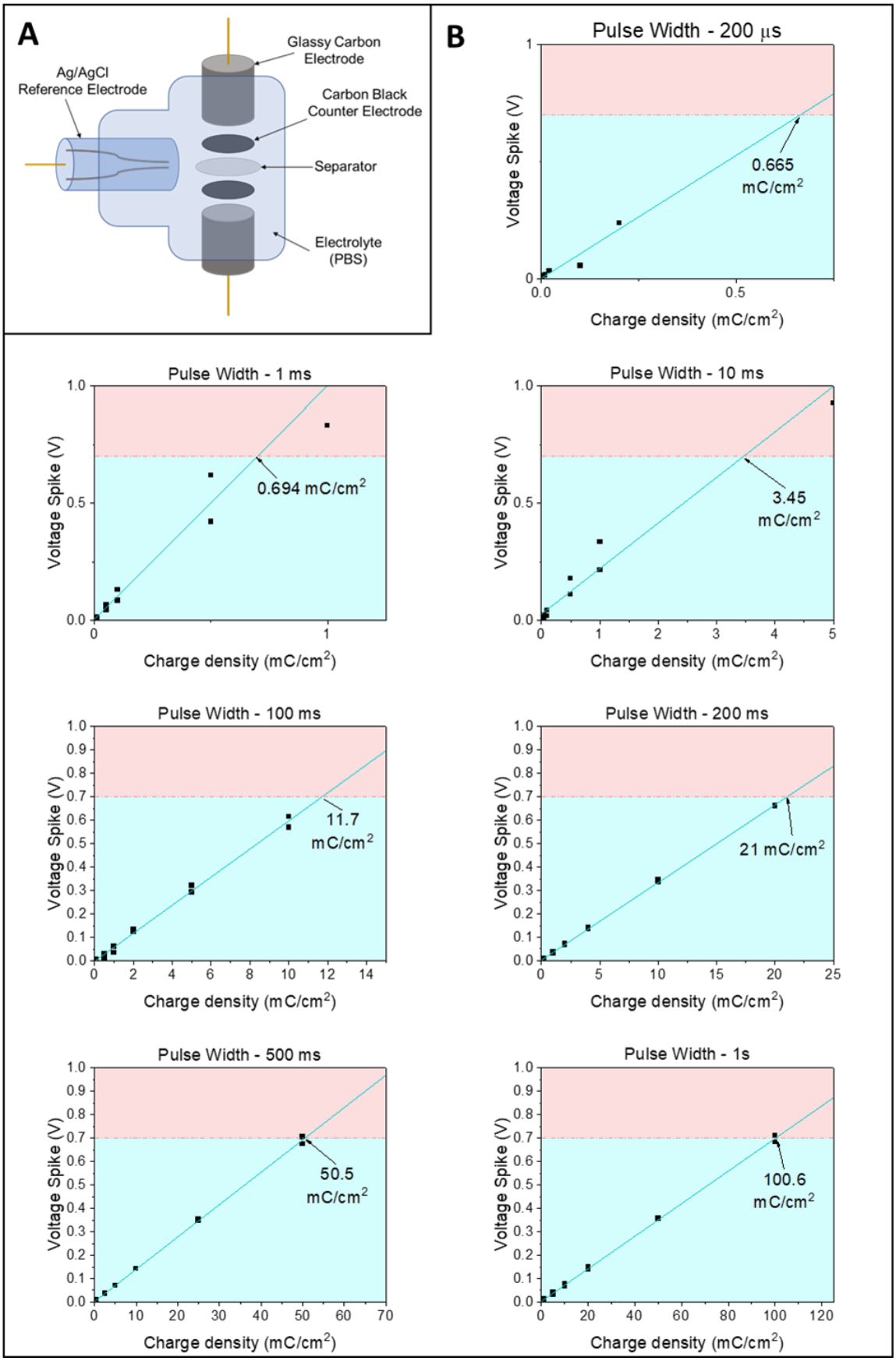

*Fig. A2.10 – **Voltage transients curves:** A three-electrode setup (A) was used to capture voltage transients following square wave excitation at a series of pulse widths ranging from 200 µs to 1 s (B) to calculate the charge injection capacity. Electrochemical potential window (~±0.7 V) shown in blue.*

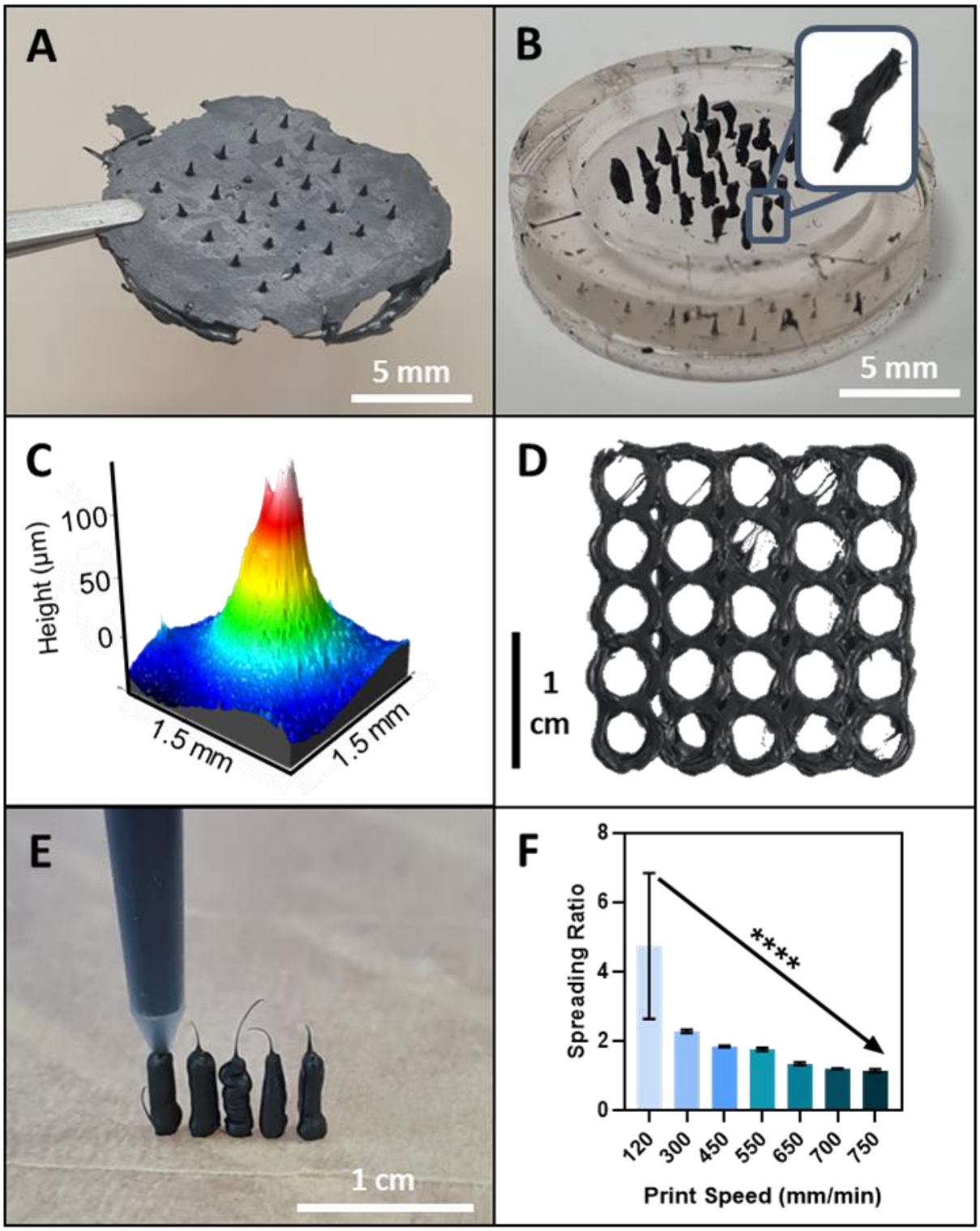

*Fig. A2.11 – **3D printing of PolyGraph:** **A)** Dry-cast microneedle array. **B)** Microneedle array in mold, with pillar backing. **C)** White-light interferometry profile of microneedle. **D)** Cylindrical construct for tissue engineering applications 3D printed from PolyGraph10% using a solvent printing method. **E)** Optical images of 3D printing process for backing pillars, allowing needle isolation. **F)** Determination of optimal printing speed for reduced spreading ratio when 3D solvent printing PolyGraph.*

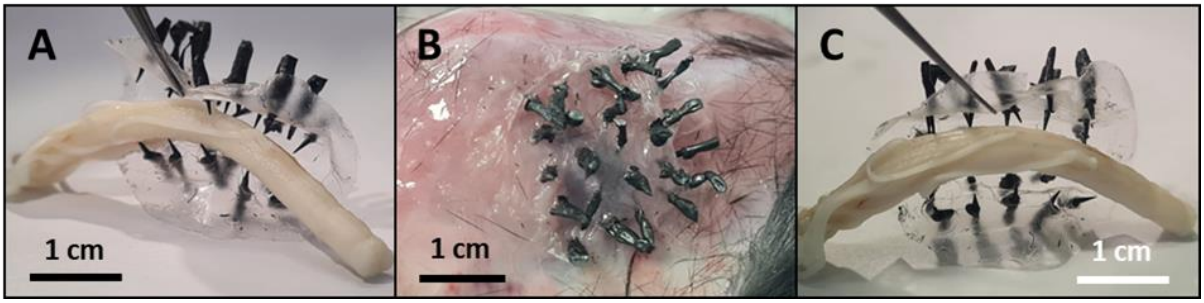

Fig. A2.12 – ***Ex vivo application of microneedle array: A-C)*** *Further images of flexible microneedle array on ex vivo samples of embalmed rat spinal cord (A & C), and mouse back tissue (B).*

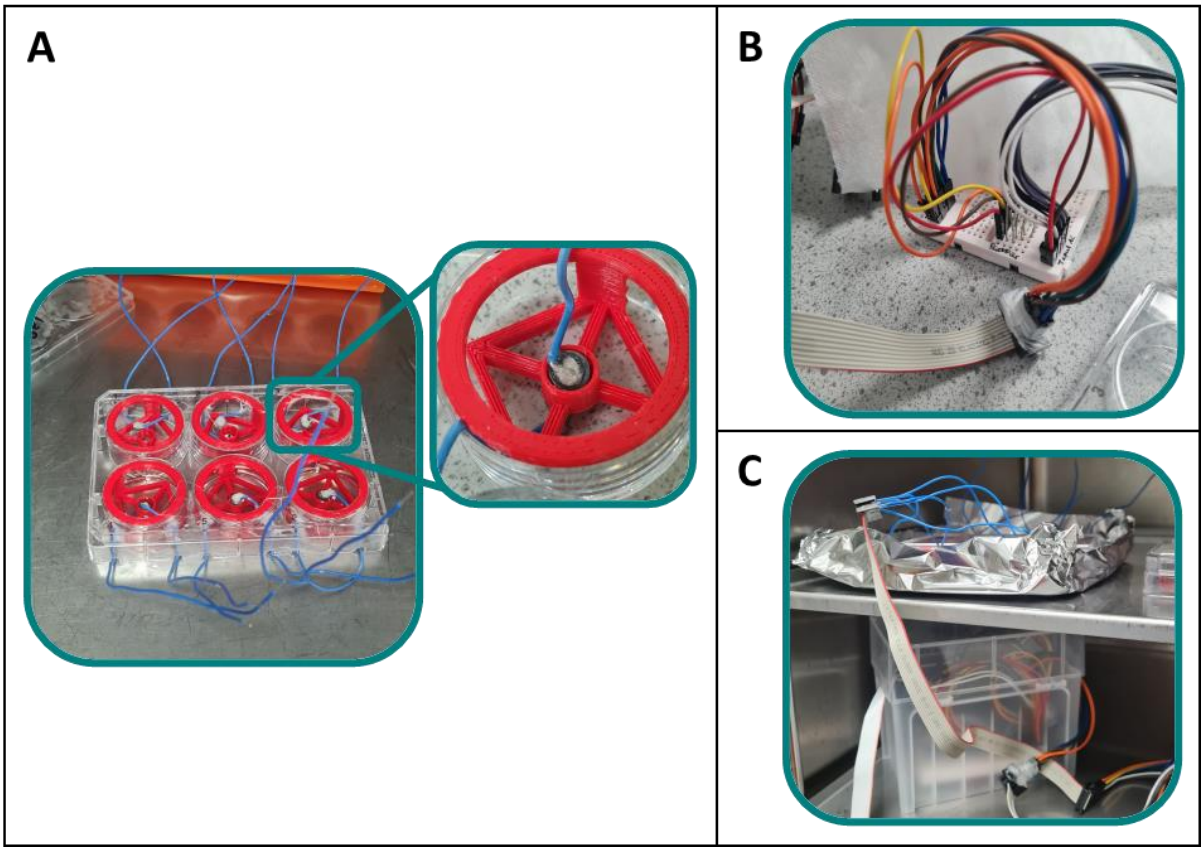

Fig. A2.13 – ***Electrical stimulation setup: A)*** *Electrical stimulation bioreactor, with 3D printed holders for disc electrodes.* ***B)*** *Combiner circuit, used to increase duty cycle of stimulation with IonOptix C-Pace rig.* ***C)*** *Setup connected within incubator.*

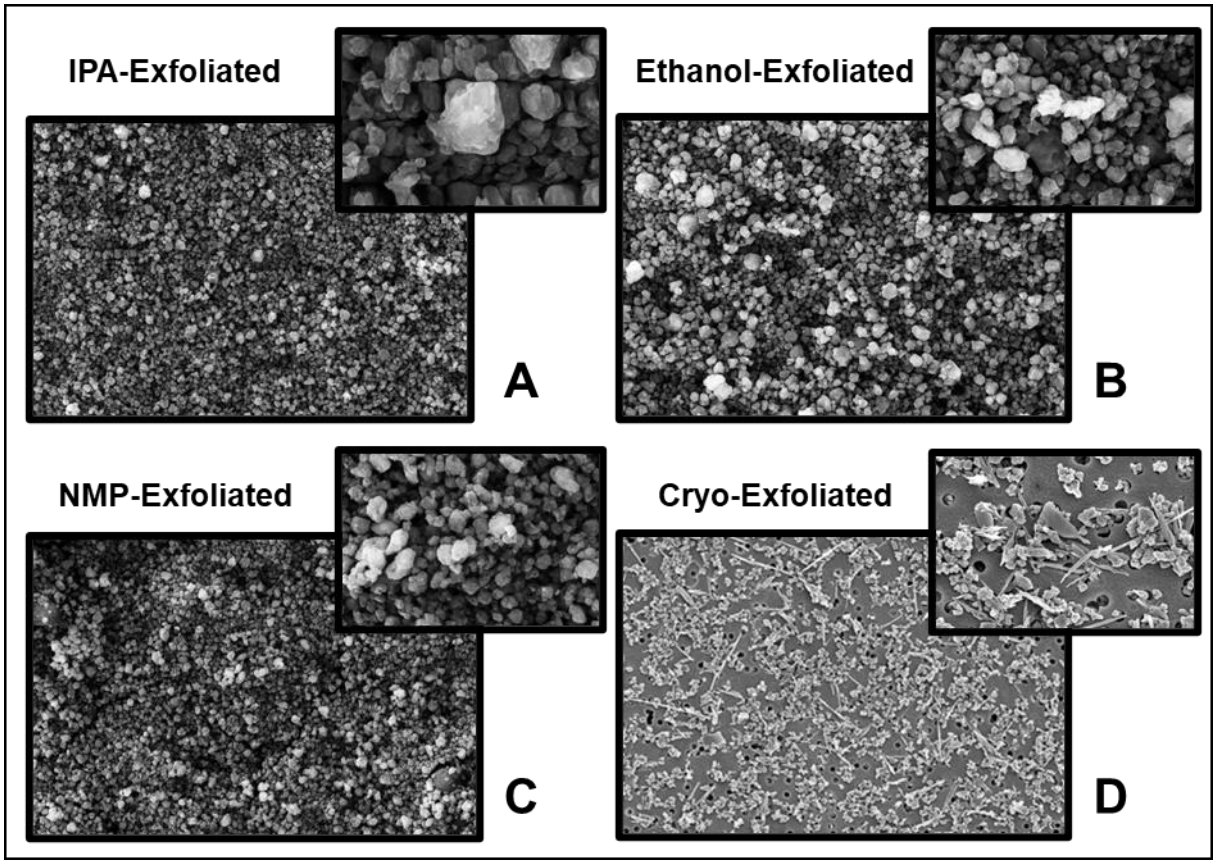

Fig. A3.1 – ***Exfoliation of boron in various solvents: A-C)*** *Exfoliation of amorphous boron using a sonic tip in isopropyl alcohol (A), ethanol (B) and NMP (C), leading to nanoparticulate morphology.* ***D)*** *Cryogenically assisted exfoliation of amorphous boron in NMP, leading to a mix of 0D, 1D and 2D morphologies.*

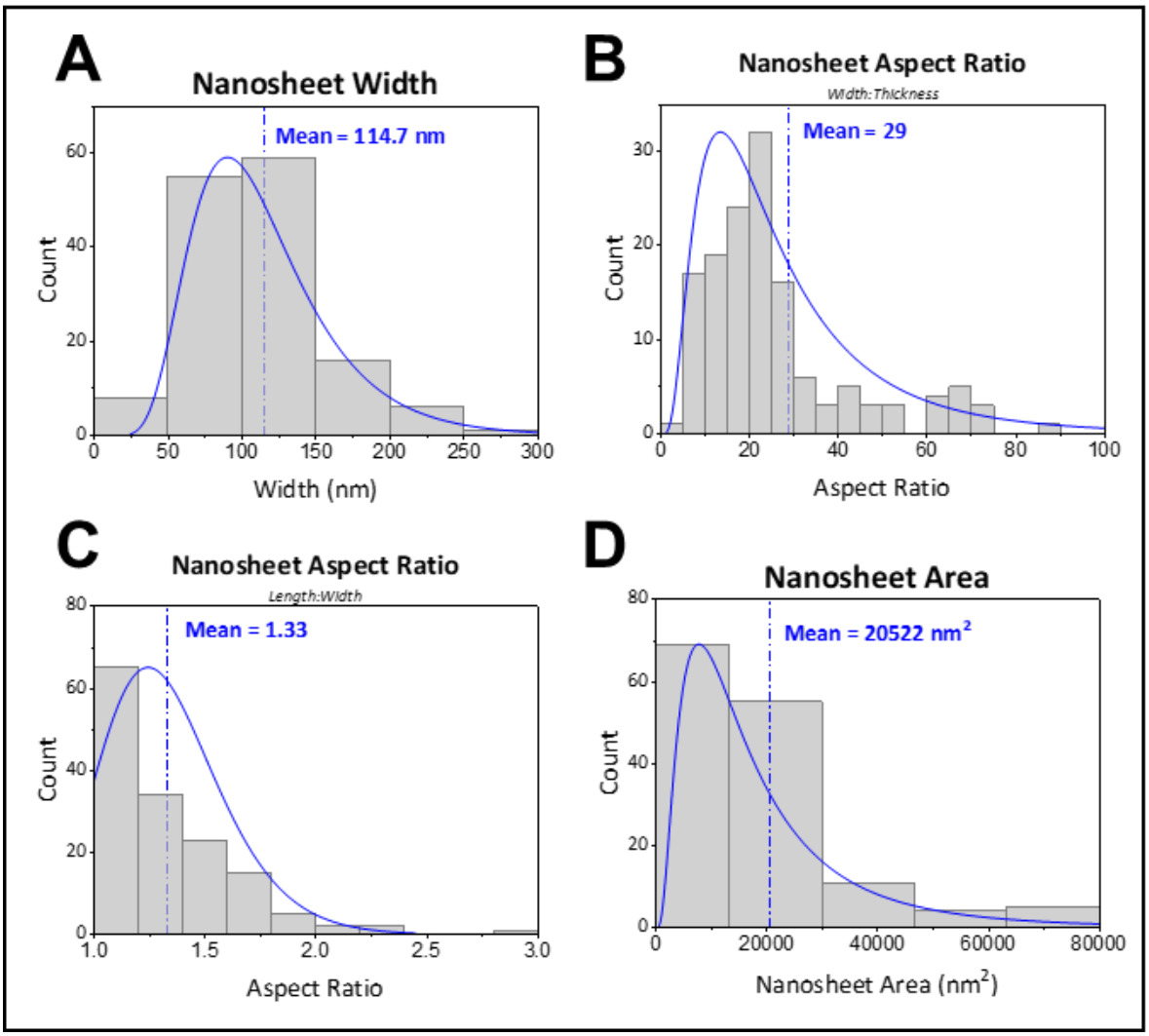

Fig. A3.2 - ***Further AFM characterisation of boron nanoplatelets:*** ***A)*** *Nanosheet width* ***B)*** *Nanosheet aspect ratio (width:thickness)* ***C)*** *Nanosheet aspect ratio (length:width)* ***D)*** *Nanosheet area.*

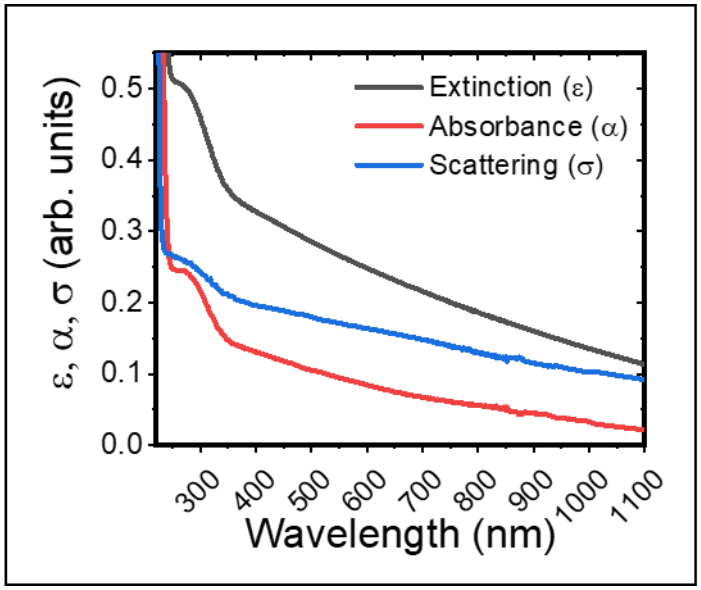

Fig. A3.3 – ***UV-Visible light spectroscopy (UV-Vis) of a boron nanosheet dispersion:*** *Extinction (ε), scattering (σ) and absorption (α) spectra typical of a semiconducting nanomaterial.*

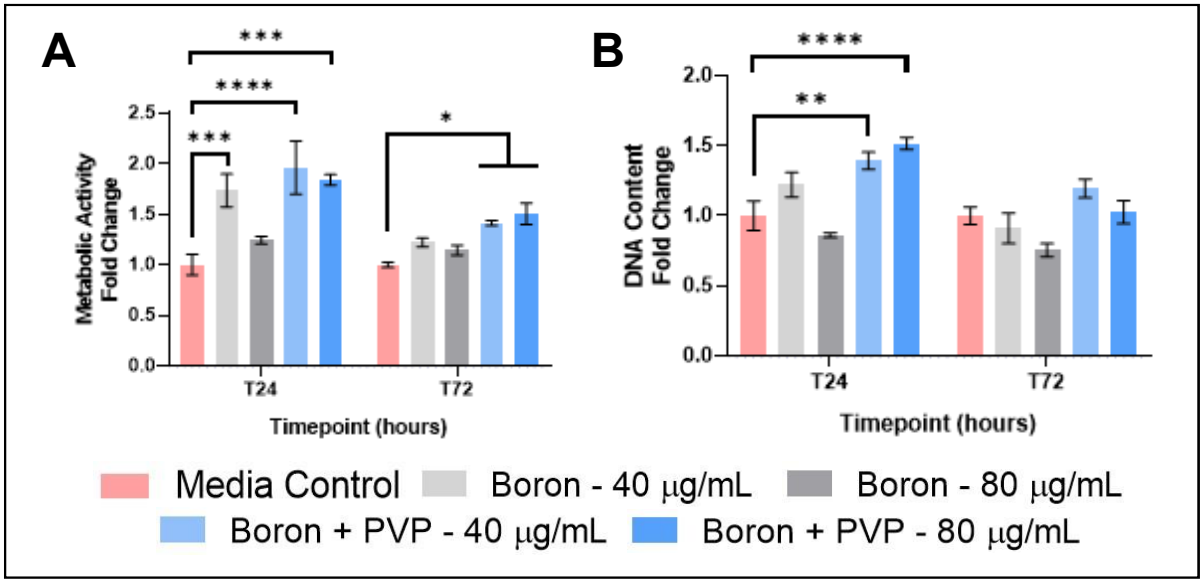

*Fig. A3.4 – **Biocompatibility of boron stabilisation: A-B)** It was necessary to determine if the nanosheets required any stabilisation to remain dispersed and sufficiently hydrophilic in physiological conditions, as is the case with many nanomaterials of non-biological origin. To investigate this, mouse motor neuron cells (NSC-34 cell line) were grown in the presence of boron, with and without stabilisation by PVP. This experiment demonstrated that PVP increased the biocompatibility of the boron nanosheets significantly, as seen by a significant increase in metabolic activity (A) and DNA content (B) for the PVP-stabilised material. Significances: *$p < 0.05$, **$p < 0.01$, ***$p < 0.001$, ****$p < 0.0001$.*

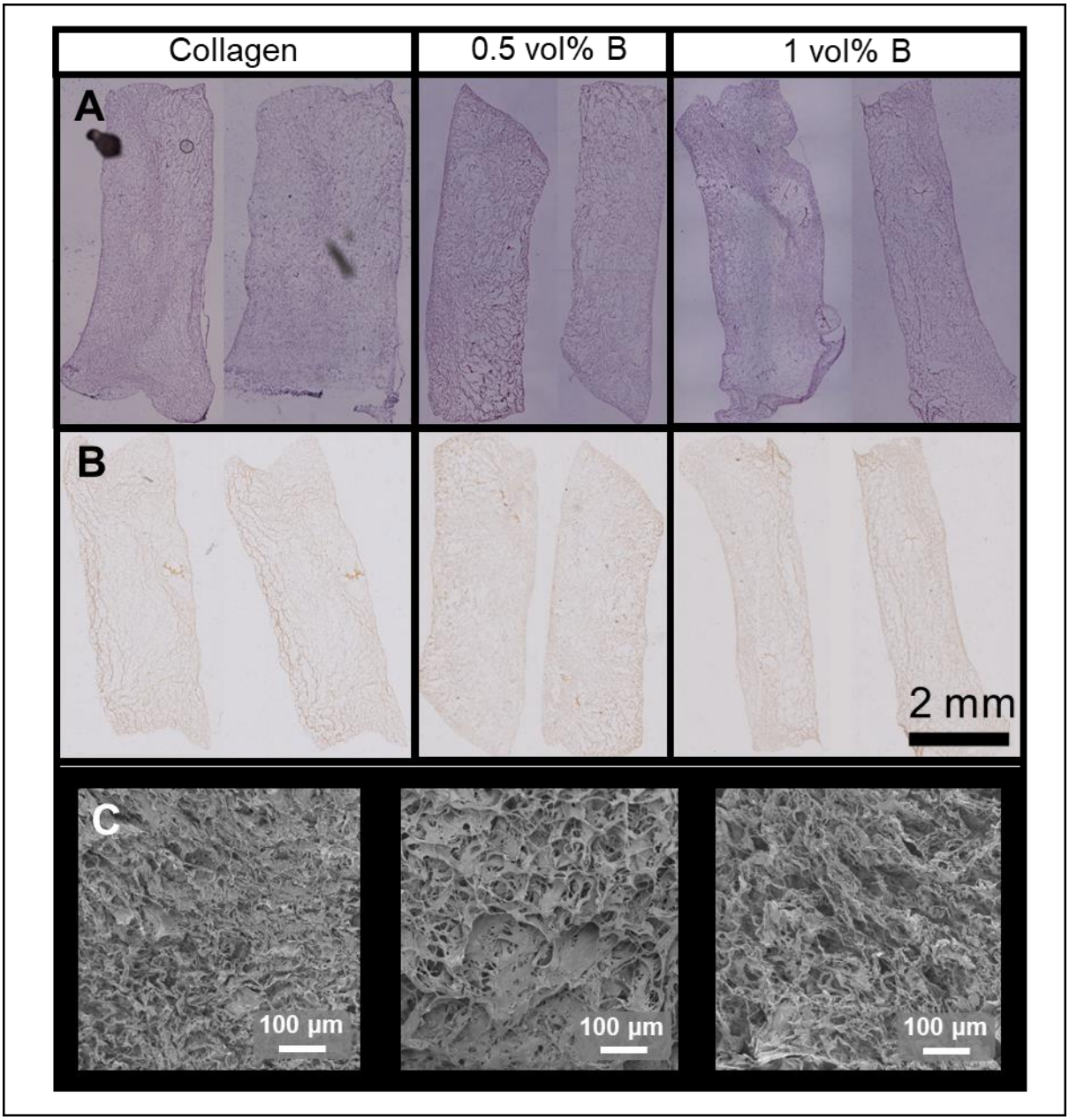

Fig. A3.5 – ***Histological staining of MC3T3s on BColl scaffolds: A)*** *H&E histological staining of collagen-boron scaffolds with MC3T3s.* ***B)*** *Alizarin Red histological staining of collagen-boron scaffolds with MC3T3s. Scalebars for A & B are 2 mm.* ***C)*** *SEM of MC3T3s in collagen-boron scaffolds. Scalebars are 100 µm.*

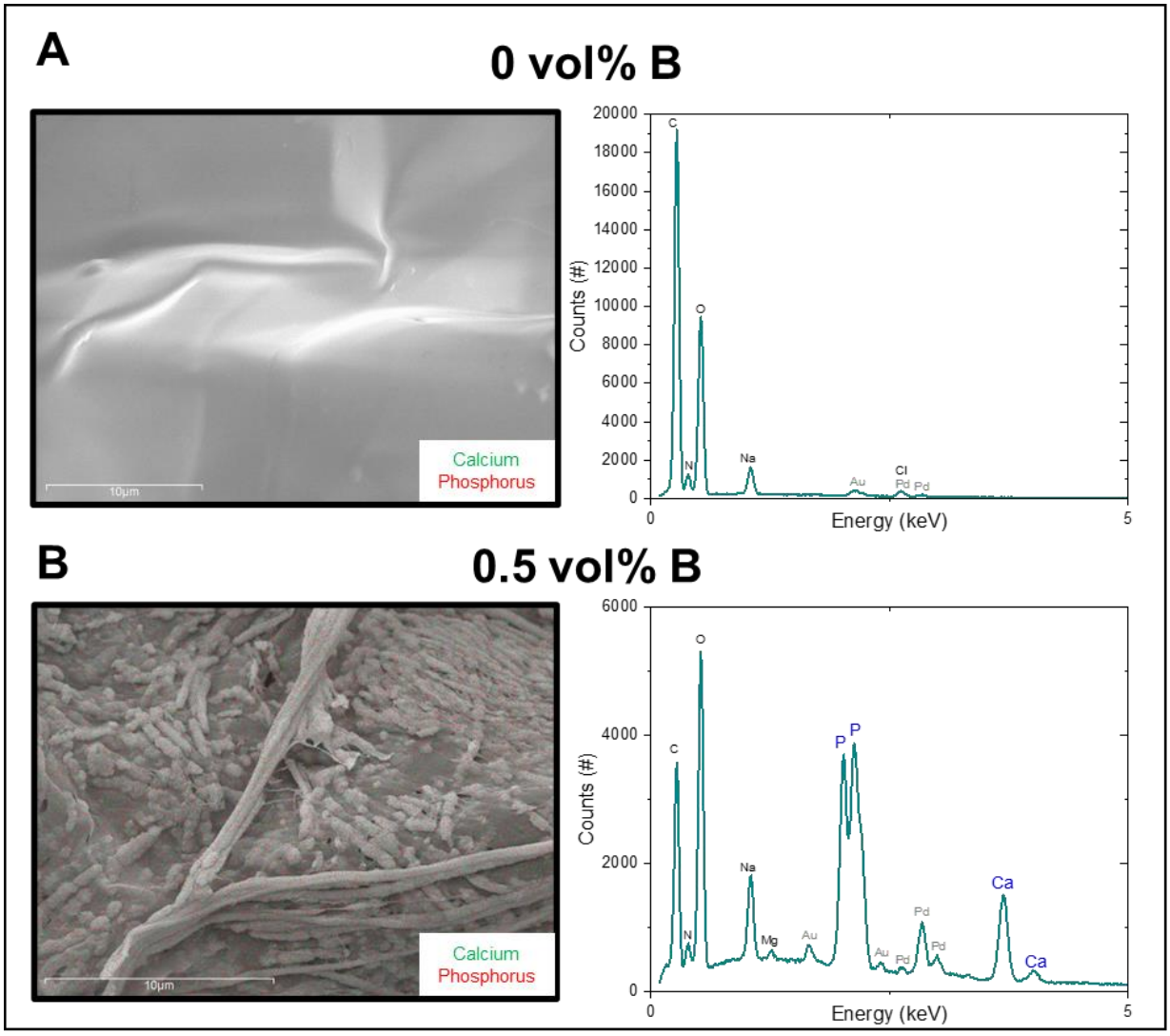

*Fig. A3.6 – **EDX of cell-laden BColl scaffolds: A-B)** EDX analysis of collagen (A) and BColl (B) scaffolds, showing that the deposits on boron-containing scaffolds consist of calcium phosphate, the main component of bone mineral, corroborating enhanced bone mineralisation in the presence of boron.*

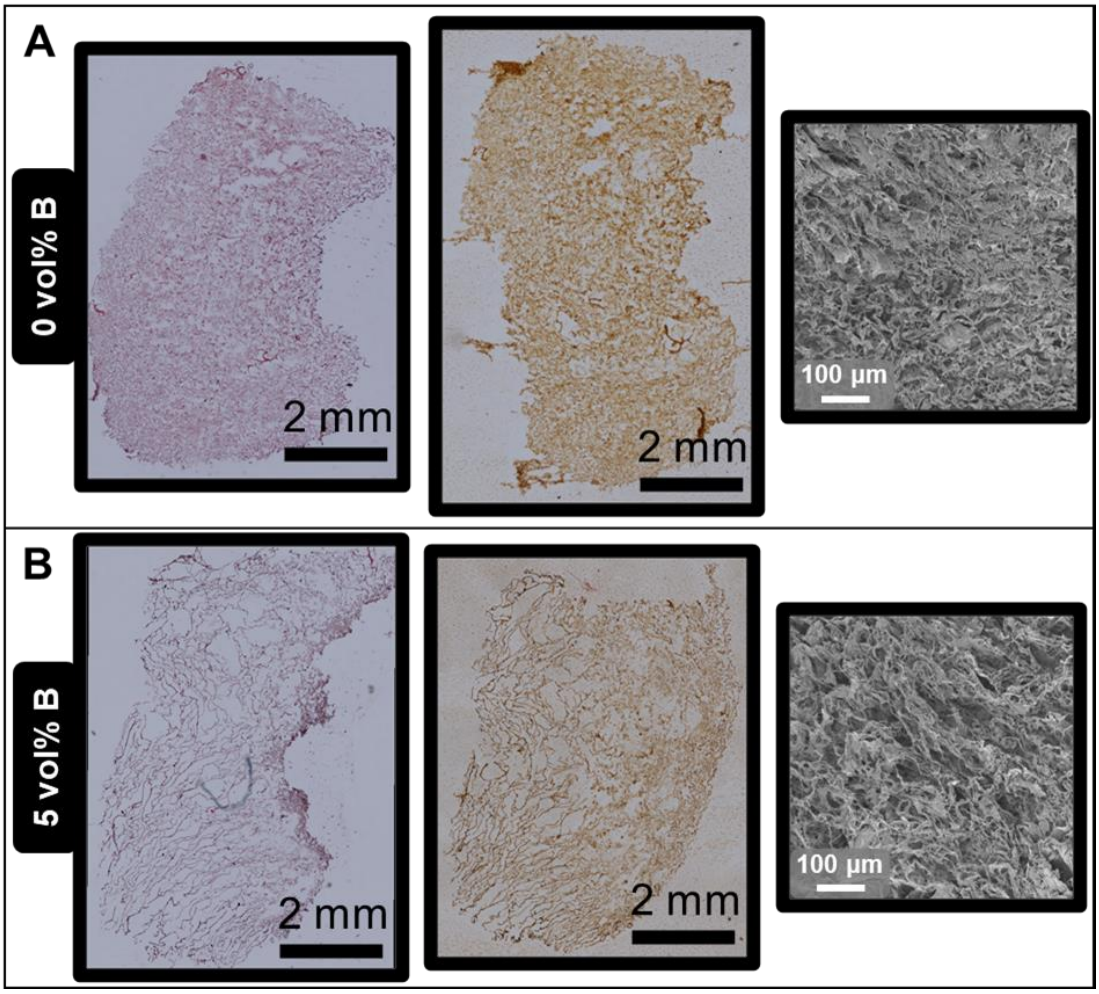

Fig. A3.7 – ***Histological analysis of rat mesenchymal stem cells on BColl scaffolds:*** *To assess the extent and distribution of calcium deposition on the scaffolds, histological staining was carried out with H&E and Alizarin Red. Alizarin Red staining indicated robust mineralisation of both collagen and BColl samples, throughout the sample. Scalebars 2 mm. SEM imaging was also carried out, to determine if there were any changes to the pore structure of the scaffolds following boron loading. Scalebars 100 µm.*

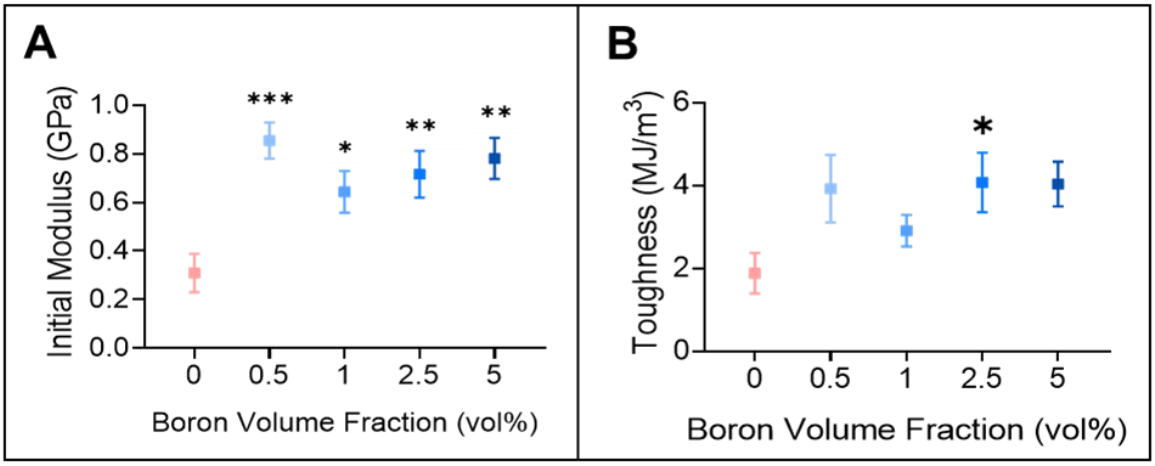

Fig. A3.8 – ***Further mechanical analysis of BColl films: A)*** *Tensile modulus of BColl films in first 0.5% of strain, the regime most often experienced by cells, showing significant reinforcement in most BColl groups.* ***B)*** *Toughness measurements for BColl films, showing a trend towards increased toughness for all samples. Significances: *$p < 0.05$, **$p < 0.01$, ***$p < 0.001$, ****$p < 0.0001$.*

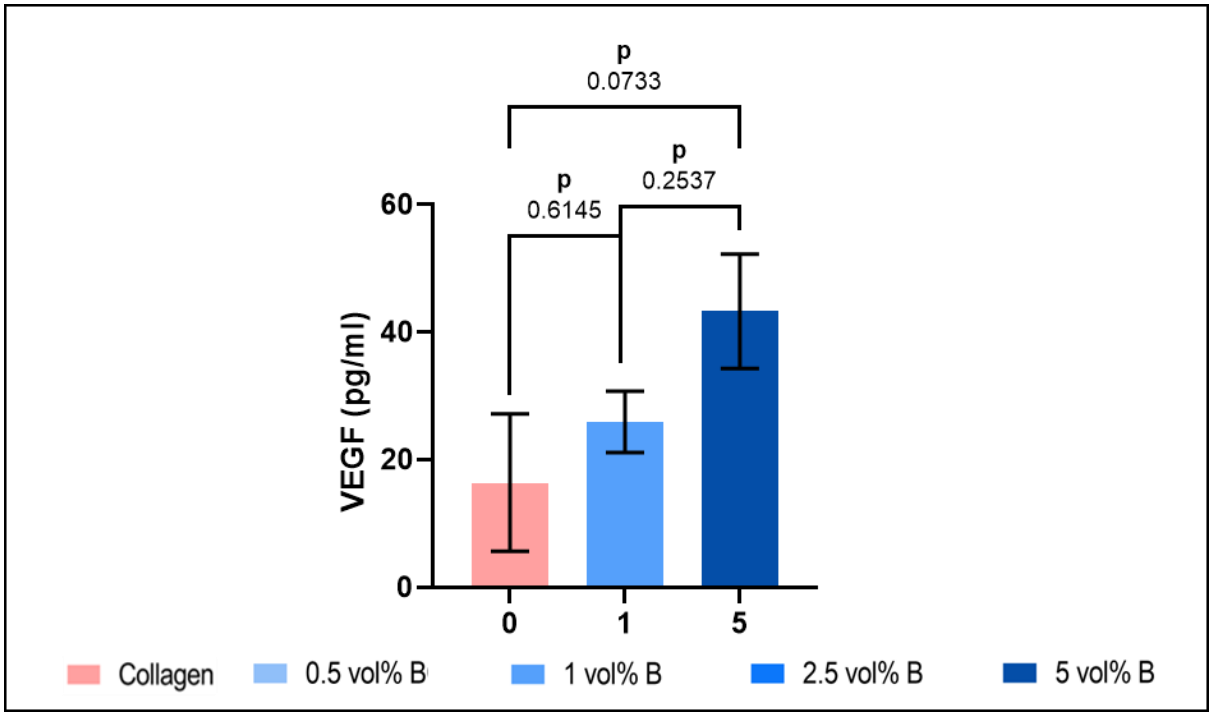

*Fig. A3.9 – **Assessment of angiogenic effect of boron:** Analysis of VEGF release by human ELISA in rat MSCs after 3D scaffold culture for 28 days, showing trend towards increased VEGF release with boron addition.*

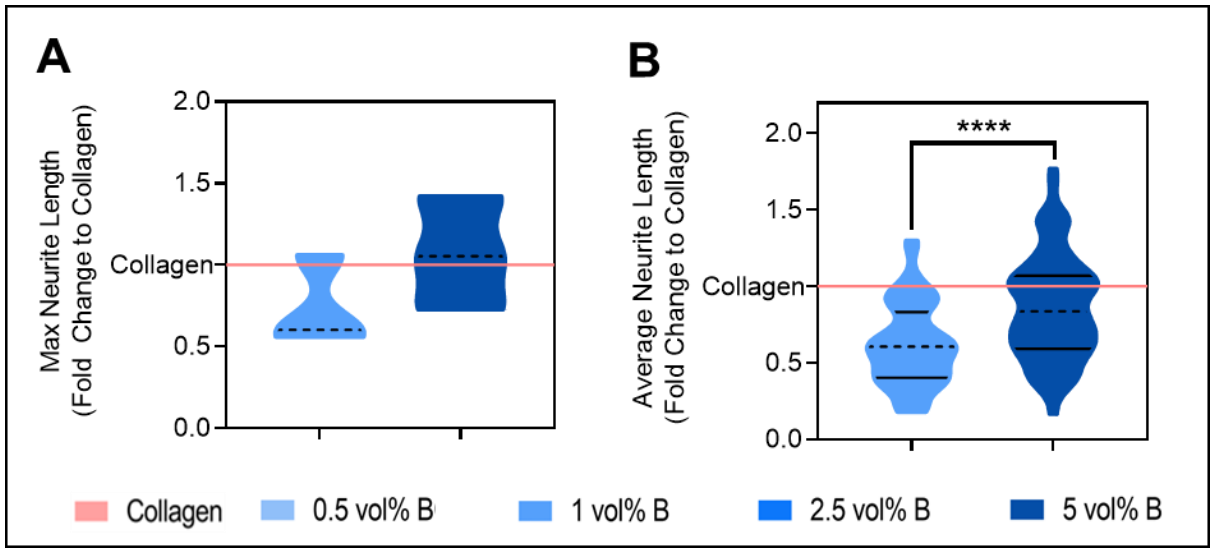

*Fig. A3.10 – **Assessment of neurogenic effect of boron: A)** Max neurite length and **B)** average neurite length of DRGs grown on surface of BColl scaffolds for 14 days.*